# DESIGN AND ANALYSIS OF ULTRA-WIDE BAND AND MILLIMETER-WAVE ANTENNAS

By

Zhang Yaqiong

SUBMITTED IN PARTIAL FULFILLMENT OF THE
REQUIREMENTS FOR THE DEGREE OF
DOCTOR OF PHILOSOPHY
AT
NATIONAL UNIVERSITY OF SINGAPORE
21 LOWER KENT RIDGE ROAD, SINGAPORE 119077
DEC 2010

NATIONAL UNIVERSITY OF SINGAPORE
DEPARTMENT OF
ELECTRICAL AND COMPUTER ENGINEERING

The undersigned hereby certify that they have read and recommend to the Faculty of Graduate Studies for acceptance a thesis entitled "**Design and Analysis of Ultra-wide Band and Millimeter-wave Antennas** " by **Zhang Yaqiong** in partial fulfillment of the requirements for the degree of **Doctor of Philosophy**.

Dated: DEC 2010

External Examiner: _____
Professor Kai-Fong Lee

Research Supervisor: _____
Guo Yong Xin, Leong Mook Seng

Examining Committee: _____
Professor Yeo Tat Soon

_____
Associate Professor Xudong Chen

_____
Assistant Professor Chengwei Qiu

# Table of Contents

# List of Figures

# List of Tables

# Abstract

Ultra-wideband (UWB) antennas and 60-GHz millimeter-wave antennas and arrays are analyzed and designed in this thesis for developing high-speed short-range wireless communications.

Firstly, a probe-fed crossed circle-disk monopole UWB antenna with stable omni-directional radiation pattern was studied. The antenna was then cut by half to form a crossed semi-circle monopole antenna with a top-loaded patch to reduce its height. Moreover, a new crossed semi-ring band-notch UWB antenna with L-shaped slots was developed.

Secondly, an effective equivalent circuit for a UWB antenna was proposed for possible co-designing with analog/digital integrated circuits in the time domain by using a new automatic physical augmentation with tuning method. The proposed method has been validated for modeling a spiral inductor and an MIM capacitor in a wide bandwidth.

Next, a new compact and multilayer UWB planar antenna was designed using the low-temperature co-fired ceramics (LTCC) technology, which gives the possibility of integrating RF circuits and antennas in a single substrate. The configuration of the proposed multilayer UWB LTCC planar antenna fully exploits the three-dimensional (3-D) integration

feature of the LTCC technology and explores a new way for antenna size reduction.

Lastly, novel 60 GHz integrated antennas and arrays using the LTCC technology were developed. A new wideband planar circularly polarized helical antenna array was designed and realized in LTCC. Moreover, a wideband LTCC aperture-coupled truncated-corner circularly polarized patch antenna with a sequential rotation feeding scheme was proposed in the 60-GHz band. The wire-bonding packaging technology with a T-network compensation was also studied in the 60-GHz band. Development of an active circularly-polarized antenna by integrating the antenna array with a low noise amplifier in LTCC was demonstrated to enhance the receiving power.

# Acknowledgements

I would like to take this opportunity to express my gratitude to my supervisors Assistant Professor Guo Yong Xin and Professor Leong Mook Seng for their invaluable guidance, constructive criticisms and encouragement throughout the course of my study. Without their kind assistance and teaching, the progress of this project would not be possible. Next, I would like to thanks my previous supervisor Associate Professor Ooi Ban Leong for his many in-depth technical suggestions and guidances in antenna design.

I would like to thank Dr. Sun Mei, Mr. Abdullah Rasmita and Mr. Liu Chang Rong for their invaluable support. I also would like to thank all the staff of RF/Microwave laboratory and ECE department, especially Mr. Sing Cheng Hiong, Mr. Teo Tham Chai, Mdm Lee Siew Choo, Ms Guo Lin, Mr. Neo Hong Keem, Mr. Jalul and Mr. Chan for their kind assistances and very professional help in fabrication, measurement and other technical and administrative support.

I would like to thank my friends in Microwave Laboratory, especially Dr. Fan Yijing, Dr. Irene Ang, Dr. Nan Lan, Dr. Wang Ying, Dr. Yu Yan Tao, Mr. Tham Jingyao, Dr. Zhong Zheng, Dr. Tang Xinyi, Dr. Zhong Yu and Dr. Ng Tiong Huat for providing the laughter, encouragement and valuable help throughout my Ph.D.

Finally, I would like to thank my family. I am very grateful to my parents for their ever-lasting supports and encouragement. I wish to express my sincere thanks and appreciation to Yang Bo for his encouragement, understanding and patience during the completion of this course.

Singapore Zhang Yaqiong

Dec 23, 2010

# Chapter 1

# Introduction

## 1.1 Background and Motivation

Recently, the requirement for wireless multimedia and wideband high rate applications has increased rapidly. At the same time, the contradiction between frequency resource and system capacity is more and more standing out with the development of modern wireless communication systems. As a result, the short distance wireless communication network has become one of the effective solution schemes.

Some emerging short distance wireless communication technologies such as Bluetooth, wireless local area network (WLAN), Ultra-wide band (UWB) and IEEE 802.15.3c (60-GHz wireless communication regulations) are all undergoing significant development due to their high date-rate transmission abilities in a short range of distance ($\leq$ 100m). Accordingly, the requirement of mobility and miniaturization of these wireless devices keep growing. As a critical part of the wireless devices, antennas have attracted a lot of attention.

The early UWB systems are mainly for radar, sensing, and military communications. Since Federal Communication Commission (FCC) of USA allocated 3.1-10.6 GHz unlicensed band for low power UWB communication, the UWB technology has attracted a lot

of attention as one of the most promising solutions for future high data-rate wireless communications, high accuracy radars, and imaging systems. Unlike the conventional narrow band systems, one kind of UWB systems utilizes very short pulses in transmission that results in an ultra-wideband spectrum with very low power spectral density. Compared with other narrow band systems, UWB systems have a high data rate around 100-500 Mb/s in the range of 10 meters. However, the output power of UWB transmitters is only around 1 mW. That is why a UWB system acts as a low power consumption one. This characteristic allows UWB radios to transmit high data rate signals without causing undesired interferences to the existing communication systems. However, some strong signal from other existing wireless communication systems may degrade the UWB system's performance. 802.11a WLAN systems occupy the 5-6 GHz spectrum and 802.11b/g WLAN systems cover 2.4-2.48 GHz frequency band. In order to suppress the strong interference signal from WLAN systems, filtering function is important to UWB systems. In the meantime, UWB antennas should have sufficiently broad operating bandwidths for impedance matching, good radiation pattern for indoor omni-directional communications and minimum distortion of the received waveforms for avoiding signal interference.

On the other hand, co-designing antennas with other function blocks could facilitate optimizing the whole communication system performance. For instance, in the traditional antenna and low-noise amplifier (LNA) design, both elements are matched to pure resistive 50-Ohm impedance. Matching the elements enables to maximize the power transfer. Nevertheless, in the context of co-integration where an antenna is close to the amplifier, other solutions than 50-Ohm impedance could be investigated in order to relax some constraints and to increase performances for the same power consumption. In this case, the challenge of co-design consists of finding the best tradeoff between the maximum power

gain of the LNA and the feasibility of an antenna with impedance which differs from 50 Ohms [1]. Even if an optimized antenna impedance is obtained for co-designing at certain frequencies, it is still difficult to evaluate the system performance in a wide bandwidth. The antenna S parameter can be used in the frequency co-simulation for the circuit design, but it would be invalid in the time-domain co-simulation with mixed analog/digital integrated circuits. Therefore, the need to have wideband modeling of UWB antennas is increased as the design complexity of the RF system increases.

The first part of this research intends to investigate the application of three-dimensional monopole antennas in UWB communications and wideband antenna modeling for system co-design based on an automatic physical augmentation method. In addition, a UWB planar antenna is also designed using the low temperature co-fired ceramics (LTCC) technology, which gives the possibility of integrating RF circuits and antennas in a single substrate.

A rapid growth of high-definition video and high-resolution imaging markets has stirred up a sudden need for extreme broadband gigabits per second (Gbps) wireless communications. Traditional wireless communication systems cannot satisfy this very high-data-rate requirement. For example, WiFi systems can only top out at 54 Mbps, where some can go as high as 108 Mbps. And UWB systems achieve around 480 Mbps data rate. The transmission data rate of all existing wireless system is far away from the Gbps requirement. In order to satisfy the future wireless communications' requirements for high speed, big capacity and good security, millimeter-wave (mmWave) solutions will be required. An IEEE standards group, 802.15.3c, is defining specifications for 60-GHz radios to use a few Gigahertz of unlicensed spectrum to enable very high-data-rate applications such as high-speed Internet access, streaming content downloads, and wireless data bus for cable replacement.

The targeted data rate for these applications is greater than 2 Gbps [2]. Accordingly, antennas have received a lot of interests.

In the second part of this thesis, various 60 GHz wideband antennas and arrays are designed. A new wideband planar circularly polarized (CP) helical antenna array is designed and realized. Moreover, an active antenna is formed through integration of a CP antenna array with an LNA in low temperature co-fired ceramics (LTCC). Through this research, power enhancement for mmWave high-speed short-range wireless communications is anticipated. The designed active receiving antenna will find applications in the 60-GHz wireless personal area networks (WPANs).

## 1.2 Literature Review

### 1.2.1 UWB Antenna Design and Wideband Circuit Modeling

A UWB antenna is a critical component in UWB radio systems. UWB antennas quite differ from the narrowband antennas, which mostly are resonant elements that support a standing-wave type current distribution and are tuned to particular centre frequencies. In contrast, as one sub-category of broadband antennas, UWB antenna designs seek sufficiently broad operating bandwidth for impedance matching and require non-resonating structures. On the other hand, for the pulse-based UWB systems, a very short time domain impulse (implying large bandwidth) is used to excite the antenna. Keeping the waveform of the impulse unchanged is another important issue of the UWB antennas. Otherwise, the ringing effect will arise and the signal is no longer impulse like, as shown in Figure. 1.1 [3].

The traveling wave antennas and frequency independent antennas are two kinds of classical broadband antennas. Frequency independent antennas, such as a log-periodic

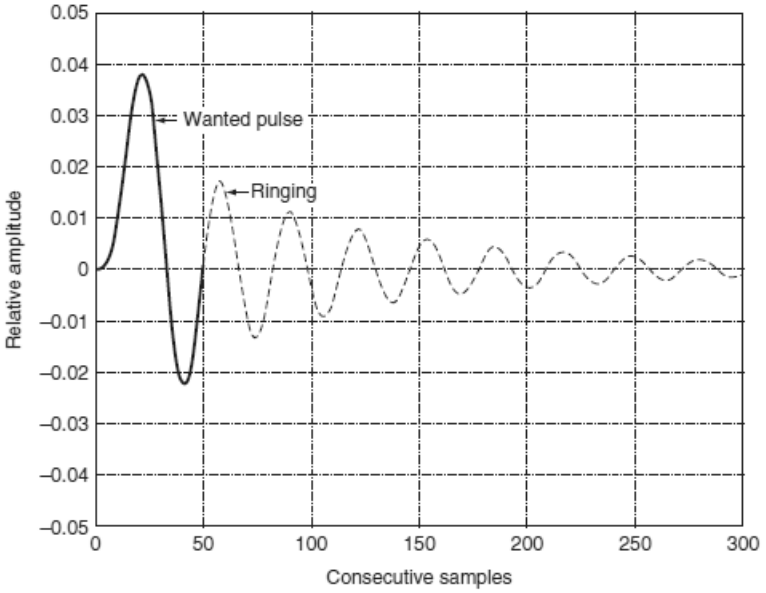


Figure 1.1: The ringing effect response of an antenna to impulse excitation.

antenna [4] and a conical log-spiral antenna [5], have a constant performance over broad bandwidth but frequency-dependent changes in their phase centers, resulting in distortion in the waveform of radiated UWB pulses [6]. Transverse electric magnetic (TEM) horns [7] and conical antennas [8] are typical representatives of the traveling wave antennas. These two kinds of antennas have very broad well-matched bandwidths and relatively stable phase centers, which are wonderful features for UWB system applications. However, the dimension of a traveling wave antenna is normally large due to the fact that sufficient length of the radiator is needed for efficient radiation. In practical UWB mobile devices, miniaturized antennas are desired due to limited device dimensions.

Since both travelling wave antennas and frequency independent antennas are not so suitable for modern UWB applications, a monopole antenna becomes a good candidate for UWB antenna designs due to its simple structure and good performance in both the time

and frequency domain [9, 10].

Three-dimensional monopole antennas have been demonstrated that they have true and stable omni-directional radiation pattern through the operation frequency band [11, 12], which is preferred by test antennas or base station antennas. Besides, since the UWB radios share part of the spectrum with the WLAN applications using the IEEE 802.1la (5.15-5.35 GHz, 5.725-5.825 GHz) protocol, ultra-wideband antennas with band-rejection property in the 5-6 GHz band have been proposed in order to mitigate the potential interference between different users and avoid degrading the performance of the affected radios [13–15].

The need to have wideband modeling for passive components/antennas is increased as the design complexity of the radio frequency (RF) system increases. In many wideband cases, a simple equivalent circuit model is not accurate anymore. The effect of parasitic elements on the component's response cannot be neglected. These parasitic effects can be simulated and modeled by using a full wave electromagnetic (EM) simulation. The obtained network scattering parameters from the EM simulation can be incorporated in the frequency co-simulation for the circuit design, but it would be invalid in the time-domain co-simulation, such as for mixed digital-analog integrated systems. In the literature, typically the equivalent circuits are accurate for narrow- or medium- frequency bandwidth. Therefore, extracting the equivalent circuit in a wide operation bandwidth would be of much interest. Normally, macromodeling or curve-fitting approaches are employed to get a non-physical mathematical model of the circuit as a black box [16]. The weakness of this approach is that this model cannot be used to correlate the model parameters with the layout parameters. Also such a black box model usually suffers from difficulty in ensuring passivity, stability and causality. To avoid such problems, physical circuit augmentation has

been implemented to realize wideband equivalent circuits [17–22]. This physical model is attractive because it can be correlated with the layout parameters and can guarantee passivity and stability of the equivalent circuits. In [20], the augmentation elements are chosen from a pre-designed SPICE-equivalent circuit library. The effect of adding a single circuit element on the admittance (Y) parameters is considered using two well-known circuit augmentation formulas, i.e., one for a parallel augmentation and the other for a series one. To simultaneously accommodate the series and shunt augmentation, a verification stage was added to identify the type of connection that was to be added to the existing series and shunt formulation [20].

Printed antennas have attractive characteristics like small, lightweight, low profile, conformal nature and mechanically robust, which make planar antennas such as microstrip patch antennas and slot antennas compatible with integrated circuits [23]. Among the proposed UWB antenna designs, the printed single-layer monopole antennas have been studied by many researchers due to their amazing characteristics such as wide impedance bandwidth, compact size and stable radiation properties [24–27]. It is also noted that LTCC planar monopole antennas for UWB applications were also reported [28], [29]. The utilization of the LTCC technology gives the possibility of building highly integrated circuits in a single substrate, as well as in different materials for RF circuits and antennas. Furthermore, some researches such as [30], [31] show the method in detail for integrating the antenna and transceiver electronics into compact modules with the LTCC technology.

### 1.2.2 60-GHz LTCC Wideband CP Antenna Design

Designs towards low-cost highly-integrated 60-GHz radios have been carried out using multi-layer LTCC based System-in-Package (SiP) technology [2, 32–34]. The specifications for antennas are defined according to the government regulations for unlicensed use, IEEE 802.15.3c standard and its usage model in the 60-GHz band [35]. Considering tolerances and variations in implementations, the targeted bandwidths of 60-GHz antennas can be simply defined as 3, 5, 7, and 9 GHz, respectively. The bandwidth covering 57-64 GHz is usually preferable. The gain of 60-GHz antennas is not specified although the maximum gain is limited by some regulations. As shown in TABLE 1.1 [36], the necessary combined gain values of transmitting and receiving antennas from a link budget analysis for 60-GHz antennas in indoor environment with a line-of-sight (LOS) path are given [35]. Taking the case of QPSK with the data rate of 2 Gbps at $d = 5$ meters as an example, one can see that the combined antenna gain required for the LOS path is 27 dBi. This requires antenna gain $\geq$ 13.5 dBi for each.

Recently, antenna designs are accordingly shifting from conventional discrete designs to Antenna-in-Package (AiP) solutions [37–41]. They have advantages over Antenna-on-Chip (AoC) solutions by providing higher gain and better package solutions [42]. The current AiP has developed from a single element to an array to achieve a higher gain [43]. In addition, in view of wireless access applications, the CP property is very desirable for 60-GHz antennas. The commonly used linear-polarized (LP) antenna necessitates rotating the transmitting and receiving antenna properly for polarization matching, particularly in the case of the line-of-sight (LOS) radio links. Using the CP antenna this problem can be mitigated while also allowing for reduction of interference from multi-path reflections.

Thus many investigations have been pursued on 60-GHz CP array antennas [44–48]. However, there is no report on the integration of the CP antenna with active circuits at 60 GHz in the package.

Table 1.1: THE COMBINED ANTENNA GAIN (dBi) REQUIRED FOR LOS PATH

| Distance(m) | QPSK(2 Gbps) | 16-QAM(4 Gbps) | 64-QAM (6 Gbps) |
|---|---|---|---|
| 1 | 13 | 19 | 24 |
| 5 | 27 | 33 | 38 |
| 10 | 33 | 39 | 44 |
| 20 | 39 | 45 | 50 |

## 1.3 Thesis Outline

This thesis consists of six chapters. Chapter 2 explores various feasibilities of probe-fed monopole antennas for UWB applications. A cross-circle monopole antenna, compact crossed semi-circle monopole antenna and band-notched crossed semi-ring monopole antenna are investigated both in frequency domain and time domain.

Chapter 3 introduces a new physical augmentation based wideband modeling technique. Firstly, the conventional circuit augmentation method is reviewed. Then, several modifications are applied to the basic physical augmentation method. For the new automatic physical augmentation with tuning method, the preliminary analysis of the circuit to decide the augmentation type is not needed. The type of augmentation to be performed can be determined automatically. This proposed methodology is validated for the broadband modeling of an spiral inductor, and an MIM capacitor. Finally, the proposed method has been successfully extended to extract the equivalent circuit for our UWB antenna.

Chapter 4 presents the design of a miniaturized UWB monopole antenna in LTCC. By fully exploiting the three-dimensional (3-D) integration feature of LTCC technology, a new compact and multilayer UWB planar monopole antenna design is introduced.

The development of an active antenna which integrates a CP antenna array with an LNA in LTCC is presented in Chapter 5. Firstly, various 60 GHz wideband antennas and arrays are designed in LTCC. A new wideband planar circularly polarized helical antenna array is designed in LTCC. Then an aperture-coupled truncated-corner patch antenna array with a sequential rotation feeding scheme is integrated with an LNA. In addition, the conventional bond wire technology is studied and a T-network bond wire compensation scheme is introduced. Furthermore, the fabricated active antenna prototype has demonstrated that wide impedance bandwidth, circularly polarized characteristic and enhanced peak gain can be achieved.

Finally, the conclusion and suggestion for future work will be given in Chapter 6.

## 1.4 Original Contributions

In this thesis, the following original contributions have been made:

1. A probe-fed crossed semi-circle monopole antenna with a top-loaded patch for height-reducing is proposed. Moreover, a new crossed semi-ring band-notch UWB antenna with L-shaped slots is developed.

2. Development of a new automatic physical augmentation with tuning method for wideband antenna modeling. The conventional circuit augmentation method is modified to remove the preliminary analysis of the circuit to decide the augmentation

type. The proposed methodology has been validated for the broadband modeling of a spiral inductor, and an MIM capacitor. Finally, the proposed method has been successfully extended to extract the equivalent circuits for our UWB antenna.

3. A new compact and multilayer UWB planar antenna design with the LTCC technology is proposed, which gives the possibility of integrating RF circuits and antennas in a single substrate. The configuration of the proposed multilayer UWB LTCC planar antenna fully exploits the three-dimensional (3-D) integration feature of the LTCC technology and explores a new way for antenna size reduction.

4. Novel 60 GHz integrated antenna and arrays using the LTCC technology are developed. A new wideband planar CP helical antenna array is designed on LTCC substrate. The modified LTCC helical antenna array achieves wide operating frequency band and good CP characteristic as well. The design takes the advantage of both traditional helical antenna and LTCC technology. The planar structure and the stripline feeding scheme give a good solution for helical antennas and circuits' integration.

5. A wideband LTCC aperture-coupled truncated-corner circularly polarized patch antenna with a sequential rotation feeding scheme is proposed for the 60-GHz band. The wire-bonding packaging technology with a T-network compensation is also studied in the 60-GHz band. Development of an active circularly-polarized antenna by integrating the antenna array with a low noise amplifier in LTCC is demonstrated to enhance the receiving power.

## 1.5 Publication List

The following publications are generated in the course of this research.

### 1.5.1 Journal Papers

1. Y. Q. Zhang, Y. X. Guo, and M. S. Leong, "A Novel Multilayer UWB Antenna on LTCC," *IEEE Trans. on Antennas & Propagat.*, Vol. 58, No. 9, pp. 3013-3019, Sep 2010.

2. M. Sun, Y. Q. Zhang, Y. X. Guo, M. F. Karim, O.L. Chuen, and M.S. Leong, "Integration of Circular Polarized Array and LNA in LTCC as a 60-GHz Active Receiving Antenna," accepted by *IEEE Trans. on Antennas & Propagat.*

3. A. Rasmita, Y. Q. Zhang, Y. X. Guo, and M.S. Leong, "Wideband Modeling of UWB Antennas Using Automatic Physical Augmentation with Tuning," submitted to *IEEE Trans. on Antennas & Propagat.*

4. Y. Q. Zhang, Y. X. Guo, and M. S. Leong, "Band-notched UWB Crossed Semi-ring Monopole Antenna," *Progress in Electromagnetic Research C (PIER)*, Vol. 19, 107-118, 2011.

### 1.5.2 Conference Presentations

1. Y. X. Guo, Y. Q. Zhang, A. Rasmita, and M. S. Leong, "Equivalent Circuit Modeling of UWB Antennas for System Co-Design," IEEE *Antennas and Propagat. Soc. Int. Symp. (APSURSI)*, pp. 1-4, 2010.

2. Y. Q. Zhang, B. L. Ooi, “The design of the cross semi-ring disc monopole antenna and the band-rejected cross semi-ring monopole antenna for UWB applications”, IEEE *AP-S Antennas and Propagat. Soc. Int. Symp.*, pp. 1-4, 2008.

3. Y. Q. Zhang, B. L. Ooi, and I. Ang, “UWB crossed circle disc monopole antenna”, IEEE *Antennas and Propagat. Int. Symp.*, pp. 677-677, 2007.

4. B. L. Ooi, Y. Q. Zhang, M. S. Leong, X. C. Shan, A. Lu, and C. H. Sing, “UWB Crossed Half Circle Disc Monopole Antenna”, IEEE *18th Int. Symp., Personal, Indoor and Mobile Radio Communications (PIMRC)*, pp. 1-5, 2007.

5. B. L. Ooi, Y. Q. Zhang, I. Ang, and M. S. Leong, “UWB half-circle cross-plate monopole antenna”, IEEE *Antennas and Propagat. Int. Symp.*, pp. 5717-5720, 2007.

# Chapter 2

# 3D Ultra Wideband Monopole Antenna Design

## 2.1 Introduction

UWB systems have recently attracted much attention for indoor communications. It has merits of high speed transmission rate, low power consumption and simple hardware configuration. Within a UWB system, the UWB antenna remains one of the challenging aspects in that the antenna should have sufficiently broad operating bandwidth for impedance matching, good radiation pattern and minimum distortion of the received waveforms in order to satisfy the FCC standard for UWB applications [49].

The study of UWB systems including antennas has been widely performed [50]. Planar monopole antennas have been extensively studied due to their very wide frequency bandwidth, good radiation performance and simple geometric structure [51–53]. However, planar monopole antennas exhibit unstable quasi omni-directional radiation pattern with frequency. In order to improve the stability of the radiation pattern, similar work has been conducted by Anob [11] and Ammann [12]. Their studies demonstrated that the

cross-shape monopole antennas can overcome the pattern distortion and keep stable omni-directional radiation pattern through the operation frequency band. On the other hand, a small-size antenna is always desired. A compact UWB antenna was proposed and studied in [54]. However, these studies did not cover the time domain impulse performance.

Although the UWB system requires a wide operating frequency band, which is from 3.1 to 10.6 GHZ (released by FCC on 2002) [49], interferences will appear in the wide bandwidth of UWB systems from other communication systems. As a result, a filtering function is needed by the UWB antennas. And the band-rejected cross-shape monopole is proposed [55].

In this chapter, we first studied a cross-plate probe-fed monopole antenna. Then two new semi-circle cross-plate monopole antennas are proposed through cutting the original cross-disc UWB monopole antenna by half and adding top-loaded circular and rectangular patches, respectively. After that, a new UWB monopole antenna with a band-rejection function is proposed. For all these proposed antennas, time domain responses are investigated by using CST microwave studio. The standard we employ to characterize the operating bandwidth is the frequency range for which $|S11| < -10$ dB. The S-parameters are measured using an HP8510A network analyzer. The far-field radiation pattern and gain are obtained by measurements in a compact antenna test range with N5230A antenna measurement system.

## 2.2 UWB Crossed Circle-Disc Probe-fed Monopole Antenna

### 2.2.1 Antenna Structure

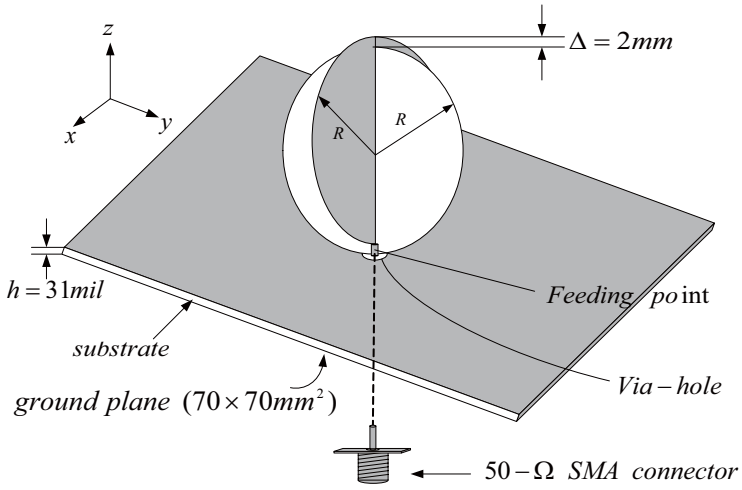


Figure 2.1: Geometry of a cross-circle disc monopole antenna

We studied with a cross-circle disk monopole antenna, which is based on the planar disk monopole antenna [56–58]. After some modification, the antenna structure is shown in Fig. 2.1. Fig. 2.2 shows the photographs of the fabricated cross-circle disc monopole antenna. It is mounted on the Rogers substrate ($\epsilon_r = 2.33, h = 31mil$) without any feed gap. The radius $R$ of the circle planar element is $14mm$ and the thickness of the copper plate is $0.2mm$. The two circle discs are placed orthogonally to form a crossed construction and are connected to a 50-$\Omega$ SMA connector through a finite ground plane ($70cm \times 70cm$). $\Delta(= 2mm)$ is the vertical distance between the two circle planar elements, which can make the fabrication easier.

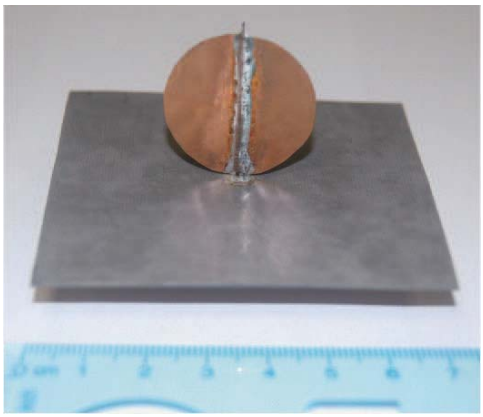

Figure 2.2: Photographs of the fabricated crossed circle-disc probe-fed monopole antenna.

### 2.2.2 Simulation and Measurement Results

The cross-circle disc monopole antenna designed for UWB applications was constructed, measured and performance evaluated. Fig. 2.3 shows the simulated and measured return loss for the antenna. Ansoft's 3D full-wave electromagnetic field software HFSS is used to simulate the 3D monopole antenna. The measured bandwidth shows to be $2.5 - 12.4GHz$. According to the papers [56–58], the circle disc monople antenna should have even wider bandwidth. Here the fabricated antenna's operation bandwidth is different with the simulated one at the upper frequency band. The reason is probably caused by fabrication and solder errors. The actual gap between the antenna and the ground is not exactly the same as those in the simulation model, which influences the upper frequency band performance significantly. However, here the frequency bandwidth from 2.5 GHz to 12.4 GHz can still satisfy the requirement of UWB systems. And the study of the radiation pattern of the antenna will be focused on for UWB applicaitions.

Fig. 2.4 shows the measured peak gain. The measured peak gains are between 2.1 and 6 dB in the frequency band.

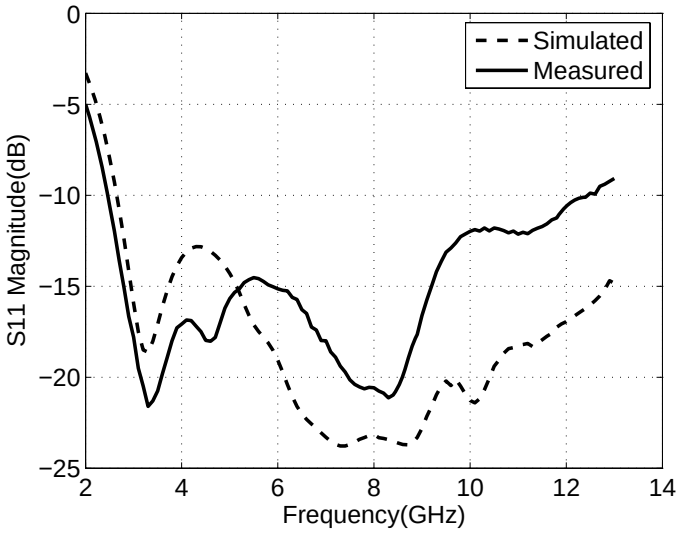


Figure 2.3: Measured and simulated return loss of the antenna shown in Figure 2.1

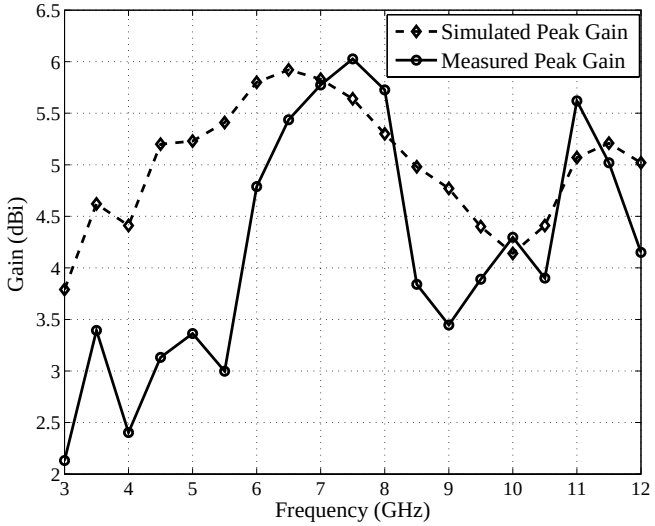


Figure 2.4: Simulated and Measured antenna gain in the UWB band

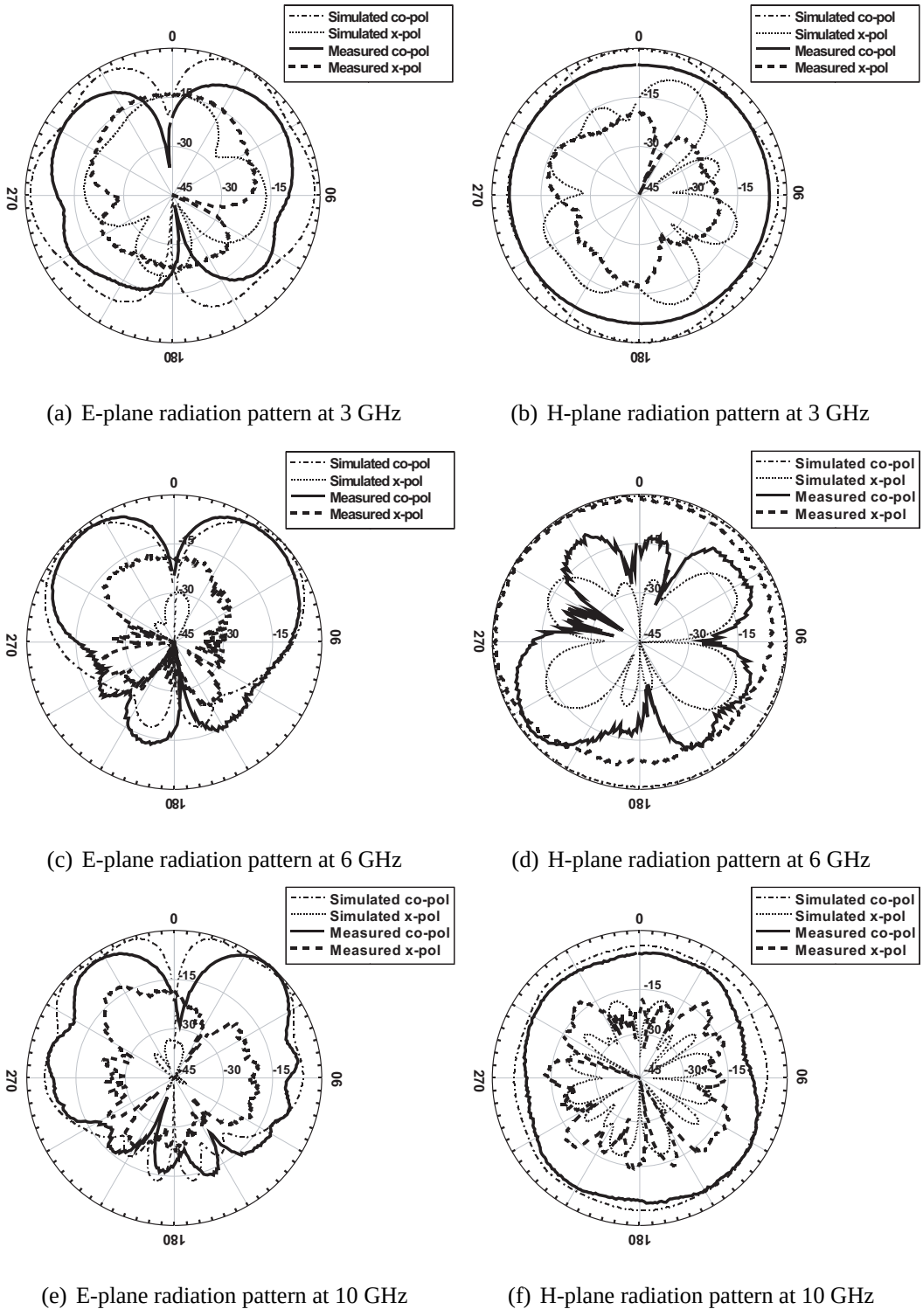


(a) E-plane radiation pattern at 3 GHz

(b) H-plane radiation pattern at 3 GHz

(c) E-plane radiation pattern at 6 GHz

(d) H-plane radiation pattern at 6 GHz

(e) E-plane radiation pattern at 10 GHz

(f) H-plane radiation pattern at 10 GHz

Figure 2.5: Simulated and Measured E- and H-plane radiation pattern for the cross-circle disc monopole antenna at $f = 3$, 6 and 10 GHz.

The measured radiation patterns are shown in Fig. 2.5 for 3, 6, and 10 GHz, respectively. The radiation patterns in the H-plane are almost omnidirectional across the ultra wide bandwidth.

### 2.2.3 Transmission Analysis in Time Domain

In addition to good impedance matching and radiation pattern, UWB antennas still require a minimum distortion of the time response waveform.

So it is necessary to perform a time-domain study of the electromagnetic fields signals emitted by the UWB antenna. Here a 3D EM simulation software CST MICROWAVE STUDIO is used to perform the time domain study. The incident voltage pulse used in the time-domain simulations is a normalized Gaussian pulse, which is shown in Fig. 2.6.

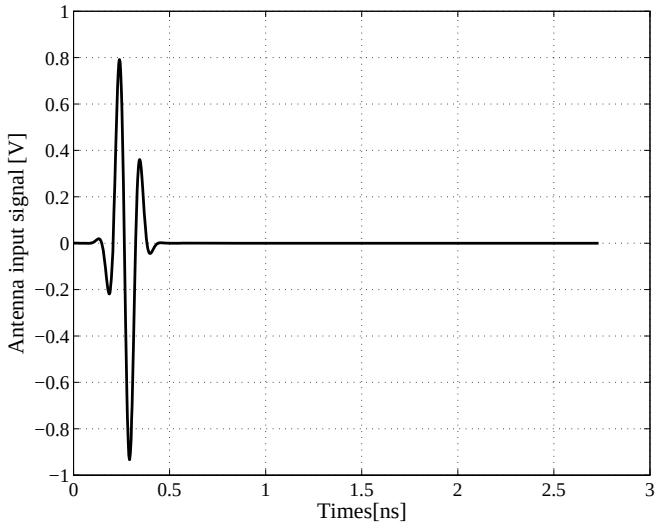


Figure 2.6: Antenna input signal in the time domain.

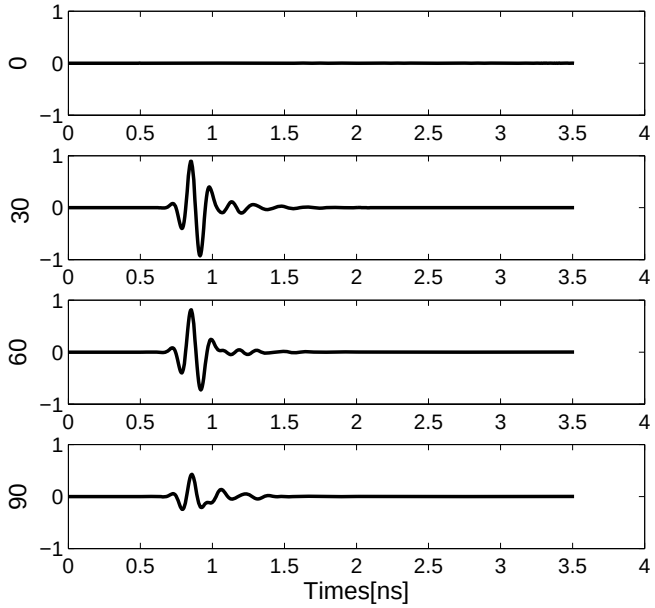


(a)

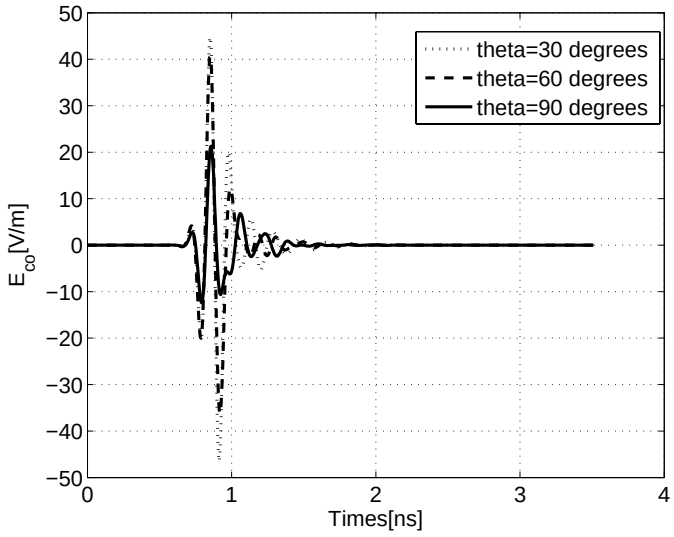


(b)

Figure 2.7: Time domain response of a Gaussian impulse for the co-polar component at different polar angles (E-plane). Due to symmetry, the cross-polar component is absent ($E_{cross} = 0$): (a) normalized E-plane response at ($\theta = 0^0, 30^0, 60^0, 90^0$); (b) superimpose E-plane response at ($\theta = 30^0, 60^0, 90^0$)

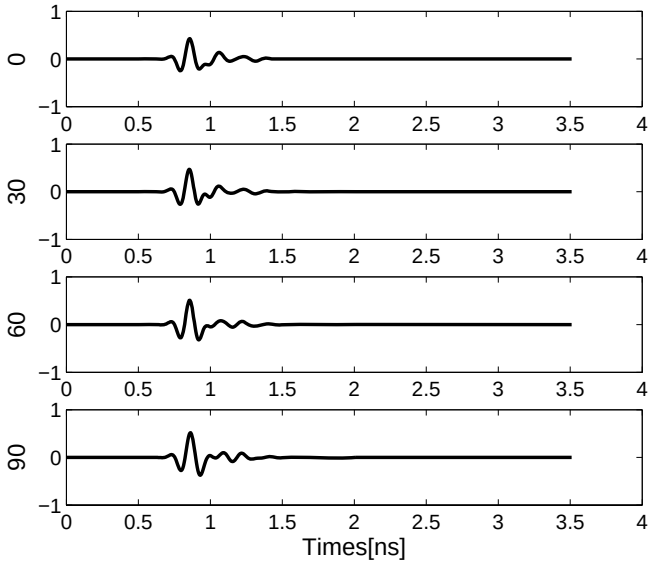


(a)

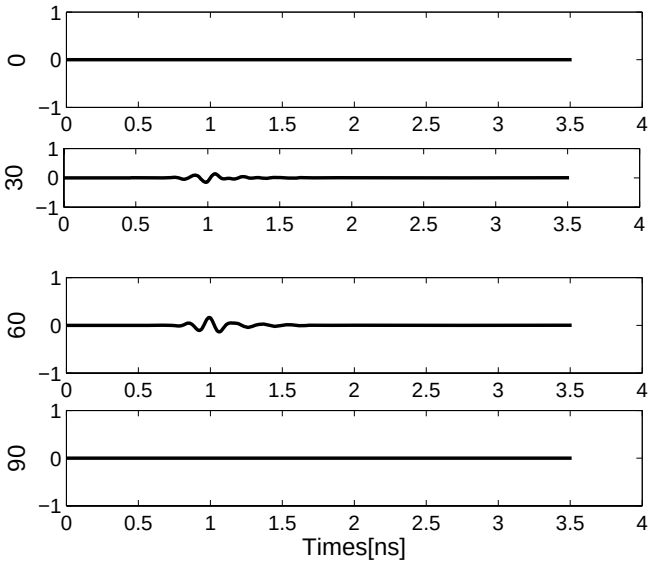


(b)

Figure 2.8: Time domain response of a Gaussian impulse at different polar angles (H-plane).(a) for the co-polar component; (b) for the cross-polar component

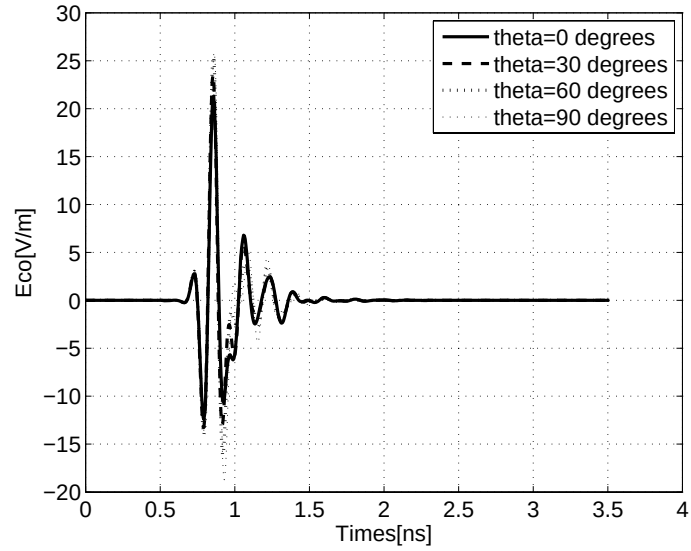


(a)

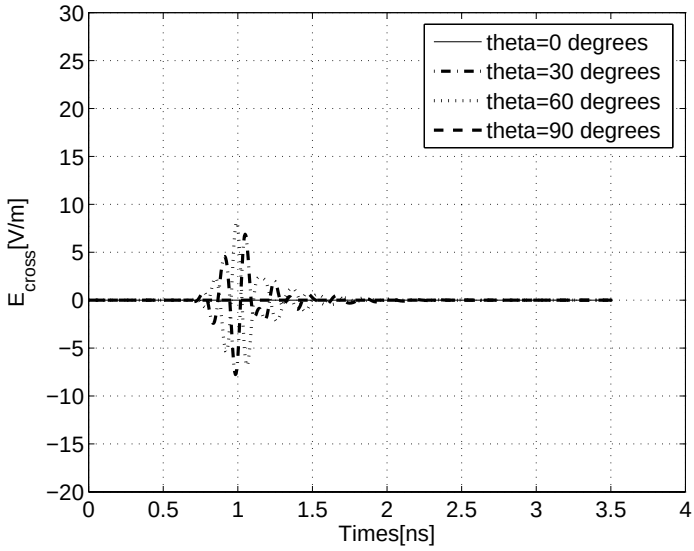


(b)

Figure 2.9: Time domain response of a Gaussian impulse (H-plane) for (a) co-polar and (b) cross-polar components ($\theta = 0^o$, $30^o$, $60^o$, $90^o$)

Fig. 2.7(a) and Fig. 2.8 show the normalized far field time-domain electrical signals at different elevation angle in the E- and H-plane, respectively. From the results, we can see that the ringing effect can be ignored.The pulse shape varies with the different observation angle; however, all entire pulse remains satisfactory at all angles.

Fig. 2.7(b) and Fig. 2.9 superimpose time-domain responses of all different angles together. It is easy to see that the cross-polar signals in the H-plane are very small as expected, compared with the co-polar signals.

## 2.3 UWB Semi-Circle Cross-Plate Probe-fed Monopole Antenna

In this section, a semi-circle cross-plate probe-fed monopole antenna is proposed through cutting the original cross-circle disc monopole antenna by half and adding a top-loaded circular and rectangular patches, respectively, to achieve ultra-wideband operation as well as size reduction.

### 2.3.1 Antenna Sturcture

The structure of the proposed antenna is shown in Fig. 2.10. It is comprised of a semi-circle cross-plate configuration with a circle-plate (Fig. 2.10(a)) or a square-plate (Fig. 2.10(b)) on the top. Fig. 2.11 shows the photographs of the fabricated proposed antennas.

This kind of semi-circle cross-plate monopole antennas is constructed with $0.2mm$ thick copper plate and mounted on the Rogers substrate ($\epsilon_r = 2.33, h = 31mil$). There is no feed gap between the feed poing and the top surface of the substrate.

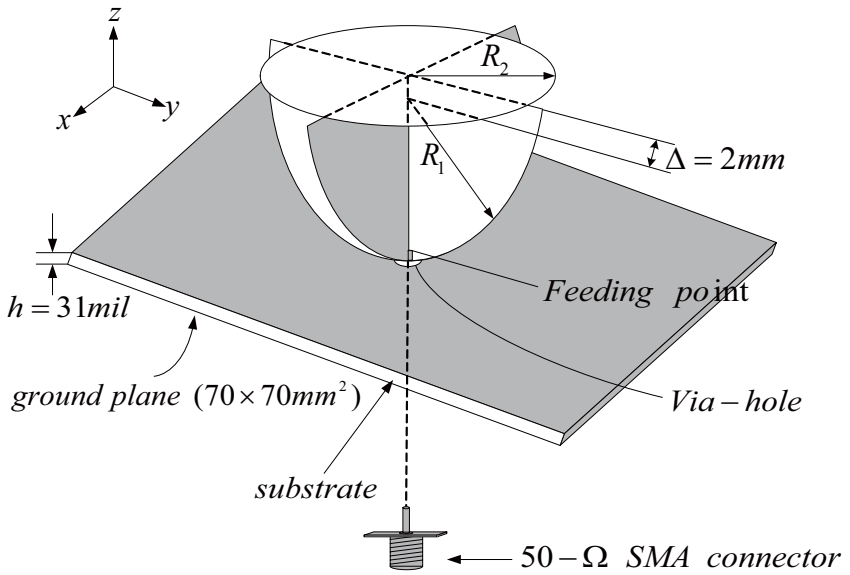


(a)

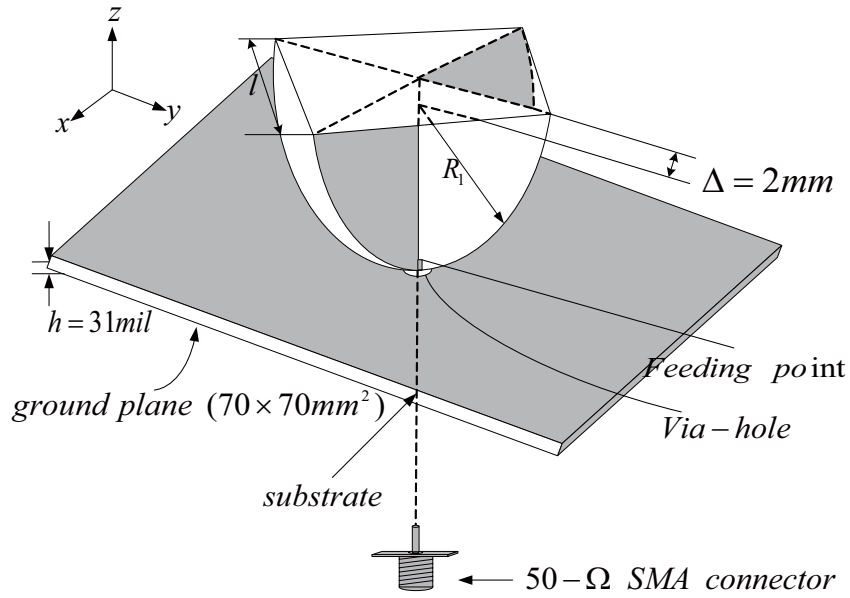


(b)

Figure 2.10: Geometry of the proposed semi-circle cross-plate probe-fed monopole antenna:(a) top-circle plate; (b) top-square plate.

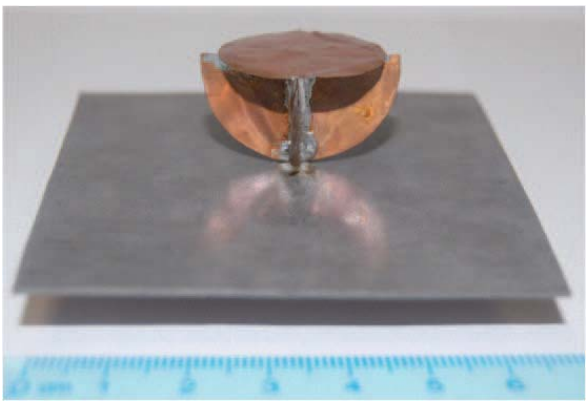

(a)

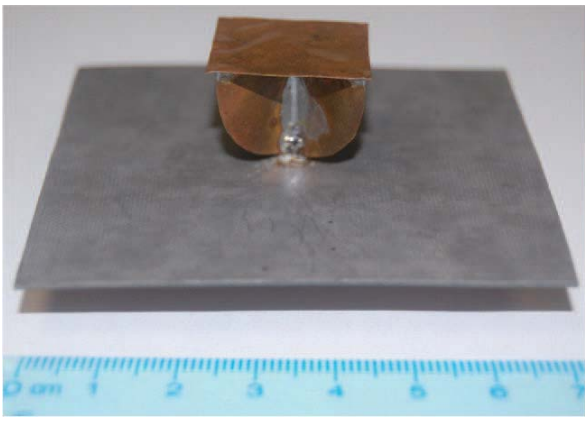

(b)

Figure 2.11: Photographs of the fabricated semi-circle probe-fed cross-plate probe-fed monopole antenna:(a) top-circle plate; (b) top-square plate.

The radius $R_1$ of the vertical semi-circle planar element is $14mm$. $\Delta$ ($= 2mm$) is the small vertical distance between the center of the two semi-circle planar elements and the center of the top small circle-plate. So the vertical height of the antenna is $R_1+\Delta = 16mm$. The two semi-circle plates are arranged to have a "crossed" structure and connected to a 50-$\Omega$ SMA connector through a finite ground plane ($70cm \times 70cm$).The radius $R_2$ of the top-circle planar element is $11mm$, and the length of the top-square element is $l = 22mm$.

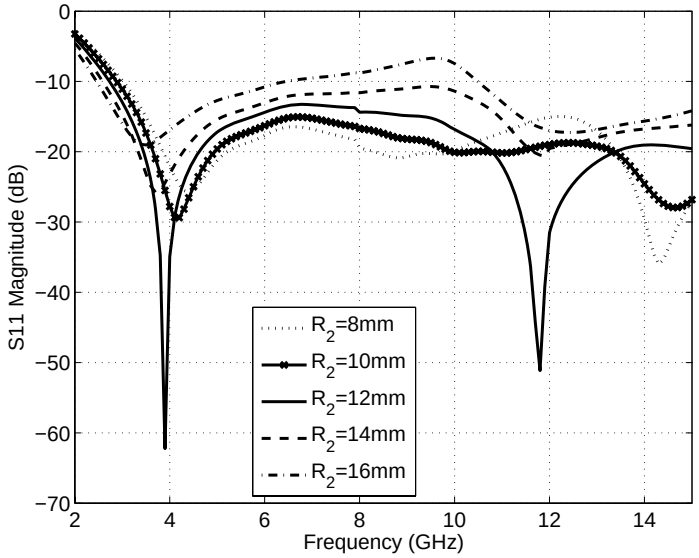


(a)

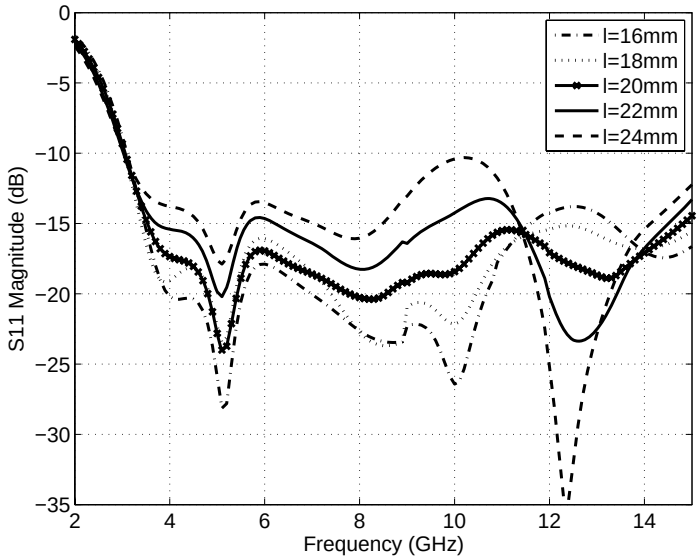


(b)

Figure 2.12: Variation of the size of the top-plate of the proposed antennas shown in Figure 2.10: (a) top-circle plate; (b) top-square plate.

In the proposed antenna design, the ”cross-plate” configuration makes it possible to improve the omnidirectional radiation performance. The use of a semi-circle plate instead of a full circle-plate reduces the size of the antenna by almost half. However, this will adversely affect the impedance matching. So we use a small top-circle/top-square copper plate to modify the impedance matching to satisfy the UWB bandwidth requirement. Fig. 2.12 exhibits the return loss of the proposed antenna with respect to its top-plate size, $R_2$ or $l$. For the top-circle plate case, when the top-circle plate's size is increased, the lower frequency band will be lowered. However, $R_2$ should be smaller than $14mm$ for keeping the ultra-wide band performance. For the top-square case, the edge length $l$ of top-square plate should not be greater than $24mm$.

### 2.3.2 Simulation and Measurement Results

Simulation and measurement results of the return loss in Figure 2.13 show that the bandwidth of the proposed antennas is from 2.8-13 GHz (about 129%), which satisfies the UWB antenna requirement.

The simulated and measured radiation patterns at 3GHz, 6GHz and 10GHz are plotted in Fig. 2.14, respectively. Since both top-circle copper plate antenna and top-square copper plate antenna have similar far-field radiation patterns, here only the far-field radiation patterns for the top-circle case are shown. In the H-plane (x-y plane), the co-polar pattern are nearly stable to be omnidirectional throughout the whole ultra-wide band of operation. Even with the size reduction, the omnidirctional characteristics of the radiation pattern are not deteriorated compared with the cross-circle plate probe-fed monopole antenna.

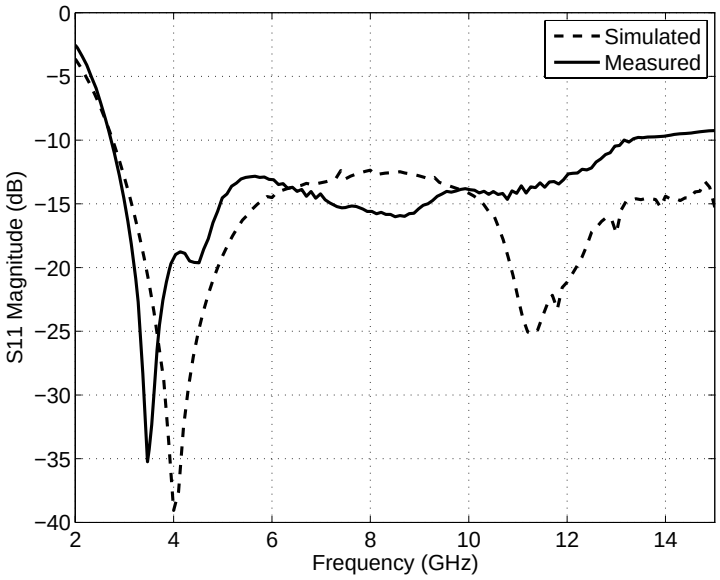


(a)

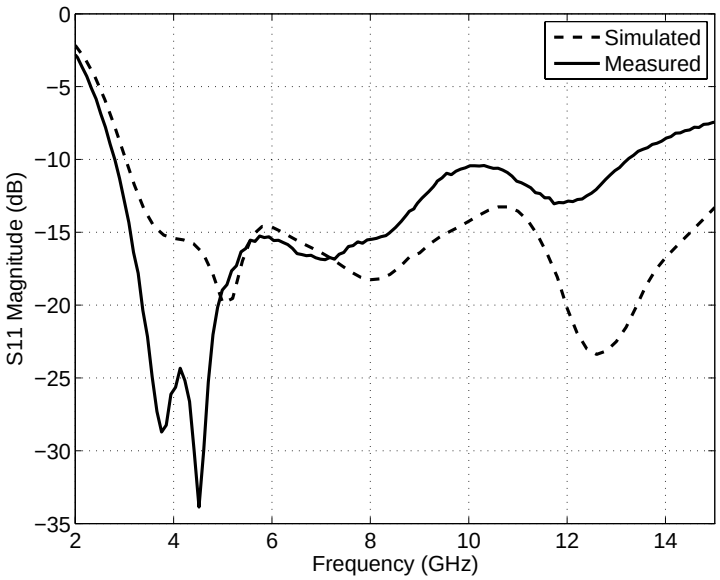


(b)

Figure 2.13: Measured and simulated return loss of the proposed antennas shown in Figure 2.10: (a) top-circle plate; (b) top-square plate.

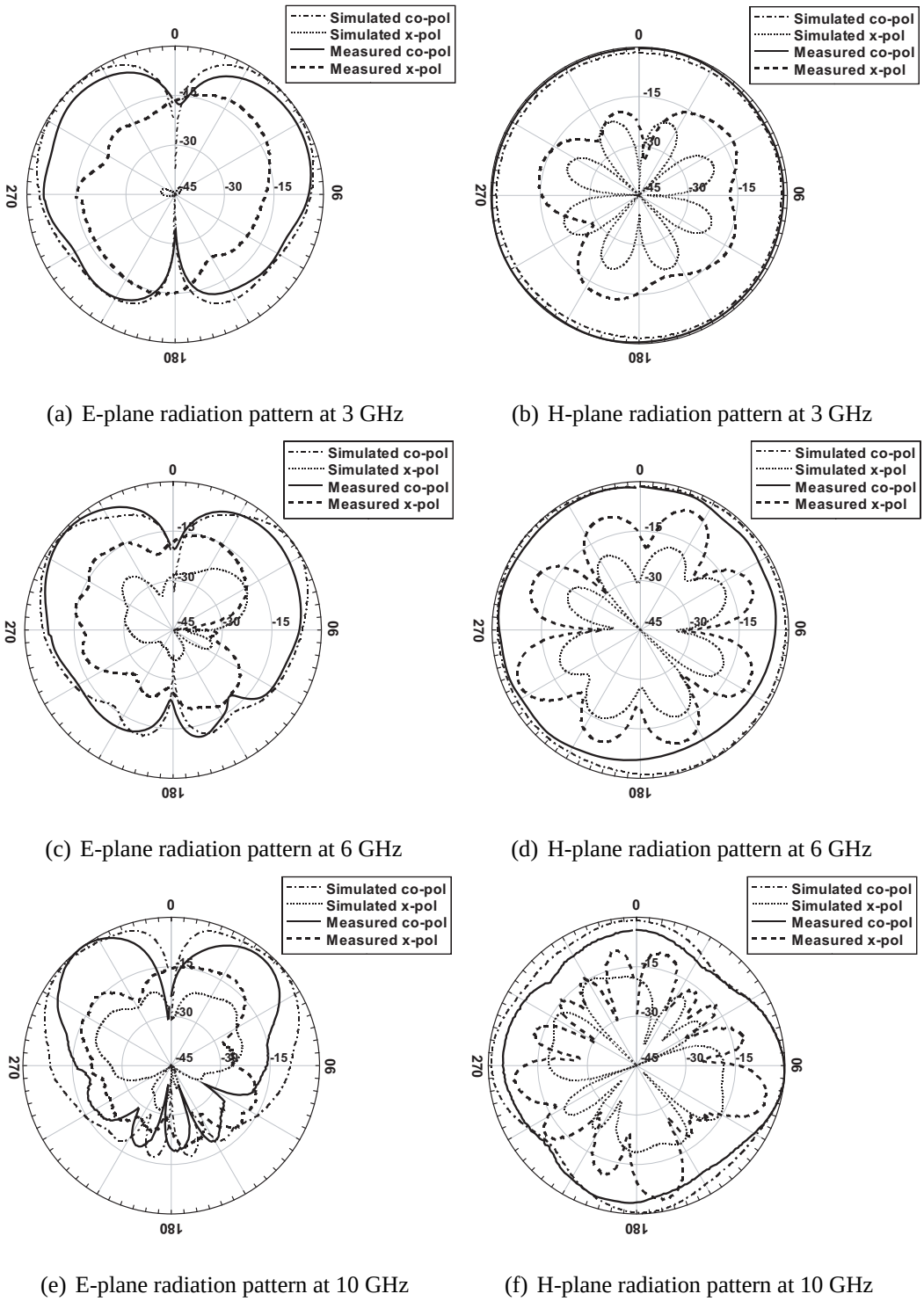


(a) E-plane radiation pattern at 3 GHz

(b) H-plane radiation pattern at 3 GHz

(c) E-plane radiation pattern at 6 GHz

(d) H-plane radiation pattern at 6 GHz

(e) E-plane radiation pattern at 10 GHz

(f) H-plane radiation pattern at 10 GHz

Figure 2.14: Simulated and measured E- and H-plane radiation patterns for the semi-circle cross-plate with top-circle plate monopole antenna at $f = 3$, 6 and 10 GHz.

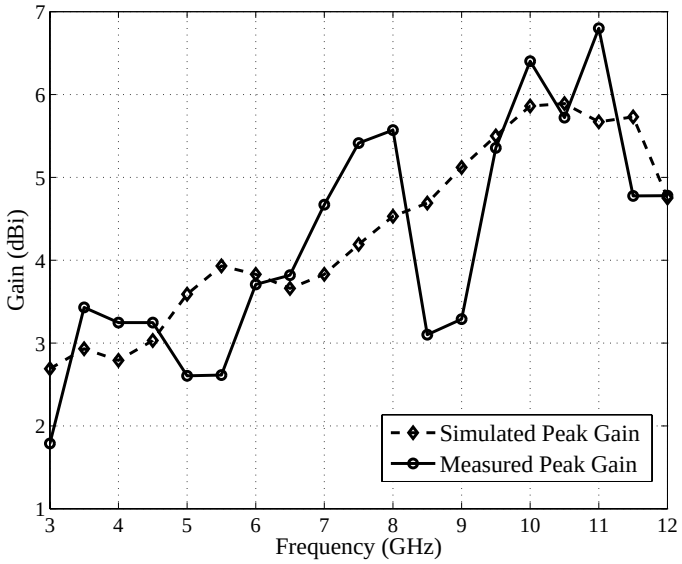


(a)

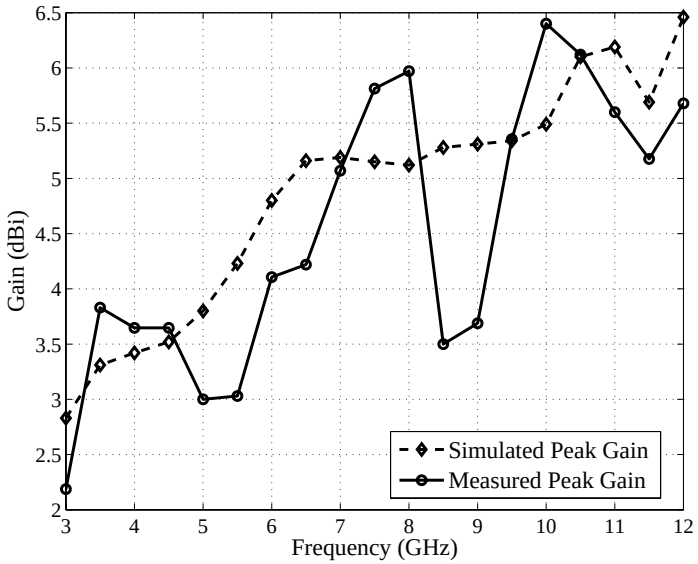


(b)

Figure 2.15: Measured and simulated peak gain of the proposed antennas shown in Figure 2.10: (a) top-circle plate; (b) top-square plate.

The measured peak gains with frequency of the top-circle copper plate antenna range from 1.78 to 6.4 dB, as shown in Fig. 2.15(a). And the measured peak gains of the top-square copper plate antenna are shown in Fig. 2.15(b). Both antennas have similar performance on peak gains. However, the measured peak gains of both antennas have a drop around 5 GHz and 8.5 GHz compared with corresponding simulated one. The peak gain drop might be caused by the fabrication tolerance.

### 2.3.3 Transmission Analysis in Time Domain

The semi-circle cross-plate probe-fed monopole antenna is reduced almost by half compared with the cross-circle plate monopole antenna. However, a good time-domain performance is one of basic requirements for UWB antennas. Here we do a detailed investigation on the time-domain response of the proposed antenna.

The incident voltage pulse used in time-domain simulations is a normalized Gaussian pulse, which is shown in Fig. 2.6. The normalized far field time-domain electrical signals of the semi-circle cross-plate top-circle probe-fed monopole antenna at different elevation angles in the E-plane and H-plane are shown in Fig. 2.16(a) and Fig. 2.17, respectively. Fig. 2.16(b) and Fig. 2.18 show the superposition of the time-domain responses at all different angles. Since the top-square copper plate antenna has similar time domain responses, here we do not show them. The ringing effects shown in these figures are so small that they can be ignored. So all the pulses still remain satisfactory at all angles after the size reduction of the antenna compared with cross-circle monopole antenna in section 2.2. It can be easily observed that the cross-polar signals in the H-plane is small as expected, compared with the co-polar signals.

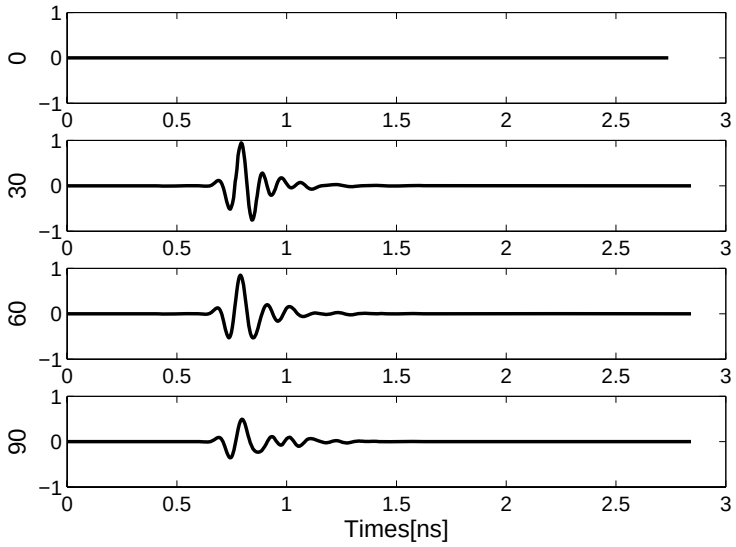


(a)

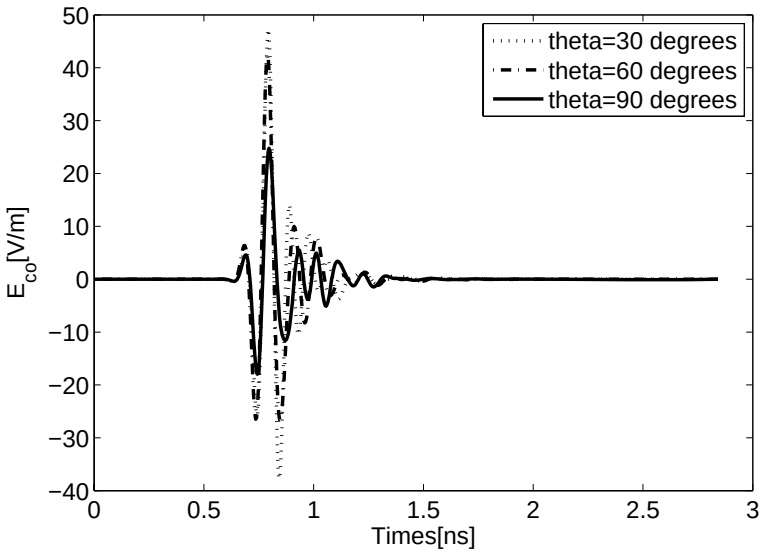


(b)

Figure 2.16: Time domain response of a Gaussian impulse for the co-polar component at different polar angles (E-plane). Due to symmetry, the cross-polar component is absent ($E_{cross} = 0$):(a) normalized E-plane response at ($\theta = 0^0, 30^0, 60^0, 90^0$);(b) superimpose E-plane response at ($\theta = 30^0, 60^0, 90^0$)

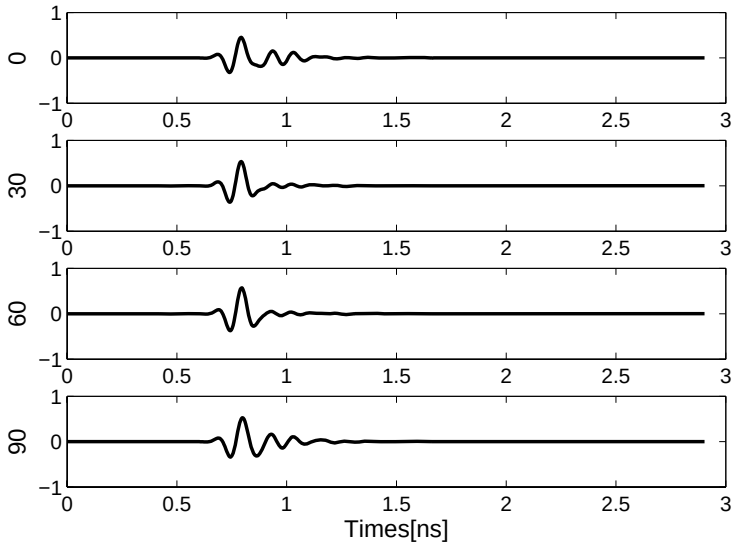


(a)

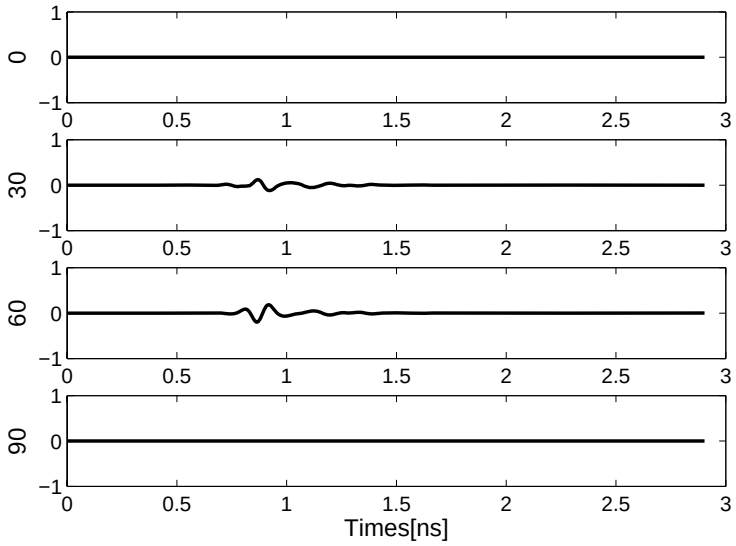


(b)

Figure 2.17: Time domain response of a Gaussian impulse at different polar angles (H-plane).(a) for the co-polar component; (b) for the cross-polar component

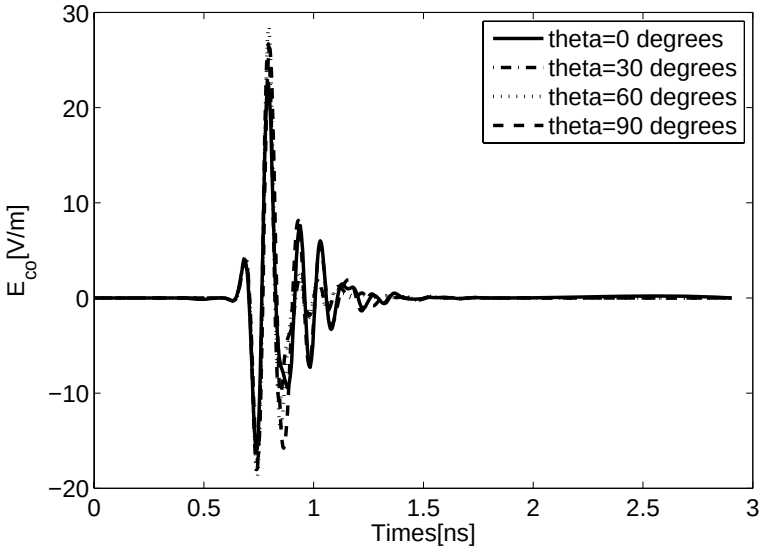


(a)

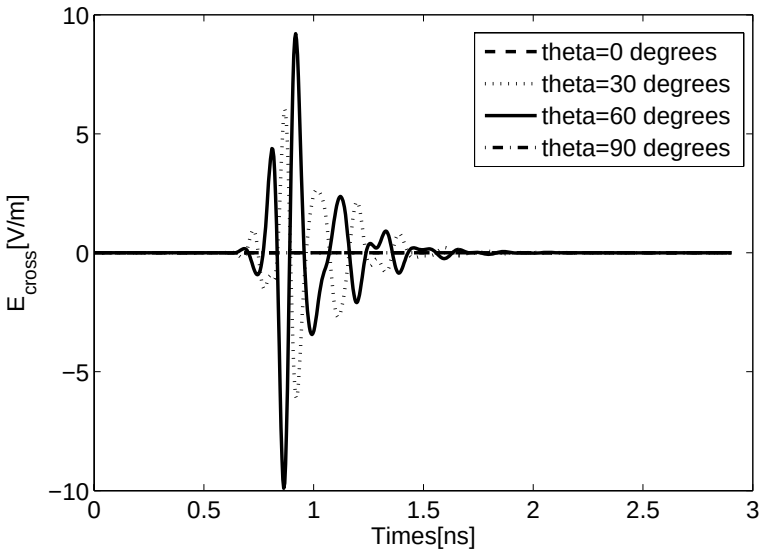


(b)

Figure 2.18: H-plane response for (a) co-polar and (b) cross-polar components ($\theta = 0^o$, $30^o$, $60^o$, $90^o$)

Simulation and measurement results have shown that the proposed semi-circle probe-fed monopole antennas are capable of providing the 7.5 GHz ultra wide bandwidth and good radiation performance across this wide operating band. Moreover, the antenna size can be reduced by half by using a semi-circle cross-plate instead of a full-circle cross plate without affecting the time domain performance.

## 2.4 UWB Semi-Ring Cross-Plate Probe-fed Monopole Antenna with Band-Rejected Functions

A UWB system is one kind of high-data-rate system, which operates in the frequency range from 3.1 to 10.6 GHz. However, interferences appear in the wide bandwidth UWB systems from some other existing communication systems. As a result, a filtering function is needed by the UWB antennas. A number of different methods can be used to achieve the band-notch function, for example, inserting a narrowband resonant slot in the radiating patch (i.e., U-shaped, arc-shaped, and a pie-shaped slot) [59–64], embedding a tuning attachment element or radiator within a slot on the radiating patch [65–67], utilizing parasitic patches near the radiator to form band-notched characteristic [68], or inserting a slit on the patch [55, 69].

In this section, a new cross typed UWB monopole antenna with band-notched characteristic is proposed. It uses a crossed semi-ring structure which can achieve stable far-field radiation pattern in the passband and size-reduction compared with planar monopoles. Meanwhile, the band-notched characteristic is obtained by embedding four L-shaped slits

in the radiating patch. The central frequency and bandwidth of notched band can be adjusted easily by controlling three key design parameters of the L-shaped slits. This approach provides more degrees of freedom in design.

Finally, a prototype is constructed and measured. The measured 10-dB return loss shows that the proposed antenna achieves a bandwidth ranging from 3.1 to over 13 GHz with a notched band of 5.4-6 GHz. The antenna radiator has a compact size of $28mm \times 28mm \times 14mm$. The proposed antenna presents omni-directional radiation pattern across the whole operating band in the H-plane.

### 2.4.1 Antenna Structure

The geometry of the band-notched crossed semi-ring monopole antenna is shown in Fig. 2.19(a) and 2.19(b). When we remove the four L-shape slots, it becomes the construction of the crossed semi-ring monopole antenna, which is transformed from the crossed semi-circle monopole antenna [70]. The crossed semi-ring monopole has similar impedance matching and far-field radiation characteristics as the crossed semi-circle monopole according to the current distribution principle. The surface current is mainly concentrated along the edge of the semi-circle disc. Hence, cutting the central part of the disc to form a semi-ring monopole will not affect the performance of the monopole.

In the proposed antenna design, the two semi-ring discs are arranged to have a "crossed" structure, and one circle disc is arranged on the top of this "crossed" structure. The cross-plate configuration makes it possible to improve the omnidirectional radiation performance, and the top circle disc is adopted to improve the impedance matching of the antenna. Furthermore, the four L-shape slots are etched on both semi-ring discs, which provide the band-notched characteristic. All prototypes fabricated in this section are vertically mounted

on a FR4 substrate ($\epsilon_r = 4.4, H = 40mil$) with an SMA connector. The size of the finite ground plane is $80 \times 80mm^2$ and the radiation element is made up of copper sheet of 0.1 $mm$.

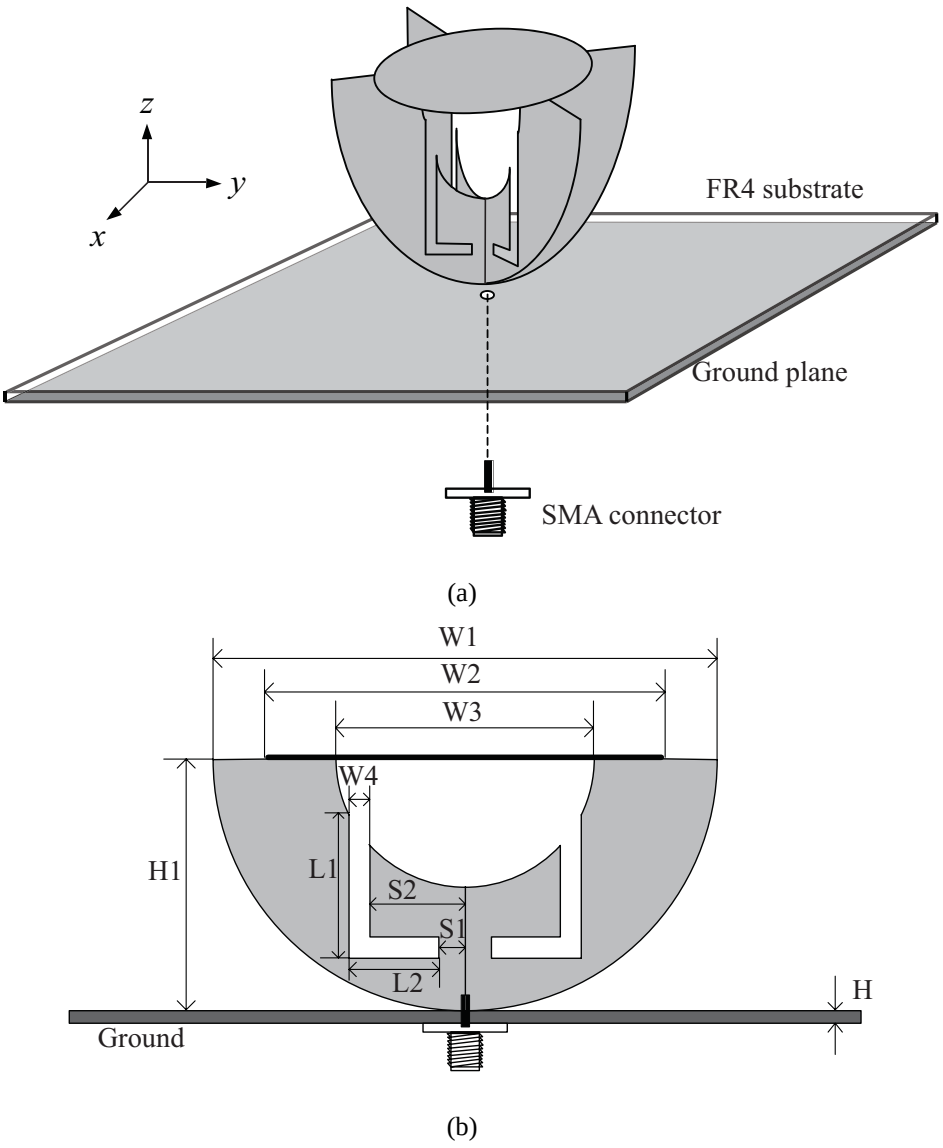


Figure 2.19: Geometry of the proposed semi-ring cross-plate probe-fed monopole antenna with L-shaped slots (a) Three-dimensional view; (b) Planar view.

### 2.4.2 Effect of The Geometrical Parameters

In order to better understand the antenna's characteristics, some key parameters are varied to analyze the structure through simulation. The first variation is performed by adjusting the diameter of the inner cutoff semi-circle of the proposed antenna without the L-shaped slots, which is shown in Fig. 2.20. It is observed that the input impedance responses do not change appreciably when $W_3 < 14mm$, but deteriorate when $W_3 >= 18mm$. That means appropriate cutting size of the central part of the antenna will not affect much on the current distribution. In order to embed the notch-band characteristic into this monopole antenna, a cutting ring with $W_3 = 14mm$ is adopted. Based on the selected value of $W_3$, the key parameters which influence the notched bandwidth ($BW_n$) and central frequency ($f_n$) of the notched band are studied.

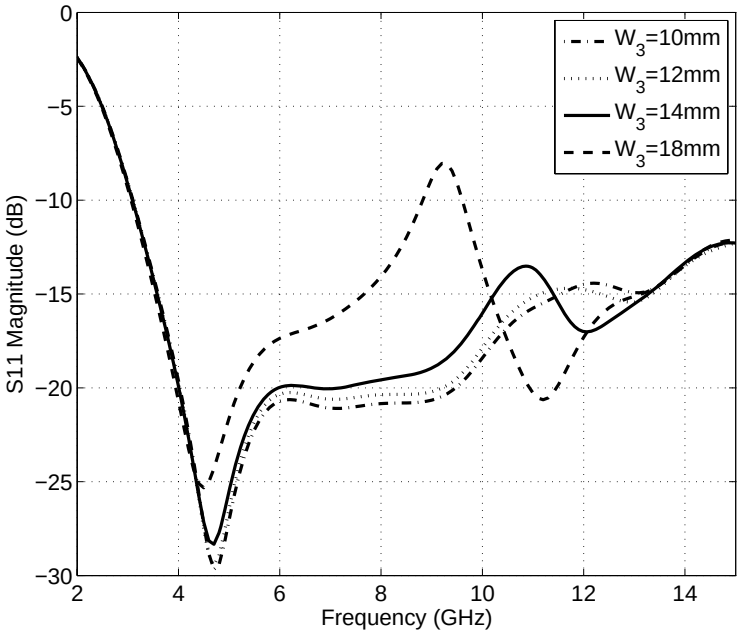


Figure 2.20: Variation of the $W_3$.

Tables 2.1, 2.2, and 2.3 show the simulated results for $BW_n$ and $f_n$ against different $L_1$, $L_2$ and $W_4$, respectively. Firstly, when $L_1$ increases, $f_n$ shifts to lower frequency band gradually and $BW_n$ becomes wider. Fig. 2.21 shows the details of the impedance response with different values of $L_1$. Secondly, when $L_2$ increases, $f_n$ shifts to lower frequency band gradually, but $BW_n$ becomes smaller at the same time. Fig. 2.22 shows the details of the impedance response with different values of $L_2$. Thirdly, the width of slots $W_4$ also influences the $BW_n$ and $f_n$ independently. When slot width $W_4$ varies from 0.5mm to 2.5mm, the central frequency of the notch shifts from 5.225GHz to 6.7GHz, and $BW_n$ increases from 0.65GHz to 1GHz. $BW_n$ stops increasing when $W_4 > 2mm$. Fig. 2.23 shows the details of the impedance response with different slot width $W_4$.

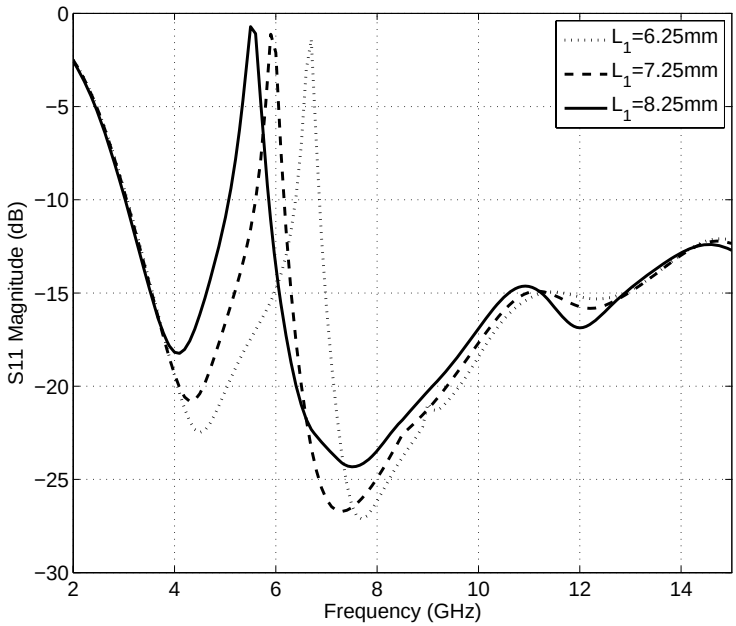


Figure 2.21: Variation of the $L_1$.

Table 2.1: Simulation Results For $f_n$ And $BW_n$ Versus $L_1$ (Unit Length: mm, Frequency: GHz, $L_2$=4.5, $W_4$=1, $W_1$=28, $W_2$=22, $W_3 = 14$, $H_1$=14, $S_1$=2, $S_2$=5.5).

| $L_1$ | $f_n$ | $BW_n$ |
|---|---|---|
| 6.25 | 6.625 | 0.45 |
| 7.25 | 5.875 | 0.55 |
| 8.25 | 5.45 | 0.7 |

Table 2.2: Simulation Results For $f_n$ And $BW_n$ Versus $L_2$ (Unit Length: mm, Frequency: GHz, $L_1$=8.25, $W_4$=1, $W_1$=28, $W_2$=22, $W_3 = 14$, $H_1$=14, $S_1$=2, $S_2$=5.5).

| $L_2$ | $f_n$ | $BW_n$ |
|---|---|---|
| 2 | 7.05 | 1.3 |
| 3 | 6.45 | 1.1 |
| 4 | 5.85 | 0.9 |
| 5 | 5.25 | 0.6 |

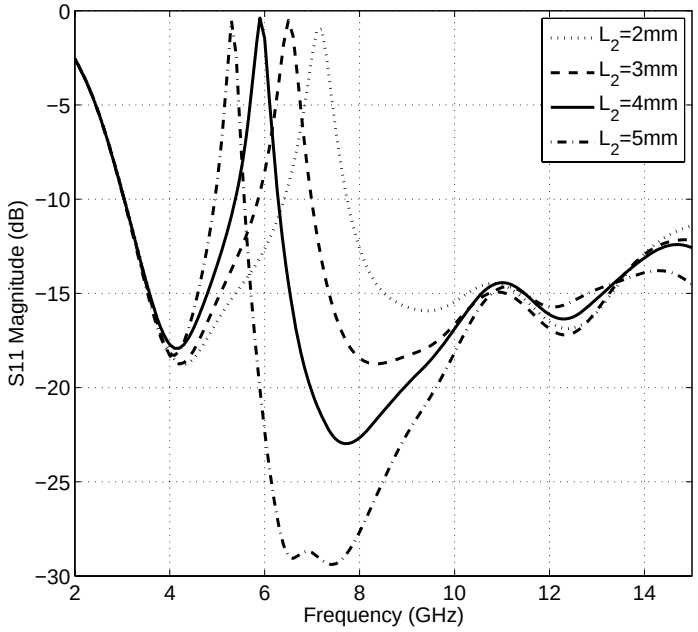


Figure 2.22: Variation of the $L_2$.

Table 2.3: Simulation Results For $f_n$ And $BW_n$ Versus $W_4$ (Unit Length: mm, Frequency: GHz, $L_1$=8.25, $L_2$=4.5, $W_1$=28, $W_2$=22, $W_3 = 14$, $H_1$=14, $S_1$=2, $S_2$=5.5).

| $W_4$ | $f_n$ | $BW_n$ |
|---|---|---|
| 0.5 | 5.225 | 0.65 |
| 1 | 5.45 | 0.7 |
| 1.5 | 5.825 | 0.85 |
| 2 | 6.3 | 1 |
| 2.5 | 6.7 | 1 |

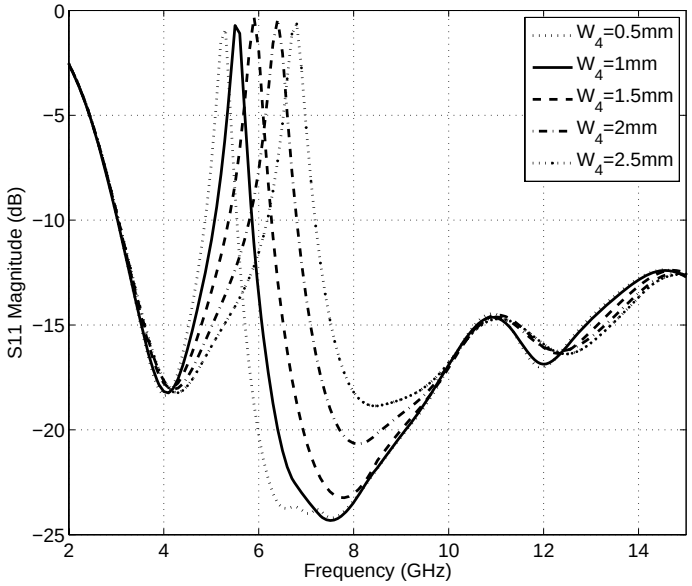


Figure 2.23: Variation of the $W_4$.

At the resonance frequency of the embedded L-shaped slots, the current distribution on the edge of the radiation plate will be disrupted, resulting in the malfunction of the semi-ring monopole in this frequency range. From the above parametric study, we can observe that the total length of the slot ($L1 + L2$) is around quarter wavelength at the notch frequency when the slot width $W_4$ is around $1.5mm$. Increasing either $L1$ or $L2$

will reduce the resonance frequency of the slots, which in turn results as a lowering of the notch frequency $f_n$. On the other hand, by enlarging the value of $W_4$ but keeping $L1$ and $L2$ unchanged, the total length of the slots' outer line is reduced. As a result, the resonance frequency for such slots is increased and the rejection band moves towards the higher frequencies. Characteristics of the notched band are mainly influenced by $L1$, $L2$. And $W_4$ will influence the notched band together since the variation of the slot width will change the current distribution. By proper selection of these parameters' values, the center frequency and bandwidth of the notched band can be adjusted.

### 2.4.3 Design Examples

The antenna is composed of two identical semi-ring plates and one circle plate. The outer and inner diameters of the semi-ring are $W1 = 28mm$ and $W3 = 14mm$, respectively. The diameter of the top circle plate is $W2 = 22mm$. The height of the proposed antenna is $H1 = 14mm$. The design parameters as shown in Fig. 2.19(b) are set to be $L1 = 8.25mm, L2 = 4.5mm, S1 = 2mm, S2 = 5.5mm$ and $W4 = 1mm$, respectively.

Fig. 2.24 shows the photographs of the fabricated semi-ring cross-plate monopole antenna and the band-notched antenna.

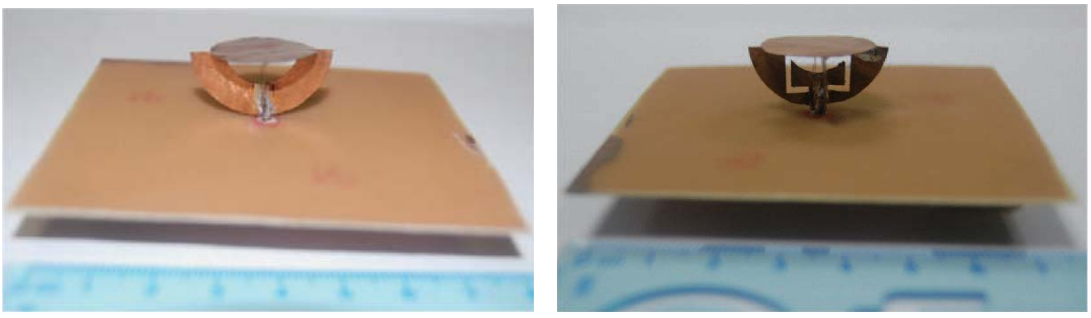

(a) Semi-ring cross-plate monopole (b) Semi-ring cross-plate band-notched monopole

Figure 2.24: Photographs of the fabricated semi-ring cross-plate monopole antenna.

Fig. 2.25 shows the measured and simulated return loss of the crossed semi-ring monopole antenna and corresponding band-notched antenna. Simulation of the proposed antennas is obtained by using ANSOFT HFSS. The results indicate that the impedance bandwidth(10dB return loss) of the crossed semi-ring monopole antenna is in the frequency range from 3.1 to 12.5 GHz, which covers the bandwidth of the FCC definition for UWB indoor communication systems.

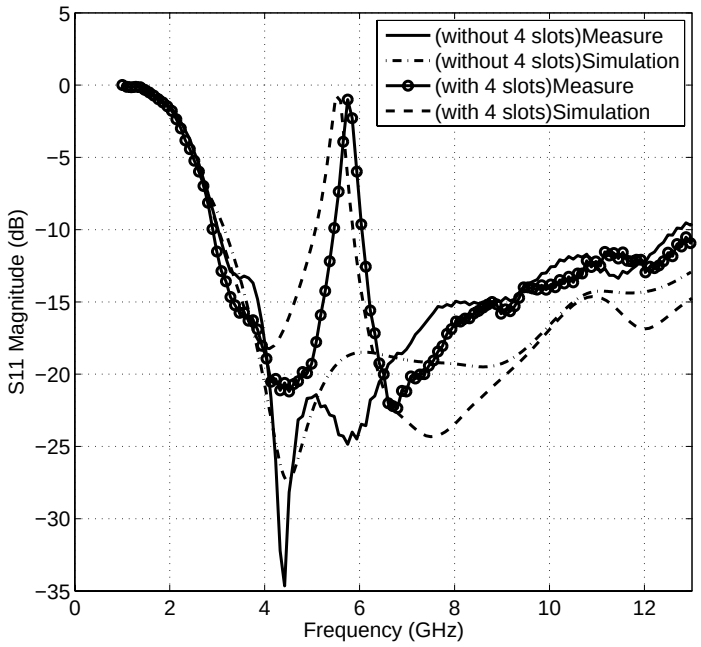


Figure 2.25: The Measured and simulated return loss of the cross semi-ring disc monopole antenna and band-rejected cross semi-ring disc monopole antenna.

The measurement result of the band-notched crossed semi-ring monopole antenna has a small shift compared with the simulated one. This may due to the fabrication errors. According to the measurement result, the operating bandwidths of the band-notched crossed

semi-ring antenna are $3.1 \sim 5.4$ GHz and $6.0 \sim 13$ GHz.

Fig. 2.26 shows the measured peak gain in the E-plane (y-z plane) from $3 \sim 11$ GHz for the proposed antenna with and without the L-shaped slots. From the figure, we can see that both the antennas have good antenna peak gains in the y-z plane. The antenna with slots has very similar gains as the one without slots, except for a sharp antenna gain drop in the notched frequency band from 5.4 to 6.0 GHz.

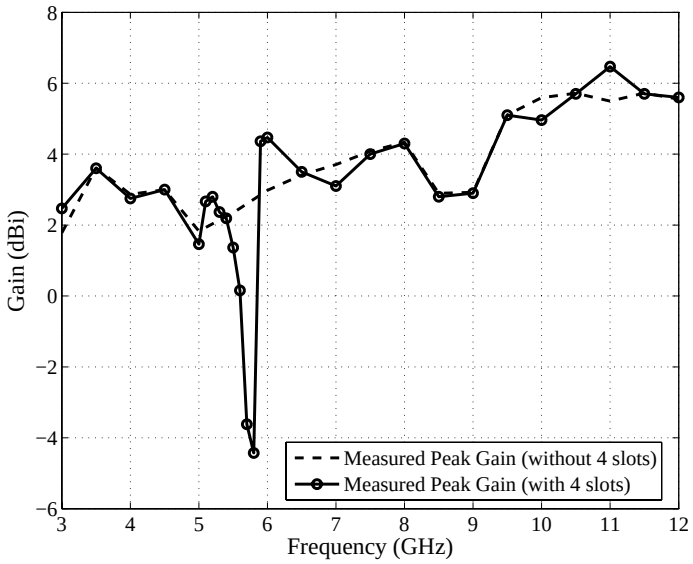


Figure 2.26: The measured y-z plane antenna gain of the cross semi-ring disc monopole antenna and the band-rejected cross semi-ring disc monopole antenna.

Fig. 2.27 shows the E- and H-plane far-field radiation patterns of the band-notched antenna at 4, 6 and 10 GHz, respectively. The radiation pattern in the H-plane is almost omnidirectional across the ultra-wide bandwidth. Even at 10 GHz, the antenna shows stable omni-directional pattern with only slight distortion.

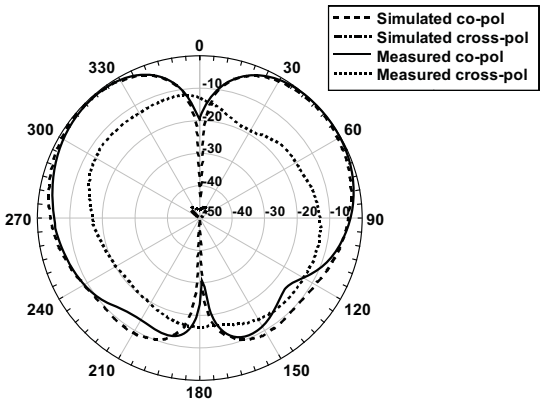


(a) E-plane radiation pattern at 4 GHz

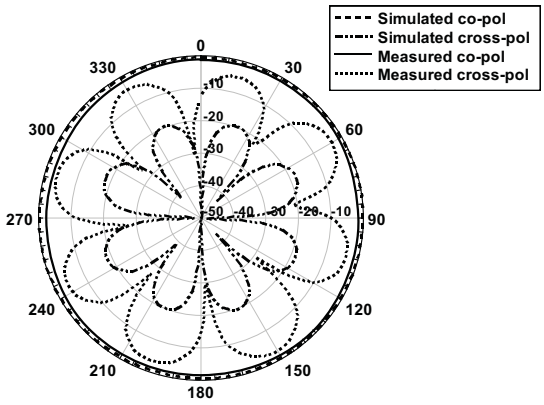


(b) H-plane radiation pattern at 4 GHz

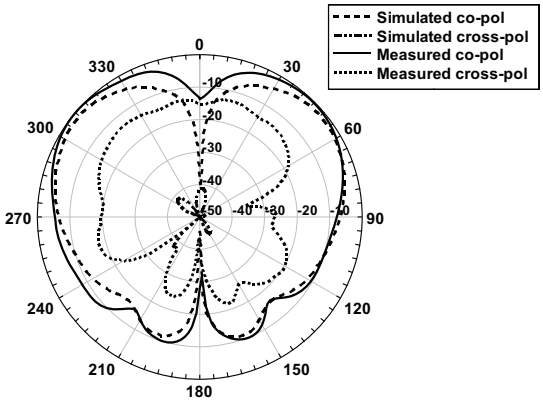


(c) E-plane radiation pattern at 6 GHz

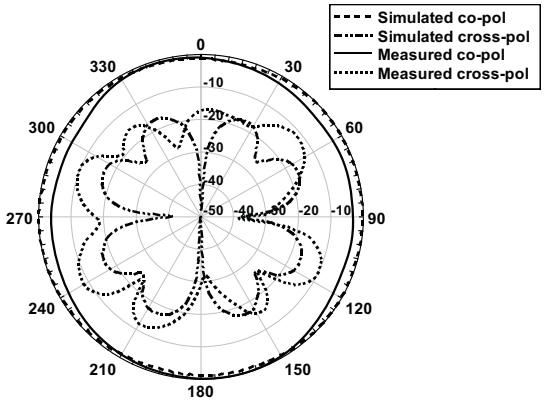


(d) H-plane radiation pattern at 6 GHz

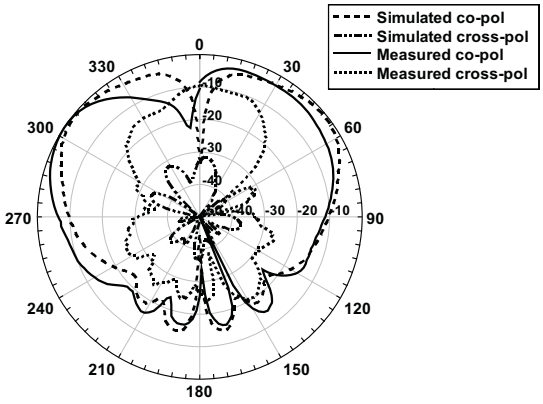


(e) E-plane radiation pattern at 10 GHz

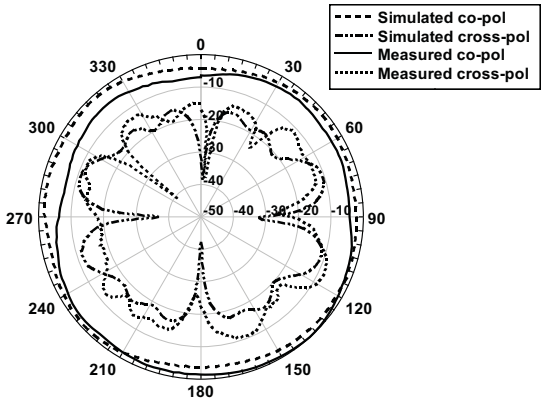


(f) H-plane radiation pattern at 10 GHz

Figure 2.27: Simulated and Measured E- and H-plane radiation patterns for the crossed semi-ring band-notch monopole antenna at $f = 4$, 6 and 10 GHz.

### 2.4.4 Transmission Analysis in Time Domain

Time domain responses of the band-notched antenna are also studied by using a 3D EM simulation software CST MICROWAVE STUDIO. The incident voltage pulse used in the time-domain simulations is a normalized Gaussian pulse, which is shown in Fig. 2.6. It can be observed that the source pulse width is 0.35 ns. Fig. 2.28(a) shows the normalized far-field time-domain electrical signals at different elevation angles in the E-plane of the antenna without four L-shaped slots, and Fig. 2.28(b) superimposes time-domain responses of all different angles together. The resulted pulse of antenna without notch has a pulse width of 0.83 ns, which has 0.48 ns extension compared with the source signal pulse. The increase in pulse width is due to the ringing effect of the antenna. The semi-ring structure and the top loaded circle disc construct a resonant structure which is equivalet to a RLC tank. At the resonance frequency, the equivalent LC network can store part of the time-varying signal energy so the oscillation will continue even without input signal, which results in the signal tail after the main pulse.

Fig. 2.29(a) shows the normalized far-field time-domain electrical signals at different elevation angles in the E-plane of the antenna with four L-shaped slots, and Fig. 2.29(b) superimposes time-domain responses of all different angles together.

From the results, it can be noticed that the main response pulses are nearly the same for the cases with or without notch. However, the band-notched antenna has more ringing effects than the antenna without notch. The reason could be due to the impedance mismatching at the notched band and the energy storage effect of the embedded four L-shaped slots. Obviously, the filtering function integrated with the antenna is realized by a compromise on the time-domain response. Nevertheless, the proposed band-notched antenna still has a limited ringing-effect and can be used in the current UWB system.

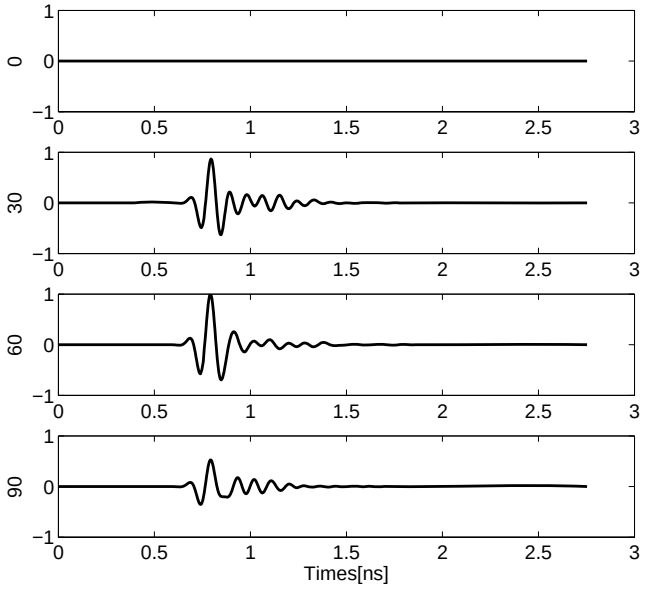


(a)

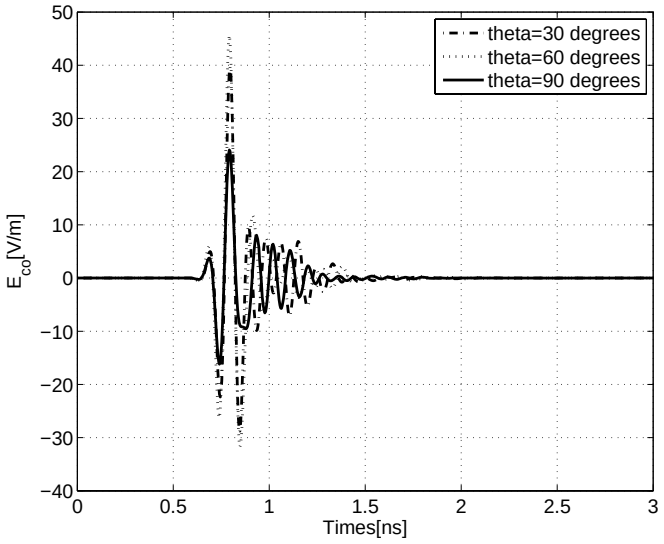


(b)

Figure 2.28: Time domain response of a Gaussian impulse for the co-polar component at different polar angles (E-plane). Due to symmetry, the cross-polar component is absent ($E_{cross} = 0$):(a)normalized E-plane response at($\theta = 0^0, 30^0, 60^0, 90^0$);(b)superimpose E-plane response at($\theta = 30^0, 60^0, 90^0$)

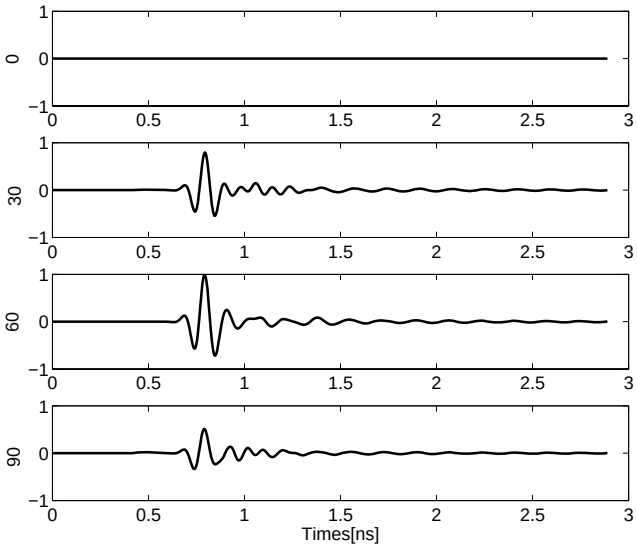


(a)

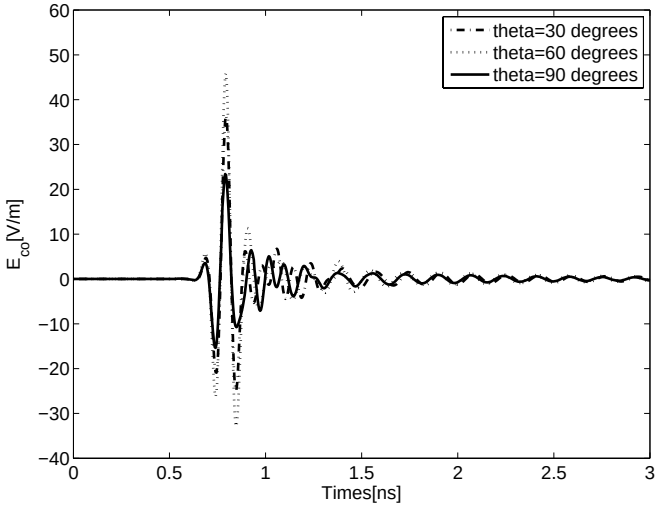


(b)

Figure 2.29: Time domain response of a Gaussian impulse for the co-polar component at different polar angles (E-plane). Due to symmetry, the cross-polar component is absent ($E_{cross} = 0$):(a)normalized E-plane response at($\theta = 0^0, 30^0, 60^0, 90^0$);(b)superimpose E-plane response at($\theta = 30^0, 60^0, 90^0$)

## 2.5 Conclusion

In this chapter, we first studied a cross-plate monopole antenna, which is used as a reference for three following new antennas proposed in this thesis. Then, two new small semi-circle cross-plate monopole antennas with top-loaded circular and rectangular patches have been investigated. Finally, a new band-rejected semi-ring cross-plate monopole antenna has been presented. All 3-D antennas studied in this chapter have shown stable far-field radiation pattern across the operation bandwidth compared with the planar monopole antennas. The cross-circle disc and semi-circle cross-plate antennas exhibit good time-domain responses at the same time. The band-rejected semi-ring cross-plate monopole antenna achieves the frequency-notch function by adding four L-shaped slots in the radiating plates. This novel design also has a compact size. Though the time domain responses of this band-rejected antenna show a ringing effect, however, it still has appropriate UWB performance to be a good candidate for practical UWB applications.

# Chapter 3

# Circuit Modeling of Ultra Wide Band Antennas

## 3.1 Introduction

In this chapter, wideband circuit modeling of UWB antennas for system co-design is discussed. Normally, macromodeling or curve-fitting approaches are employed to get a non-physical mathematical model of the circuit as a black box [16]. The weakness of this approach is that this model cannot be used to correlate the model parameters with the layout parameters. Also such a black box model usually suffers from the difficulty in ensuring passivity, stability and causality. To avoid such problems, physical circuit augmentation has been implemented to realize wideband equivalent circuits [17–22]. This physical model is attractive because it can be correlated with the layout parameters and can guarantee passivity and stability of the equivalent circuits. Here we will focus on modeling based on physical augmentation. Particularly we would explain the details of modeling based on automatic physical augmentation proposed in [21], where all series augmentation elements were transformed into the parallel ones for the wideband physical augmentation. Using this technique, the preliminary analysis of the circuit to decide the augmentation type is not

needed. The type of augmentation to be performed can be determined automatically. In this chapter, some modifications to improve the method in [20] and [21] are suggested.

One of the modifications is in the way that we view the initial simple equivalent circuit. In many methods (e.g. [17], [19], [20], [71]), circuit elements from the initial equivalent circuit are treated differently than any other elements in the under-developed equivalent circuit. In this thesis, we propose a different approach in using this simple equivalent circuit. Unlike the method in [20], here we do not differentiate between augmented elements and original elements.

The second modification is that, unlike in [21], we incorporate a separate tuning module in order to minimize number of augmented elements. This module is run alternately with the augmentation module. In this module, we only allow tuning of the elements' values without introducing new elements.

This new approach is implemented following the methods described in [20] and [21] resulting in our pseudo-new and new method, respectively. Comparison between these two methods is made by observing their performance in the case studies involving a spiral inductor modeling and an MIM capacitor modeling. The results, which are given in Section 3.4, show that both methods perform well and that the new method is superior to the pseudo-new method. Finally, the proposed method is successfully extended to extract the equivalent circuit for two UWB antennas.

## 3.2 Automatic Physical Augmentation

### 3.2.1 Review of Circuit Augmentation

According to basic circuit theory there are two ways to solve circuit equations. They are mesh analysis and nodal analysis. In computer aided analysis, these analyses are not used. The reason is nodal analysis and mesh analysis are not easy to be implemented numerically. There is another method named modified nodal analysis (MNA) that is easy to be implemented numerically. In the MNA, voltage source is represented by one current variable (**i**) and one current source (**E**). Every node is represented by one current source (**J**) and one node voltage (**V**). The MNA matrix, **A**, gives a connection between $\begin{bmatrix} \mathbf{V} \\ \mathbf{i} \end{bmatrix}$ and $\begin{bmatrix} \mathbf{J} \\ \mathbf{E} \end{bmatrix}$. Let $\mathbf{x} = \begin{bmatrix} \mathbf{V} \\ \mathbf{i} \end{bmatrix}$ and $\mathbf{y} = \begin{bmatrix} \mathbf{J} \\ \mathbf{E} \end{bmatrix}$, then we have $\mathbf{Ax} = \mathbf{y}$. Since $\mathbf{J} = 0$ we can rewrite the MNA equation into

$$\mathbf{Ax} = \mathbf{By} \tag{3.2.1}$$

where **B** is a binary selector matrix $\begin{bmatrix} \mathbf{0} \\ \mathbf{I}_n \end{bmatrix}$ with $\mathbf{I}_n$ is $n \times n$ identity matrix ($n$ is the size of matrix **E**) and **0** is zero matrix with appropriate size. The $y$-parameters matrix $Y$ has the relationship as $\mathbf{YV} = \mathbf{E}$. With some manipulations, the $y$-parameters matrix can be written as

$$\mathbf{Y} = -\mathbf{B}^T\mathbf{A}^{-1}\mathbf{B} \tag{3.2.2}$$

where the superscript $T$ denotes the matrix transpose operator.

Let the measured $y$-parameters of the actual device be represented as $\mathbf{Y}_{meas}$. The goal of circuit augmentation is to modify the equivalent circuit with additional two-terminal

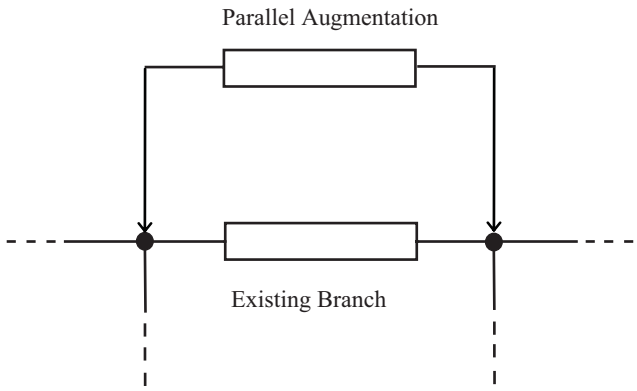


Figure 3.1: Parallel augmentation

passive element such that it matches measurement/EM data over the entire broadband frequency range. Let the corresponding new $y$-parameters matrix be represented by

$$\hat{\mathbf{Y}} = \mathbf{Y} + \Delta\mathbf{Y} \tag{3.2.3}$$

The effect of adding one passive element into a circuit has been previously well researched [72]. In this case, it is relatively easy to calculate the augmentation effect on circuit's $y$-parameters using exact formulas.

There are two formulas that are available for doing this job: one for parallel augmentation (Fig. 3.1) and one formula for series augmentation (Fig. 3.2). We can understand the need to differentiate the type of augmentation by considering that parallel connected elements have the same voltages while series connected elements have the same currents. The derivation of parallel augmentation formula based on this characteristic can be seen from [72]. The series augmentation formula can be derived following the same reasoning in [72] with appropriate modification, like changing voltage with current and vice versa.

The formulas and their derivation for calculating the effect of parallel and series augmentation on the $y$-parameters are shown below. These formulas are based on the formulas

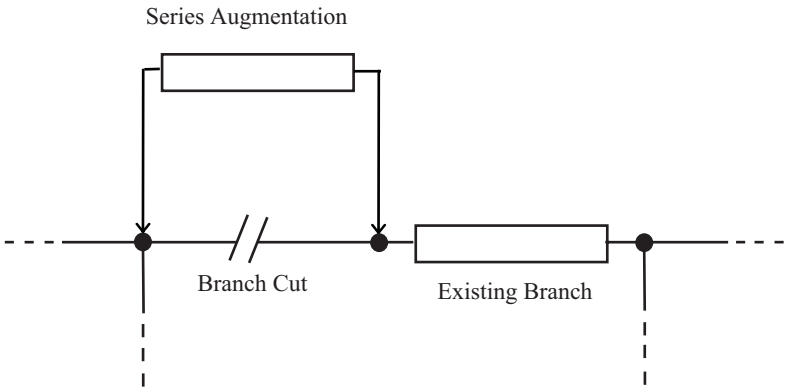


Figure 3.2: Series augmentation

in [20].

***A***. Parallel Augmentation

Firstly, Sherman-Morisson formula [73] is intorduced to update the matrix inverse.

$$(\mathbf{A}+\mathbf{u}\mathbf{v}^T)^{-1} = \mathbf{A}^{-1} - \frac{\mathbf{A}^{-1}\mathbf{u}\mathbf{v}^T\mathbf{A}^{-1}}{1+\mathbf{v}^T\mathbf{A}^{-1}\mathbf{u}} \tag{3.2.4}$$

The augmentation will be lead to change in the MNA matrix, hence change in the inverse MNA matrix. In other words

$$\Delta\mathbf{Y} = -\mathbf{B}^T\Delta(\mathbf{A}^{-1})\mathbf{B} \tag{3.2.5}$$

Combining (3.2.4) and (3.2.5) we get

$$\Delta\mathbf{Y} = \frac{\mathbf{B}^T\mathbf{A}^{-1}\mathbf{u}\mathbf{v}^T\mathbf{A}^{-1}\mathbf{B}}{1+\mathbf{v}^T\mathbf{A}^{-1}\mathbf{u}} \tag{3.2.6}$$

The only task remained is in defining **u** and **v**.

The change because of parallel augmentation on the MNA matrix can be derived easily.

Let $\boldsymbol{\xi}$ be a slector column vector with the $m^{th}$ and $n^{th}$ entries set to "+1" and "-1", respectively and zeros elsewhere if the augmentation is conducted on the nodes $m$ and $n$. $\boldsymbol{\xi}$ can be written as

$$\boldsymbol{\xi} = \begin{bmatrix} 0 \\ \vdots \\ 0 \\ +1 \\ 0 \\ \vdots \\ 0 \\ -1 \\ 0 \\ \vdots \\ 0 \end{bmatrix} \tag{3.2.7}$$

Then we can write the change of parallel augmentation on the MNA matrix as $\Delta\mathbf{A} = \frac{\boldsymbol{\xi}\boldsymbol{\xi}^T}{z_{aug}}$, hence $\mathbf{u} = \mathbf{v} = \frac{\boldsymbol{\xi}}{\sqrt{z_{aug}}}$.

Inserting these two values onto (3.2.6) we get

$$\Delta\mathbf{Y} = \frac{\mathbf{B}^T\mathbf{A}^{-1}\boldsymbol{\xi}\boldsymbol{\xi}^T\mathbf{A}^{-1}\mathbf{B}}{z_{aug} + \boldsymbol{\xi}^T\mathbf{A}^{-1}\boldsymbol{\xi}} \tag{3.2.8}$$

So we can write the formula to calculate the effect of parallel augmentation on $y$-parameters as

$$\Delta\mathbf{Y} = \mathbf{B}^T\mathbf{A}^{-1}\boldsymbol{\xi}\boldsymbol{\xi}^T\mathbf{A}^{-1}\mathbf{B}\gamma_{aug} \tag{3.2.9}$$

where $\mathbf{A}$ is the MNA matrix and $\gamma_{aug}$ is defined to be

$$\gamma_{aug}^{-1} = z_{aug} + \boldsymbol{\xi}^T\mathbf{A}^{-1}\boldsymbol{\xi} \tag{3.2.10}$$

***B***. Series Augmentation

Series augmentation is a little bit tricky. Firstly we note that series augmentation adds one more node. We need to set the last diagonal entry of **A** to $-z_{aug}$. Hence $\Delta\mathbf{A} = -\boldsymbol{\xi}\boldsymbol{\xi}^T z_{aug}$, so **u** = **-v** = $\boldsymbol{\xi}\sqrt{z_{aug}}$. Inserting this value here into (3.2.6) we got the series augmentation formula

$$\Delta\mathbf{Y} = \frac{\mathbf{B}^T\mathbf{A}^{-1}\boldsymbol{\xi}\boldsymbol{\xi}^T\mathbf{A}^{-1}\mathbf{B}}{\boldsymbol{\xi}^T\mathbf{A}^{-1}\boldsymbol{\xi} - z_{aug}^{-1}} \tag{3.2.11}$$

Actually, Eq.(3.2.9) can still be used to calculate the effect of the series augmentation on the Y parameters but the definitions of some variables have to be changed [19], [20]. The definition is as below:

**A** is the modified MNA matrix. If the augmented variable is on the $k^{th}$ row, the $k^{th}$ diagonal entry of **A** is set to $-z_{aug}$. $\gamma_{aug}$ is defined as

$$\gamma_{aug}^{-1} = \boldsymbol{\xi}^T\mathbf{A}^{-1}\boldsymbol{\xi} - z_{aug}^{-1} \tag{3.2.12}$$

$\boldsymbol{\xi}$ is the column vector with the $k^{th}$ row is ”1” and ”0” elsewhere.

One more step has to be added to the series augmentation formulation if we are to allow series augmentation to be done at any terminal pairs including the terminal pairs related to the augmented series element. This modification is necessary for implementing pseudo-new method and to get a fairer comparison with the method in [21]. The additional step is described in box below.

**Additional steps** (after series augmentation calculation):

1. If the $-z_{aug}$ value is at the $m^{th}$ row and $m^{th}$ column of MNA matrix, delete the $m^{th}$ row and $m^{th}$ column.
2. Update the rows and columns corresponding to the nodes connected to the new circuit element.

In [21], these steps are not performed. Hence the results are not accurate enough. A

more accurate result is shown in this thesis where we compare the new and pseudo-new method.

The effect of multiple augmentations can be approximated using formula below [20]:

$$\Delta \mathbf{Y} = \sum_i \mathbf{B}^T \mathbf{A}^{-1} \boldsymbol{\xi}_i \boldsymbol{\xi}_i^T \mathbf{A}^{-1} \mathbf{B} \gamma_{augi} \tag{3.2.13}$$

There are some disadvantages of the circuit augmentation approach described as above. Some of them are:

1. The user of the formulas above has to know which type of augmentation must be performed without knowing which one gives more desired effects. This is because the definition of variables in the formulation of series and parallel augmentation is different. As the consequence of this disadvantage, the type of augmentation must be specified in advance.

2. Two rows and two columns have to be added into the MNA matrix before calculating using the series augmentation formula; hence it adds the calculation burden.

### 3.2.2 Transform Series Augmentation into Parallel Augmentation

In order to overcome the disadvantages stated above, especially the first one, a new formulation of circuit augmentation is needed. One possible solution is to transform the series augmentation into the parallel augmentation. As shown in Fig. 3.3, if the augmentation is taken place between $j^{th}$ node and $l^{th}$ node, this can be achieved by considering the relation below

$$\frac{1}{z_p^{-1} + z_{jl}^{-1}} \quad = \quad z_{jl} + z_s$$

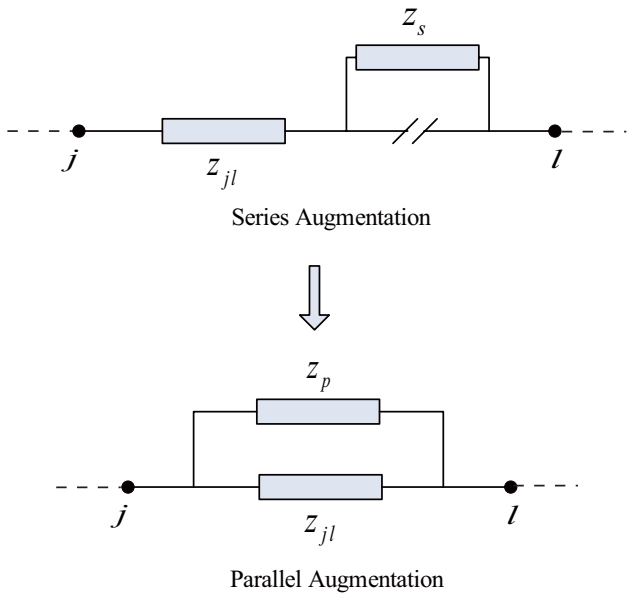


Figure 3.3: Transform Series Augmentation into Parallel Augmentation

$$z_p^{-1} = (z_{jl} + z_s)^{-1} - z_{jl}^{-1} \tag{3.2.14}$$

where $z_p$ is the parallel-equivalent impedance, $z_s$ is the series augmented impedance, and $z_{jl}$ is the impedance between the $j^{th}$ node and the $l^{th}$ node.

This formulation can detect which type of augmentation that can give the desired result. Another minor advantage is that there is no need to increase the size of MNA matrix before the augmentation calculation is done. The addition of new columns and rows is done after the augmentation calculation is completed.

In this work, we call this formulation of physical augmentation as automatic (physical) augmentation. The reason of this name is because using this formulation the type of augmentation that has to be done can be decided automatically. The details are described in the subsection below.

### 3.2.3 Modeling based on Automatic Physical Augmentation

In the method presented in [20], a verification stage is needed to identify the type of connection. Based on the type of augmentation for each element, either the series or shunt element is applied to carry out the augmentation. The augmentation type has to be determined before the main calculation. Although simultaneous multiple series and/or shunt augmentations can be conducted, the procedure cannot decide which combination of augmentation type will give the best result.

Using the new formulation of series augmentation, it is possible to eliminate this verification stage. Every possible series augmented element can be converted into a parallel one. Hence, all augmented elements can be considered as the parallel augmentation. If the augmentation is actually a series augmentation, we insert one row and one column to the MNA matrix to represent the new node. This is done after the augmentation calculation is finished. In this way, more flexible augmentation can be done. The flowchart of this method is shown in Fig. 3.4.

As in [20], the improvement on $Y_{aug}$ is measured by calculating the error using formula below

$$\epsilon = \frac{1}{N_f} \sum_{f} \sqrt{\sum_{i,j} \left| Y_{ij}^{meas} - Y_{ij}^{target} \right|^2} \tag{3.2.15}$$

We will discuss some important parts of the flowchart above in the subsections below.

***A***. Element Comparison

An important part of this new method is to find the element that is closest to $z_{aug}$ (i.e., corresponding to block (*) in the flowchart). There are many ways to define this closeness. Ideally, the definition should be such that if an element is closer to $z_{aug}$, the error $\epsilon$ will be

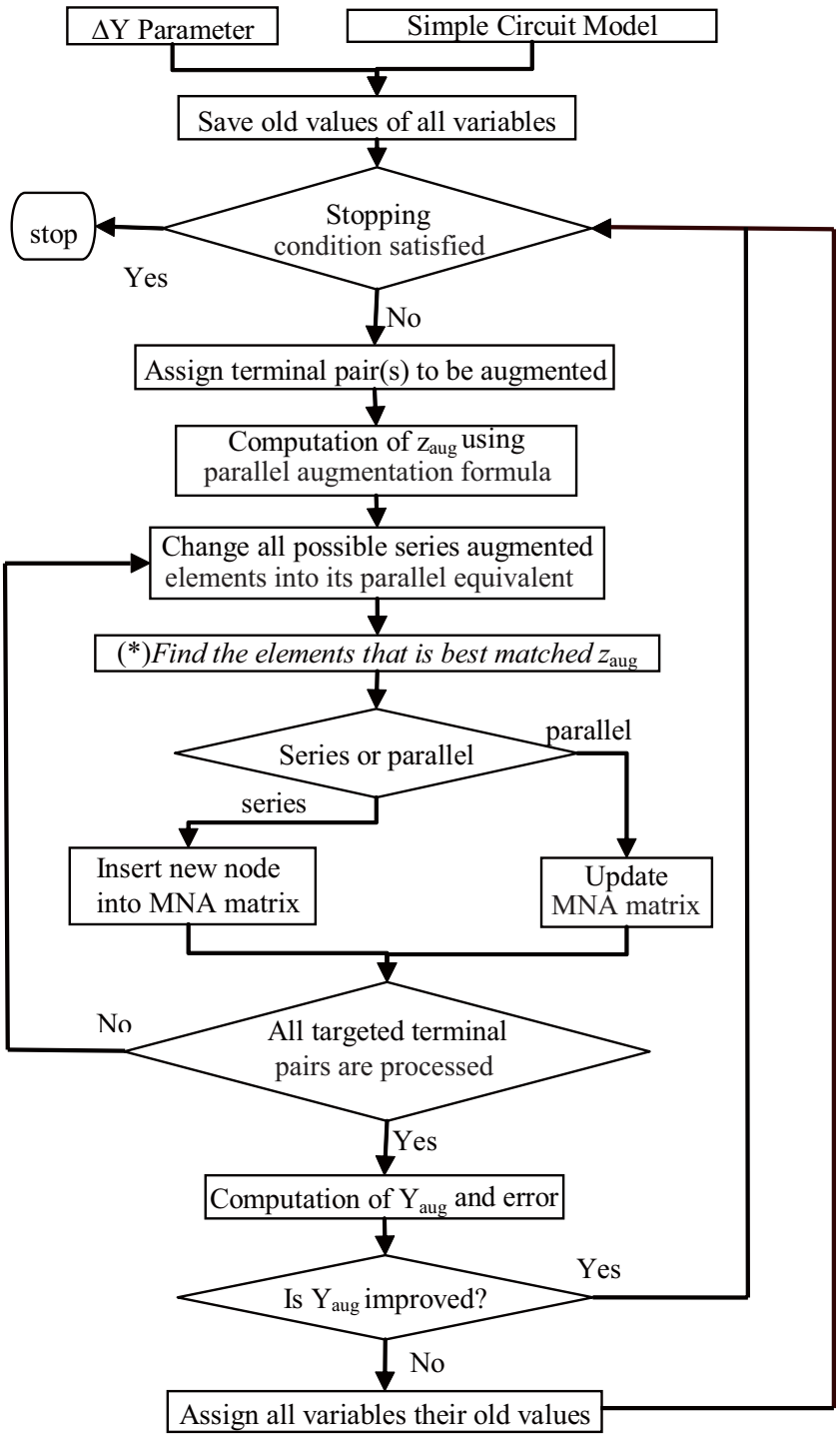


Figure 3.4: Modeling based on automatic physical augmentation

smaller. Unfortunately, to implement this ideal definition, nonlinear problem has to be solved. Because of that, we use a simpler definition. The closeness between an element and $z_{aug}$ is defined as

$$\Delta = \frac{1}{N_f}\sqrt{\sum_f |z(f) - z_{aug}(f)|^2} \tag{3.2.16}$$

or in other words it is equivalent with the Euclidean distance between them. We call this method as **direct method** because of its nature.

There is another method that we call **indirect method**. The method is described in **Box 1**.

**Box 1. Indirect method for single augmentation**

*Step 1:* Divide all possible augmented impedance into several groups (e.g. $\{$(inductor, series augmentation), (inductor, parallel augmentation), (resistor, series augmentation),$\dots\}$).

*Step 2:* For each group find one element that satisfy constraints and minimize (3.2.16). Create one set of elements consisting of these best elements.

*Step 3:* Calculate directly for those elements in the set and choose the element that has minimum $\epsilon$ value.

In the indirect method, for multiple augmentations, it is assumed that the inverse of MNA matrix does not change. Hence the method becomes as in **Box 2**.

**Box 2. Indirect method for multiple augmentations**

Let the number of single augmentations in one multiple augmentation = $N_{aug}$.

*Step 1:* Decide the sequence of single augmentations. Assign $i = 1$.

*Step 2:* For the $i^{th}$ augmentation, do **indirect method for single augmentation**.

*Step 3:* Assign $i = i + 1$. If $i > N_{aug}$, stop. Else, repeat *Step 2* assuming the inverse of MNA matrix does not change.

As can be seen from the description above, the indirect method is more calculation-extensive than the direct method. However, it is potentially better than the direct one.

Hence we still consider it. Another thing that has to be noted is $z(f)$ in (3.2.16) is the impedance of the parallel equivalent element in the case of series augmentation.

Let us call resistor, capacitor, and inductor as basic elements. In our implementation, one single augmentation will only add up to one basic element. The reason for this is to allow high flexibility in the circuit structure. Moreover the basic element's value has to be positive.

Exception is made if the nodes, corresponding to terminal pair under study, are connected directly by a basic element. In that case, the basic element value has to be chosen such that the resulted circuit contains only positive valued elements. We name the case where negative element is allowed as **tuning case**. In tuning case the closeness is not measured using (3.2.16). Instead it is measured using formula below.

$$\Delta = \frac{1}{N_f}\sqrt{\sum_f \left| \frac{z(f) * z_0(f)}{z(f) + z_0(f)} - \frac{z_{aug}(f) * z_0(f)}{z_{aug}(f) + z_0(f)} \right|^2} \tag{3.2.17}$$

where, $z(f)$ and $z_{aug}(f)$ are the same as those in (3.2.16) and $z_0(f)$ is the existing basic element between terminal pairs' nodes that has the same type as $z(f)$. In other words, rather than comparing the augmented elements, we compare the closeness of the resulted elements. In the case $z_0(f) >> z_{aug}(f)$ and $z_0(f) >> z(f)$, equation (3.2.17) will give the same result as equation (3.2.16).

One example is given in **Box 3**.

This requirement on the element value is different from the requirement used in [21]. In [21], the requirement is that all augmented elements have to be positive.

Here implement (3.2.16) and (3.2.17) by using *lsqnonneg()* function available in MATLAB. It is possible that this function will give zero impedance result. In that case, we change the zero impedance with very small impedance after the element comparison is

done. We choose $L$, $R$, $1/C = 10^{-30}$ ($H$, $ohm$, $F^{-1}$) to create the very small impedance.

**Box 3. Example**
The nodes of terminal pair $1$ is directly connected only by one capacitor with capacitance $= C$. Parallel augmentation will be done to this terminal pairs. The possible augmented elements are:
-Inductor with positive inductance
-Resistor with positive resistance
-Capacitor with capacitance $> -C$
For the inductor and resistor, the closeness is measured using (3.2.16). For capacitor the closeness is measured using (3.2.17).

***B***. Sequence Generator

Another important part of the physical augmentation method is the method used to decide at which terminal pairs the augmentation has to be done. Thus far, this problem has not been solved completely.

Here a sequence generator is used to create a sequence of augmented terminal pairs for each iteration. The sequence generator's characteristics are explained in **Box 4**.

Note that the rule for terminal pairs assignment and central node assignment is sorted from the most important to the least important ones.

In this algorithm, series augmentation is only allowed to be done at terminal pairs where their nodes are connected directly by a basic element. That is why we use point $1$ as our generator's characteristic. This is to ensure that series augmentation has the same chance to be done as parallel augmentation.

In the following sections we will give some case studies to show the performance of the proposed method.

**Box 4. Sequence Generator**

1. For odd numbered iterations, only terminal pairs with their nodes directly connected by basic element are allowed to be generated. For even numbered iterations, this restriction is not used.

2. Terminal pairs assignment for odd numbered iterations:

   - The ones that have been visited least are preferred.

   - The ones that appear first in the netlist file are preferred.

3. For even numbered iterations, our sequence generator assigns one or more nodes as a central node and produces all known terminal pairs associated with those central nodes.

4. Central node assignment:

   - Node that has never been a central node is preferred

   - Node which has smallest node's number is preferred.

5. Terminal pairs assignment for even numbered iterations:

   - The first node in each terminal pairs has smaller node's number than the second one. Terminal pairs contain the central node as the first node.

   - The ones that have been visited least are preferred

   - The ones with the second node has smallest node's number are preferred.

6. Node corresponds to ground has node's number $0$. If there is $N$ non-ground nodes corresponded to external ports, they will have node's number $1$ to $N$.

7. After all terminal pairs corresponded to last central node have been visited, the central node is assigned to $0$ and the sequence generator is reset.

8. If no more improvement is possible, stop the algorithm.

## 3.3 Testing Automatic Augmentation

In order to test the ability of automatic augmentation formulation to decide augmentation type, we use circuit 1 shown in Fig. 3.5. All resistors have 1-$\Omega$ resistance, capacitor has 250-$pF$ capacitance, and inductor has 1-$nH$ inductance.

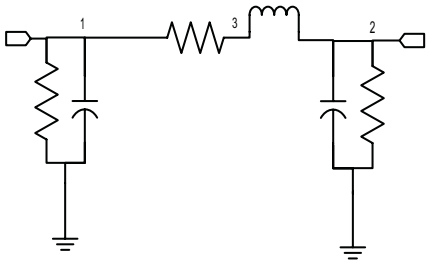


Figure 3.5: Desired resulted circuit (testing automatic augmentation)

The testing method is as follows:

1. Find the response of circuit 1 at some frequencies. In this case the frequency range of 1-5 $GHz$ is divided into 40 frequency points with equal separation.
2. Alter circuit 1 to become circuit 2 as shown in Fig. 3.6.
3. Use the modeling method to regain circuit 1 from circuit 2.

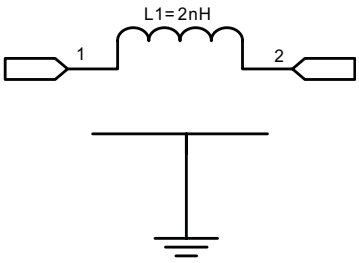


Figure 3.6: Initial circuit (testing automatic augmentation)

The Y parameter response comparison between circuit 2 (initial) and circuit 1 (desired) is shown in Fig. 3.7.

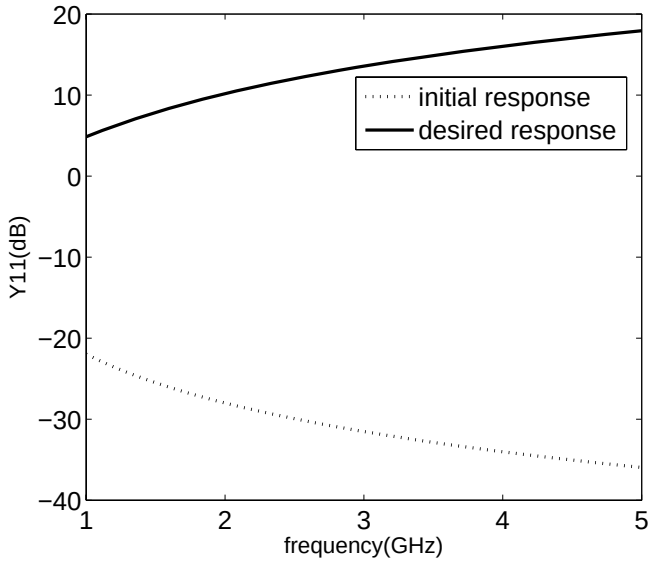


(a)

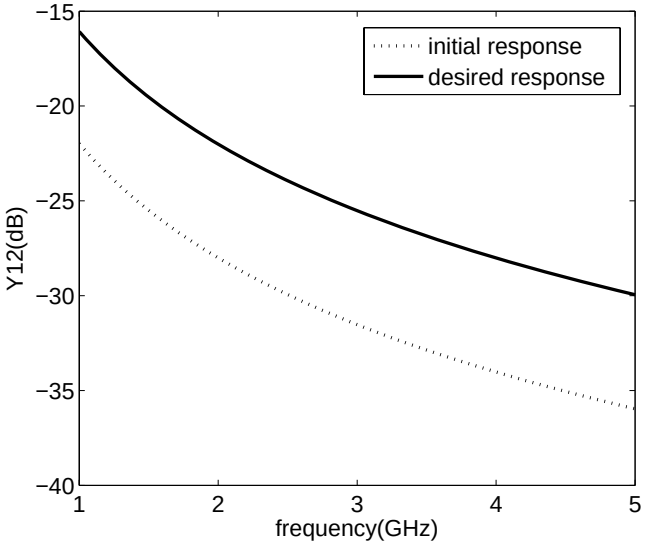


(b)

Figure 3.7: Initial circuit response (testing automatic augmentation)

Three terminal pairs will be augmented simultaneously. We will not use sequence generator explained in section III.C2. This is because the answer to at which terminal pairs the augmentation has to be chosen is quite trivial. Observe that the available number of terminal pairs is only three. They are [[0 1], [0 2], [1 2]] where 0 represents the ground. As we see here we need at least to do multiple augmentation twice. What we expect is

*Iteration 1*: L1 will be tuned to 1nH. C1, C2 = 250 pF will be added at [0 1] and [0 2], respectively.

*Iteration 1*: Node 3 will be created with R1= 1 ohm added at [2 3]. R2, R3 = 1 ohm will be added at [0 1] and [0 2], respectively.

Hence, the type of augmentation that we expect will be performed by the algorithm is

*Iteration 1*: [parallel, parallel, parallel]

*Iteration 2*: [parallel, parallel, series]

The direct element comparison is used to decide what element has to be augmented.

We use this augmentation type assignment in the old method (the one that is based on physical augmentation, not based on the automatic physical augmentation). Then we compare the result between the new method (based on automatic augmentation) and old method.

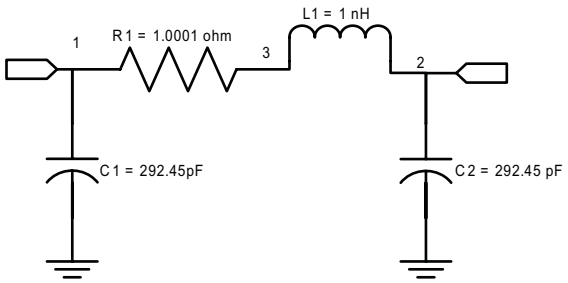


Figure 3.8: Resulted circuit (testing automatic augmentation)

It is found that both of them produce the same result. The resulted circuit after 2 iterations is shown in Fig. 3.8.

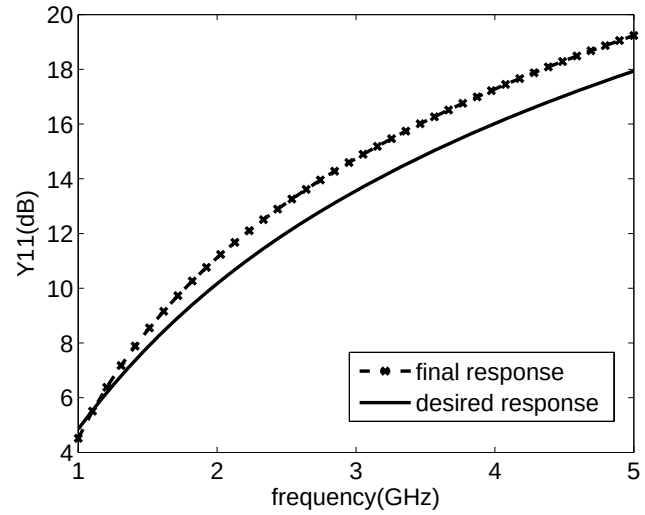


(a)

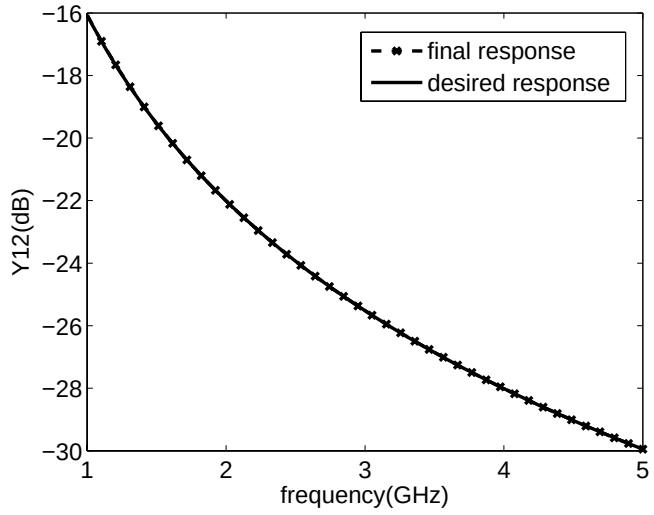


(b)

Figure 3.9: Final circuit response (testing automatic augmentation, new method gives the same results as the old method)

The Y parameter response comparison between the resulted circuit (final) and circuit 1 (desired) is shown in Fig. 3.9.

From the result, we find that the new method can decide the type of augmentation accurate enough. The reason why the equivalent circuit is not the same as circuit 1 is because we use many approximations to get the value of augmented elements. But, since their responses are not so different, the approximations are acceptable generally.

## 3.4 Spiral inductor and MIM Capacitor Modeling

In this section we will use the new method for modeling an MIM capacitor and a spiral inductor. In order to be able to make comparison with the old method, we need to decide how the augmentation type assignment is done in the old method. The procedure that we use is described below.

Odd sequence: all augmentations are series

Even sequence: all augmentations are parallel.

This procedure is used to ensure the probability for the series augmentation is the same as that for the parallel case. This is reasonable since we assume there is no prior knowledge about the structure of the correct equivalent circuit. In this thesis, we call the old method combined with this augmentation type assignment as the pseudo-new method.

There is one important thing in the pseudo-new method. It is that, like in the new method, we do not differentiate between the original circuit element and the augmented circuit element.

The maximum number of iteration allowed is 30. The algorithm can stop before 30 iterations if it detects that no further improvement is possible.

The MIM capacitor structure is shown in Fig. 3.10. The response of this capacitor is

obtained using IE3D simulation.

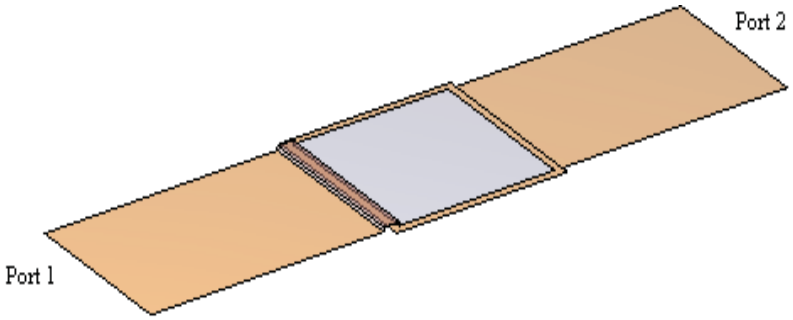


Figure 3.10: MIM capacitor layout

The initial equivalent circuit for the MIM capacitor is obtained using IE3D at 1 GHz. This circuit and its responses are shown in Fig. 3.11 and Fig. 3.12, respectively.

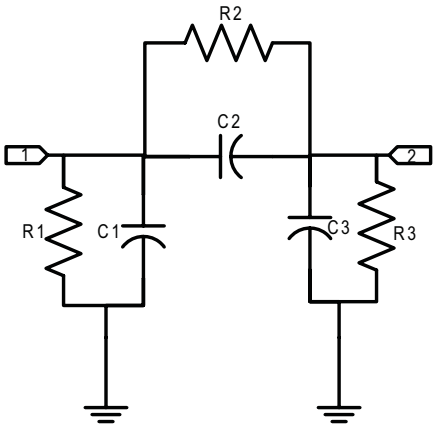


| Element | Value(ohm)(pF)(nH) |
|---|---|
| R1 | 4k |
| C1 | 0.06 |
| R2 | 46k |
| C2 | 3 |
| R3 | 27M |
| C3 | 0.03 |

Figure 3.11: Initial MIM equivalent circuit

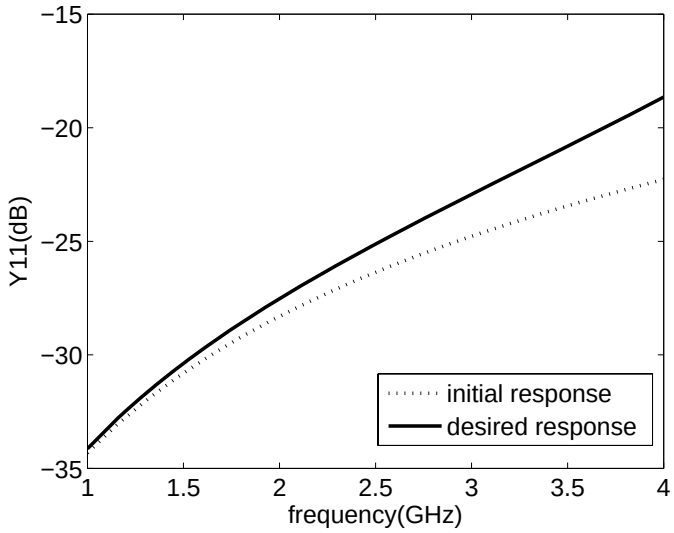


(a)

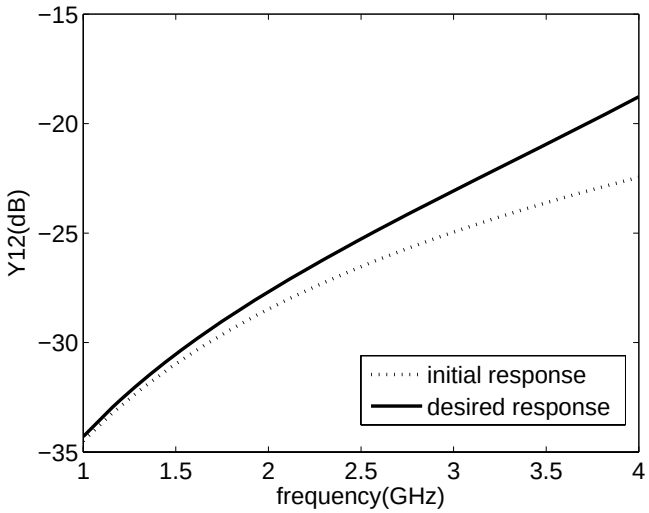


(b)

Figure 3.12: Response of initial MIM capacitor equivalent circuit

The responses of the final equivalent circuit when the direct element comparison is used are shown in Fig. 3.13. Since in this case the new and pseudo-new method gives the same

result, only one graph is drawn. We see in this case that both methods give bad results.

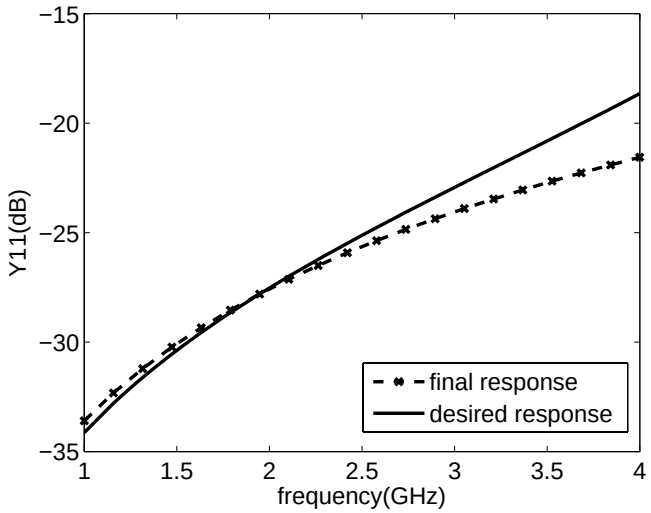


(a)

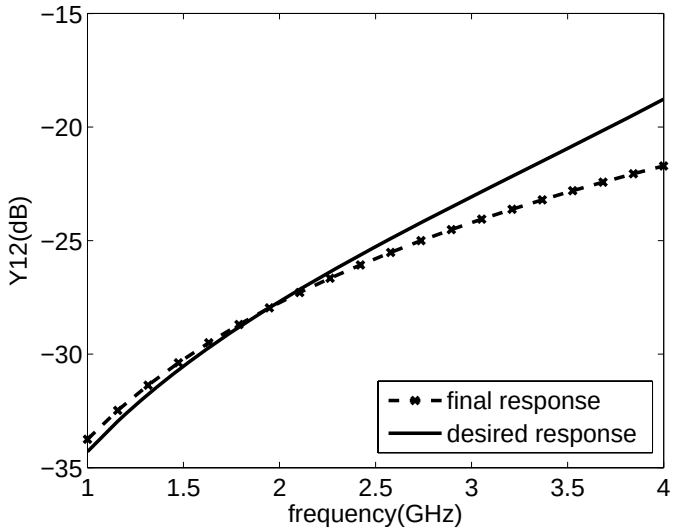


(b)

Figure 3.13: Response of final MIM capacitor equivalent circuit (direct element comparison, pseudo-new method gives the same result as new method)

The responses of the final equivalent circuit when the indirect element comparison is used are shown in Fig. 3.14 and Fig. 3.15.

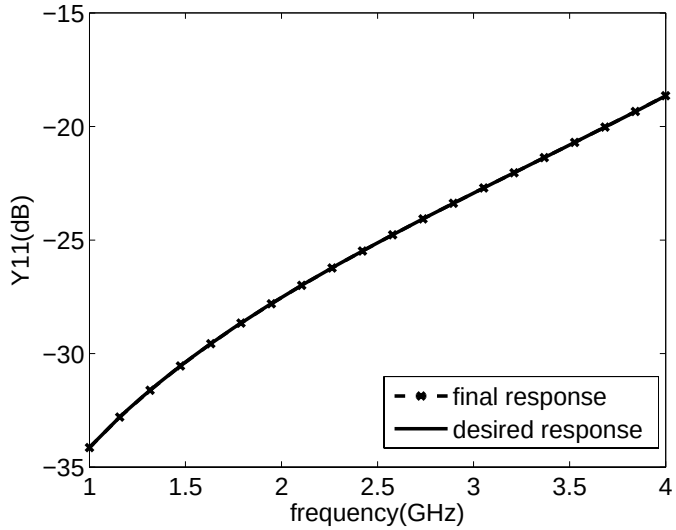


(a)

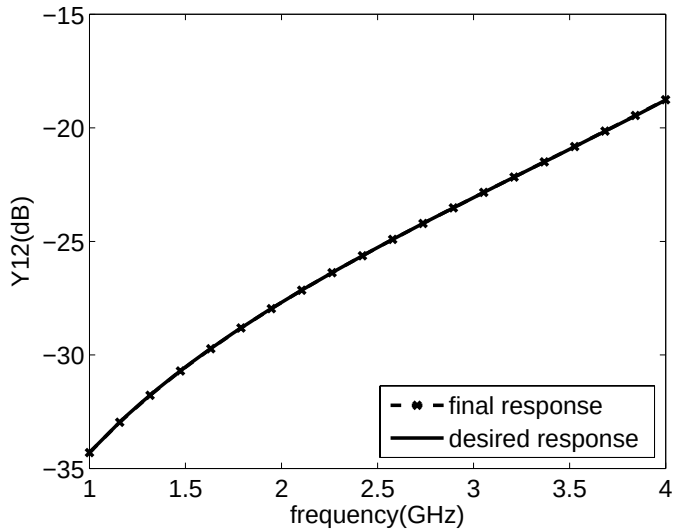


(b)

Figure 3.14: Response of final MIM capacitor equivalent circuit (indirect element comparison, pseudo-new method)

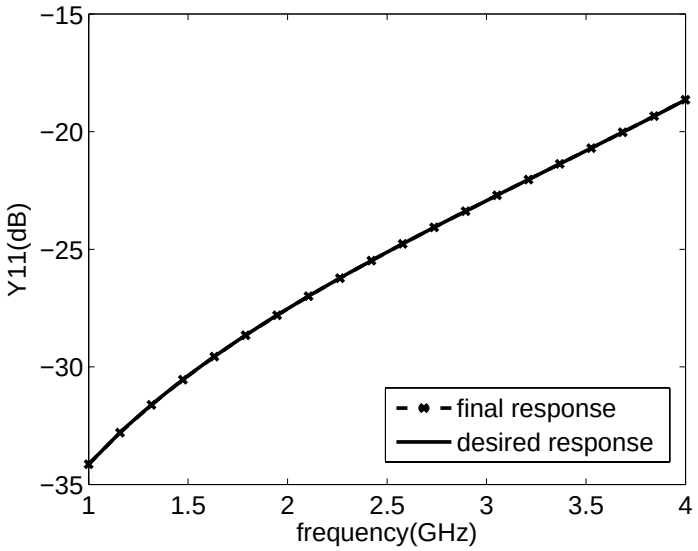


(a)

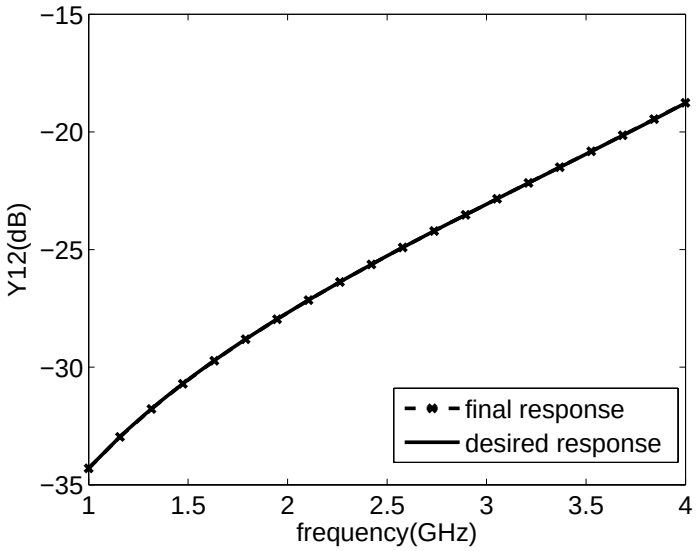


(b)

Figure 3.15: Response of final MIM capacitor equivalent circuit (indirect element comparison, new method)

Fig. 3.16 shows the final equivalent circuit when the new method with indirect element comparison is used.

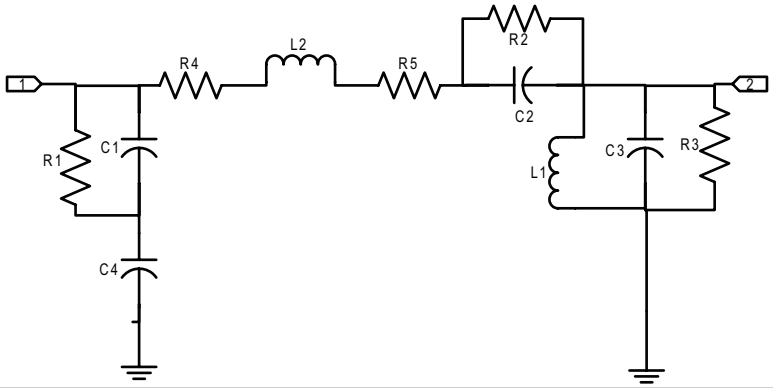


| Element | Value(ohm)(pF)(nH) | Element | Value(ohm)(pF)(nH) |
|---|---|---|---|
| R1 | 25699.2262 | R2 | 8744.702 |
| C1 | 6.712e-2 | C2 | 3 |
| R3 | 27M | R4 | 2.3756e-5 |
| C3 | 3.3906e-2 | C4 | 2.4927e-1 |
| L1 | 1178.4 | L2 | 1.8285e-1 |
| R5 | 0.038978 | | |

Figure 3.16: Final MIM Capacitor equivalent circuit (indirect element comparison, new method, not simplified)

We see that the circuit can be simplified by combining elements with the same type which are connected in series. Unfortunately, a general algorithm to do this combining is not available. Hence, this job has to be done manually. In the following parts, only the simplified equivalent circuit is shown.

Fig. 3.17 shows the final equivalent circuit when the pseudo-new method with indirect

element comparison is used. Initially this circuit contains 15 nodes (including ground) and 18 elements, which are larger than those for the circuit obtained using the new method. Hence, when the final responses are roughly the same, the new method produces a simpler equivalent circuit than the old method.

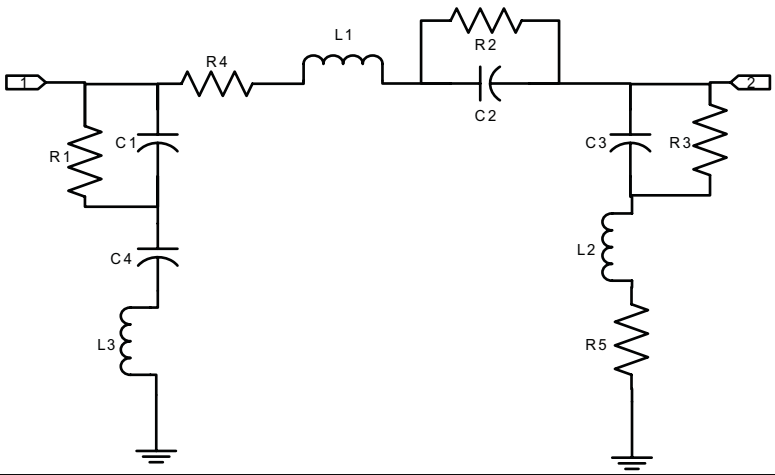


| Element | Value(ohm)(pF)(nH) | Element | Value(ohm)(pF)(nH) |
|---|---|---|---|
| R1 | 4k | R2 | 46k |
| C1 | 6e-2 | C2 | 3 |
| R3 | 27M | R4 | 0.051789 |
| C3 | 3e-2 | C4 | 2.13274e-1 |
| L1 | 1.8329e-1 | L2 | 5.5435e-1 |
| R5 | 67.6925 | L3 | 5.9535 |

Figure 3.17: Final MIM Capacitor equivalent circuit (indirect element comparison, pseudo-new method, simplified)

The spiral inductor structure is shown in Fig. 3.18. The inductor is simulated using IE3D.

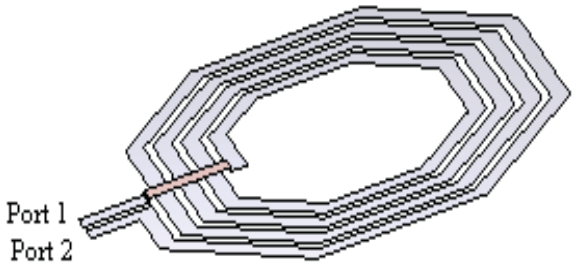


Figure 3.18: Spiral inductor layout

Initially, the initial equivalent circuit for the spiral inductor is obtained using IE3D at 1 GHz. In order to test the method for a bad initial equivalent circuit, a different initial circuit is produced by slightly modifying the values of elements in the IE3D-produced initial equivalent circuit. This circuit and its responses are shown in Fig. 3.19 and Fig. 3.20, respectively.

The new procedure gives better result than the pseudo-new procedure regardless of the element comparison method used. It is also found that the indirect element comparison gives better result regardless which procedure is used.

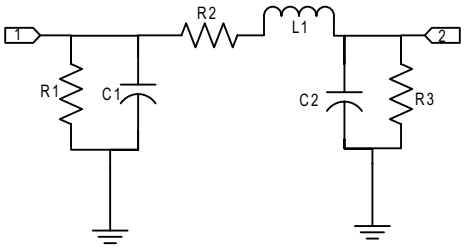


| Element | Value(ohm)(pF)(nH) |
|---|---|
| R1 | 400 |
| C1 | 1e-2 |
| R2 | 4 |
| L1 | 4 |
| R3 | 200 |
| C2 | 2e-2 |

Figure 3.19: Initial spiral inductor equivalent circuit

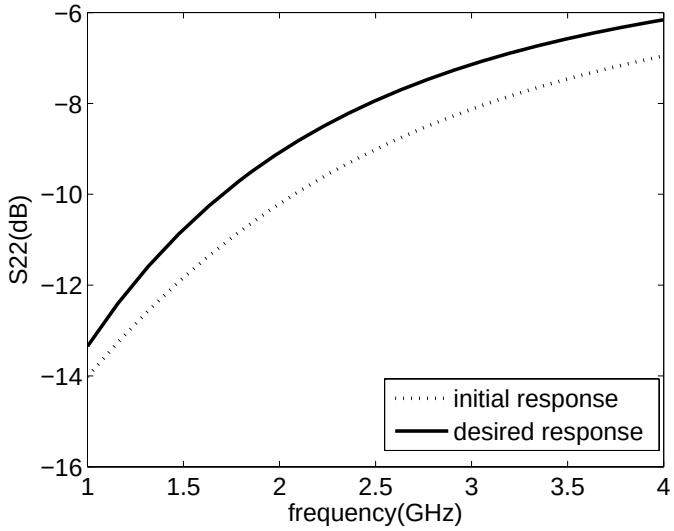


(a)

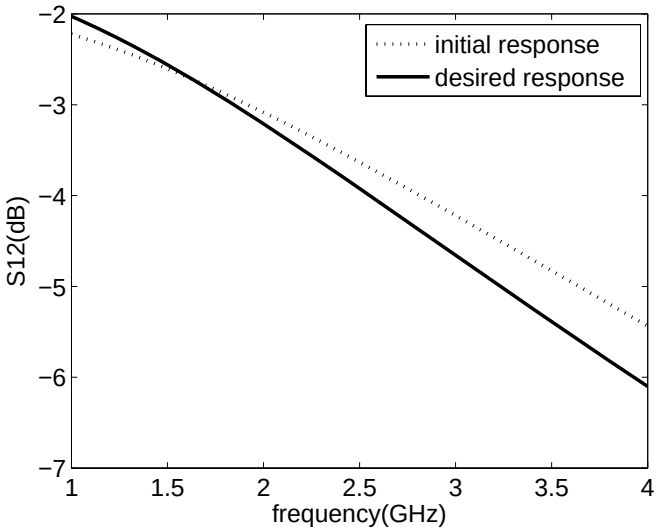


(b)

Figure 3.20: Response of initial spiral inductor equivalent circuit

The responses of the final equivalent circuit when the indirect element comparison is used are shown in Fig. 3.21 and Fig. 3.22. We see here that the new method gives much

better result than the pseudo-new method.

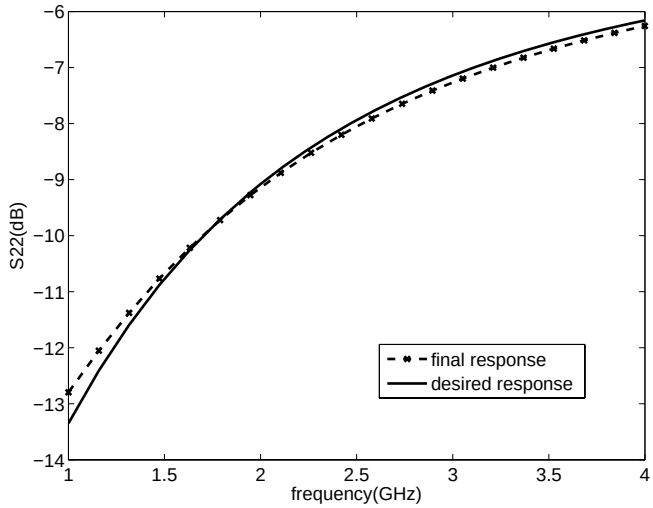


(a)

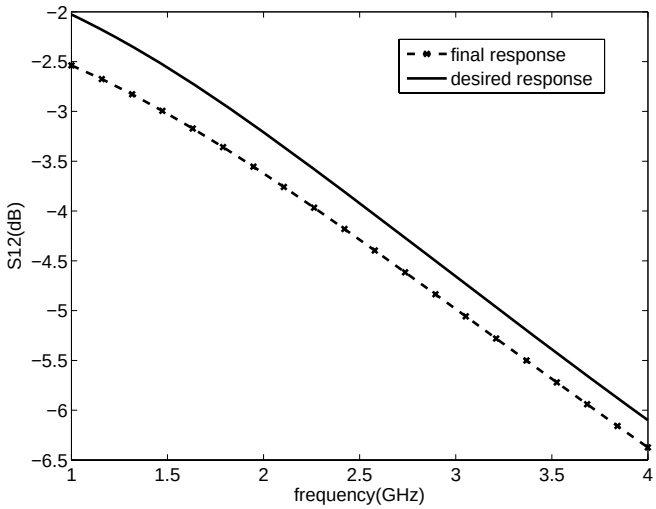


(b)

Figure 3.21: Response of final spiral inductor equivalent circuit (indirect element comparison, pseudo-new method)

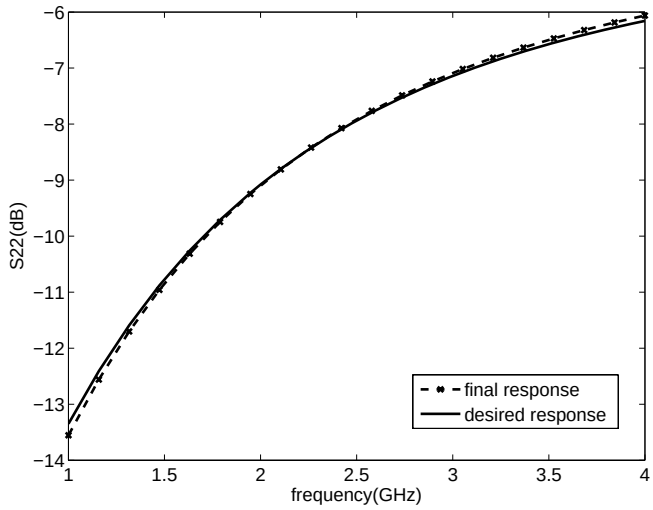


(a)

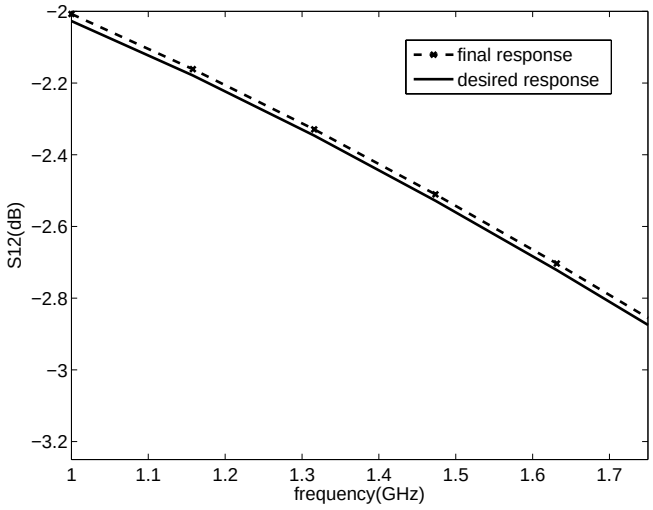


(b)

Figure 3.22: Response of final spiral inductor equivalent circuit (indirect element comparison, new method)

Fig. 3.23 shows the final equivalent circuit when the new method with indirect element comparison is used.

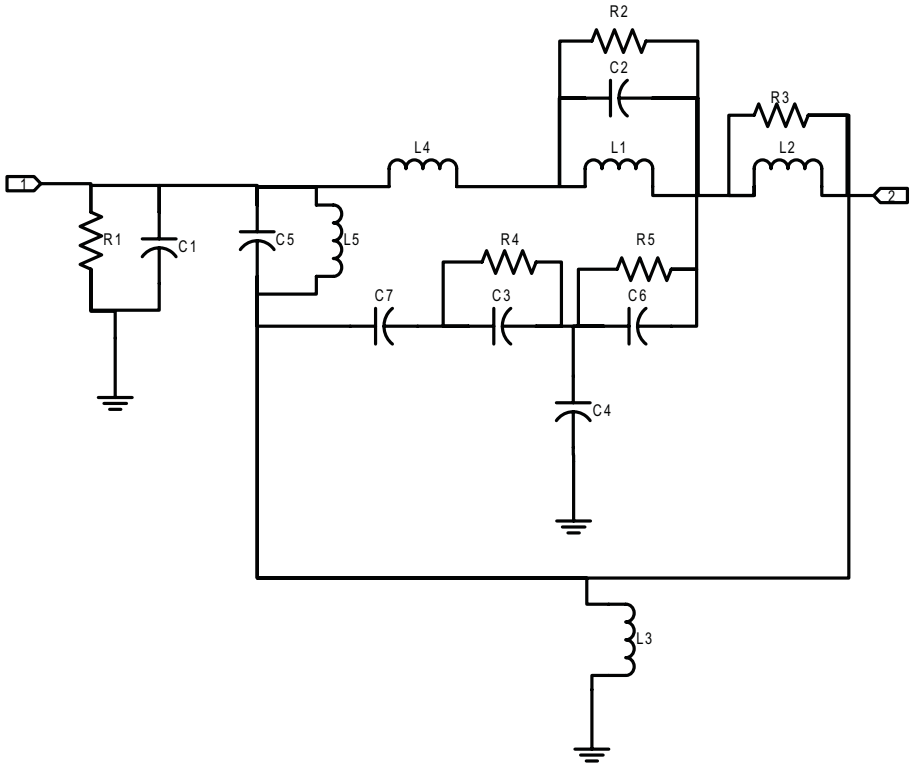


| Element | Value(ohm)(pF)(nH) | Element | Value(ohm)(pF)(nH) |
|---|---|---|---|
| R1 | 417.3625 | R2 | 4 |
| C1 | 1e-2 | C2 | 2.636 |
| R3 | 725.5941 | R4 | 290.5619 |
| C3 | 2e-2 | C4 | 8.5926 |
| L1 | 1.1092e4 | L2 | 4.5147 |
| R5 | 26847.6235 | L3 | 5.7555e2 |
| L4 | 5.0945e-6 | L5 | 7.7028e2 |
| C5 | 4.734665e-3 | C6 | 9.6192e-3 |
| C7 | 5.9084 | | |

Figure 3.23: Final spiral inductor equivalent circuit (indirect element comparison, new method, simplified)

## 3.5 UWB Antenna Modeling

There are three modifications in the method used for UWB antenna modeling. They are:

1. It is still not clear which one is better, the direct or indirect element comparison. For UWB antenna modeling, we use switching method in our new method. We implement this by modifying our sequence generator. The sequence generator used for UWB antenna modeling is described below.

   **Sequence Generator 2**

   1-7. As in **Sequence Generator** box

   8. If the modeling algorithm fails to produce improvement in the first iteration after reset, switch from indirect (direct) to direct (indirect) element comparison.

   9. If the modeling algorithm fails to produce improvement in the first iteration after switching, stop the algorithm.

   The next problem is that which one has to be executed first, direct or indirect element comparison. Because we still cannot answer this question, we try both ways and choose the best results.

2. A separate tuning method is added. The method becomes as in Fig. 3.24. Here we use a special block for tuning since negative element augmentation is not allowed in circuit augmentation block.

   We use tuning based physical augmentation in our implementation. Tuning based

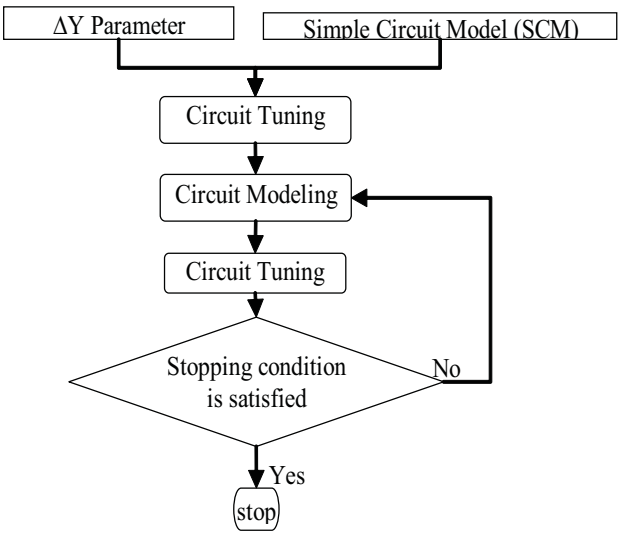


Figure 3.24: Modeling method with additional separate tuning method

physical augmentation is basically the same as modeling based physical augmentation for tuning case (see box **Example**). Moreover, the element comparison is based on element's admittance. Hence, (3.2.16) in tuning method will be changed to

$$\Delta = \frac{1}{N_f}\sqrt{\sum_f |y(f) - y_{aug}(f)|^2} \tag{3.5.1}$$

3. In series augmentation, the comparison between elements is divided into two cases. When comparing elements with the same type (resistor, inductor, or capacitor), the series-equivalent of $z(f)$ and $z_{aug}(f)$ is used in (3.2.16) while when comparing elements that have different type parallel-equivalent of $z(f)$ and $z_{aug}(f)$ is used in (3.2.16). Note that the series-equivalent of $z_{aug}(f)$ is $z_{aug}(f)$, and parallel-equivalent of $z(f)$ is $z(f)$. We found that this rule can improve the resulted equivalent circuit.

In our implementation, the maximum number of iterations allowed to be executed within the circuit modeling (tuning) is 200. In total the circuit tuning block is executed for 3 times and circuit modeling block is executed for 2 times.

Since the number of port is 1, in order to make the linear equation (3.2.13) not to be underdetermined, only single augmentation can be performed. However we found that the result is not good enough when only single augmentation is allowed. Hence we use multiple augmentations. Due to this, (3.2.13) will have many solutions. In order to find unique solution of (3.2.13) we add one more condition. The solution of (3.2.13) that will be chosen is the one that has minimum 2-norm value. In a sense, it is the one that minimize the change in the circuit.

For circuit tuning block, the number of augmentations done simultaneously is 2. For circuit augmentation block, single augmentation is used for the odd numbered iterations, while two augmentations are done simultaneously for even numbered iterations.

The first UWB antenna structure is shown in Fig. 3.25. The Z parameter responses of this antenna are obtained using IE3D simulation.

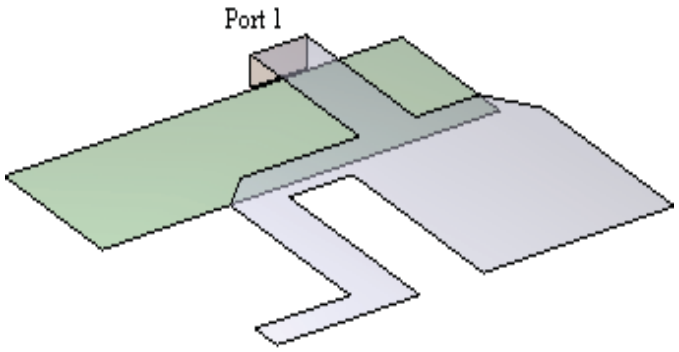


Figure 3.25: UWB antenna 1 layout

The initial equivalent circuit for the UWB antenna and its responses are shown in Fig. 3.26 and Fig. 3.27 respectively.

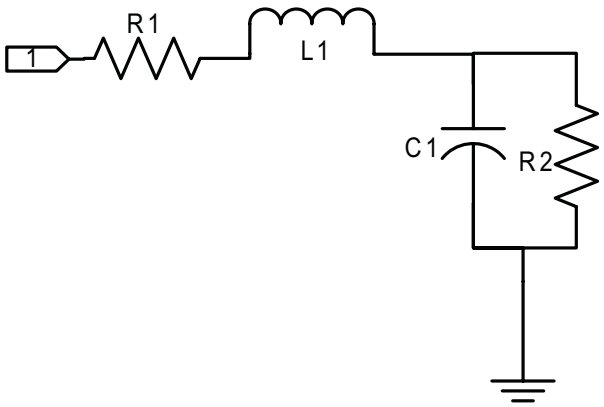


| Element | Value(ohm)(pF)(nH) |
|---|---|
| R1 | 10 |
| C1 | 1 |
| R2 | 10 |
| L1 | 1 |

Figure 3.26: Initial UWB Antenna 1 equivalent circuit

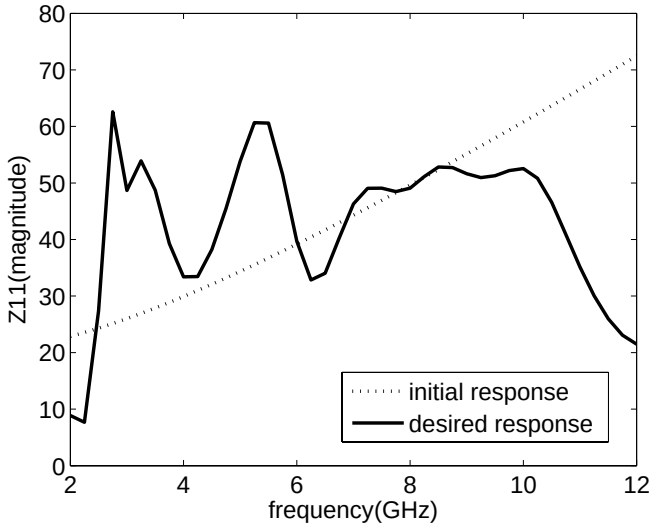


(a)

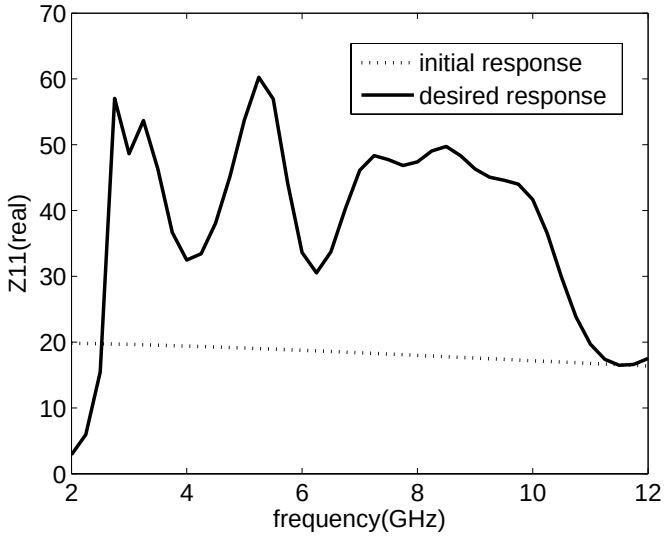


(b)

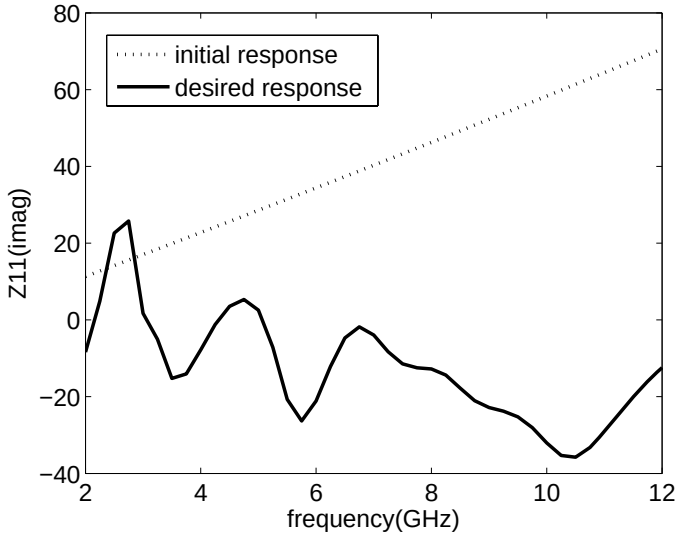


(c)

Figure 3.27: Response of initial UWB Antenna 1 equivalent circuit

The final equivalent circuit is shown in Fig.3.28 and its netlist is shown in Table 3.1. Its responses are shown in Fig. 3.29.

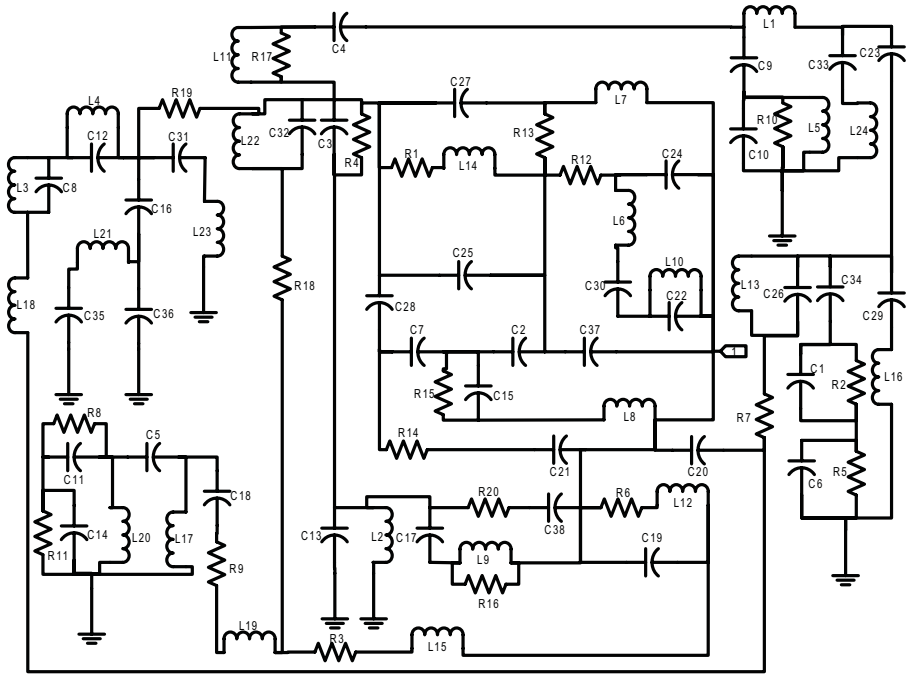


Figure 3.28: UWB Antenna 1 equivalent circuit (simplified)

Table 3.1: Netlist of UWB Antenna 1 Equivalent Circuit
(resistor in $\Omega$, inductor in $H$, capacitor in $F$)

| | | |
|---|---|---|
| .subckt inpMNA 22 | R11 0 16 0.011286 | R20 33 41 643.608 |
| R1 1 34 52.2607 | C15 0 16 153.03e-12 | C29 1 23 0.020328e-12 |
| L1 2 14 1.2576e-9 | R12 5 19 397.582 | R21 17 1 112.209 |
| R2 3 4 70.5847 | L7 19 20 1.48092e-9 | L16 5 34 1.03282e-9 |
| C1 3 4 1.0184e-12 | R13 21 5 613.948 | L17 28 35 0.16068e-9 |
| C2 5 9 1.0351e-12 | L8 22 21 3.9972e-9 | C30 32 36 0.091381e-12 |
| R4 1 6 302.915 | R14 23 30 0.0090857 | L18 0 36 4.5957e-9 |
| C3 1 6 0.10213e-12 | R15 24 9 101286 | L19 0 27 1.5563e-9 |
| C4 7 14 1.4485e-12 | C16 24 9 5.1122e-19 | L20 13 29 1.96827e-9 |
| C5 8 27 2.7082e-12 | C17 25 17 0.35524e-12 | C31 31 20 2.68179e-12 |
| R5 3 0 0.27315 | L9 22 24 481440e-9 | L22 0 8 0.0046286e-9 |
| C6 3 0 180910e-12 | C18 6 26 1.6399e-12 | L23 25 37 0.87732e-9 |

| | | |
|---|---|---|
| C7 9 23 5.1612e-12 | C19 27 42 1.2672e-12 | C32 38 17 0.00035176e-12 |
| R6 10 22 3.5349 | C20 22 28 1.0945e-12 | C33 1 33 1.2463e-12 |
| R7 11 29 914.58 | R17 26 22 0.15746 | L25 1 33 0.68261e-9 |
| L2 6 0 2.99352e-9 | L10 26 22 4.3789e-15 | C34 2 39 0.10809e-12 |
| C8 12 13 0.44097e-12 | C21 22 29 0.09144e-12 | L27 0 38 3162.1e-9 |
| L3 12 13 1.0327e-9 | C22 30 22 0.72688e-12 | L28 0 39 4.8637e-9 |
| C9 14 15 2.9765e-12 | C23 22 31 4549.8e-12 | C36 4 32 21.55e-12 |
| C10 15 0 662.27e-12 | L11 22 31 0.00024446e-9 | C38 0 37 20.345e-12 |
| R8 8 16 12.925 | C24 32 2 7.1164e-12 | C39 0 25 0.001104e-12 |
| C11 8 16 244.19e-12 | C25 22 19 0.30053e-12 | C40 22 5 0.06224e-12 |
| C12 12 17 1.1457e-12 | C26 1 5 0.1678e-12 | R22 6 40 35429.5 |
| L5 12 17 0.37186e-9 | R19 1 7 0.099726 | C42 40 22 4.3647e-19 |
| C13 0 6 0.1055e-12 | L12 1 7 0.10665e-9 | C28 1 21 0.46483e-12 |
| R9 18 42 0.1533 | L13 28 10 0.21664e-9 | L21 41 18 0.0588604e-9 |
| R10 0 15 2.38112e+007 | C27 32 11 0.64344e-12 | R3 41 35 119.327 |
| L6 0 15 7904.6e-9 | L14 32 11 1.7427e-9 | .ends inpMNA |

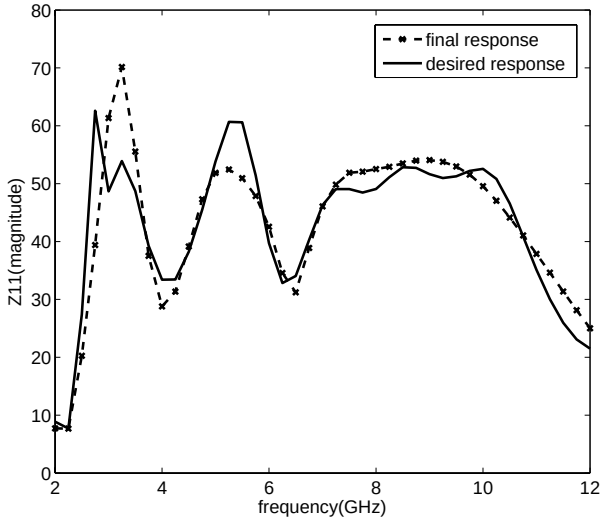


(a)

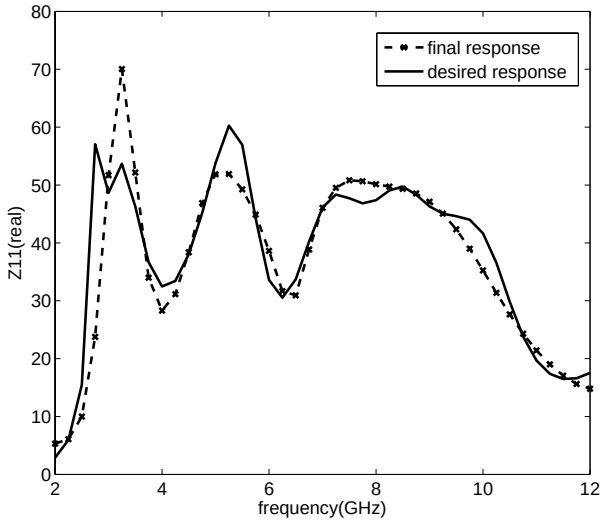


(b)

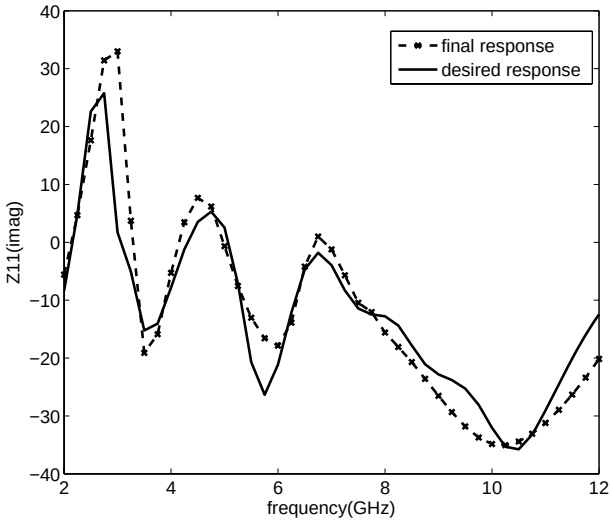


(c)

Figure 3.29: Response of final UWB Antenna 1 equivalent circuit

The second UWB antenna structure is our 3D monopole structure which is shown in Fig. 3.30. This antenna is simulated using ANSOFT HFSS.

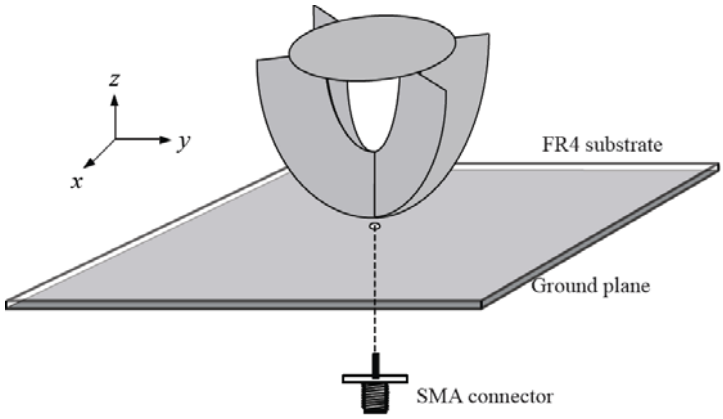


Figure 3.30: UWB antenna 2 layout

The initial equivalent circuit for the second UWB antenna and its responses are shown in Fig. 3.31 and Fig. 3.32 respectively.

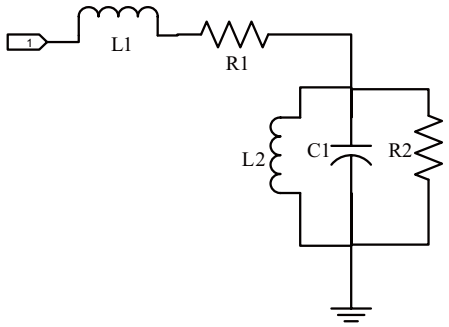


| Element | Value(ohm)(pF)(nH) |
|---|---|
| C1 | 1 |
| L1 | 1 |
| C2 | 1 |
| L2 | 1 |
| R1 | 10 |

Figure 3.31: Initial UWB Antenna 2 equivalent circuit

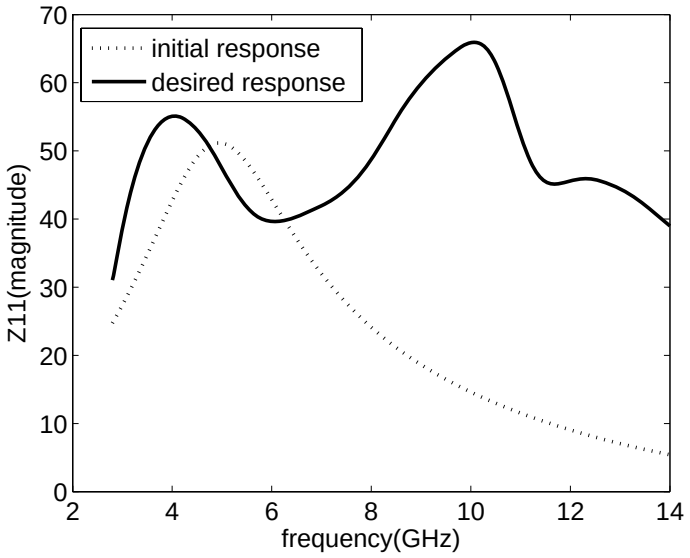
initial response
desired response
Z11(magnitude)
frequency(GHz)
0
10
20
30
40
50
60
70
2
4
6
8
10
12
14

(a)

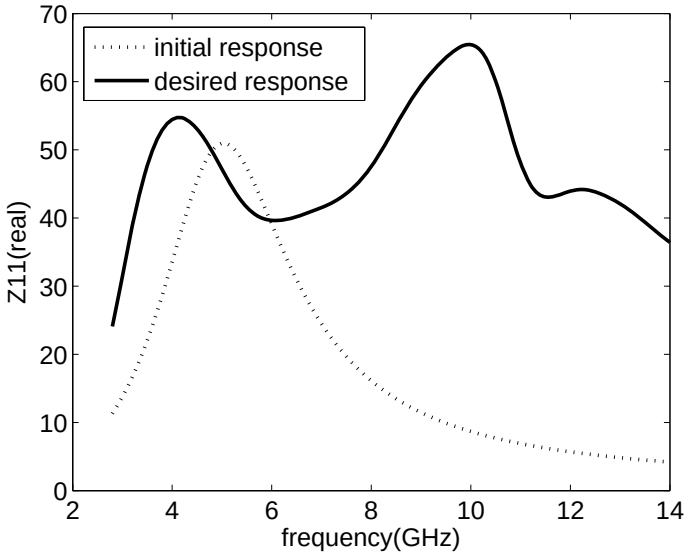
initial response
desired response
Z11(real)
frequency(GHz)
0
10
20
30
40
50
60
70
2
4
6
8
10
12
14

(b)

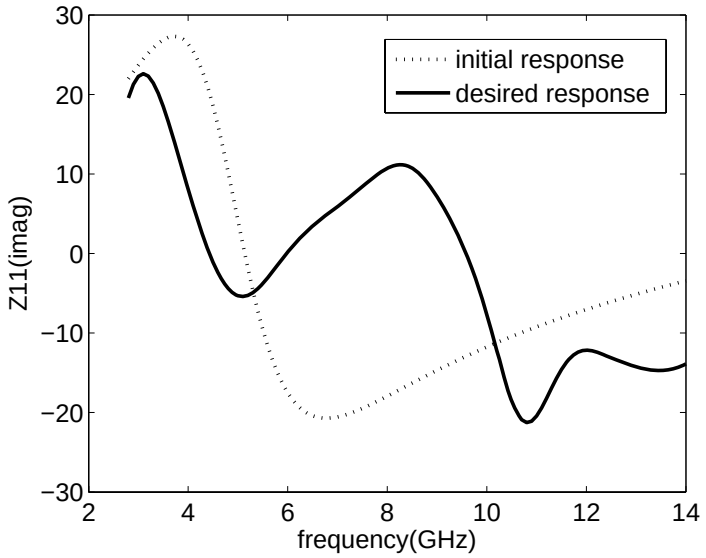


(c)

Figure 3.32: Response of initial UWB Antenna 2 equivalent circuit

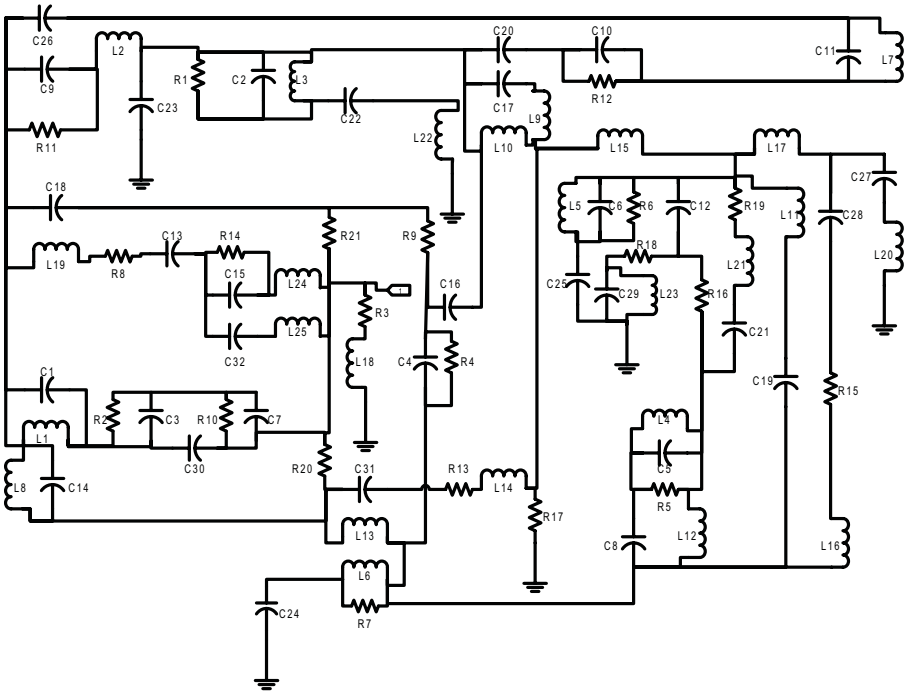


Figure 3.33: UWB Antenna 2 equivalent circuit (simplified)

The final equivalent circuit is shown in Fig.3.33 and its netlist is shown in Table 3.2. Its responses are shown in Fig. 3.34.

Table 3.2: Netlist of UWB Antenna 2 Equivalent Circuit
(resistor in Ω, inductor in $H$, capacitor in $F$)

| | | |
|---|---|---|
| .subckt final 10 | L12 24 47 0.36611e-9 | C8 8 22 0.081918e-12 |
| R1 1 2 28.5398 | L13 3 21 0.18034e-9 | C9 23 46 1.88648e-12 |
| R2 3 4 1.0828 | L14 22 25 3.5589e-9 | C10 4 8 0.12986e-12 |
| R3 3 5 58.1529 | L15 26 28 4.0622e-9 | C11 3 21 1.6476e-12 |
| R4 6 30 42.244 | L16 6 27 0.0010784e-9 | C12 6 27 96.508e-12 |
| R5 4 7 10.8492 | L17 3 25 0.0027947e-9 | C13 3 25 110.49e-12 |
| R6 8 9 13348 | L18 11 7 7.3561e-9 | C14 2 29 4.54851e-12 |
| R7 10 11 1.1876 | L19 30 38 0.14269e-9 | C15 11 14 0.01692e-12 |
| R8 19 50 192.19 | L20 9 32 0.031767e-9 | C16 31 36 10.594e-12 |
| R9 8 22 825.798 | L21 34 42 16.597e-9 | C17 33 14 3.63658e-12 |
| R10 4 8 291.557 | L22 13 39 1.7008e-17 | C18 24 8 0.624794e-12 |
| R11 4 26 44.6455 | L23 41 15 0.087004e-9 | C19 35 49 8.7032e-12 |
| R12 3 25 1.5792 | L24 8 35 0.052475e-9 | C20 36 37 0.80562e-12 |
| R13 11 28 68.8572 | L25 11 29 0.0082388e-9 | C21 36 38 2.0543e-12 |
| R14 11 34 83.0091 | L26 0 8 122.98e-9 | C22 13 39 3.854e-5 |
| R15 7 37 0.6895 | L27 18 46 0.01199e-9 | C23 7 17 0.00054738e-12 |
| R16 7 17 8.1026e-005 | L28 0 48 23.152e-9 | C24 1 40 0.85025e-12 |
| R17 7 43 37.6399 | L29 0 20 0.00016011e-9 | C25 12 23 6.816e-12 |
| R18 21 44 112.166 | L30 0 6 28.211e-9 | C26 26 42 0.050459e-12 |
| R19 7 40 0.52702 | L31 27 49 0.070992e-9 | C27 18 43 0.13337e-12 |
| R20 16 12 16.0301 | L32 0 32 726.25e-9 | C28 0 5 19.177e-12 |

| | | |
|---|---|---|
| R21 23 51 23926.5 | L33 0 24 32.714e-9 | C29 17 45 1918.8e-12 |
| L1 1 2 37.16e-9 | L34 0 27 24.371e-9 | C30 0 9 0.0025499e-12 |
| L2 3 4 3.2346e-14 | L35 48 50 0.494243e-9 | C31 47 48 1.64277e-12 |
| L3 3 5 0.7387e-9 | L36 0 51 2.5365e-9 | C32 0 20 4094.8e-12 |
| L4 4 7 0.062447e-9 | L37 35 52 530.4e-9 | C33 0 6 0.0013562e-12 |
| L5 8 9 0.047981e-9 | C1 3 4 43401e-12 | C34 7 39 7.0557e-3 |
| L6 13 45 0.0003416e-9 | C2 3 5 1e-12 | C35 7 44 6.2204e-12 |
| L7 14 31 0.316577e-9 | C3 10 11 3.0125e-12 | C36 0 41 0.0012582e-12 |
| L8 12 17 0.026919e-9 | C4 12 3 4.3845e-12 | C37 35 52 0.0034489e-12 |
| L9 18 33 0.135775e-9 | C5 15 32 1.70916e-12 | C38 0 52 0.0028013e-12 |
| L10 12 1 0.042583e-9 | C6 4 16 0.012207e-12 | .ends final |
| L11 20 41 0.397406e-9 | C7 19 21 0.701758e-12 | |

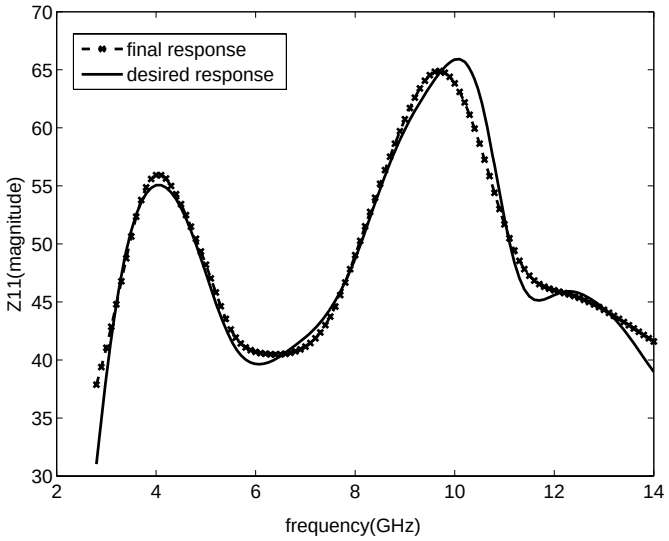


(a)

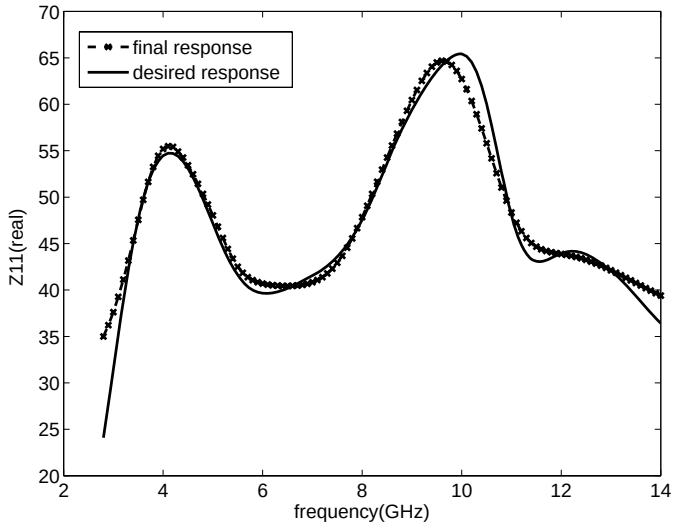


(b)

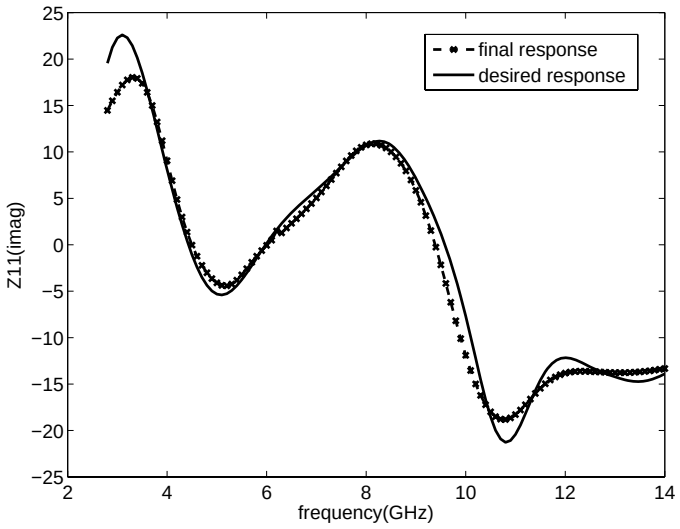


(c)

Figure 3.34: Response of final UWB Antenna 2 equivalent circuit

## 3.6 Conclusion

In this chapter, a new physical augmentation based wideband modeling technique has been presented. In this method, all series augmentation elements are transformed into their parallel equivalents. The initial circuit elements is treated the same as the augmented elements. Tuning is treated as a special case of augmentation. This is achieved by allowing negative valued element augmentation in some circumstances. Using this technique, the preliminary analysis of the circuit to decide the augmentation type is not needed. The type of augmentation to be performed can be determined automatically. The proposed methodology has been validated for broadband modeling of a spiral inductor, and an MIM capacitor. The method has also been successfully extended to extract the equivalent circuits for two UWB antennas. The results show good correlation with the EM data. The final equivalent circuit netlist for the two UWB antennas can be imported to the time-domain software directly, which would be very useful for co-design in the mixed analog/digital circuits in the time domain.

# Chapter 4

# Miniaturized Ultra Wideband antenna Design in LTCC

## 4.1 Introduction

Since Federal Communication Commission of USA allowed 3.1-10.6 GHz unlicensed band for low power UWB communication, the UWB technology has attracted a lot of attention as one of the most promising solutions for future high data-rate wireless communications, high-accuracy radars, and imaging systems [49, 74, 75]. Consequently, as a critical part of the entire system, UWB antennas have been receiving increasing interests from both the academia and industries [76–79].

Accompanied by the decreasing sizes of transistors and chips, electronics components are getting smaller and smaller inside a single integrated circuit. Hence, besides bandwidth enhancement requirement of the UWB system, the miniaturization of UWB antennas has become an important focus. Compared with the traditional PCB technology, the LTCC technology has great advantages on miniaturized multilayer antennas' design. The LTCC process is capable of using the blind, buried and through vias anywhere in the substrate, which gives great flexibility on antenna design. Considering the easy integration, flexible

via-holes distribution, and mechanically strong, hermetically sealed, dimensionally stable process properties, the LTCC has been regarded as the promising technology of light weight, compactness and excellent high frequency performance which is suitable for single integrated circuit solutions of modern microwave and millimeter-wave communication systems [80].

In this chapter, we propose a new compact and multilayer UWB planar antenna designed with the LTCC technology. The configuration of the proposed multilayer UWB LTCC planar antenna fully exploits the three-dimensional (3-D) integration feature of the LTCC technology. The proposed LTCC multilayer UWB antenna is composed of a ground plane, transmission lines and two open asymmetrical rectangular loops on various layers. To minimize the total antenna's size,the two open asymmetrical rectangular loops as the radiation elements of the antenna are separated on two different layers of the LTCC substrate and partly overlaped with each other. The major advantage of flexible via holes distribution of LTCC technology is fully utilized in the antenna design. The vias fulfilled the connections perfectly between the transmission lines and the radiation elements on various layers. A typical antenna design is implemented and the measurement results are presented and discussed. The experimental result shows that the prototype antenna achieves a bandwidth of 7 GHz ($|S11| < -10dB$ from 3.6 to 10.6 GHz). Radiation characteristics over its bandwidth of interest have been examined and are stable in the passband.

## 4.2 LTCC Technology

LTCC is a multilayer ceramic technology (Fig. 4.1). LTCC circuit boards are created by cofiring of a glass ceramic material designed for sintering at temperatures below $1000°C$.

LTCC technology provides an ability to embed passive components in layers, which is suitable for size-reduction of mixed signal RF products since they tend to use up a large number of passive components. Recently, LTCC is also used to create passive circuit elements such as capacitors, resistors, inductors, filters and resonators in a ceramic interconnector package due to its high performance, high integration density, and high reliability.

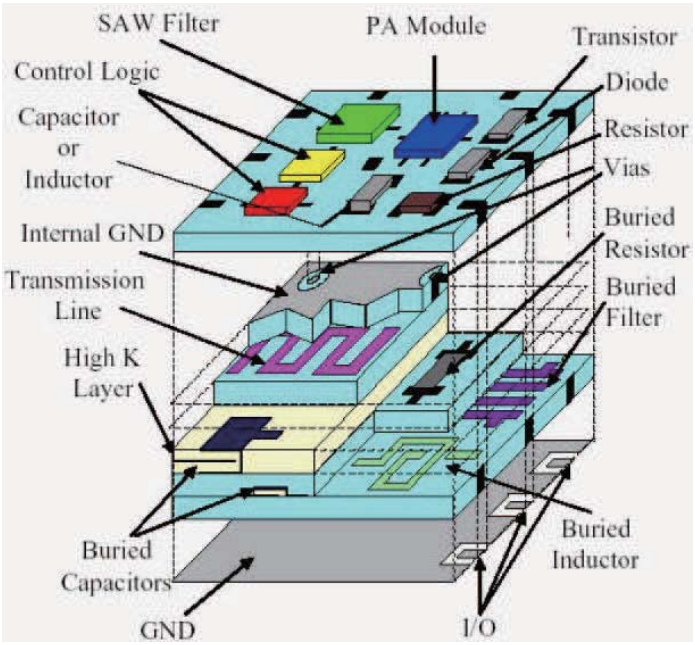


Figure 4.1: LTCC Technology.

LTCC technology also offers the possibility to integrate various chips in one package, which supports the system-in-package (SIP) approach. SIP is a functional block or subsystem that integrates multiple chipsets with embedded passive components in a single package, as shown is Fig.4.2. SIP has the ability to stack die vertically 3D or horizontally side-by-side. Moreover, SiP allows flexible integration of different elements such as MEMS, optoelectronics, active and passive components, bio-electronics and antennas into

the packaging, thus improving performance and reducing system cost.

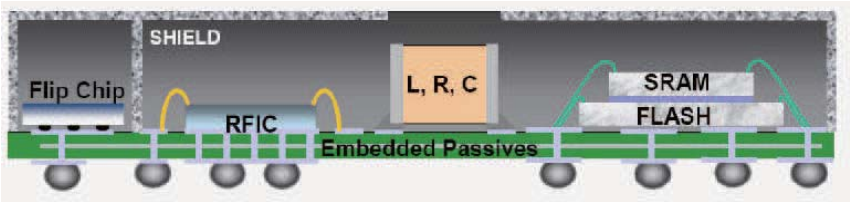


Figure 4.2: System in Package.

Fig.4.3 shows an example of 60 GHz Antenna-in-Package (AiP) solution proposed by IBM [81]. As we can see, LTCC technology gives the possibility of integrating RF circuits and antennas in a single substrate, which in turn makes the antenna design very attractive.

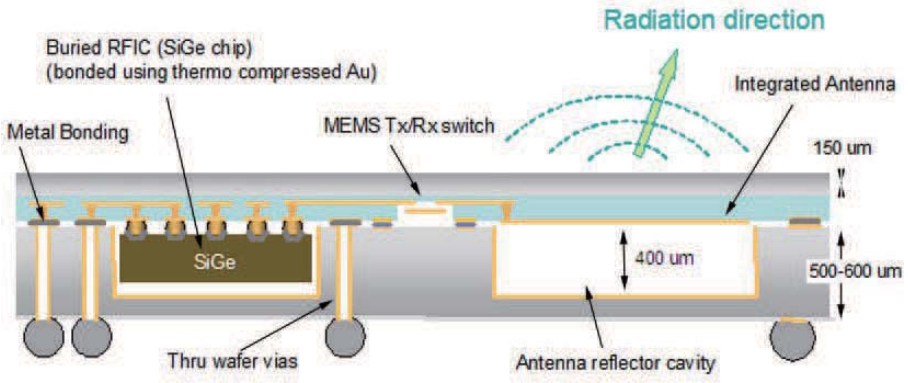


Figure 4.3: Antenna in Package.

## 4.3 A Novel Multilayer UWB Antenna in LTCC

The compact antenna is fabricated on a six-layer LTCC substrate with dielectric constant of 5.9, each layer thickness of 0.19 $mm$ and loss tangent (tan$\delta$) of 0.0026. The configuration of the proposed multilayer patch antenna is shown in Fig. 4.4.

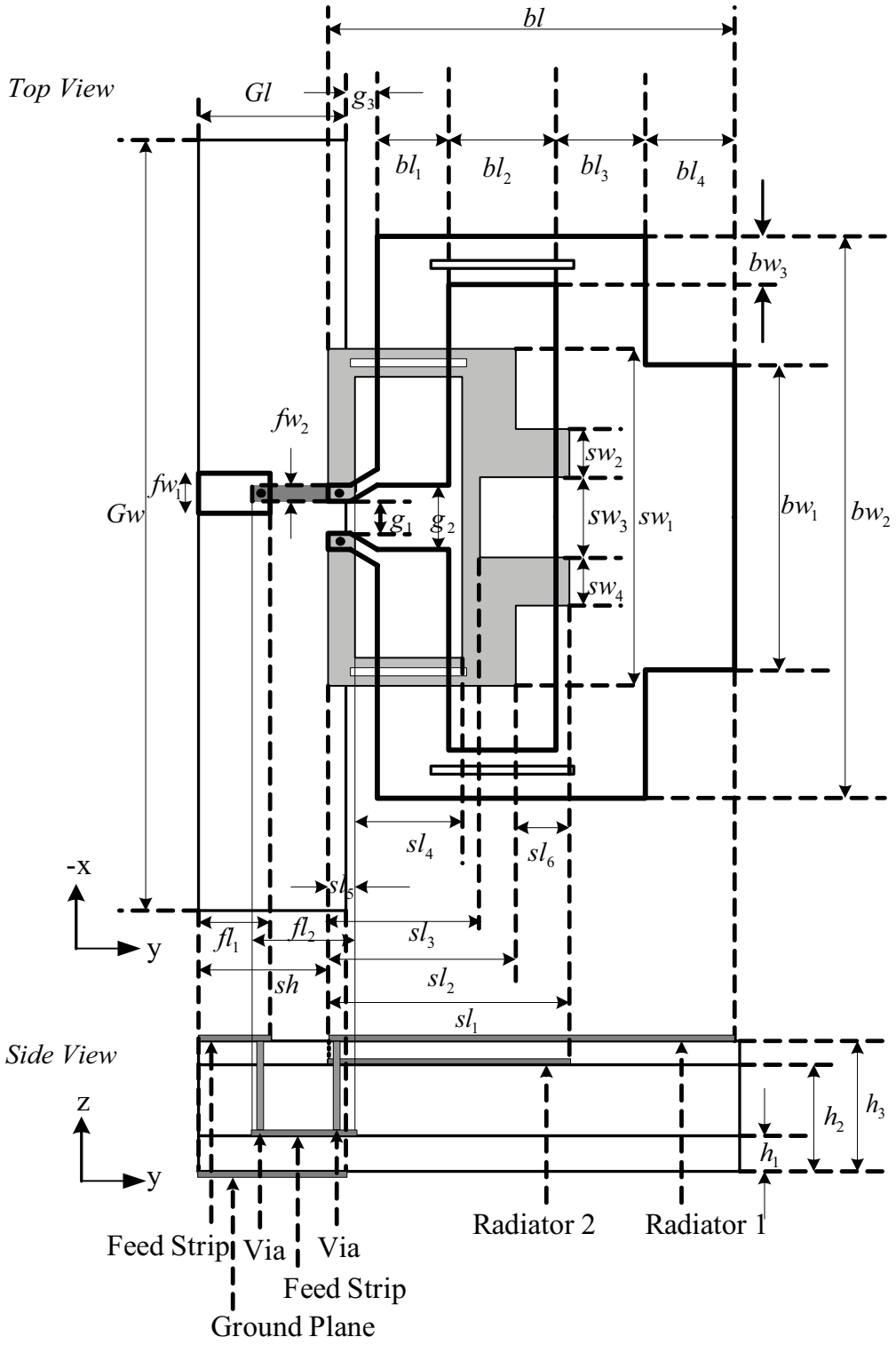


Figure 4.4: Geometry of the proposed multilayer UWB antenna on LTCC.

The detailed dimensions are shown in the Table 4.1. Various parameters are introduced in the proposed antenna design due to the multilayer stuctures, which may add more complexity but give more flexibility on the antenna tuning as well.

Table 4.1: ANTENNA DIMENSIONS IN MILLIMETERS

| $h_1$ | $h_2$ | $h_3$ | $Gw$ | $Gl$ | $fw_1$ | $fw_2$ | $fl_1$ |
|---|---|---|---|---|---|---|---|
| 0.38 | 0.95 | 1.14 | 40 | 4.437 | 1.77 | 0.352 | 2.3 |
| $fl_2$ | $g_1$ | $g_2$ | $g_3$ | $sw_1$ | $sw_2$ | $sw_3$ | $sw_4$ |
| 2.737 | 1.032 | 1.638 | 0.923 | 13.115 | 1.881 | 1.638 | 1.881 |
| $sl_1$ | $sl_2$ | $sl_3$ | $sl_4$ | $sl_5$ | $sl_6$ | $sh$ | $bw_1$ |
| 6.364 | 4.349 | 3.649 | 2.144 | 0.934 | 2.015 | 4.153 | 14.627 |
| $bw_2$ | $bw_3$ | $bl_1$ | $bl_2$ | $bl_3$ | $bl_4$ | $bl$ | |
| 20.748 | 1.313 | 1.666 | 2.596 | 2.511 | 3.111 | 11.091 | |

The antenna consists of two open rectangular loops as its radiation elements which lie on two different layers of the LTCC substrate ($h_3 = 1.14\ mm$ and $h_2 = 0.95\ mm$).The two open rectangular loops are connected with each other by two vias at the feeding point and the end point. And both of the open rectangular loops are connected to the microstrip feedline which lies on the $h_1 = 0.38\ mm$ layer through a via. The microstrip feeding line is embedded inside the substrate with the LTCC technology, which can feed the two open rectangular loop radiators vertically at the same time and achieve the best impedance match. The top layer ($h_3 = 1.14\ mm$) contains a short 50-$\Omega$ microstrip line which acts as a pad for soldering a SMA connector. This top layer short microstrip line connects to the $h_1 = 0.38\ mm$ layer feedline through a via. A rectangular shaped ground with size of $Gl \times Gw$ is located on the bottom layer.

The two open rectangular loops are playing the main role in the antenna operating bandwidth. The total lengths of the two open rectangular loops are assigned to one wavelength at two different frequencies. The top layer one ($h_3 = 1.14\ mm$) is assigned at around 3 GHz. The other one is assigned at around 5 GHz. For each of these two open rectangular loops, it is definitely a narrow band radiation element. Here, utilizing the multilayer processing characteristics of the LTCC technology, we can combine two narrow band radiation elements to one broadband radiation antenna. The bandwidth was improved intrinsically because the combined radiation elements introduce different current paths with different lengths which produce multi-resonances. Considering the mutual coupling effects when we combined the two open rectangular loops, these two loops are not strictly symmetrical rectangular loops any more. The right sides of the loops have extended stubs, which are used to improve the impedance matching of the final broadband antenna. Meanwhile, each open rectangular loop has two slots on both upper and lower sides, as shown in Fig. 4.4. These slots are just used to improve the current distribution on both rectangular loops. The top layer ($h_3 = 1.14\ mm$) slots have a dimension of 3.5 $mm \times$ 0.3 $mm$. The $h_2 = 0.95$ $mm$ layer's slots have a dimension of 2.8 $mm \times$ 0.3 $mm$. The radii of all the vias used for connection between different layers is 0.1 $mm$.

### 4.3.1 Parametric Study

The main purpose of the multilayer structure of the proposed LTCC antenna is to achieve an ultra-wide operating bandwidth. Initially, the dimensions of the antenna were selected so that the total lengths of the big and small open rectangular loops equal to one wavelength at around 3 GHz and 5 GHz, respectively. The other parameters are optimized based on the numerical results until it can achieve an ultra-wideband operation. The initial

dimensions of the antenna parameters are shown in Table 4.1. Here we perform the antenna parametric study based on the simulated results to further understand each parameter's effect and improve the antenna performance. When one antenna parameter is analyzed, the other parameters are all kept unchanged as shown in Table 4.1. All the parametric analyses are simulated with a commercial software HFSS, which is a full wave electromagnetic field solver based on the finite element method (FEM).

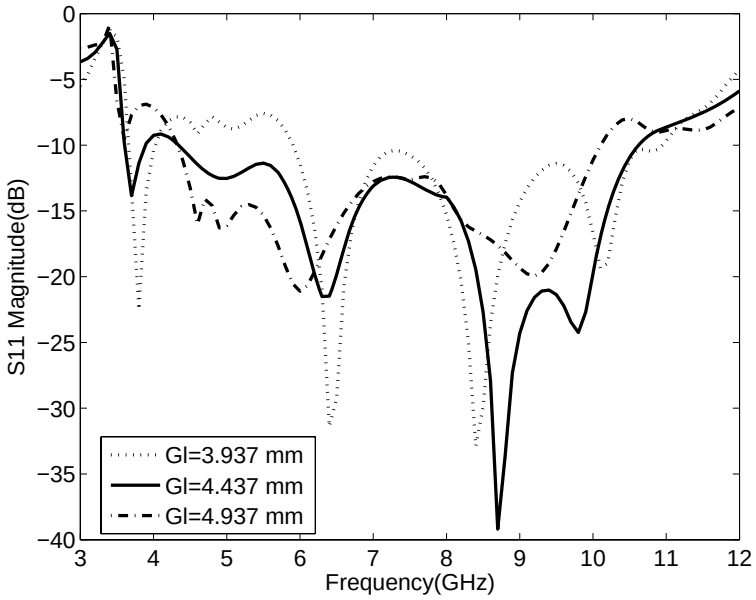


Figure 4.5: Effect of $Gl$.

Fig. 4.5 shows the effect of the '$Gl$' parameter on the simulated S11. As we can see, with a change of $\pm$0.5 $mm$ of '$Gl$', the antenna performance can be kept almost unchanged in the central frequency band but get worse at both low and high frequency band. So the dimensions of the ground have an effect on the input impedance matching of the antenna. We should choose the optimized ground size for achieving the best antenna performance.

Fig. 4.6 shows the effect of '$bl_4$', which refers to an extended stub on the right longer edge of the big rectangular open loop. Increasing '$bl_4$' improves the S11 level between 3.6 GHz-4 GHz and 5.5 GHz-6 GHz, but deteriorates S11 between 6.3 GHz-8 GHz and 9 GHz-10 GHz.

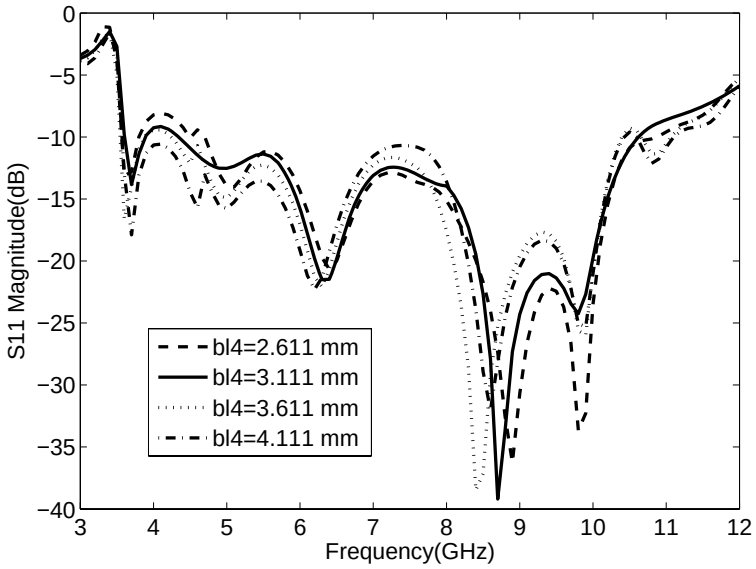


Figure 4.6: Effect of $bl_4$.

Fig. 4.7 shows the effect of '$bw_1$'. When '$bw_1$' is decreased, the impedance matching is improved around 5 GHz-7.3 GHz. Within 8 GHz-10 GHz, appropriate value of '$bw_1$' should be chosen for the best S11 performance.

Fig. 4.8 shows the effect of '$sl_3$', which controls the size of the cut away slot on the edge of the extended stub on the right longer edge of the small rectangular open loop. Tuning '$sl_3$' can slightly tune the lowest frequency band. As '$sl_3$' was decreased from 6.364 $mm$ to 3.649 $mm$, the lowest operating frequency band varies from 4 GHz to 3.6 GHz.

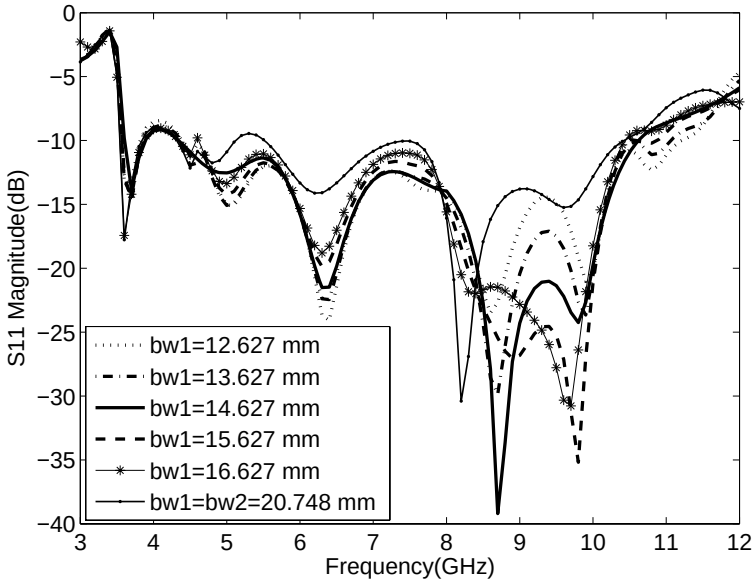


Figure 4.7: Effect of $bw_1$.

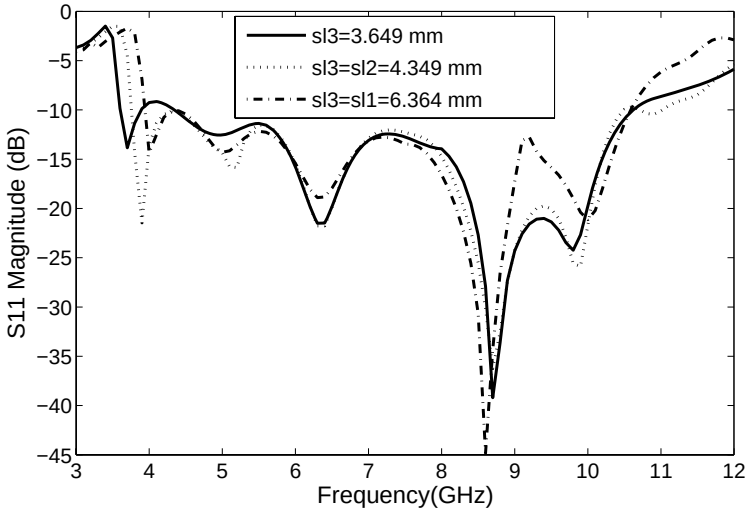


Figure 4.8: Effect of $sl_3$.

'$sl_6$' controls the length of the extended stub on the right longer edge of the small rectangular open loop. From Fig. 4.4, we can see that '$sl_6$' directly controls the overlapped areas between the big and small open rectangular loops, which affects the coupling influence between the two radiator elements. Fig. 4.9 shows that '$sl_6$' mainly has an effect on the lower frequency band but has a small influence on the higher frequency band.

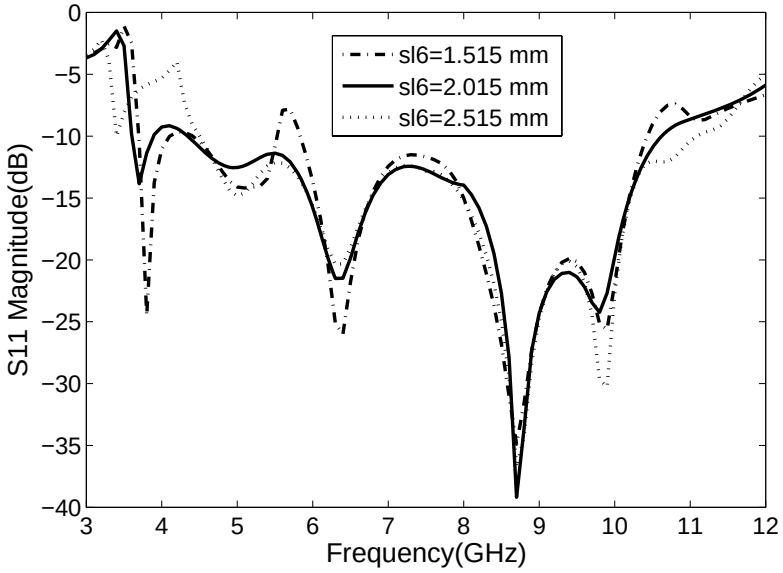


Figure 4.9: Effect of $sl_6$.

Fig. 4.10 shows the effect of the relative position of the two open loops which lie on two separated layers. When we increases the '$g_3$', which means the relative distance between the two open loops is increased, the impedance matching is obviously improved at lower and central frequency range, between 3.6-4.6 GHz and 6.8-8 GHz. The impedance matching is improved between 8-10 GHz with decreasing '$g_3$' when $g_3 \geq 0.923\ mm$. However, it will be deteriorated by decreasing '$g_3$' between 8-10 GHz when $g_3 \leq 0.923\ mm$. On both upper and lower sides of the two open rectangular loops, there are four narrow slots,

as shown in Fig.4.4. Fig. 4.11 shows the compared S11 parameters of the antenna with and without these four narrow slots. It has an obvious improvement on impedance matching around 7.5 GHz.

Fig. 4.12 shows the compared S11 parameters of the antenna with only one small rectangular open loop and with only one big rectangular open loop. It can be seen that the resonant frequencies are around 5 GHz, 7.8 GHz and 8.8 GHz when there is only one small rectangular open loop. And the resonant frequencies are around 4 GHz, 6.5 GHz, 8 GHz and 11 GHz when there is only one big rectangular open loop. Each of the open rectangular loops acts as a multi-frequency radiation element. With the LTCC technology, the small and big rectangular open loops can be combined together to form a multilayer radiation structure, which can be operated in the UWB frequency range finally.

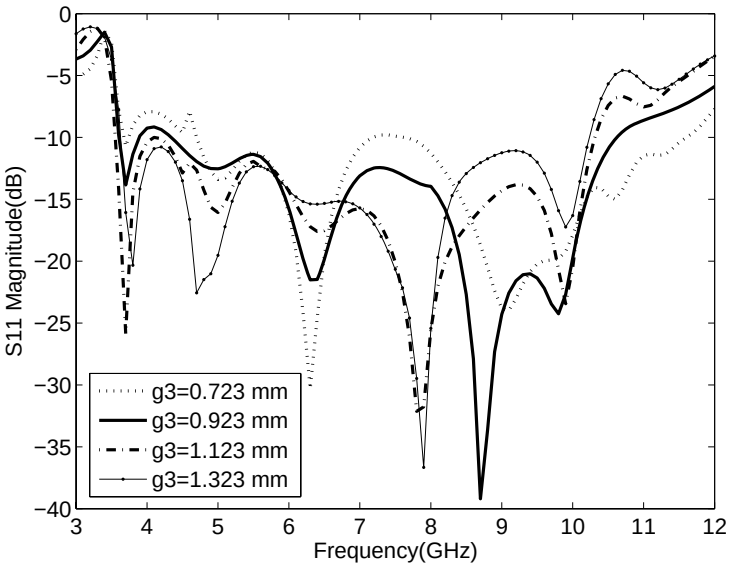


Figure 4.10: Effect of $g_3$.

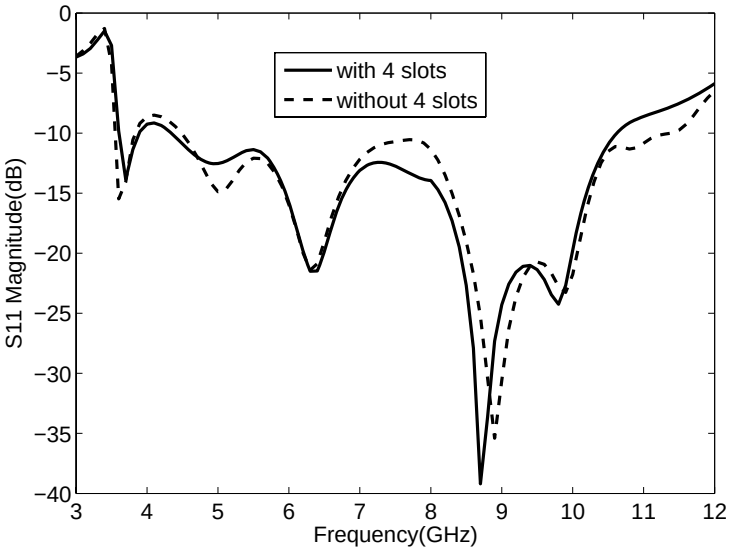


Figure 4.11: Effect of 4 small slots.

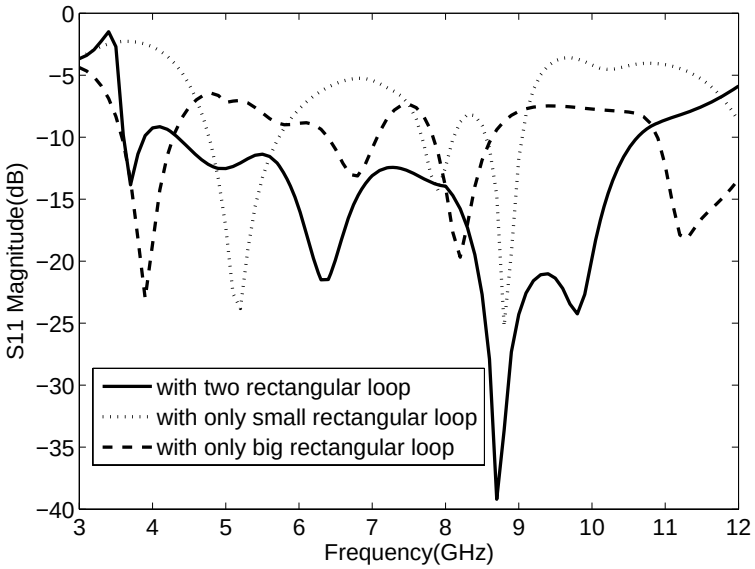


Figure 4.12: Effect of multilayer structures.

### 4.3.2 A Typical Design

A prototype of the proposed multilayer patch antenna fabricated on a six-layers LTCC substrate is shown in Fig. 4.13.

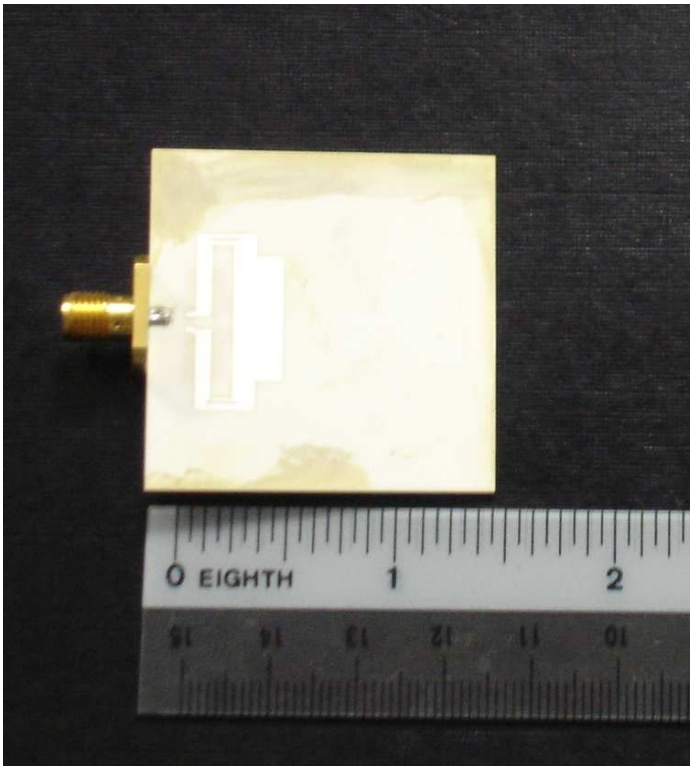


Figure 4.13: Photo of the multilayer patch antenna

Fig.4.14 shows a reasonable agreement between the measured and simulated $|S11|$. Some discrepancies between the simulated and measured results may occur because of the effect of the SMA connector. The bandwidth of the antenna is around 98% and ranges from 3.6 GHz to 10.6 GHz.

Fig. 4.15 shows the simulated and measured gains of the antenna. From 3.6 to 10.6

GHz, the proposed antenna exhibits an average simulated peak gain of 1.45 dBi, ranging from -0.74 dBi to 3.33 dBi, and an average measured E-plane peak gain of 1.24 dBi, ranging from -1.72 dBi to 3.64 dBi. From 3.6 to 10.6 GHz, the proposed antenna exhibits an average simulated boresight ($\phi = 0^o, \theta = 0^o$) gain of -1.33 dBi, ranging from -4.41 dBi to 0.89 dBi, and an average measured boresight gain of -1.47 dBi, ranging from -3.74 dBi to 0.64 dBi. The simulated and measured average gains of all the directions on the E- and H-planes are ranging from -3.17 dBi to 0.04 dBi and from -4.93 dBi to -2.12 dBi, respectively.

Fig. 4.16 shows the simulated and measured normalized radiation patterns of the multilayer LTCC antenna at frequencies 4, 7, and 10 GHz, respectively for the E- and H-planes. As observed, the radiation pattern of the antenna almost can remain constant at low frequency bandwidth. However, it shows some little distortion at higher frequencies.

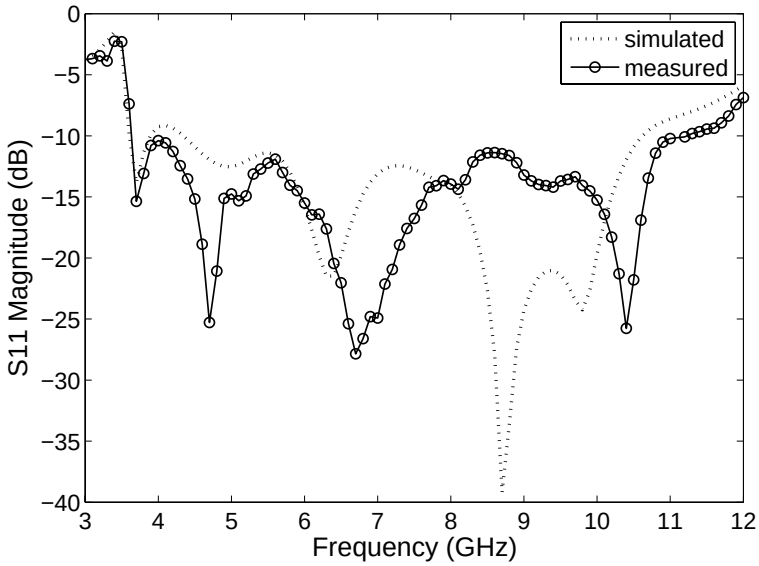


Figure 4.14: Simulated and measured $|S11|$ of the multilayer UWB antenna.

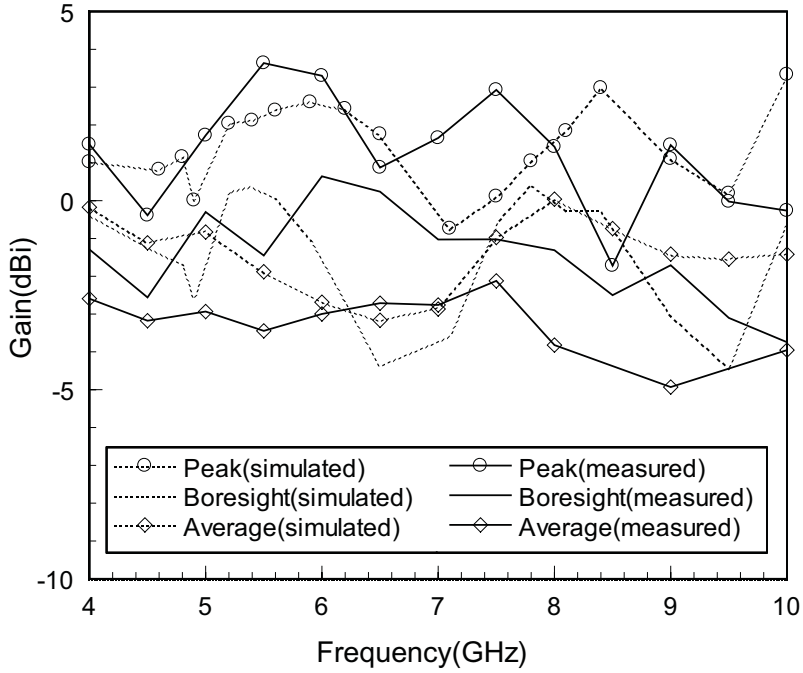


Figure 4.15: Simulated and measured gain of the multilayer UWB antenna.

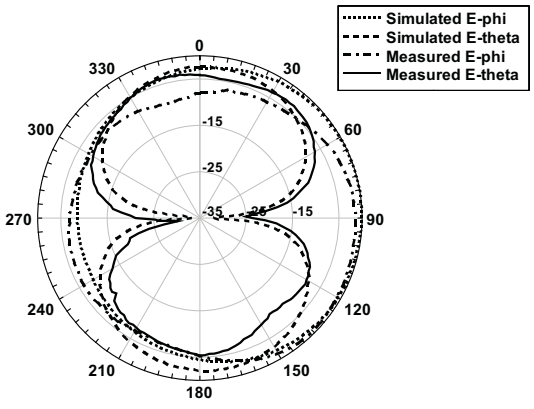


(a) E-plane radiation pattern at 4 GHz

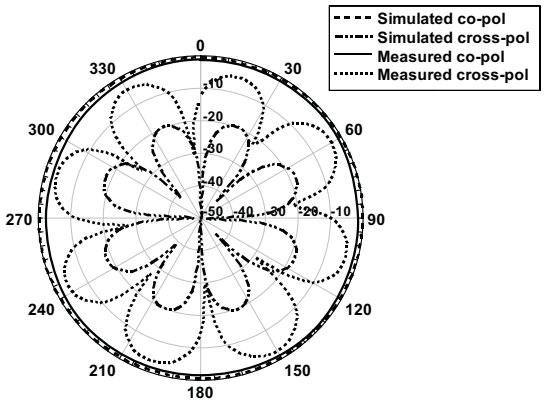


(b) H-plane radiation pattern at 4 GHz

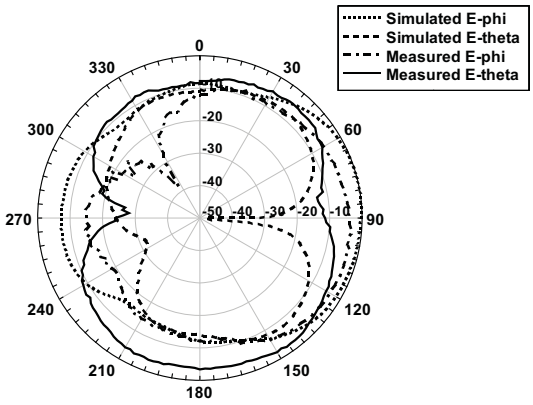


(c) E-plane radiation pattern at 7 GHz

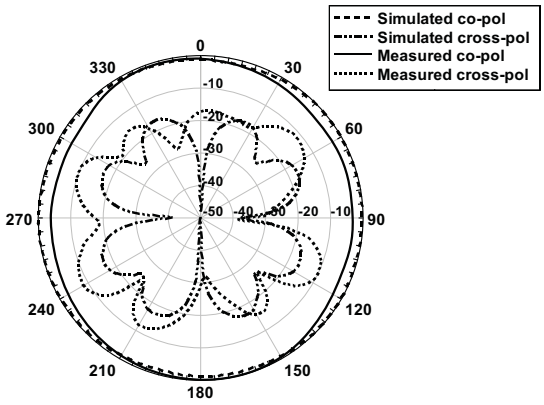


(d) H-plane radiation pattern at 7 GHz

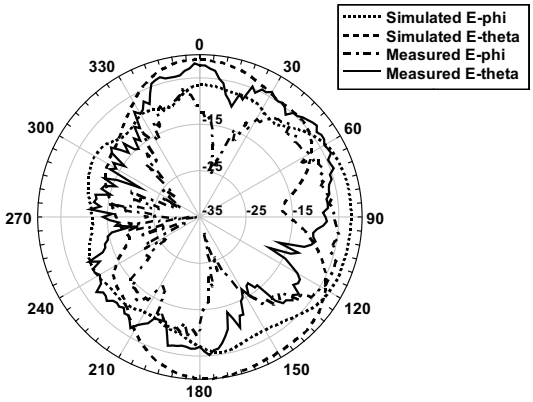


(e) E-plane radiation pattern at 10 GHz

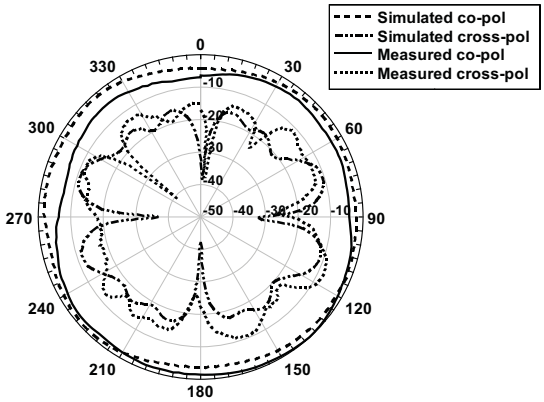


(f) H-plane radiation pattern at 10 GHz

Figure 4.16: Simulated and Measured E- and H-plane radiation patterns for the multilayer UWB antenna at $f = 4$, 7 and 10 GHz.

## 4.4 Conclusion

Utilizing the LTCC technology, two narrow band radiation elements are combined together to achieve an UWB antenna over 7 GHz, which results in a new compact and multilayer UWB planar antenna design and gives the possibility of integrating RF circuits and antennas in a single substrate. The configuration of the proposed multilayer structure fully

exploits the three-dimensional (3D) integration feature of the LTCC technology and offers a wide impedance bandwidth as well as a miniaturized antenna size. Moreover, the embedded feeding network makes the proposed antenna suitable for integrating with other LTCC circuits.

# Chapter 5

# 60-GHz Millimeter-wave Wideband Antennas and Arrays in LTCC

## 5.1 Introduction

In this chapter, we will integrate a circularly-polarized (CP) array with a low noise amplifier (LNA) in LTCC. The conventional method to enhance the array antenna gain with increased array elements inevitably narrows the antenna beamwidth and increases the antenna size. Compared with it, our proposed active antenna provides a promising solution for power enhancement while keeping the antenna beamwidth [82].

Various wideband antennas and arrays are designed in LTCC at 60 GHz. Our CP antenna is designed with aims to achieve a high gain, a wide impedance bandwidth, a wide axial ratio bandwidth, as well as good beam pattern and reasonable beam width. In Section 5.2 and Section 5.3, the microstrip feeding is used, while the stripline feeding is more suitable for antenna integration with chip and also easy to be tested in the probe station. In Section 5.4 the design of a circularly polarized antenna element is presented. This antenna will be integrated with an LNA in Section 5.6. It is an aperture-coupled truncated-corner patch antenna. Then by using the sequential rotation feeding scheme [83], a $4 \times 4$ array

is designed to achieve a wide impedance and axial ratio bandwidth. All these make the antenna performance less sensitive to the surrounding package- and PCB-level dielectric and metal layers. They also decouple the design of the antenna from the exact physical properties of the package, simplifying simulation and modeling complexity in the antenna integration with active devices.

In Section 5.5 the design of a wideband circularly polarized planar helical antenna is proposed. It is well known that the axial-mode helical antenna is a directive antenna with good circularly polarized characteristic on its axis over a wide frequency band. However, the traditional helix design is usually to keep its helical shape by some supporting materials such as dielectric rod, which is inconvenient for integration with other circuits. In [84], a stacked multilayer planar microstrip helical antenna is introduced. This microstrip helical antenna is much easier to be integrated with other circuits compared with the traditional helix. However, the probe-fed of the antenna is still not so convenient for integrations. Besides, there is still no planar helical antenna designed with LTCC technology for mmWave communications. In this chapter, wideband circularly polarized planar helical antenna and array in LTCC at 60 GHz are developed by taking the advantage of traditional helical antenna and LTCC technology. And the stripline is used in feeding network scheme that gives a more convenient solution for antenna and circuits integration.

The integration of an LNA into the package is challenging with wire bonding technology at 60 GHz. A number of studies on the electrical performance of wire-bonding interconnection have been reported for microstrip and coplanar configurations, indicating that insertion loss for a bonding wire will be drastically increased with frequency as the bond wire acts as a series inductor [85–87]. The flip-chip bonding technology uses metallic bumps for device connections. Compared to the length of the bond wire, the size of these

bumps is kept very small (less than 100 $\mu m$) to result in better impedance matching, and reduce interconnection losses and parasitic effects of transition discontinuities in mmWave systems [88]. The advanced ribbon or double bond wire techniques are also possible be used to decrease the bond wire inductance, where the ribbon is much more commonly used to bond mmwave devices than double bond wires due to their complexity [83,89]. Nonetheless, the wire-bonding technique, well established in consumer electronics, remains a very attractive solution since it is robust and inexpensive. In addition, it has the advantage of being tolerant on chip thermal expansion, an important requirement for many applications. In order to improve the high-frequency performance of a bond-wire interconnect, efforts have usually focused on reducing the length of the bond wire and also reducing the chip-to-package spacing. However, limitations in manufacturing require longer bond-wire lengths and wider chip-to-package spacing to improve the yields of mmWave chip-package assemblies. In this chapter we will use a T-network bond wire compensation scheme [90] to enable the longer 2-mil bond wire of length 500 $\mu m$ to be used, which is almost a tripled length of the shortest bond wire supported by the current technology and would thus greatly improve the yield of assembly of the chip with the package. This also makes our integration solution suitable for mass production. From chip-antenna interconnect aspect, low loss transitions have to be developed. In this chapter, we will optimize these transitions to achieve the lowest interconnection loss.

In what follows of this chapter, we will present the active circularly polarized antenna array. Section 5.6 describes the integration of the designed antenna array with an LNA chip to further form an active antenna. The key integration challenges are solved by designing the bond wire compensation scheme and developing low loss transitions. A proof-of-concept prototype is designed. It is then fabricated and tested to obtain the integration

performance as well as the polarization characteristics.

## 5.2 Narrow-band Microstrip-line-fed Aperture-coupled Linearly Polarized Patch Antenna and Array

### 5.2.1 Antenna Element

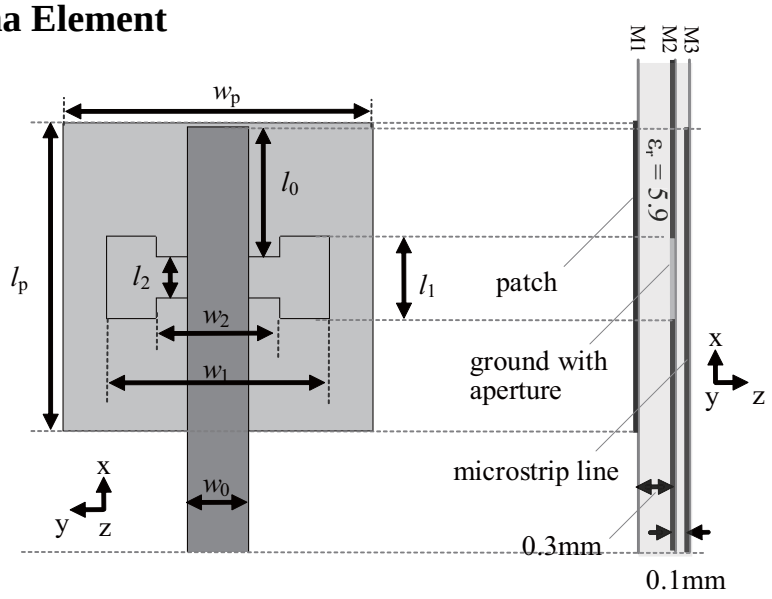


Figure 5.1: Geometry of the single antenna element ($w_p = 0.75\ mm$, $l_p = 0.75\ mm$, $l_0 = 0.315\ mm$, $w_1 = 0.54\ mm$, $w_2 = 0.3\ mm$, $l_1 = 0.2\ mm$, $l_2 = 0.1\ mm$, $w_0 = 0.15\ mm$). (The simulated size: $5 \times 5 \times 0.4\ mm^3$).

Fig. 5.1 shows the configuration of a single antenna element. It is an aperture-coupled patch antenna. It is fed by a micrtostrip line as in [43], [47] through a slot on the ground plane. The width of the 50-$\Omega$ microstrip line $w_0$ as shown in Fig. 5.1 is easily characterized

to be 0.15 $mm$ with the commercial full-wave electromagnetic simulation software Ansoft HFSS. The patch is implemented on the 300-$\mu m$ thick LTCC substrate. The antenna parameters are optimized with final values shown in the subtitles of Fig. 5.1. The final simulated antenna element size is $5 \times 5 \times 0.4\ mm^3$.

Fig. 5.2 shows the simulated antenna element performance. Fig. 5.2 (a) depicts the antenna return loss. The antenna has a narrow impedance bandwidth of $7.8\%$ at 60 GHz (58.5-63.2 GHz) for return loss $>$ 10 dB.

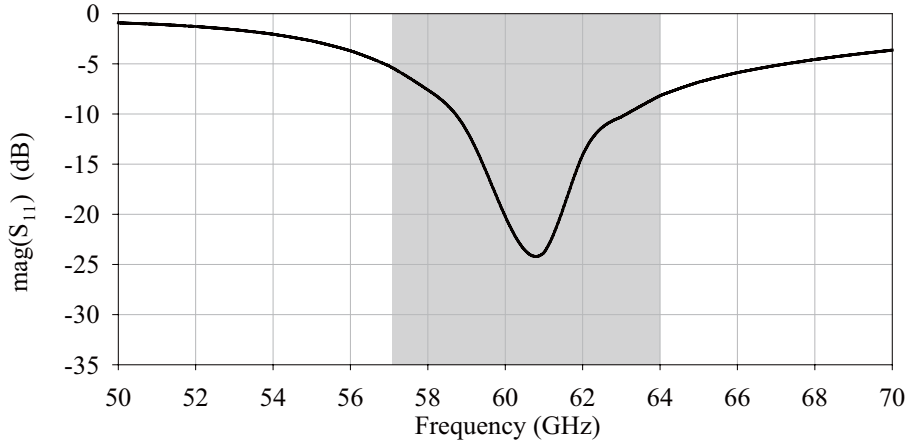


(a)

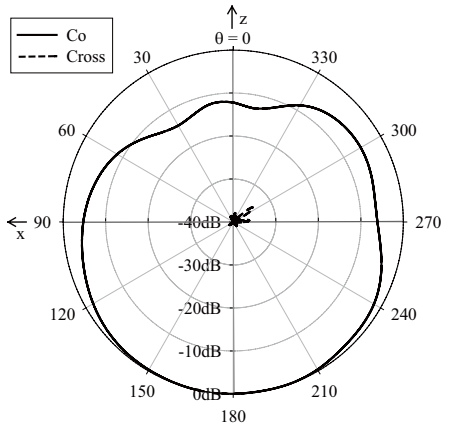


(b)

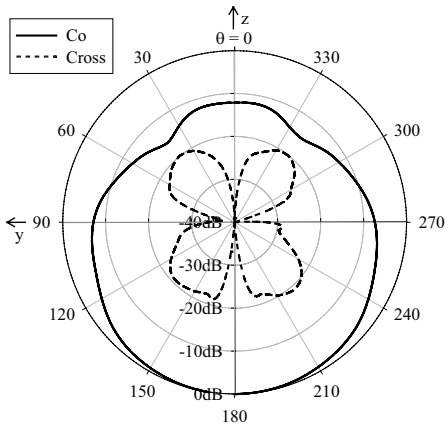


(c)

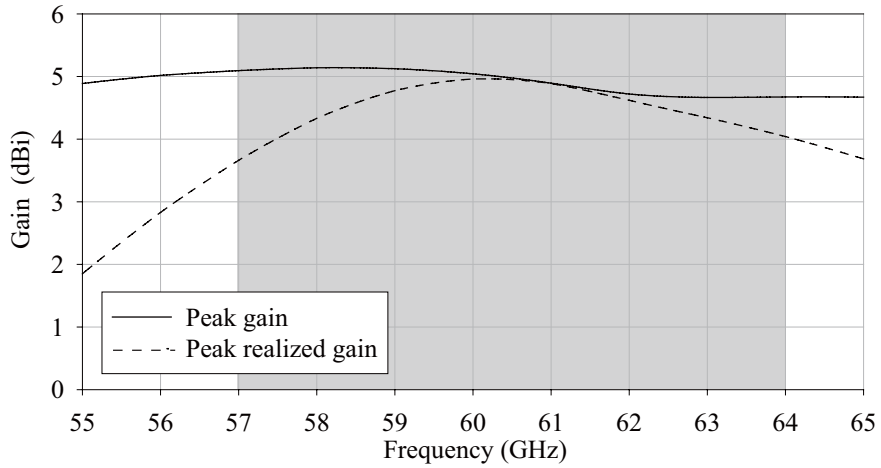


(d)

Figure 5.2: Simulated performance of the single element: (a) return loss, (b) xz-plane & (c) yz- plane radiation pattern at 60 GHz, and (d) gain.

Figs. 5.2(b)-(c) show the simulated antenna radiation pattern in the $xz$- and $yz$-planes at 60 GHz. As expected, the antenna is linearly polarized and its radiation pattern has a main lobe of radiation in the upper hemisphere (in the -$z$ direction) with a front-to-back ratio better than 22 dB. The 3-dB beam width is $140^{\circ}$ in the $xz$-plane and $100^{\circ}$ in the $yz$-plane.

Fig. 5.2 (d) shows the simulated antenna peak gain and peak realized gain, which are the simulation parameters provided by commercial software Ansoft HFSS. The peak gain is an ideal parameter which does not consider whether the impedance matching of antenna is good or not. The peak realized gain is a parameter which has included the mismatched impedance loss from ideal peak gain. Obviously, when the impedance matching of antenna is good enough, the parameter values of peak gain and peak realized gain are almost the same. The antenna has peak gain of 5.14 dBi.

### 5.2.2 $4 \times 4$ Patch Antenna Array

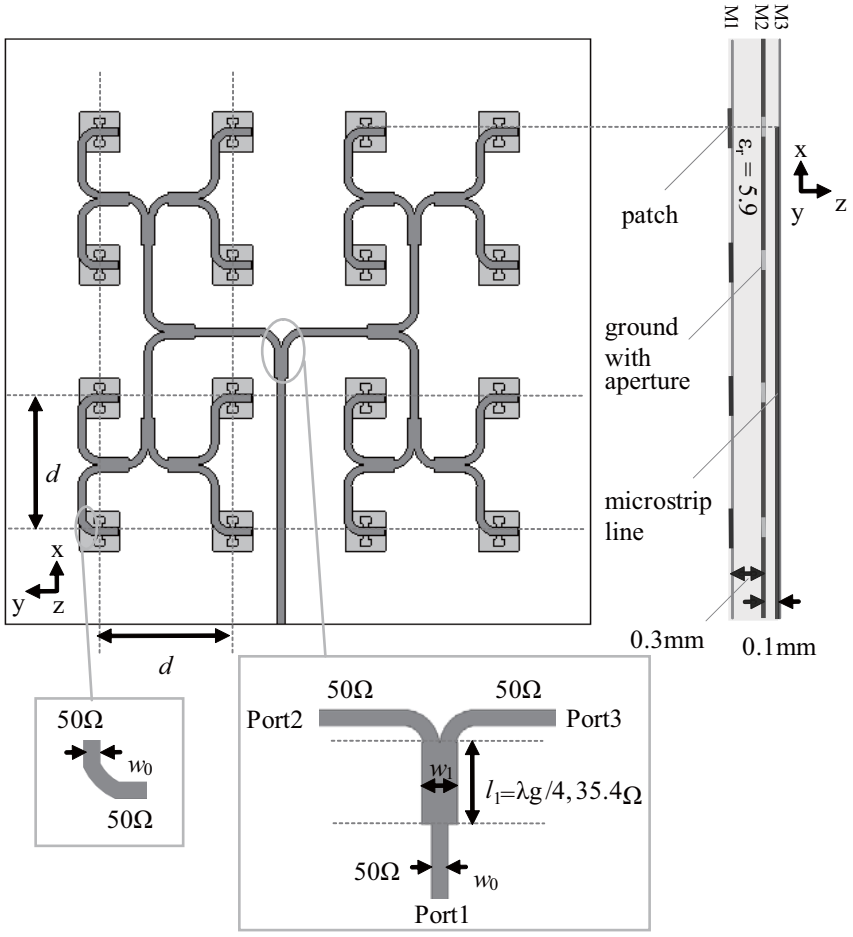


Figure 5.3: Geometry of the array antenna and zoom in view of the $90^\circ$ corner bent and the quarter-wave matched T-junction.

Fig. 5.3 shows the geometry of the array. It is realized by the identical antenna element in respect to its neighbouring element. The microstrip line feeding network is designed to feed each radiation element with equal amplitude and phase. In the microstrip line feeding network, the $90^\circ$ corner bent is used instead of mitering the lines. The characteristic

impedance for each port is 50 $\Omega$ with $w_0 = 0.15\ mm$. In addition, a quarter-wave matched T-junction is used as the power divider to split the power equally. Its width $w_1$ and length $l_1$ are easily characterized to be 0.26 $mm$ and 0.58 $mm$, respectively. The final input matching at the input port is $|S11| = -24$ dB and the coupling from the input port to the output port is $|S21| = -3.25$ dB at 60 GHz. It is reasonable with a 0.25 dB more insertion loss in the output port for this power divider.

Table 5.1: DESIGN SUMMARY

| | |
|---|---|
| T-junction | $\|S11\| = -24$ dB, $\|S21\| = -3.25$ |
| Dimensions | d = 2.5 $mm$, size: $11 \times 11 \times 0.4\ mm^3$ |
| 10-dB bandwidth | 6.3% (59.2-63 GHz) |
| Patterns | Linearly polarized |
| 3-dB beam width | $30^\circ$ both in $xz$- and $yz$-planes |
| Peak realized gain | 16.5 dBi@60GHz |
| 3-dB Gain BW | $>$7.5 GHz (57.5-65 GHz) |
| Efficiency | $>$80% |

Fig. 5.4 shows the simulated array performance. It is found from Fig. 5.4(a) that the antenna has a narrow impedance bandwidth of $6.3\%$ (59.2-63 GHz) for (return loss $>$10 dB).

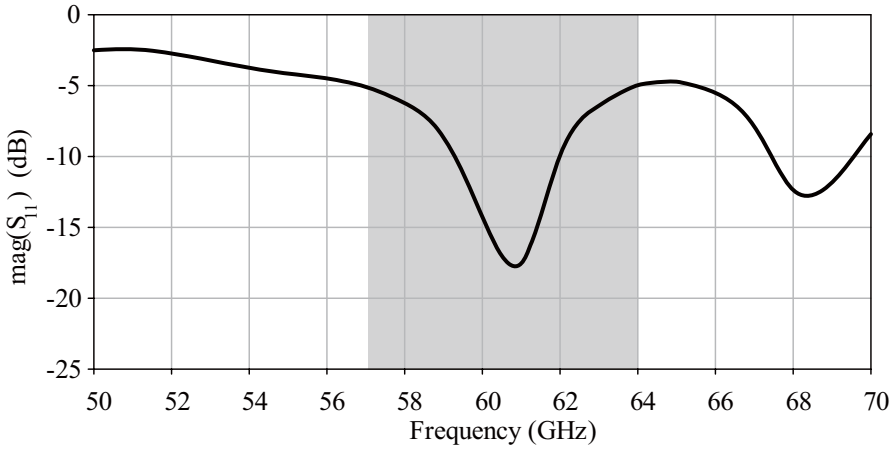


(a)

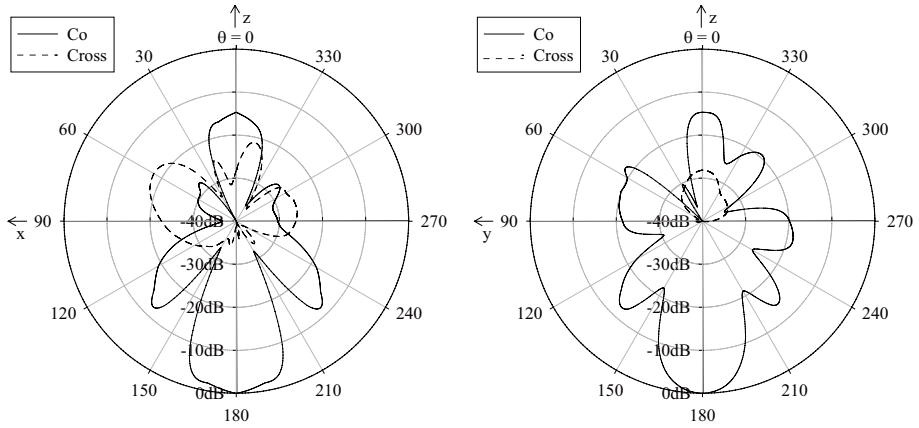


(b) (c)

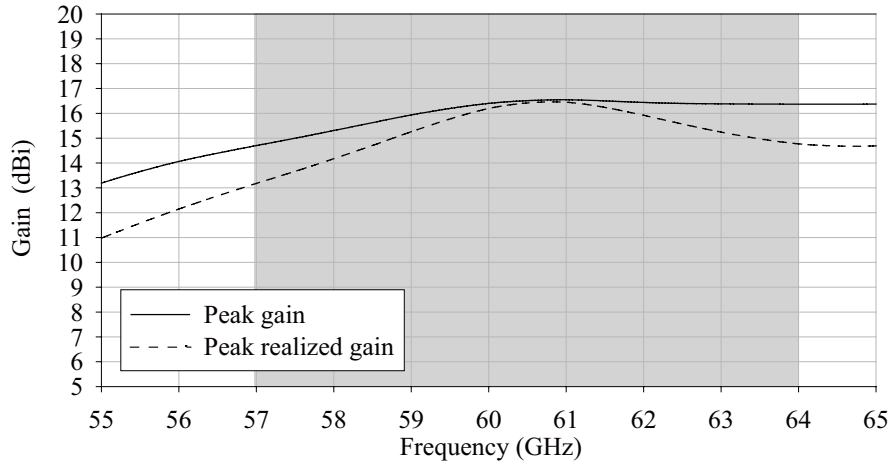


(d)

Figure 5.4: Simulated performance of the array antenna:: (a) return loss, (b) $xz$-plane &(c) $yz$- plane radiation pattern at 60 GHz, and (d) gain.

Figs. 5.4 (b)-(c) also show the simulated antenna radiation pattern in the $xz$- and $yz$-planes at 60 GHz. It can be clearly seen that the radiation is linearly polarized. The antenna radiation pattern is beam-shaped with a 3-dB beam width of $30^\circ$ both in the $xz$- and $yz$-planes. Fig. 5.4 (d) shows the simulated antenna peak gain. As we can see the antenna has high peak realized gain of 16.5 dBi. The simulated efficiency is $> 80\%$ over 7-GHz

bandwidth. As summarized in TABLE 5.1, the designed array exhibits narrow impedance matching at 60 GHz. Obviously, the bandwidth of the antenna and array should be further improved, which will be addressed in the next section.

## 5.3 Wideband Microstrip-line-fed Aperture-coupled Circularly Polarized Patch Antenna and Array

### 5.3.1 Antenna Element

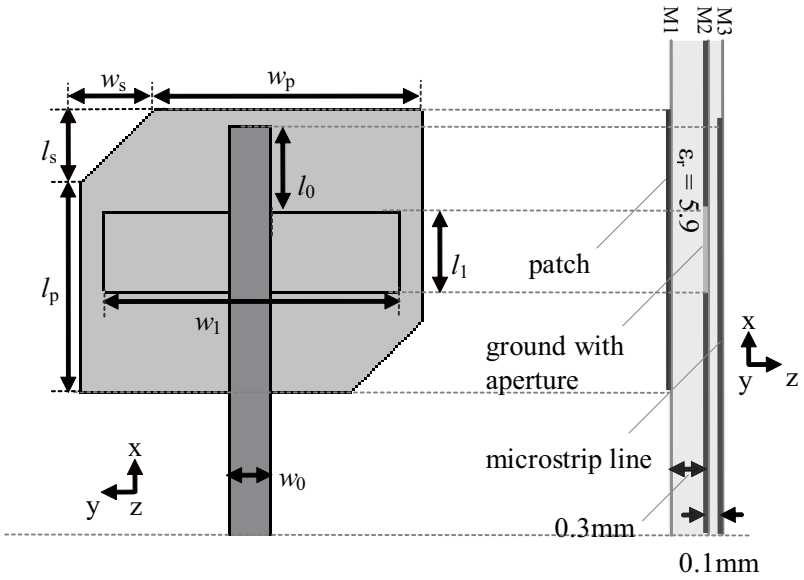


Figure 5.5: Geometry of the single antenna element ($w_p = 0.671\ mm$, $l_p = 0.609\ mm$, $w_s = l_s = 0.21\ mm$, $l_0 = 0.264\ mm$, $w_1 = 0.735\ mm$, $l_1 = 0.2\ mm$, $w_0 = 0.15\ mm$). (The simulated size: $4 \times 4 \times 0.4\ mm^3$).

Based on the previous design on a narrow band antenna element, the element bandwidth is enhanced by using an aperture-coupled truncated-corner patch antenna as shown in Fig.

5.5. At the same time, the circular polarization can be obtained by cutting the two opposite corners of the square patch. This generates two orthogonal resonance modes which yield two linear polarizations along the patch diagonals. The antenna parameters are optimized with final values shown in the subtitles of Fig.5.5. The final simulated antenna element size is $4 \times 4 \times 0.4\ mm^3$.

Fig. 5.6 shows the simulated antenna element performance. Fig. 5.6 (a) depicts the antenna return loss. The antenna has a wide impedance bandwidth of 14% at 60 GHz (56.8-65.3 GHz) for return loss $>$ 10 dB.

Figs. 5.6 (b)-(c) show the simulated antenna radiation pattern in the $xz$- and $yz$-planes at 60 GHz. As expected, the antenna is circularly polarized at 58 GHz and its radiation pattern has a main lobe of radiation in the upper hemisphere (in the -$z$ direction) with a front-to-back ratio better than 19 dB.

Fig. 5.6 (d) shows the simulated antenna peak gain and axial ratio. The antenna has peak gain of 5.8 dBi. The 3-dB gain bandwidth is over 16.5 GHz.

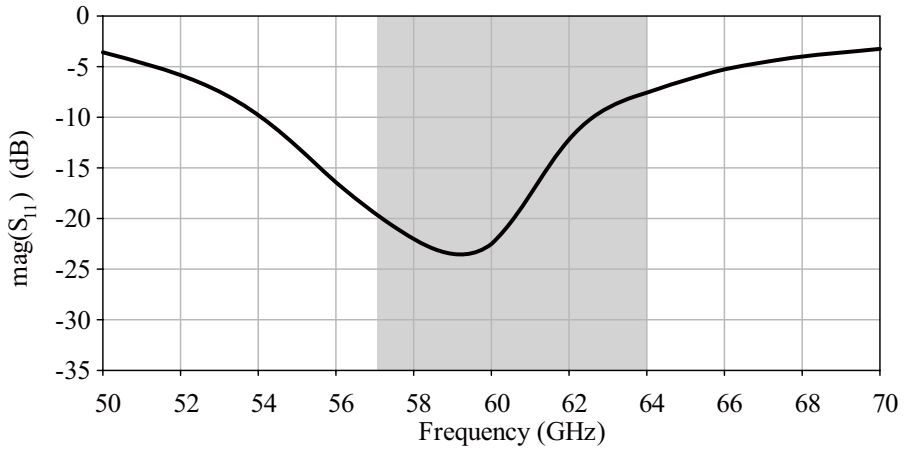


(a)

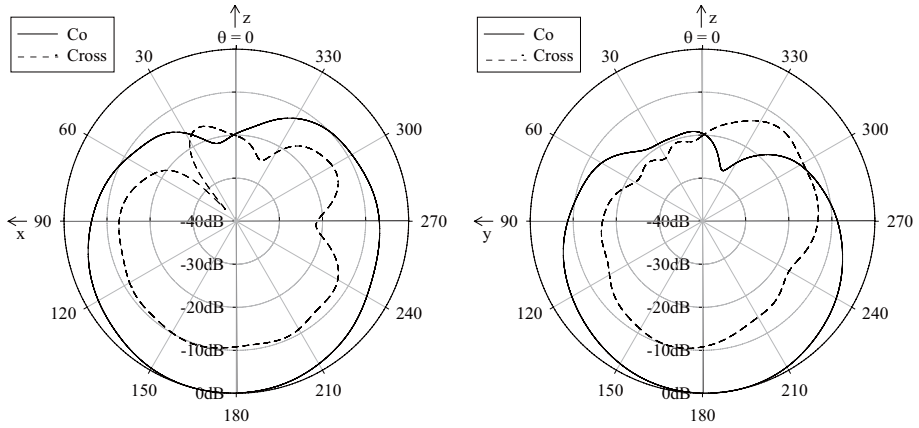


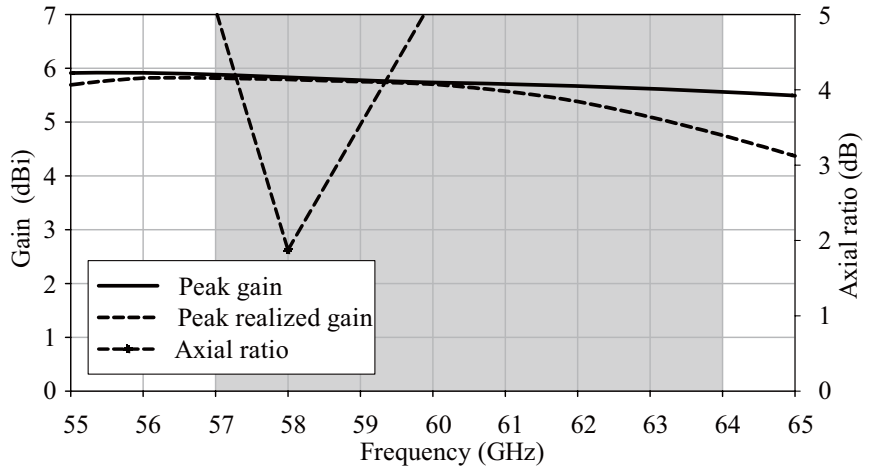


(d)

Figure 5.6: Simulated performance of the single element: (a) return loss, (b) $xz$-plane & (c) $yz$- plane radiation pattern at 60 GHz, and (d) gain and axial ratio.

It should be noted that the 3-dB axial ratio bandwidth is only 1 GHz (57.8$-$ 58.8 GHz). Although the radiation patch with truncated-corner can generate two orthogonal resonance modes which yield two orthogonal linear polarizations along the patch diagonals, this kind of circular polarization characteristic is quite poor and only with narrow bandwidth.

### 5.3.2 Wideband $4 \times 4$ Patch Antenna Array

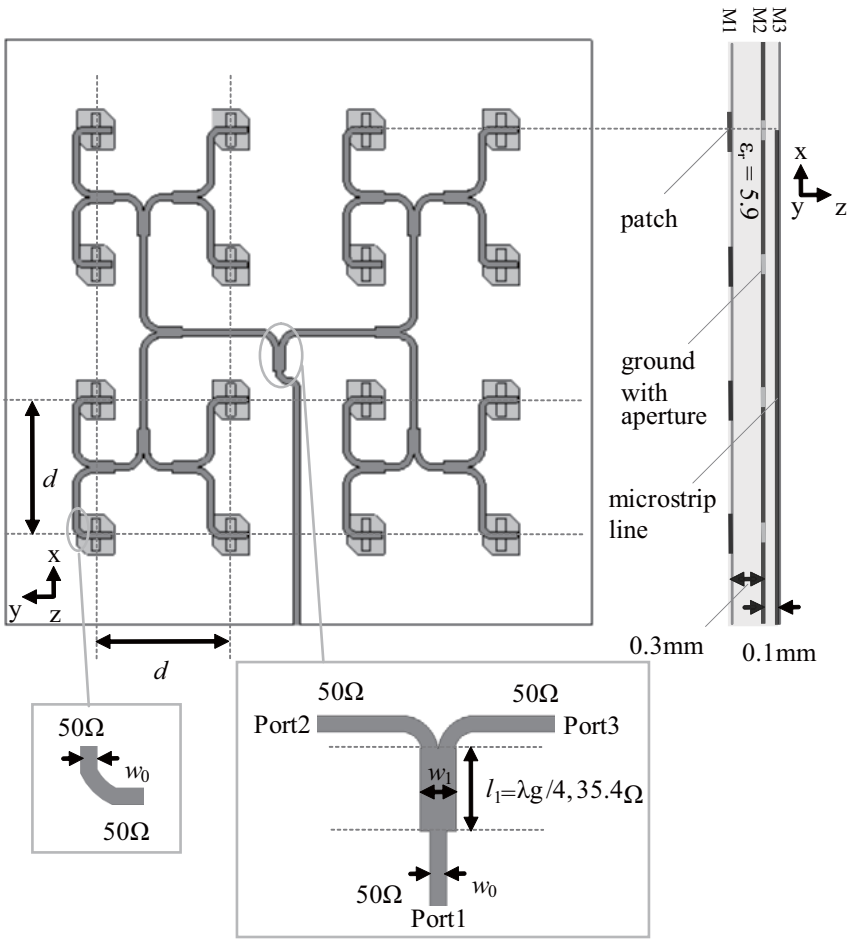


Figure 5.7: Geometry of the array antenna and zoom in view of the $90^\circ$ corner bent and the quarter-wave matched T-junction.

Fig. 5.7 shows the geometry of the array. It is realized by the same antenna element in respect to its neighbouring element. The microstrip line feeding network is designed to feed each radiation element with equal amplitude and phase. Fig. 5.8 shows the simulated array performance. TABLE 5.2 summarizes the antenna performance.

Table 5.2: DESIGN SUMMARY

| | |
|---|---|
| T-junction | $\|S11\| = -24$ dB, $\|S21\| = -3.25$ |
| Dimensions | $d = 2.5\ mm$, $w_0 = 0.15\ mm$, $w_1 = 0.26\ mm$, $l_1 = 0.55\ mm$, size: $13 \times 13 \times 0.4\ mm^3$ |
| 10-dB bandwidth | 15% (56-65 GHz) |
| Patterns | Poor RHCP |
| 3-dB AR BW | 0 GHz |
| 3-dB beam width | $30^\circ$ both in $xz$- and $yz$-planes |
| Peak realized gain | 17.6 dBi@62GHz, 17.2 dBi@60GHz |
| 3-dB Gain BW | $>$10 GHz (55-65 GHz) |
| Efficiency | $>$80% |

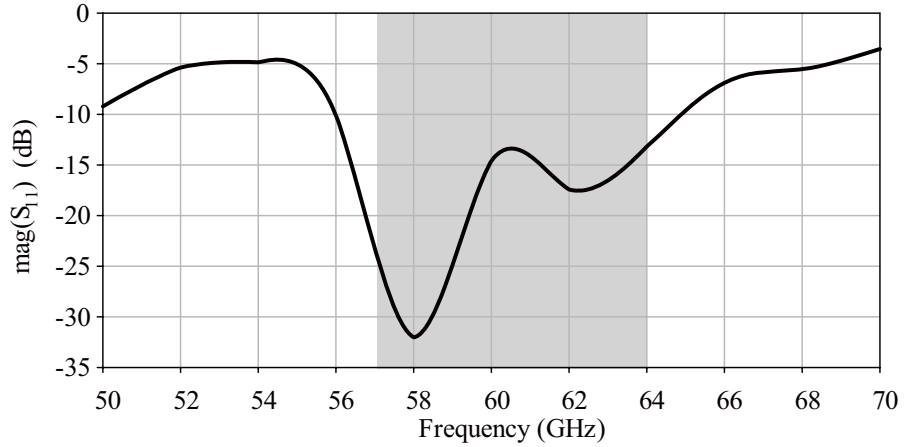


(a)

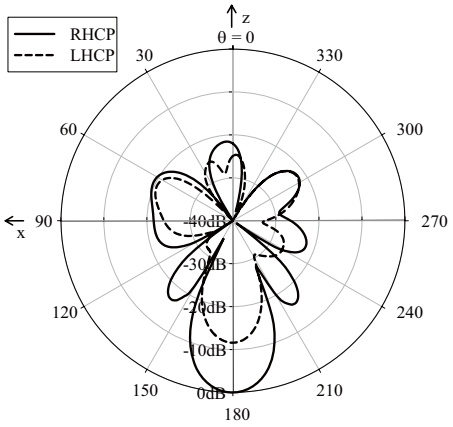


(b)

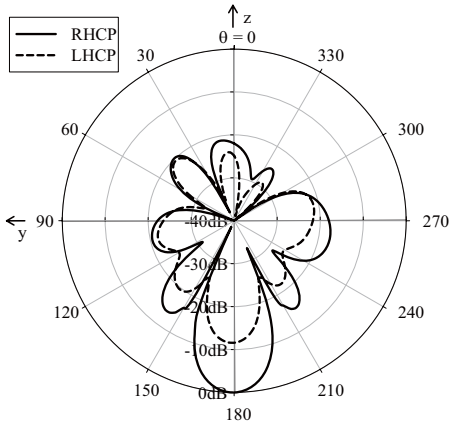


(c)

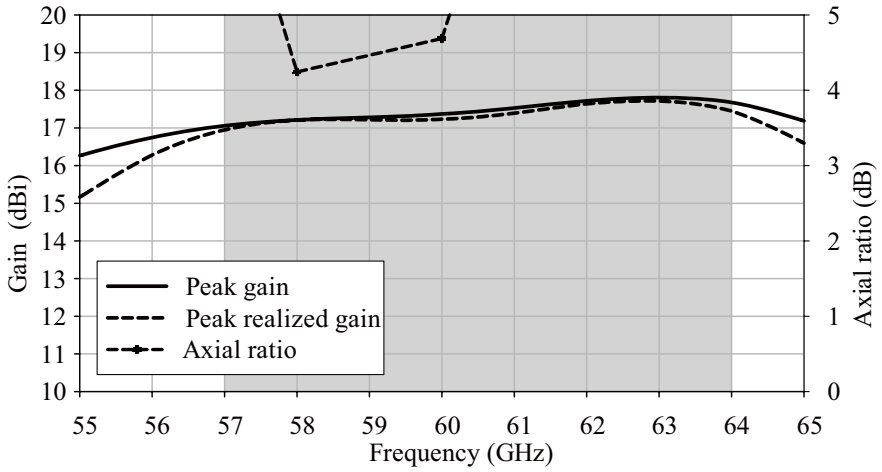


(d)

Figure 5.8: Simulated performance of the array antenna with dimensions in Table 5.2: (a) return loss, (b) $xz$- plane & (c) $yz$- plane radiation pattern at 60 GHz, and (d) gain and axial ratio.

It is found that the array has an impedance bandwidth to cover the whole 7-GHz bandwidth with high gain performance. However, it is not a good right-handed circularly polarized (RHCP) antenna. The axial ratio at 60 GHz is 4.6 dB and the 3-dB axial ratio bandwidth is zero. Even the antenna element still has a narrow band circular polarization characteristic, the $4 \times 4$ antenna array with an equal amplitude and phase feeding network lost all axial ratio bandwidth. The strength of two orthogonal linear polarizations of single antenna element is weakened by the coupling effect between neighbouring antenna elements. So the coupling effect between antenna elements should be considered in CP antenna array design, and the 3-dB axial ratio bandwidth of this design has to be enhanced.

### 5.3.3 Wideband Circularly Polarized Patch Antenna Array

As we know, the circularly polarized property is desirable for 60-GHz antennas in view of wireless access applications. And the wide axial ratio bandwidth is one of the important

targeted characteristics. So in this section we use a sequentially feeding rotation scheme to increase the axial ratio bandwidth as well as the impedance bandwidth of the antenna array. This feeding scheme is a well known technique to enhance the axial ratio and impedance bandwidth [83]. According to different application requirments, $2 \times 4$ and $4 \times 4$ antenna arrays are presented, respectively.

**A.** $2 \times 4$ Wideband Circularly Polarized Patch Antenna Array

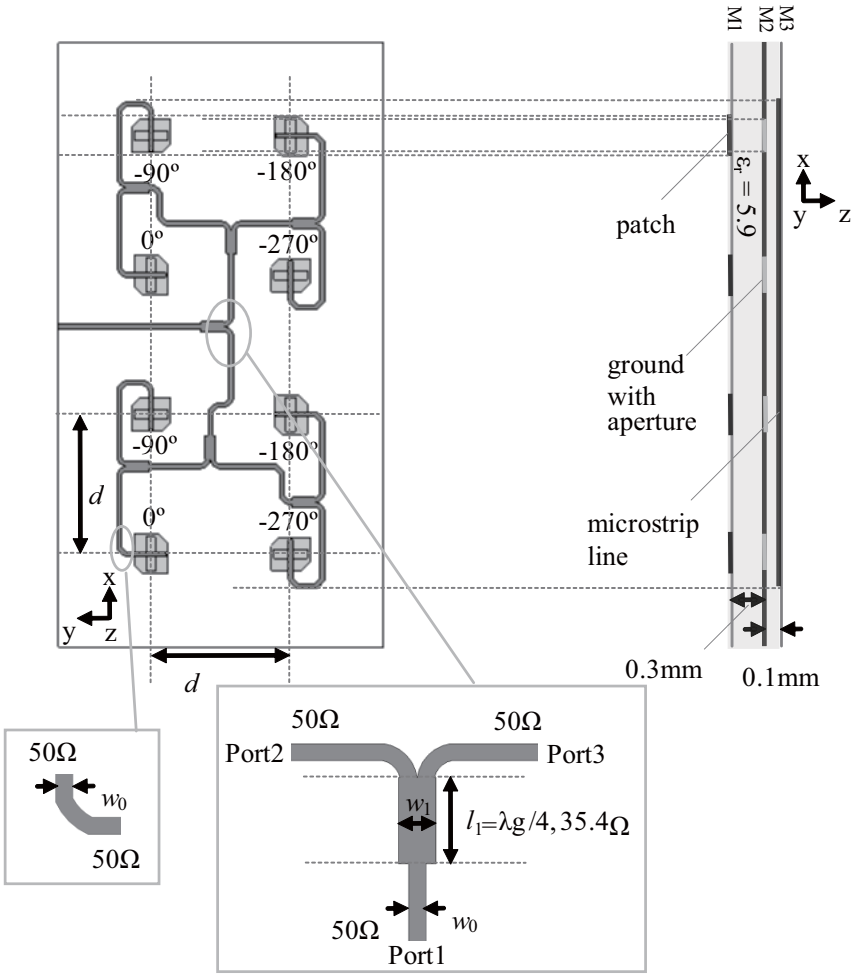


Figure 5.9: Geometry of the sequential feeding array antenna and zoom in view of the $90°$ corner bent and the quarter-wave matched T-junction.

In this design, we use a sequential rotation feeding technique to achieve a wideband axial ratio bandwidth. The element used is the same as shown in Fig. 5.5.

Fig. 5.9 shows the geometry of the sequential feeding array. It is realized by rotating each antenna element in respect to its neighbouring element. In this design, we have chosen to produce RHCP by arranging the element with the fashion of $0°$,$-90°$, $-180°$, $-270°$ as shown in Fig. 5.9. Accordingly the microstrip line feeding network is designed to feed each radiation element with equal amplitude but with phase corresponding to their individual rotation angles as denoted in Fig. 5.9. The required different phases in feeding network are achieved by the microstrip line delays, e.g. an increase of a quarter guided wavelength in length corresponds to a delay of 90 degrees in phase. In the microstrip line feeding network, the $90°$ corner bent is used instead of mitering the lines. In addition, the quarter-wave matched T-junction is used as the power divider to split the power equally.

Fig. 5.10 shows the simulated array performance. TABLE 5.3 summarizes the antenna performance. It is found that the array has achieved wide impedance bandwidth. The most important is that the 3-dB AR bandwidth is enhanced to 10 GHz and the antenna shows good RHCP characteristics.

Table 5.3: DESIGN SUMMARY

| | |
|---|---|
| Dimensions | $d = 3\ mm$, $w_0 = 0.15\ mm$, $w_1 = 0.26\ mm$, $l_1 = 0.55\ mm$, size: $13 \times 7 \times 0.4\ mm^3$ |
| 10-dB bandwidth | 24.6% (54.2-69 GHz) |
| Patterns | RHCP |
| 3-dB AR BW | 10 GHz (55.5-65.5 GHz) |
| 3-dB beam width | $30°$ both in $xz$- and $yz$-planes |
| Peak realized gain | 14.5 dBi@60GHz |
| 3-dB Gain BW | $>$8 GHz (57-65 GHz) |
| Efficiency | $>$80% |

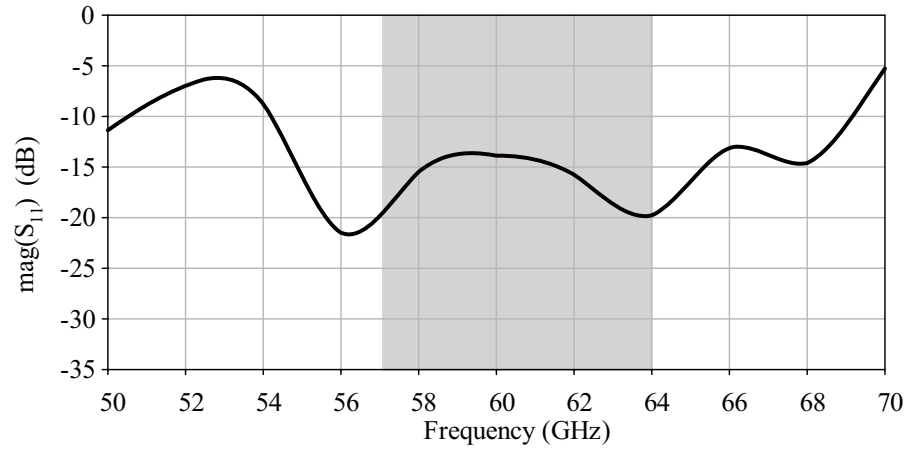


(a)

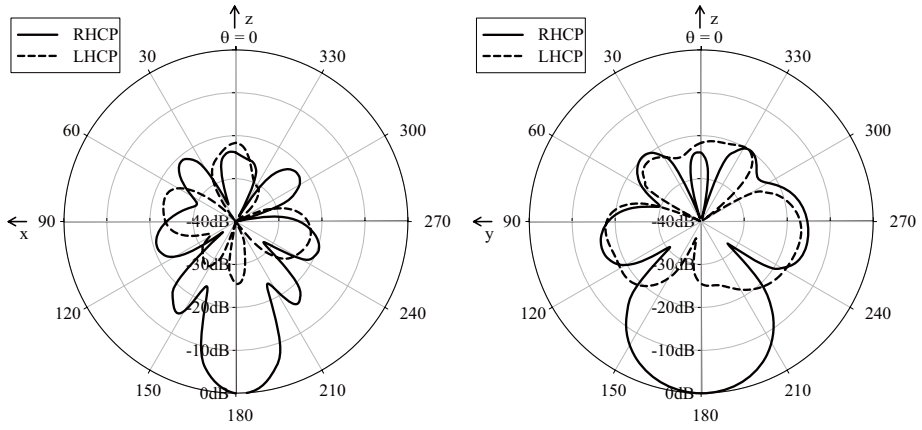


(b) (c)

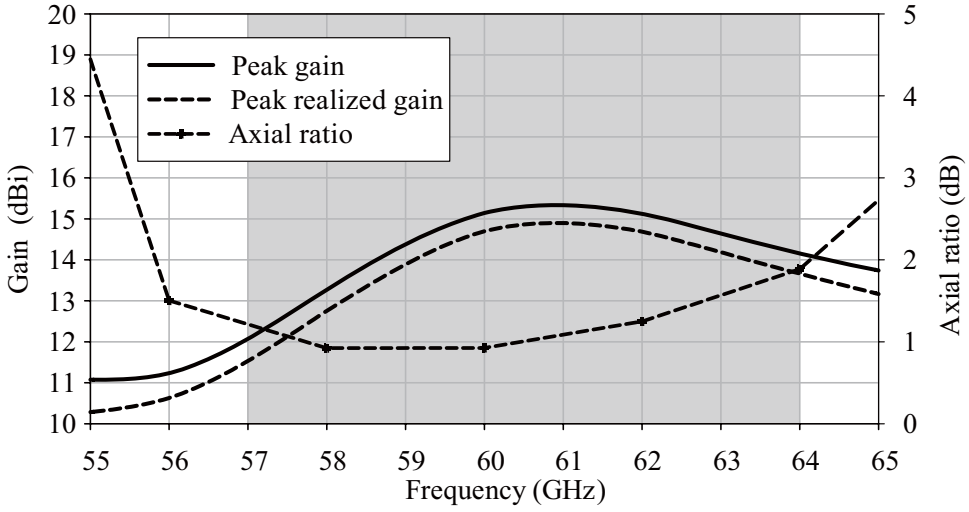


(d)

Figure 5.10: Simulated performance of the array antenna: (a) return loss, (b) $xz$-plane & (c) $yz$- plane radiation pattern at 60 GHz, and (d) gain and axial ratio.

**B.** $4 \times 4$ Wideband Circularly Polarized Patch Antenna Array

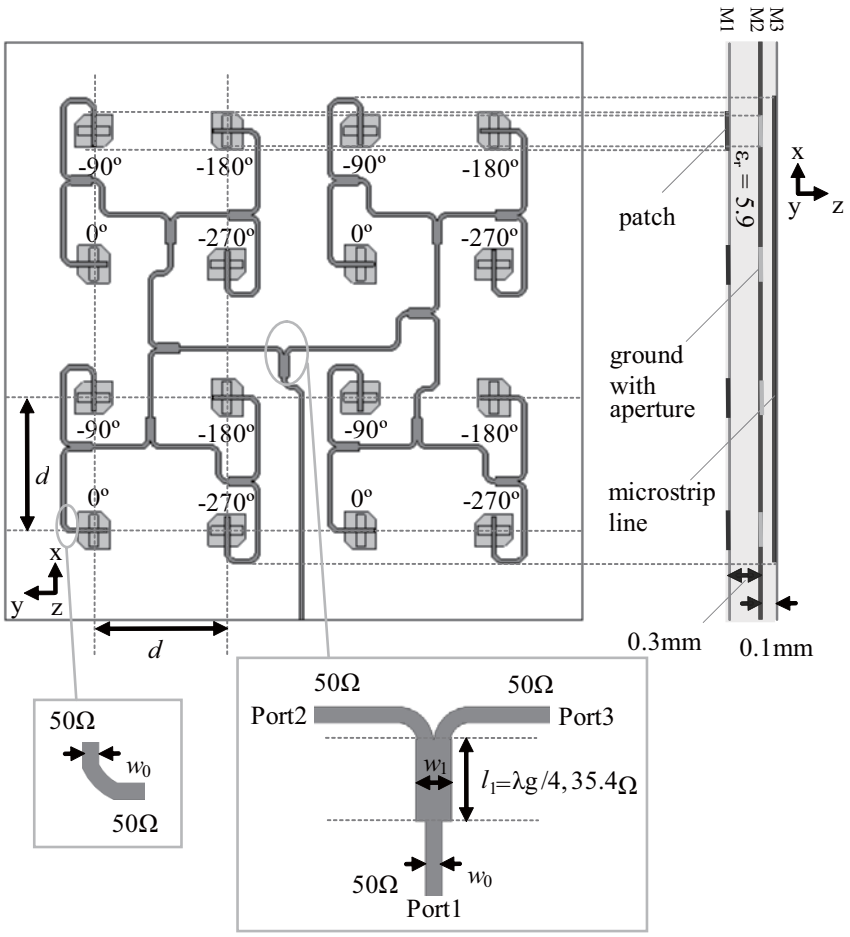


Figure 5.11: Geometry of the sequential feeding array antenna and zoom in view of the $90°$ corner bent and the quarter-wave matched T-junction.

Fig. 5.11 shows the geometry of the sequentially feeding $4 \times 4$ array. Fig. 5.12 shows the simulated array performance. It is found that the array has achieved a wide impedance bandwidth with high gain. The most important is that the 3-dB axial ratio bandwidth is enhanced to 9 GHz and the antenna shows good RHCP characteristics. TABLE 5.4 summarizes the antenna performance.

Table 5.4: DESIGN SUMMARY

| | |
|---|---|
| Dimensions | $d = 3\ mm$, $w_0 = 0.15\ mm$, $w_1 = 0.26\ mm$, $l_1 = 0.55\ mm$, size: $13 \times 13 \times 0.4\ mm^3$ |
| 10-dB bandwidth | 31% (51-69.5 GHz) |
| Patterns | RHCP |
| 3-dB AR BW | 9 GHz (55.5-64.5 GHz) |
| 3-dB beam width | $30^\circ$ both in $xz$- and $yz$-planes |
| Peak realized gain | 17.5 dBi@62GHz, 17.1 dBi@60GHz |
| 3-dB Gain BW | $>$7 GHz (58-65 GHz) |
| Efficiency | $>$80% |

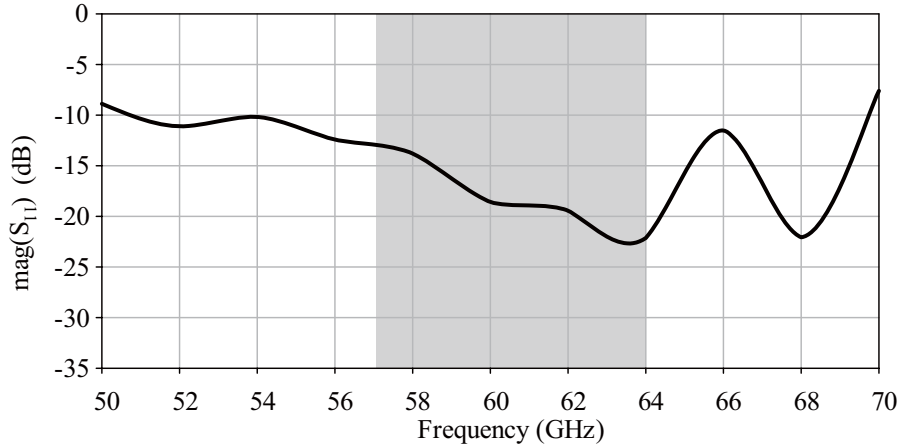


(a)

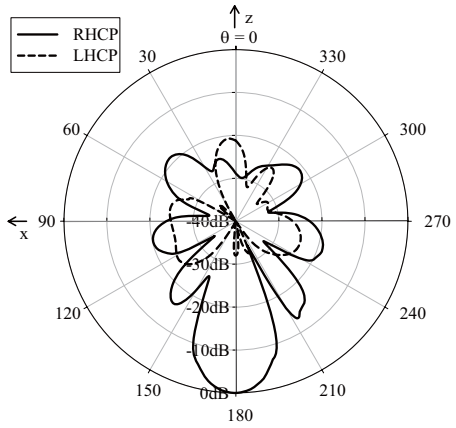


(b)

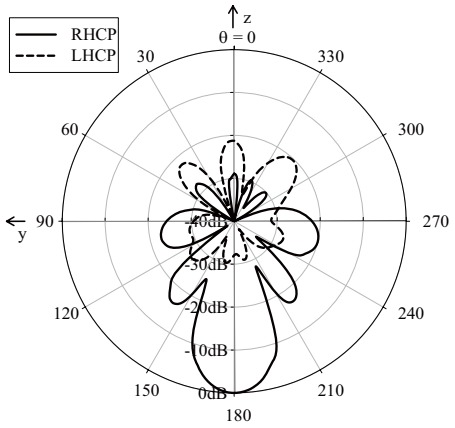


(c)

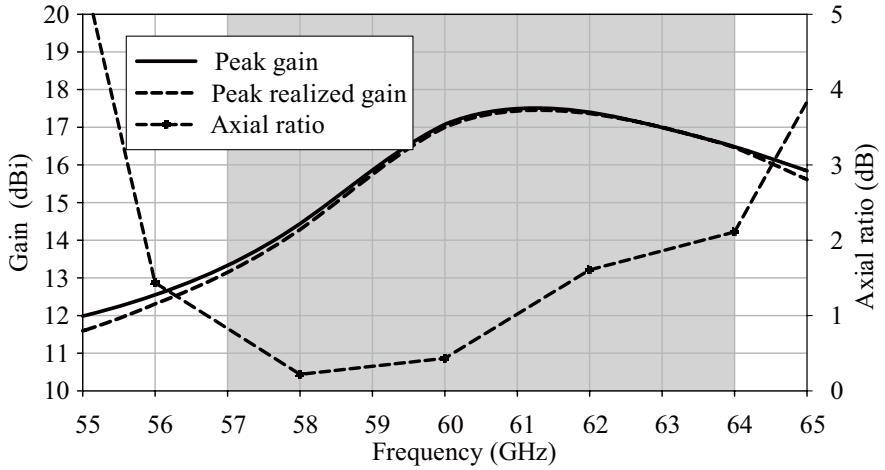


(d)

Figure 5.12: Simulated performance of the array antenna: (a) return loss, (b) $xz$-plane & (c) $yz$- plane radiation pattern at 60 GHz, and (d) gain and axial ratio.

## 5.4 Wideband Stripline-fed Aperture-coupled Circularly Polarized Patch Antenna and Array

In Section 5.2 and Section 5.3, the microstrip feeding is used, while the stripline feeding is more suitable for antenna integration with chip and also easy to be tested in the probe station. Combined with the advantage of the aperture couple antenna topology and stripline feeding, the antennas will be less sensitive to the surrounding package- and PCB-level dielectric and metal layers. They also decouple the design of the antenna from the exact physical properties of the package, simplifying simulation and modeling complexity. The above reasons lead us to design stripline-fed wideband circularly polarized patch arrays in this section. Similar to Section 5.3, both $2 \times 4$ and $4 \times 4$ antenna arrays are presented, respectively.

### 5.4.1 Antenna Element

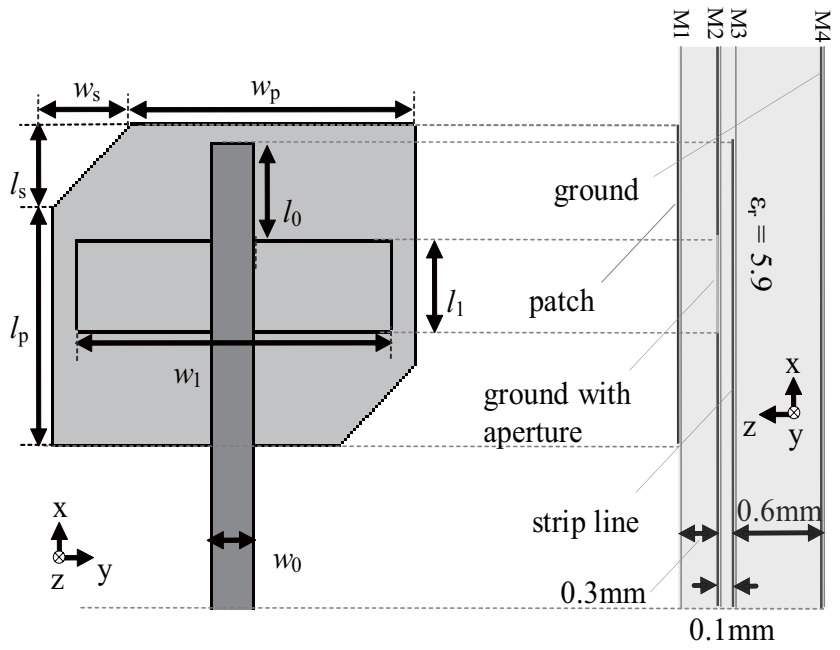


Figure 5.13: Geometry of the single antenna element (size: $4 \times 4 \times 1\ mm^3$, $w_p = 0.6682\ mm$, $l_p = 0.5278\ mm$, $w_s = l_s = 0.182\ mm$, $l_0 = 0.2155\ mm$, $w_1 = 0.735\ mm$, $l_1 = 0.2\ mm$, $w_0 = 0.1\ mm$).

Fig. 5.13 shows the configuration of a single antenna element. It is an aperture-coupled truncated-corner patch antenna. It is not fed by a micrtostrip line but by an asymmetrical stripline through a slot on the ground plane. The stripline is sandwiched between the 100-$\mu m$ and 600-$\mu m$ thick LTCC substrates with the top and bottom grounded. The width of the 50-$\Omega$ stripline $w_0$ as shown in Fig. 5.13 is easily characterized to be 0.1 $mm$. The patch is implemented on the 300-$\mu m$ thick LTCC substrate. The circular polarization is obtained by cutting the two opposite corners of the square patch. This generates two orthogonal resonance modes which yield two linear polarizations along the patch diagonals. The antenna

parameters are optimized with final values shown in the subtitles of Fig. 5.13. The final simulated antenna element size is $4 \times 4 \times 1\ mm^3$.

Fig. 5.14 shows the simulated antenna element performance. Fig. 5.14 (a) shows an impedance bandwidth of 9.7 GHz (56.5-66.2 GHz) for SWR$<$2 ($|S11| <$-9.542 dB).

Fig. 5.14 (b)-(c) show the simulated antenna radiation pattern in the $xz$- and $yz$-planes at 60 GHz, where the radiation is decomposed into a RHCP wave and a left-handed circularly polarized (LHCP) wave. It can be clearly seen that the radiation is RHCP around the $z$-axis. As expected, the antenna radiation pattern has a main lobe of radiation in the upper hemisphere (in the-$z$ direction) with a front-to-back ratio better than 20 dB. The 3-dB beam width is $120^\circ$ in $xz$-plane and $90^\circ$ in $yz$-plane.

Fig. 5.14 (d) shows the simulated antenna peak gain and axial ratio. The antenna has peak gain of 5 dBi. The 3-dB gain bandwidth is over 14.5 GHz. It should be noted that the 3-dB axial ratio bandwidth is narrower than 2 GHz.

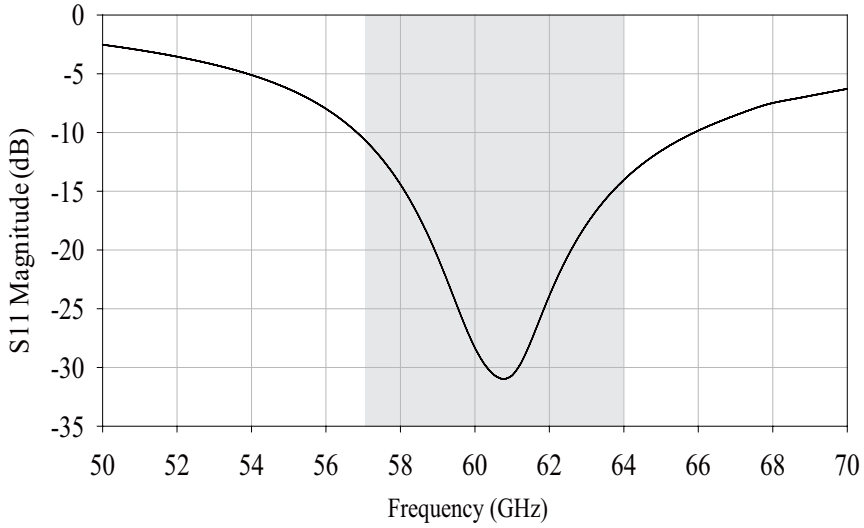


(a)

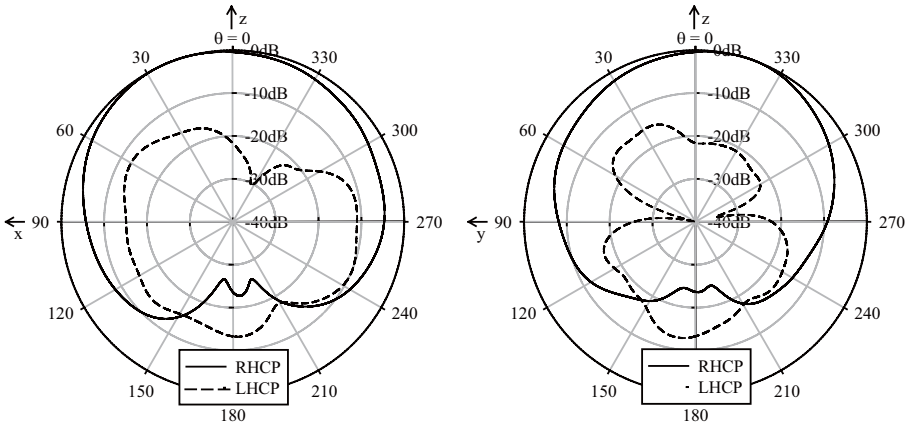


(b)




(c)

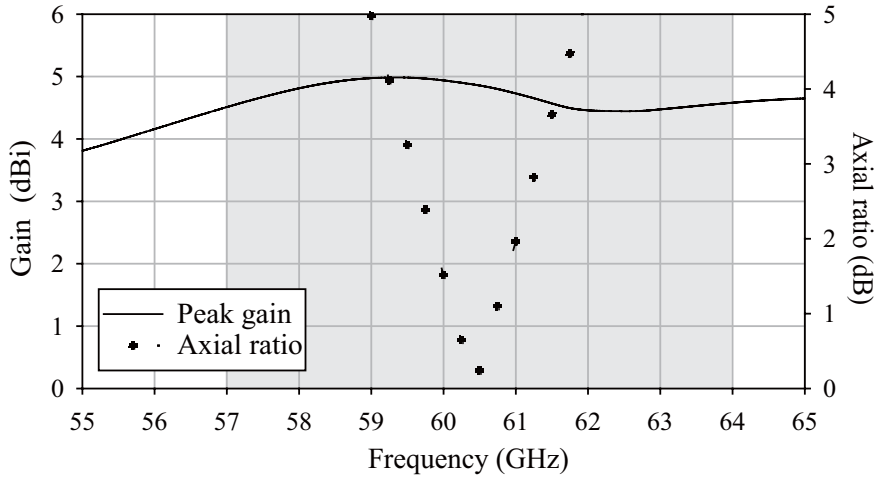


(d)

Figure 5.14: Simulated performance of the single element: (a) $|S11|$, (b) $xz$- plane and (c) $yz$- plane radiation pattern at 60 GHz, (d) gain and axial ratio at the main radiation direction.

### 5.4.2 Wideband $2 \times 4$ Circularly Polarized Patch Antenna Array

Fig. 5.15 shows the geometry of the sequentially feeding array. It is realized by rotating each antenna element in respect to its neighbouring element.

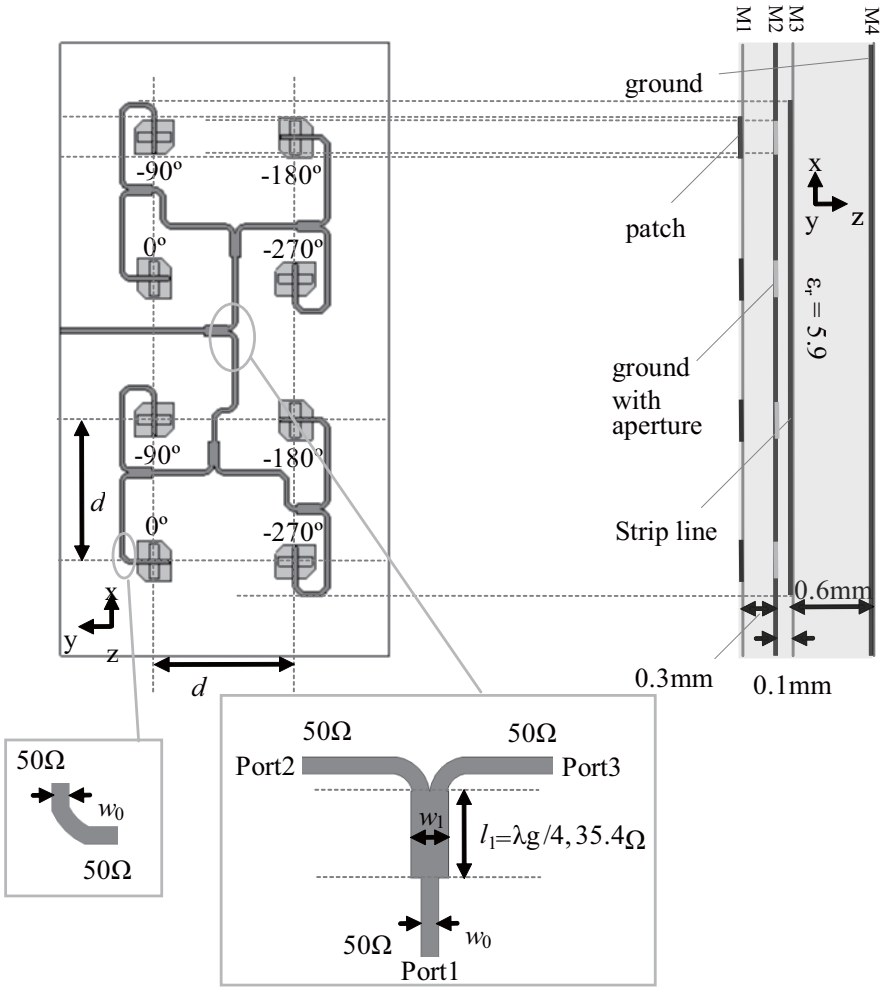


Figure 5.15: Geometry of the sequential feeding array antenna and zoom in view of the $90^{\circ}$ corner bent and the quarter-wave matched T-junction.

In this design, we have chosen to produce right handed polarization by arranging the element with the fashion of $0^{\circ}$, $-90^{\circ}$,$-180^{\circ}$,$-270^{\circ}$ as shown in Fig. 5.15. Accordingly the stripline feeding network is designed to feed each radiation element with equal amplitude but with phase corresponding to their individual rotation angles as denoted in Fig. 5.15. The required different phases in feeding network are achieved by the stripline delays, e.g.

an increase of a quarter guided wavelength in length corresponds to a delay of 90 degrees in phase. In the stripline feeding network, the $90^{\circ}$ corner bent is used instead of mitering the lines. In addition, the quarter-wave matched T-junction is used as the power divider to split the power equally.

Fig.5.16 shows the simulated array performance. It is found that the array has achieved a wide impedance bandwidth. The most important is that the 3-dB axial ratio bandwidth is enhanced to 7.5 GHz and the antenna shows good RHCP characteristics.

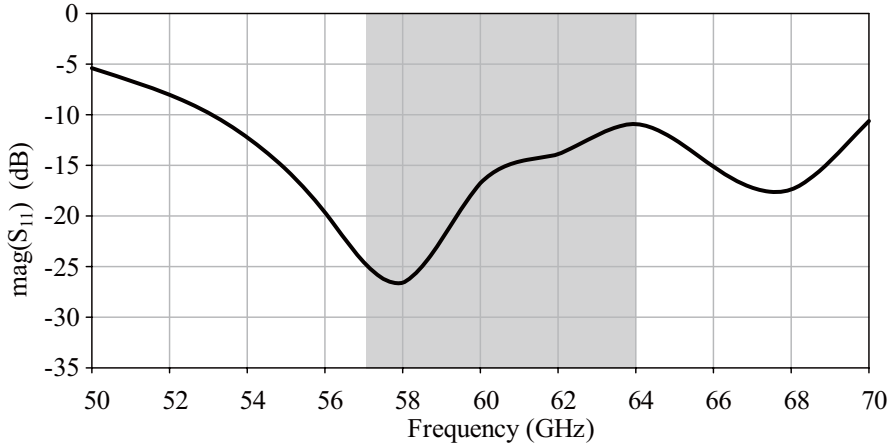


(a)

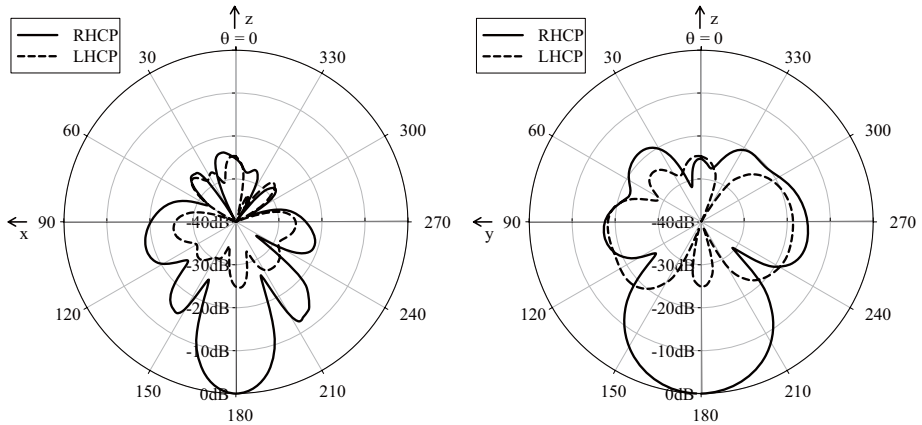


(b) (c)

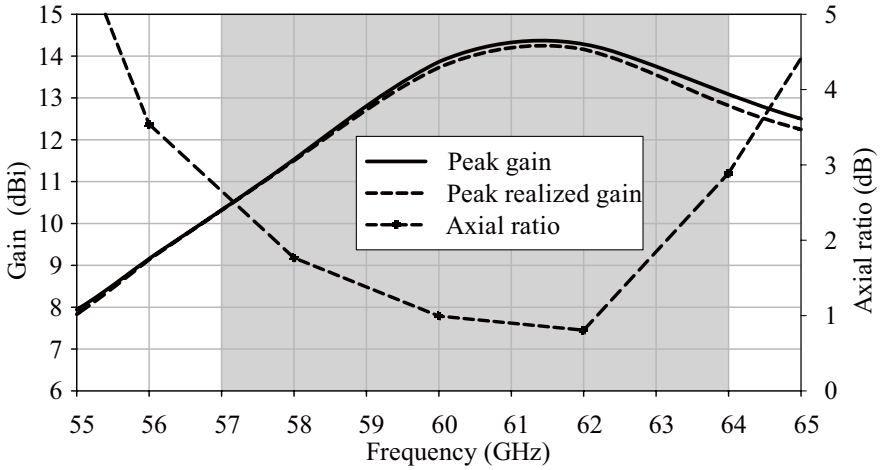


(d)

Figure 5.16: Simulated performance of the array antenna: (a) return loss, (b) $xz$-plane & (c) $yz$- plane radiation pattern at 60 GHz, and (d) gain and axial ratio.

### 5.4.3 Wideband $4 \times 4$ Circularly Polarized Patch Antenna Array

Fig. 5.17 shows the geometry of the sequentially feeding array with a size of $13 \times 13 \times 1$ $mm^3$. It is realized by rotating each antenna element in respect to its neighboring element. In this design, we have chosen to produce right handed polarization by arranging the element with the fashion of $0°$, -$90°$, -$180°$, -$270°$ as denoted in Fig. 5.17. Accordingly the stripline feeding network is designed to feed each radiation element with equal amplitude but with phase corresponding to their individual rotation angles. The required different phases in feeding network are achieved by the stripline delays, e.g. an increase of a quarter guided wavelength in length corresponds to a delay of 90 degrees in phase. In the stripline feeding network, the $90°$ corner bent is used instead of mitering the lines. The characteristic impedance for each port is 50 $\Omega$ with $w_0 = 0.1\ mm$. In addition, the quarter-wave matched T-junction is used as the power divider to split the power equally. Its width $w_1$

and length $l_1$ are easily characterized to be $0.22\ mm$ and $0.501\ mm$, respectively. The final input matching at input port is $|S11| = -20.5$ dB and the coupling from the input port to the output port is $|S21| = -3.29$ dB at 60 GHz. It is reasonable with a 0.29 dB loss in the output port for this power divider.

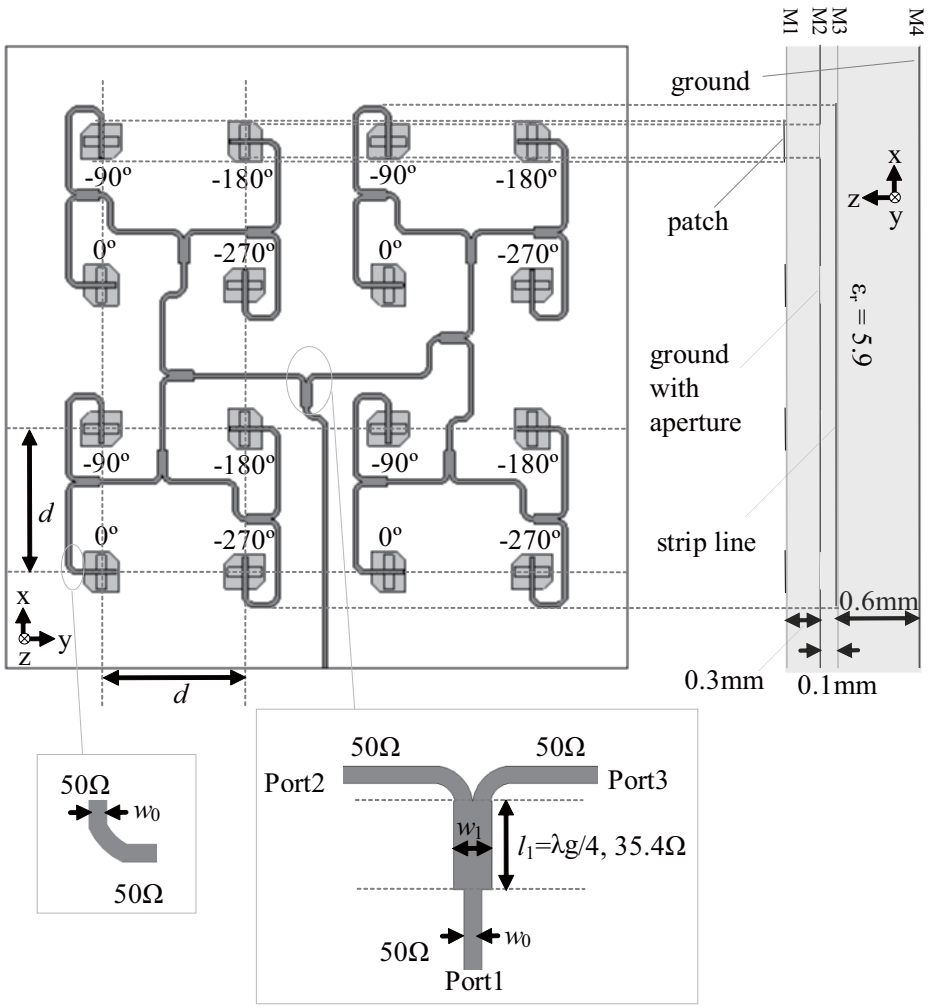


Figure 5.17: Geometry of the sequential feeding array antenna (size: $13 \times 13 \times 1\ mm^3$, $d = 3\ mm$) and zoom in view of the $90^\circ$ corner bent and the quarter-wave matched T-junction.

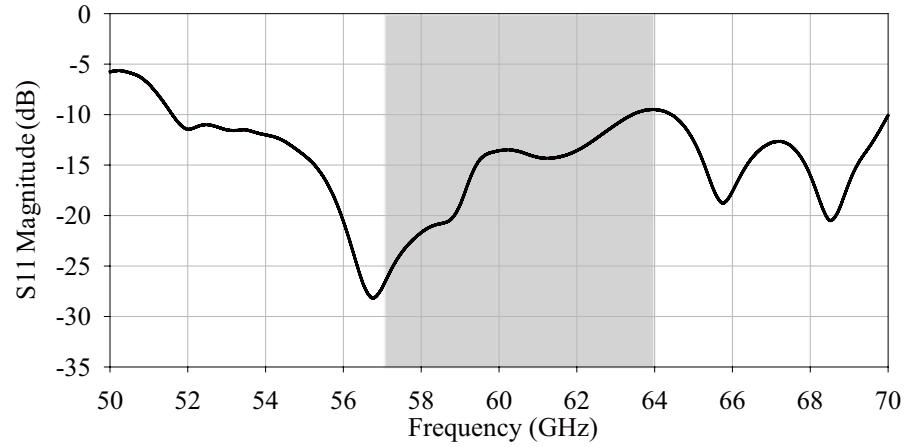


(a)

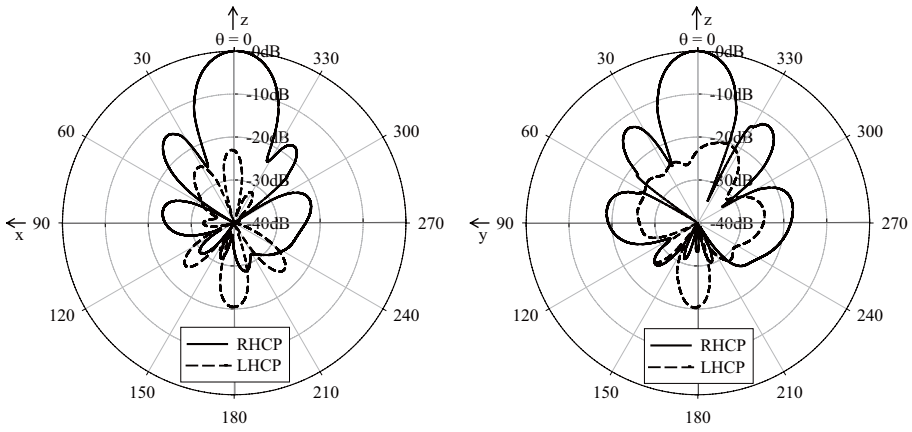


(b) (c)

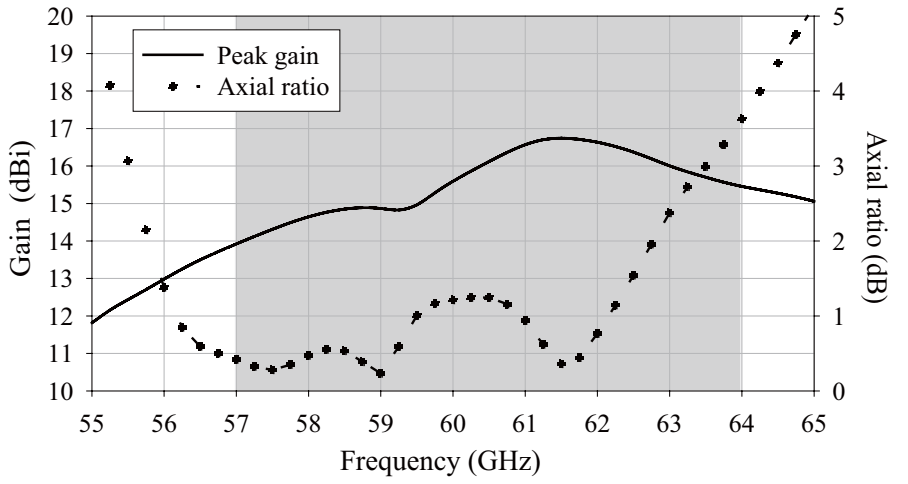


(d)

Figure 5.18: Simulated performance of the array antenna: (a) $|S11|$, (b) $xz$- plane and (c) $yz$- plane radiation pattern at 60 GHz, (d) gain and axial ratio at the main radiation direction.

Fig. 5.18 shows the simulated array performance. It is found from Fig. 5.18 (a) that the antenna has a wide impedance bandwidth of 18.5 GHz (51.5-70 GHz) for SWR$<$2. It is almost double that of the single element.

Figs. 5.18 (b)-(c) also show the simulated antenna radiation pattern in the $xz$- and $yz$-planes at 60 GHz. It can be clearly seen that the radiation is RHCP around the $z$-axis. The antenna radiation pattern is beam-shaped with a 3-dB beam width of $20^{\circ}$ both in the $xz$- and $yz$-planes.

Fig. 5.18 (d) shows the simulated antenna peak gain and axial ratio. As we can see the antenna has peak gain of 16.8 dBi. The 3-dB gain bandwidth is 10 GHz (56.8-66.8 GHz). It should be noted that the 3-dB axial ratio bandwidth has been successfully broadened to 8 GHz (55.5-63.5 GHz). It is more than four times of that of the single element. As a summary the designed array exhibits wideband impedance matching and AR performances at 60 GHz. We will further improve its gain using a 21-dB active LNA in Section 5.6.

## 5.5 Wideband Stripline-fed Circularly Polarized Planar Helical Antenna and Array

### 5.5.1 Antenna Element

Fig. 5.19 shows the configuration of a single planar helical antenna element. This modified helical antenna is designed in a twenty-layer LTCC substrate with dielectric constant of 5.9, each layer thickness of 0.1 $mm$. The antenna consists of eleven metallic layers, which can be divided into two parts. The first part is the radiation-patch of the helical antenna which is implemented on the upper eight metal layers as shown in Fig. 5.19(b) (M1-M8).

The second part is the feeding network of the helical antenna which is implemented on the lower three metal layers as shown in Fig. 5.19(b) (M9-M11). From M1 to M8, the thickness between every two neighbouring metal layers is $h_1 = 0.2\ mm$. And the distance between M8 and M9 is 0.1 $mm$. The radiation-patch consists of one quarter-annular-patch lies on metal layer M8 and seven half-annular-patches lie on metal layers M1-M7. Vertical vias are used to connect every two neighbouring metal layers. So all the eight metal layers' traces are connected together by these vias, which form the raidation-patch of the helical antenna. The radiation-patch implemented on the $h_2 = 1.4\ mm$ thick LTCC substrate is fed vertically by a feeding via which connects to a stripline through a circle slot on the ground plane. The stripline is sandwiched between the 200-$\mu m$ and 300-$\mu m$ thick LTCC substrate with the top and bottom grounded. The width of the 50-$\Omega$ stripline $w_0$ as shown in Fig. 5.19 is easily characterized to be 0.15 $mm$.

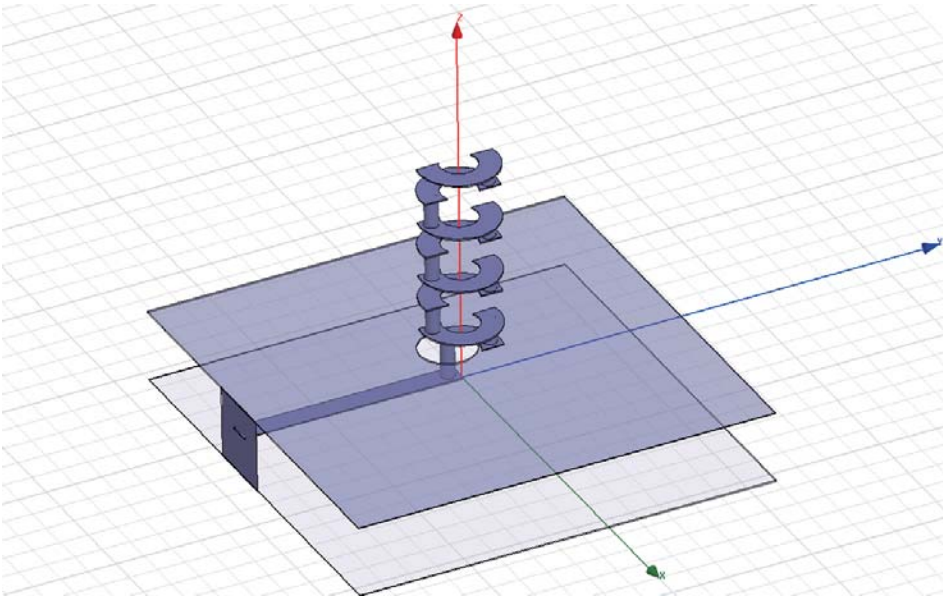

(a) 3D view

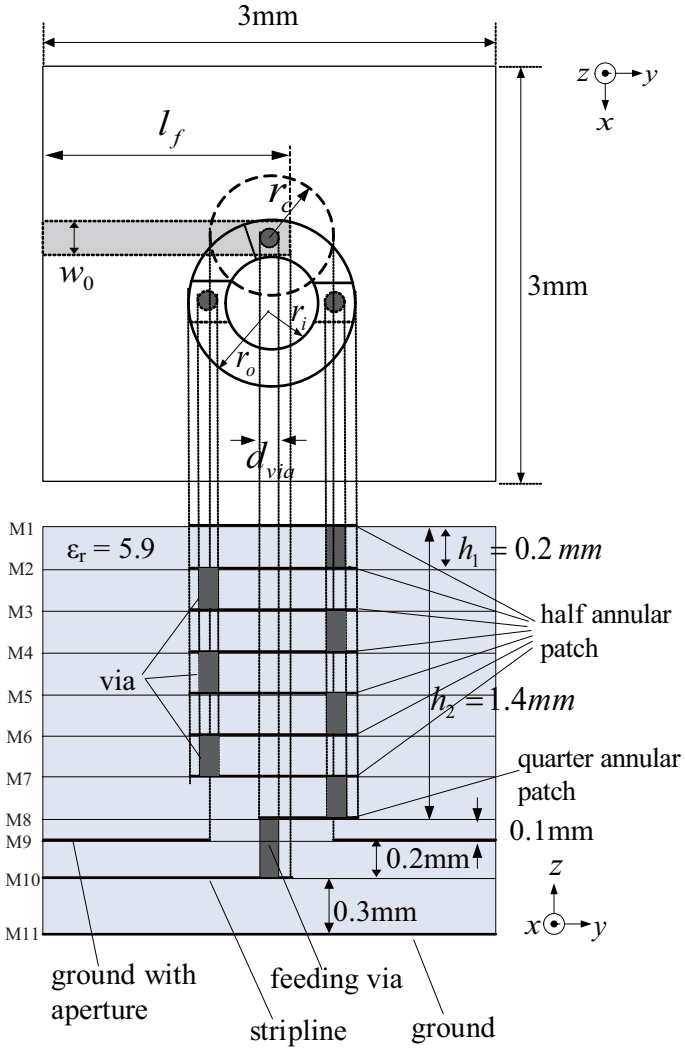


(b) 2D view

Figure 5.19: Geometry of the single antenna element (size: $3 \times 3 \times 2\ mm^3$, $w_0 = 0.15\ mm$, $l_f = 1.65\ mm$, $r_o = 0.3\ mm$, $r_i = 0.15\ mm$, $r_c = 0.3\ mm$, $d_{via} = 0.1\ mm$), $h_1 = 0.2\ mm$, $h_2 = 7 \times h_1 = 1.4\ mm$.

The circular polarization can be obtained by appropriate selection of the geometrical parameters of the radiation-patch. Fig. 5.20 and Fig. 5.21 show S11 and axial ratio performance with three different cases.

Case 1: $h_1 = 0.2\,mm$, $h_2 = 7 \times h_1 = 1.4\,mm$.

Case 2: $h_1 = 0.2\,mm$, $h_2 = 6 \times h_1 = 1.2\,mm$.

Case 3: $h_1 = 0.1\,mm$, $h_2 = 7 \times h_1 = 0.7\,mm$.

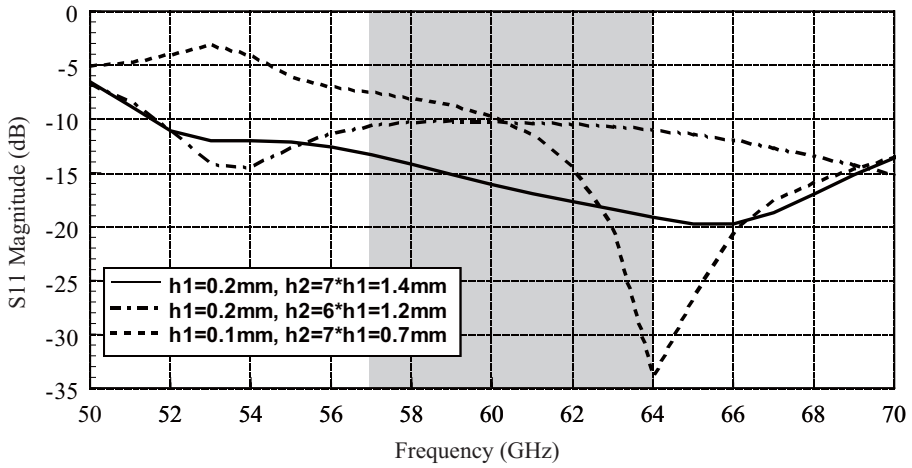


Figure 5.20: Simulated S11 of the single antenna for three different cases.

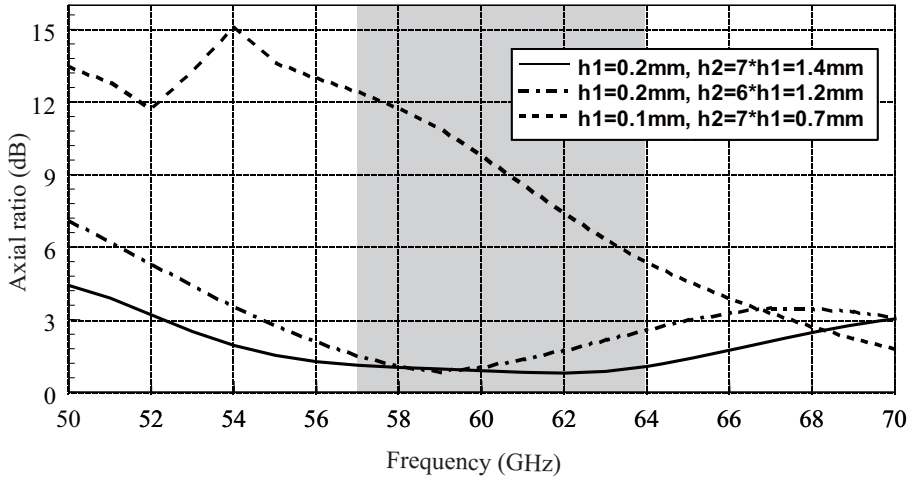


Figure 5.21: Simulated axial ratio performance of the single antenna for three different cases.

Case 1 is exactly the same situation as shown in Fig. 5.19. One quarter-annular-patch and seven half-annular-patches are assigned on the 1.4 $mm$ thick LTCC substrate with equal distance ($h_1 = 0.2\ mm$). In case 2, there are one quarter-annular-patch and six half-annular-patches are assigned on the 1.2 $mm$ thick substrates with equal distance 0.2 $mm$. Case 2 has one less half-annular-patch compared with case 1. In case 3, there are one quarter-annular-patch and seven half-annular-patches are assigned on the 0.7 $mm$ thick substrates with equal distance 0.1 $mm$. Case 3 has the same radiation patches with case 1 but smaller separate distance.

Comparing case 1 with case 2, both S11 and axial ratio become worse in the same operating bandwidth when the number of radiation patches is reduced. Comparing case 1 with case 3, even with the same number of radiation patches, the distance between two radiation patches is critical for deciding the operating frequency. When the value of $h_1$ is reduced, the operating frequency of the helical antenna is going higher for both S11 and axial ratio.

The antenna parameters are optimized with final values shown in the subtitles of Fig. 5.19. The final simulated antenna element size is $3 \times 3 \times 2\ mm^3$.

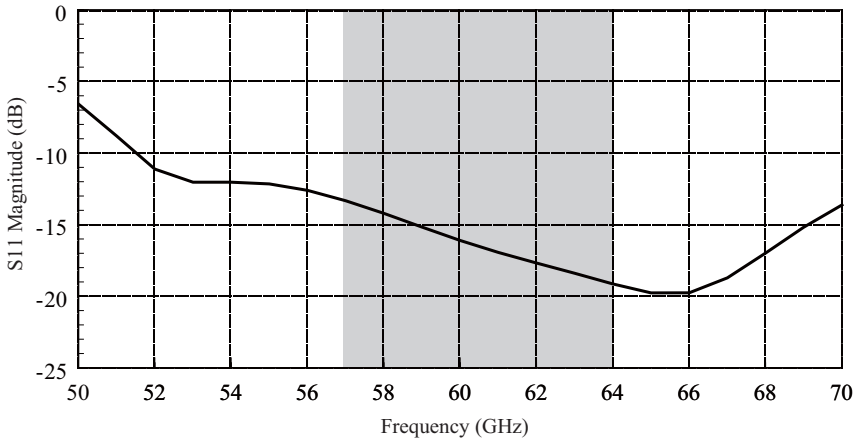


(a)

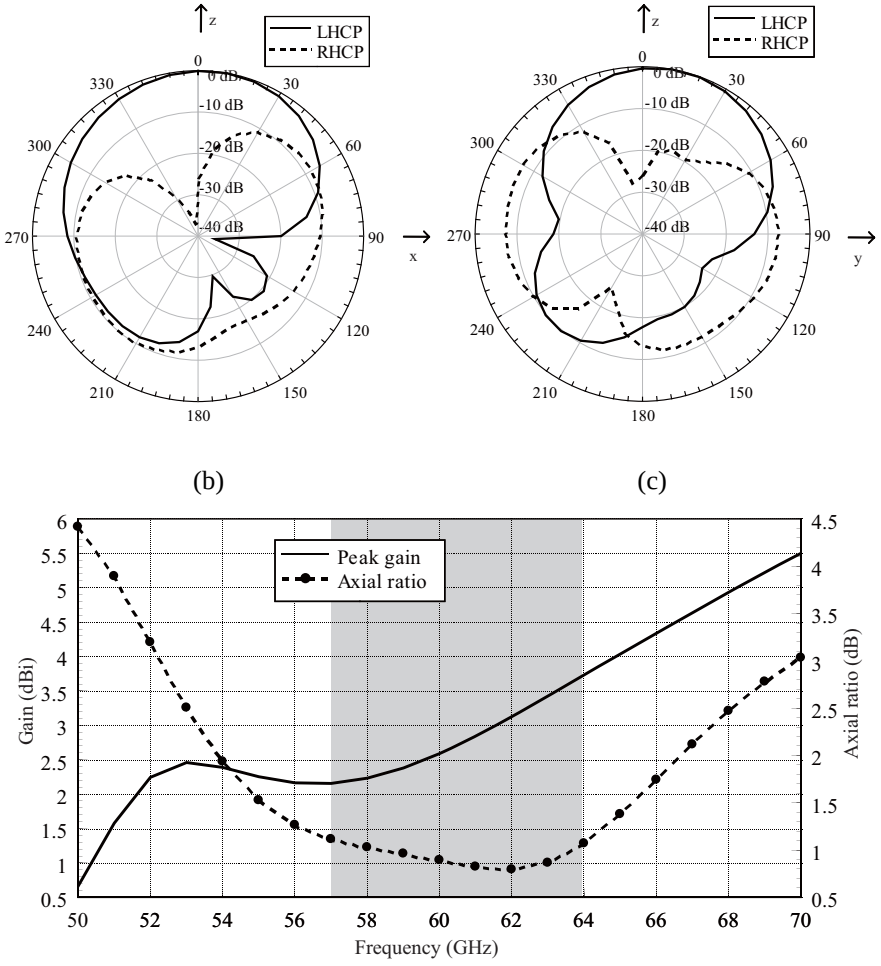


Figure 5.22: Simulated performance of the sigle antenna: (a) return loss, (b) $xz$-plane & (c) $yz$- plane radiation pattern at 60 GHz, and (d) gain and axial ratio.

Fig. 5.22 shows the simulated antenna element performance. Fig. 5.22 (a) shows an impedance bandwidth over 18 GHz (52-70 GHz) for $|S11| < -10$ dB. Figs. 5.22 (b)-(c) show the simulated antenna radiation pattern in the $xz$- and $yz$-planes at 60 GHz, where the radiation is decomposed into a RHCP wave and a left-handed circularly polarized (LHCP) wave. It can be clearly seen that the radiation is LHCP around the $z$-axis. As expected, the antenna radiation pattern has a main lobe of radiation in the upper hemisphere. The

3-dB beam width is $90^\circ$ in the $xz$-plane and $70^\circ$ in the $yz$-plane. Fig. 5.22 (d) shows the simulated antenna peak gain and axial ratio. The antenna has peak gain of 2.2-3.7 dBi in the band (57-64 GHz). The 3-dB gain bandwidth is 10 GHz. Compared with the aperture-coupled CP antenna, the modified helical antenna has thicker substrate. As a result, the antenna peak gain is lowered due to increased substrate loss. However, it should be noted that even the single antenna element has a 3-dB axial ratio bandwidth over 14 GHz. The modified helical antenna inherits great CP characteristic from traditional helical antenna.

### 5.5.2 Wideband $4 \times 4$ Circularly Polarized Helical Antenna Array

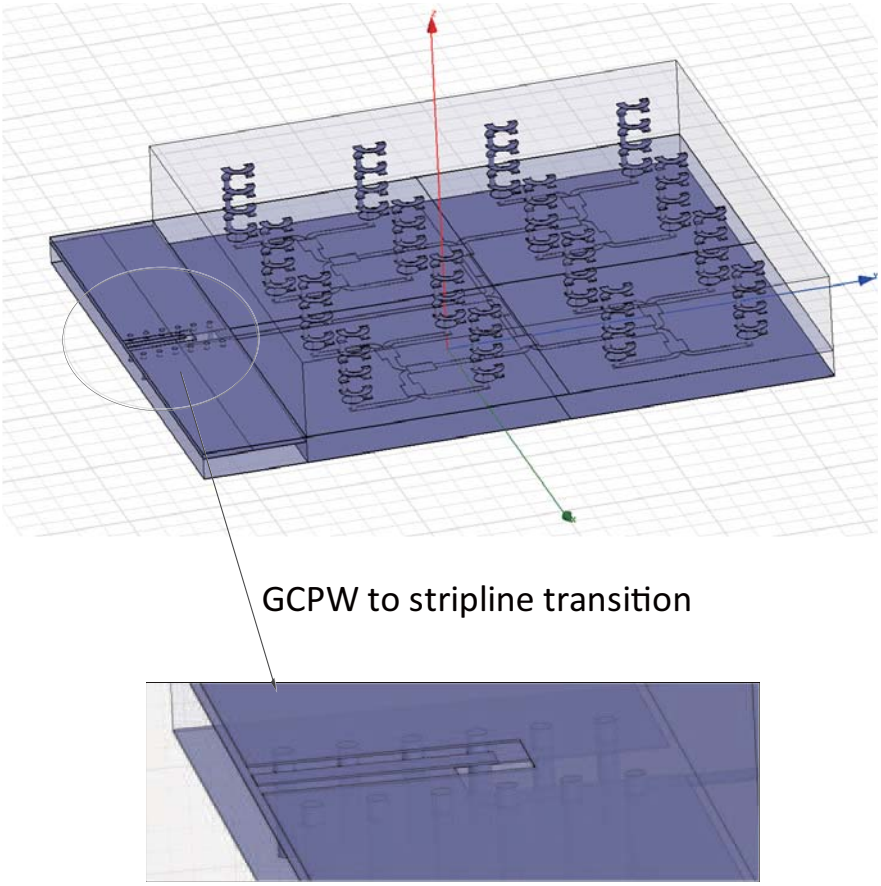


(a) 3D view

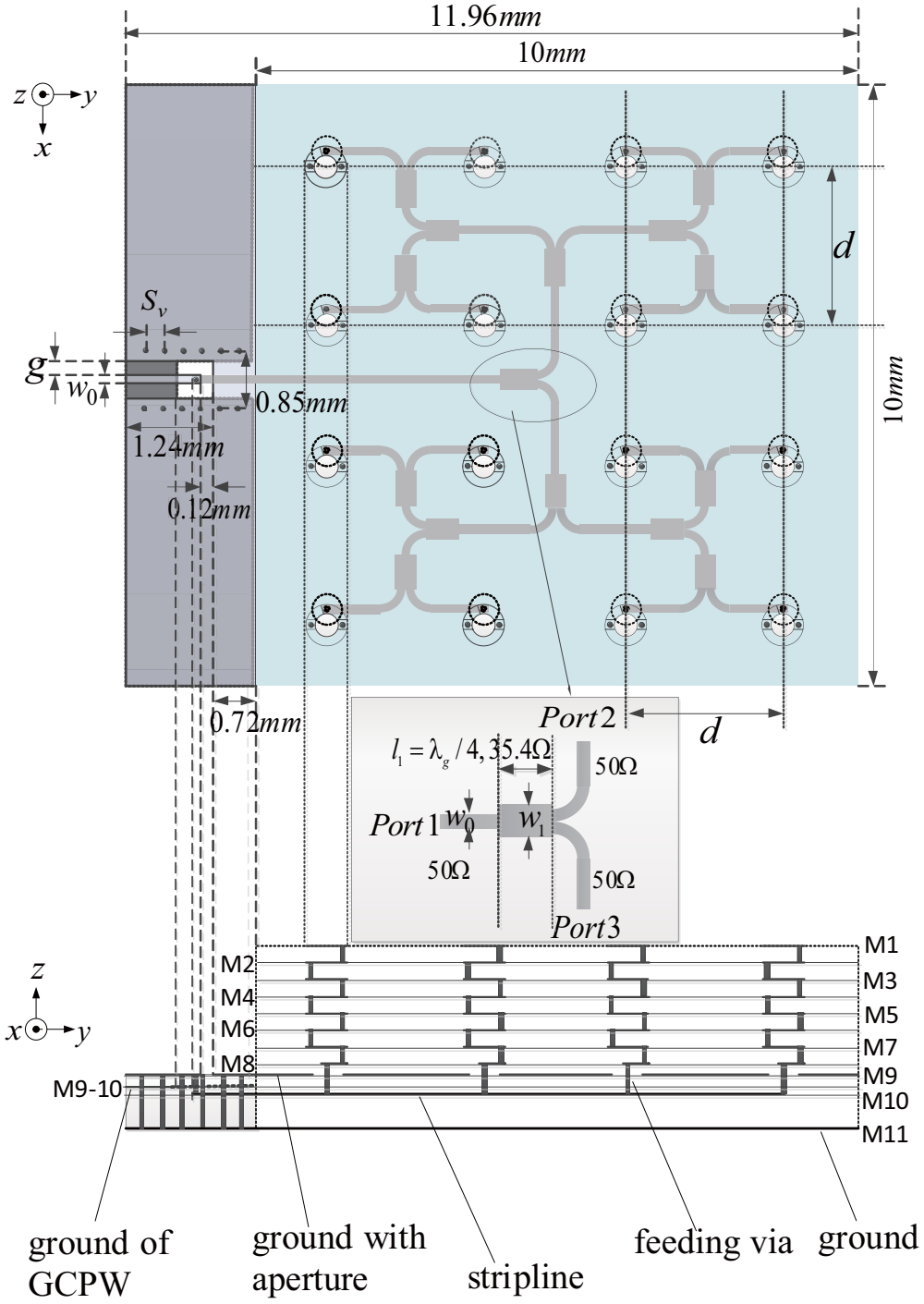


(b) 2D view

Figure 5.23: Geometry of the $4 \times 4$ Array. (size: $10 \times 11.96 \times 2\ mm^3$, $d = 2.5\ mm$, $w_0 = 0.15\ mm$, $g = 0.15\ mm$, $S_v = 0.3\ mm$, $w_1 = 0.35\ mm$, $l_1 = 0.501\ mm$)

Since the gain of the single element of planar LTCC helical antenna is low (2.2-3.7 dBi in 57-64 GHz band), a $4 \times 4$ LTCC helical CP antenna array is exploited.

Fig. 5.23(a) shows 3D configuration of the helical antenna array with a GCPW-to-stripline transition. The detailed geometry is shown in Fig. 5.23(b). The stripline feeding network is designed to feed each radiation element with equal amplitude and phase. The characteristic impedance for each port is 50-$\Omega$ with $w_0 = 0.15\ mm$. In addition, the quarter-wave matched T-junction is used as the power divider to split the power equally. Its width $w_1$ and length $l_1$ are easily characterized to be $0.35\ mm$ and $0.501\ mm$, respectively. The transition from GCPW-to-stripline has a length of $1.96\ mm$. The GCPW is designed at 60 GHz with $w_0 = g = 0.15\ mm$. The signal line of the GCPW is on the metal layer M9 and the ground plane of the GCPW is on M9-10. The thickness between M9 and M9-10 is $0.1\ mm$.

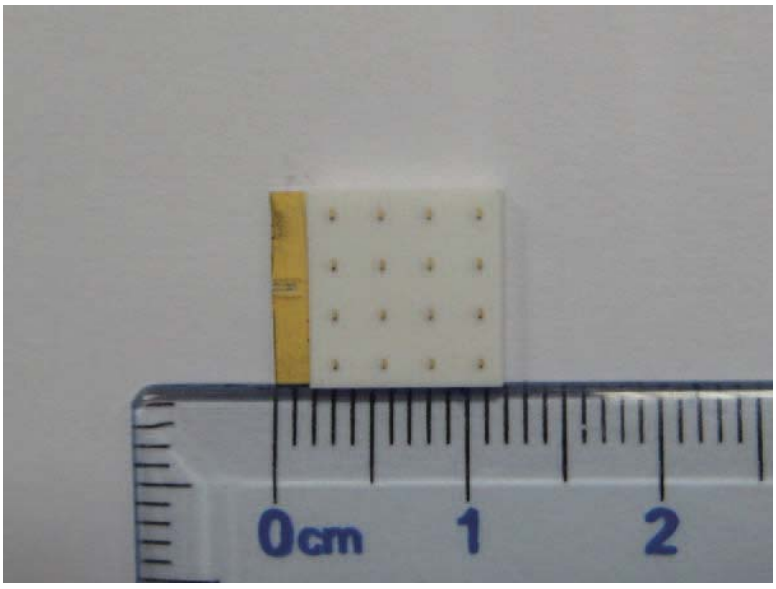


Figure 5.24: Photograph of the fabricated $4 \times 4$ Helical CP Antenna Array.

The $4 \times 4$ planar helical CP antenna array was fabricated as shown in Fig. 5.24. The antenna was tested by Rohde & Schwarz ZVA50 vector network analyzer (VNA) up to a frequency of 75 GHz. A GSG RF probe with a pitch of 250 $\mu m$ was touched on the GCPW line of the antenna for testing.

Fig. 5.25 shows the measured and simulated array performance. It is found from Fig. 5.25(a) that the antenna has a wide impedance bandwidth of 13 GHz (52-65 GHz) for $|S11| < -10$ dB. It is narrow than that of the single element. Figs. 5.25(b)-(c) show the measured and simulated antenna peak gain and axial ratio. As we can see the antenna has peak gain of 15.4 dBi at 60 GHz. The 3-dB gain bandwidth is 12 GHz (53-65 GHz). It should be noted that the 3-dB axial ratio is 12 GHz (54-66 GHz). It is almost the same as that of the single element. In this modified helical antenna array design, the wideband CP characteristic is achieved without usage of sequentially feeding rotation scheme in feeding network. The coupling effect between neighbouring antenna elements will not deteriorate the CP performance of single element, which reduces design complexity of the feeding network.

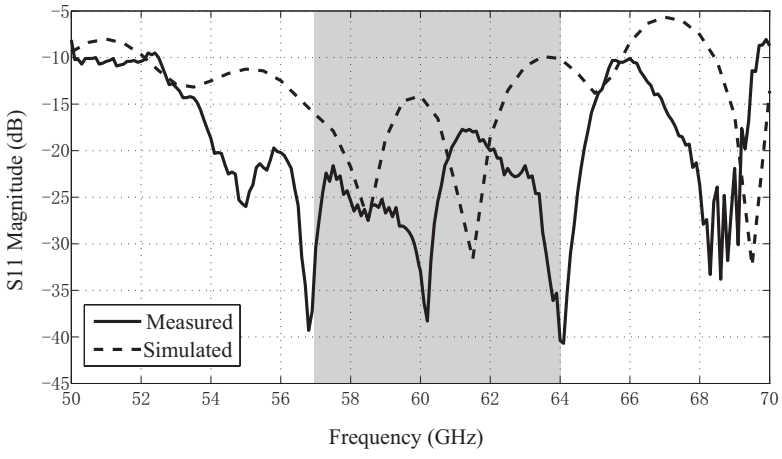


(a)

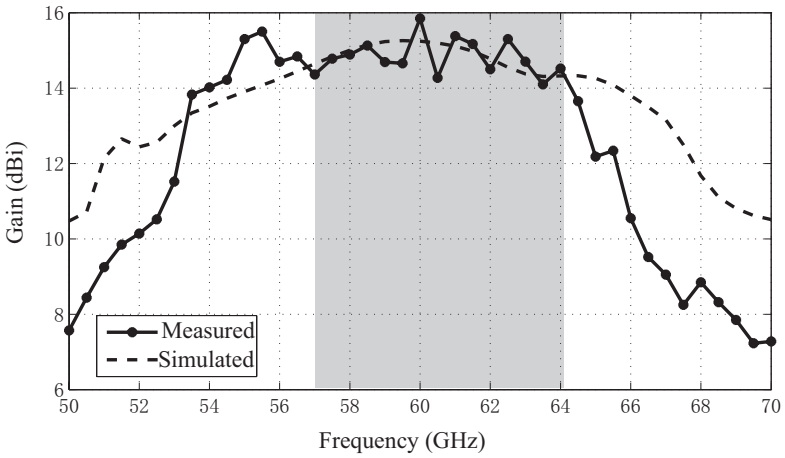


(b)

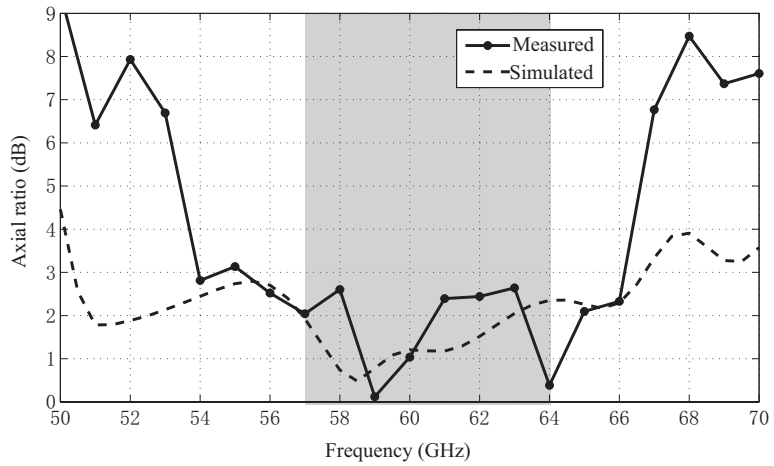


(c)

Figure 5.25: Measured and simulated performance of the array antenna: (a) return loss, (b) peak gain, (c)axial ratio at the main radiation direction.

Figs. 5.26, 5.27 and 5.28 show the measured and simulated antenna radiation pattern in the $yz$- and $xz$-planes at 55 GHz, 60 GHz and 64.5 GHz, respectively. The antenna radiation pattern is beam-shaped with a 3-dB beam width around $20^{\circ}$ at 60 GHz.

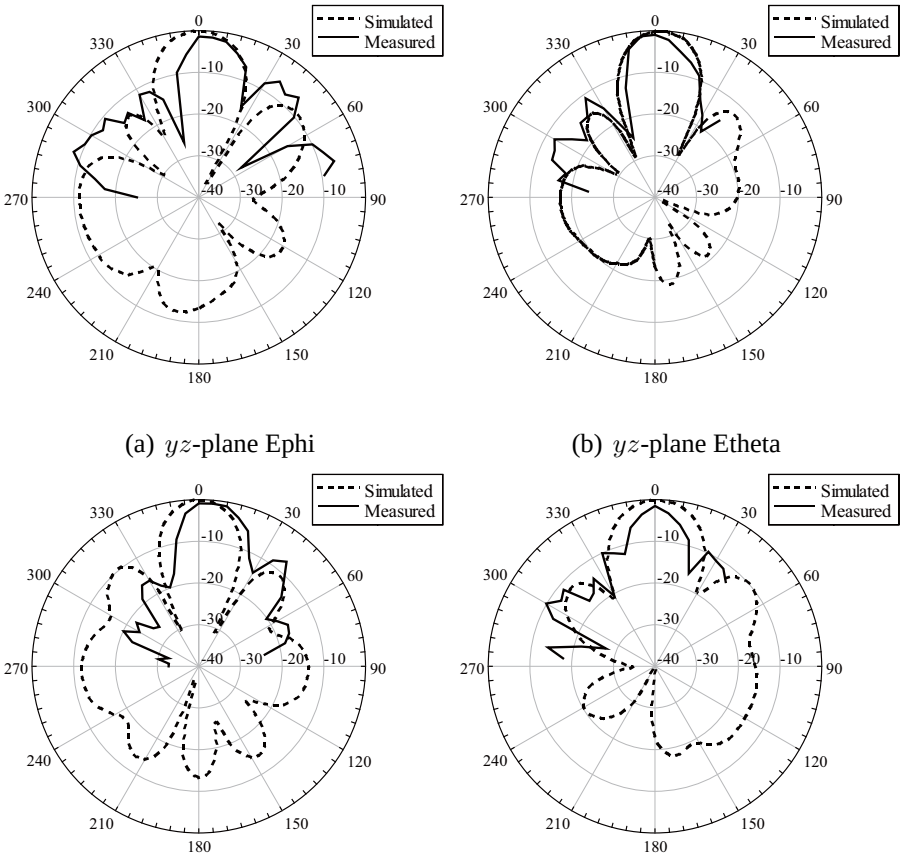


(a) $yz$-plane Ephi

(b) $yz$-plane Etheta

(c) $xz$-plane Ephi

(d) $xz$-plane Etheta

Figure 5.26: Radiation patterns at 55 GHz.

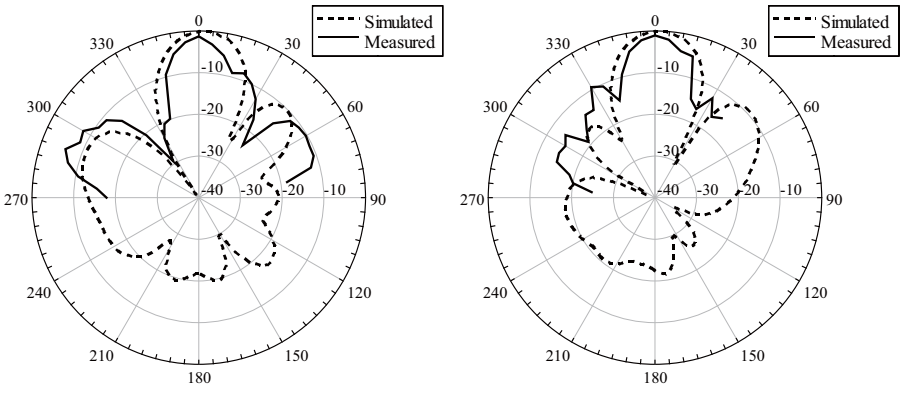


(a) $yz$-plane Ephi

(b) $yz$-plane Etheta

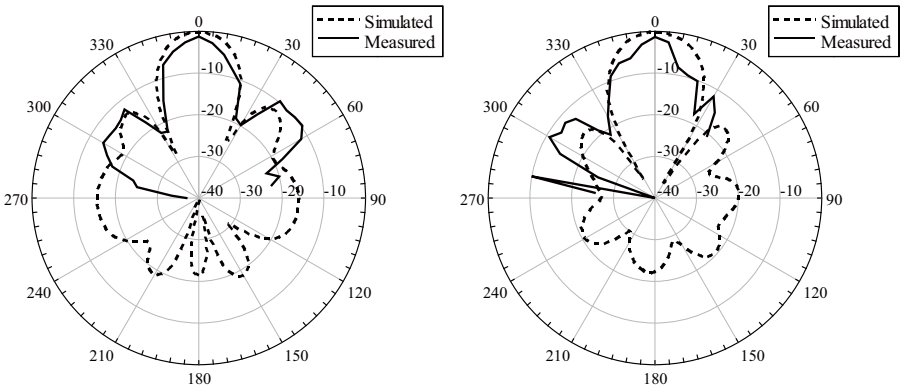


(c) $xz$-plane Ephi (d) $xz$-plane Etheta

Figure 5.27: Radiation patterns at 60 GHz.

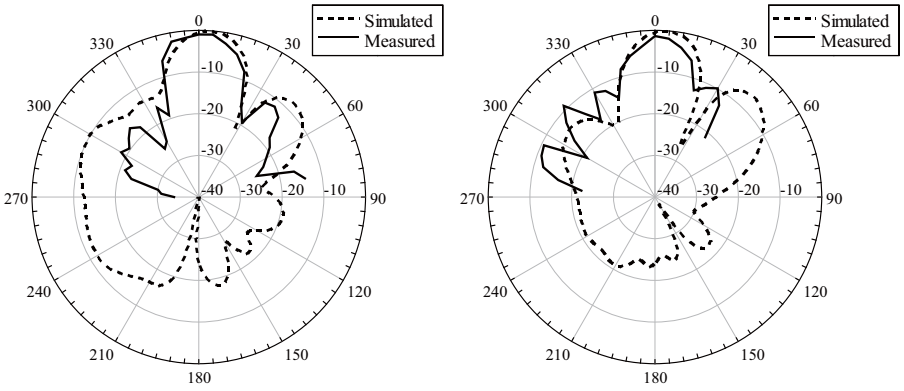


(a) $yz$-plane Ephi (b) $yz$-plane Etheta

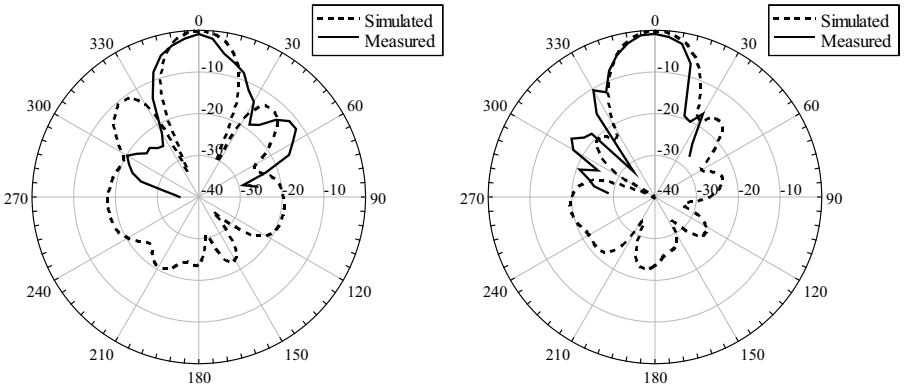


(c) $xz$-plane Ephi (d) $xz$-plane Etheta

Figure 5.28: Radiation patterns at 64.5 GHz.

From our previous study, we can see that the proposed planar helical antenna and array in LTCC in the 60-GHz band achieve a good CP characteristic over wide operating frequency band (around 12 GHz). The design takes the advantage of both traditional helical antenna and LTCC technology. The planar structure and the stripline feeding scheme give a good solution for helical antennas and circuits' integration.

## 5.6 Integration of Circularly Polarized Array and LNA in LTCC as a 60-GHz Active Receiving Antenna

Fig. 5.29 shows the geometry of the 60-GHz active receiving antenna in LTCC package. It integrates the 4×4 antenna array presented in Section 5.4 with a LNA. As shown the package consists of five cofired laminated ceramic layers with their thickness denoted respectively in Fig. 5.29 (b). There are also five metallic layers, where M1, M2, M3, M4 layers are the same as those in Fig. 5.13 and Fig. 5.17. The M1 layer provides the metallization for the patch array antenna, the M2 layer the metallization for the antenna ground with aperture and the Grounded Co-Planar Waveguide (GCPW) for chip interconnection as well as chip DC biasing layout, the M3 layer the metallization for the antenna stripline feeding traces, the M3-4 layer the metallization for the GCPW ground, and the M4 layer the metallization for the system ground plane. The size of the whole package is $13 \times 19.85 \times 1.4\ mm^3$. Note that the active antenna features standard wire bonding to chip. A T-junction structure as shown in Fig. 5.29 (c) is used to compensate the bond wire larger inductance at 60 GHz. This enables the longer bond wire of 500 $\mu m$ to be used, which is almost a tripled length of the shortest bond wire supported by the current technology and would thus greatly improve the yield of assembly of the chip with the package. This also

makes our integration solution suitable for mass production. The bond wire compensation will be presented in the following Section 5.6.1. In addition, the active antenna features low loss transitions as denoted in Fig. 5.29 (c). Their design and performance optimization will be presented in the following Section 5.6.2. Based on the bond wire compensation and transition optimization, by using a 50- dummy microstrip line on chip as shown in Fig. 5.29 (c) the whole receiving antenna is simulated. This will give us an idea of the transitions effect on the integration performance. The details will be presented in the following Section 5.6.2. Finally in Section 5.6.3, the active antenna is tested.

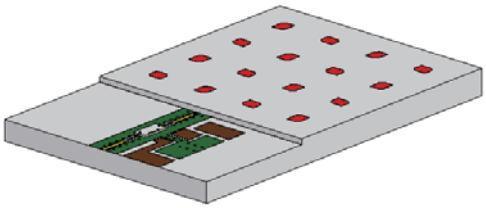

(a)

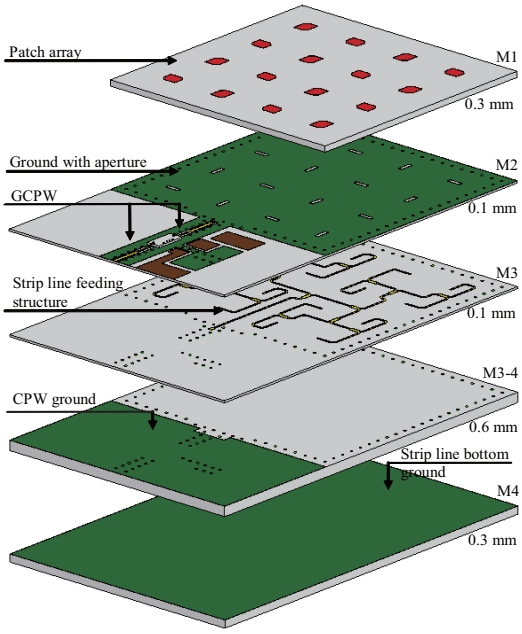


(b)

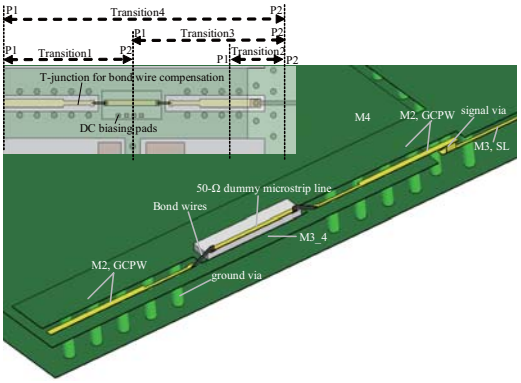


(c)

Figure 5.29: Geometry of the integrated array antenna with LNA (size: $13 \times 19.85 \times 1.4$ $mm^3$): (a) 3D top view, (b) 3D explored view, and (c) zoom in view of the transitions with a 50-$\Omega$ dummy microstrip line on chip.

### 5.6.1 Millimeter Wave Bond Wire Compensation Study

#### Review of Bond Wire Compensation Structures

The goal for mmWave interconnect designs is to maximize bond-wire length to improve manufacturability and maximize bond pad size so that mechanical tolerances are eased. Budka has demonstrated that this is possible with a filter theory approach to interconnect design as shown in Fig. 5.30 [95]. He has considered the conventional bond wire design as a single-stage low pass filter while his novel design as a five-stage low pass filter. Thus, for the same cutoff frequency of the single- and five-stage filter, the center inductor in the five-stage design can have a 3.6 times higher inductance than a single inductor design. This directly translates into a 3.6 times longer bond wire for the same cutoff frequency.

Budkas wirebond design technique enables the use of significantly longer bond wires but the chip must have filter-like compensation on the mmWave bonding pads. This is

usually impossible unless the co-design of the chip and package can be done. Also Budkas method is not suitable for connecting the radio chip to the antenna because it is difficult to implement the DC blocking capacitor between them. However, it can realize the wideband compensation.

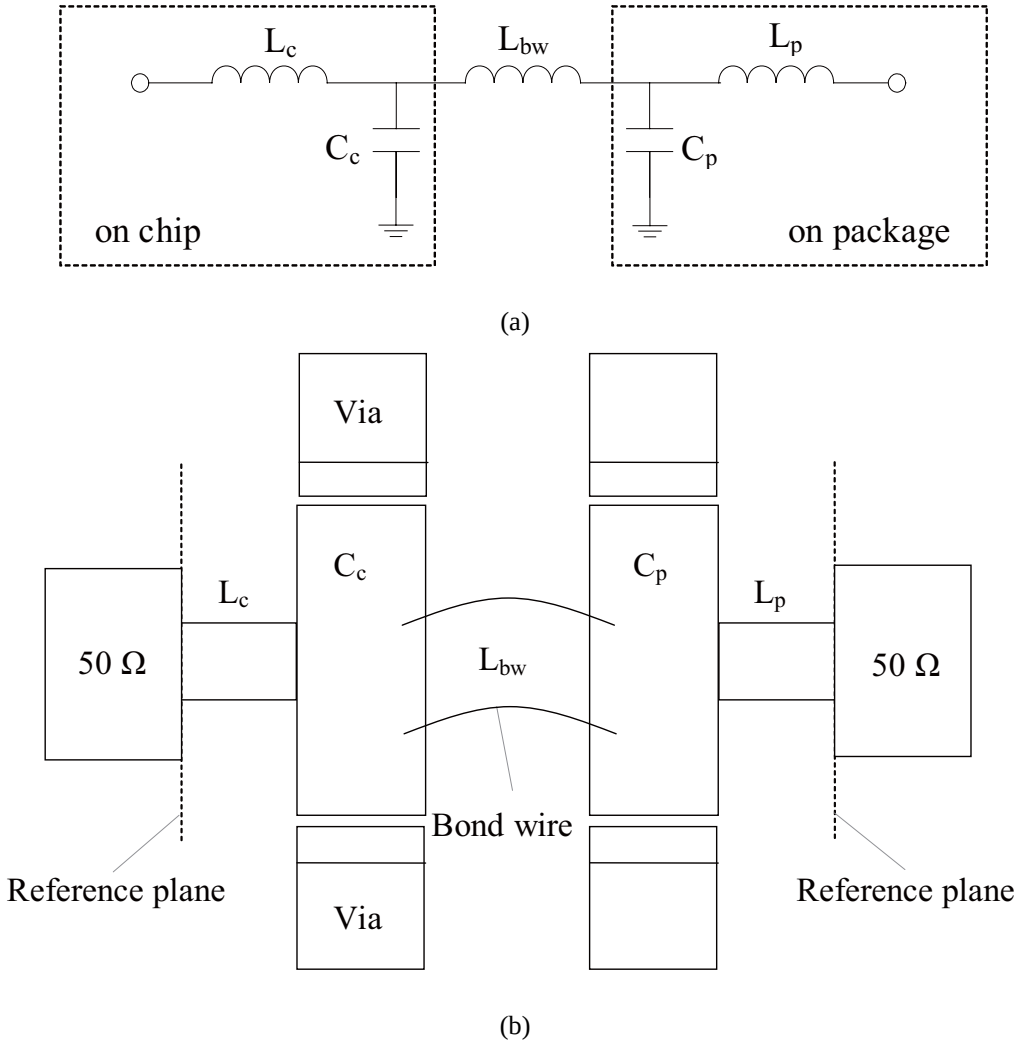


Figure 5.30: Budkas bondwire compensation scheme: (a) circuit model and (b) layout.

A T-network was used to compensate for the series inductance introduced by the bond wire as shown in Fig. 5.31 [90]. The inductor $L_{bw}$ models the bond-wire inductance.

Inductor $L_p$ and capacitor $C_p$ are realized on package.

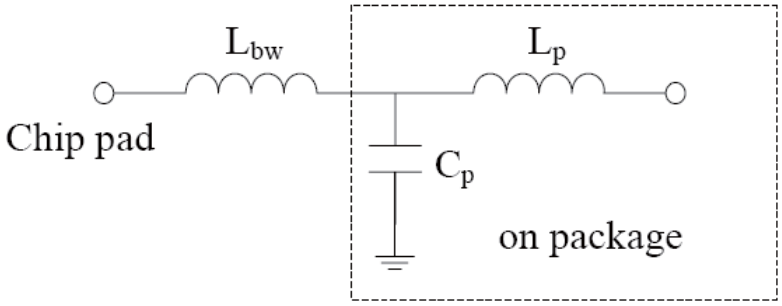


(a)

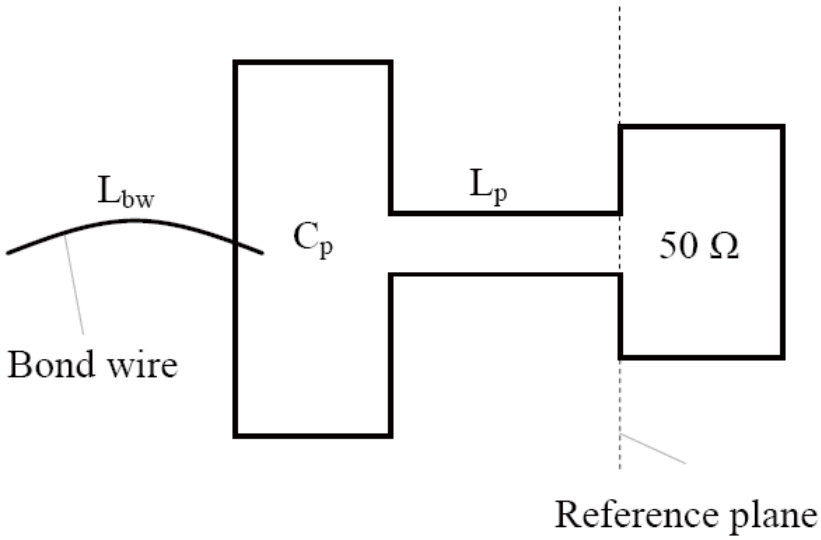


(b)

Figure 5.31: Bondwire compensation scheme used in [82] and [90]: (a) circuit model and (b) layout.

This compensation network has also been used in [82]. It is noted that it has the drawback of a large on-package area required to implement $L_p$ and $C_p$. In addition, the compensation is still narrowband. However, its compensation structure is on the same layer with the traces to be connected by bond wires, which makes it useful and convenient in most cases.

In the following parts, the compensation structure of Fig. 5.31 will be applied to the wire bonded chip-to-package interconnect.

**Bond Wire Compensation in LTCC at 60 GHz**

TABLE 5.5 lists the LTCC technology data as well the 50-$\Omega$ microstrip line (MSL) and coplanar waveguide (CPW) dimensions as denoted in Fig. 5.32 (a) and (b). These 50-$\Omega$ MSL and CPW will be used in the wire bonding interconnects as port interfaces as shown in Fig. 5.32.

Table 5.5: LTCC TECHNOLOGY DATA @ 60 GHZ

| | |
|---|---|
| LTCC substrate | 200-$\mu m$ thick ($\epsilon_r$ =5.9, $tan\delta$ = 0.002 ) |
| metal | 10-$\mu m$ thick gold |
| basic design rule | smallest line width / spacing: 100 $\mu m$ |
| 50-$\Omega$ MSL @ 60GHz | w = 0.3 $mm$ |
| 50-$\Omega$ CPW@ 60GHz | w = 0.2 $mm$, s = 0.1 $mm$, $w_g$ = 0.7 $mm$, $s_v$ = 0.45 $mm$, $d_v$ = 0.15 $mm$ |

Fig. 5.32(c) shows the gold bond wire parameters with a total length of $TL_{bw}$, a height of $H_{bw}$ and a diameter $D_{bw} = 1mil$ or $2mil$. It is known that a bond wire presents high impedance because of its high inductance and low capacitance. Thus, keeping $TL_{bw}$ minimum and using the bond wires with the largest possible $D_{bw}$ are critical to minimizing their disruptive influences on electrical signals.

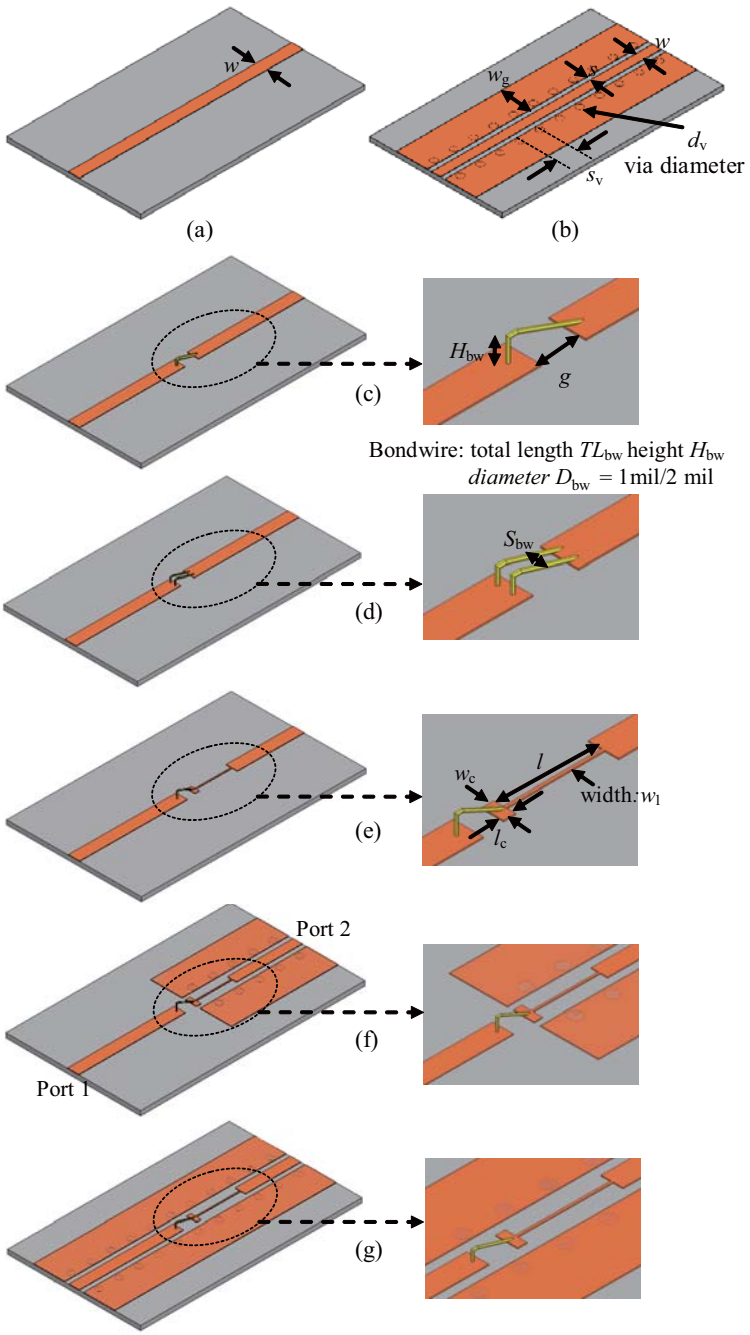


Figure 5.32: Bond wire (bw) interconnect and its compensation (bwc): (a) MSL, (b) CPW, (c) bw MSL-MSL, (d) double bw MSL-MSL, (e) bwc MSL-MSL, (f) bwc MSL-CPW, and (g) bwc CPW-CPW (Note: the substrate has a ground plane at the bottom).

One technique to reduce the bond wire inductance is using double bond wires with a separation distance of $S_{bw}$ as shown in Fig. 5.32 (d). It is effective, reliable and cost-effective. Fig. 5.32 (e) shows the T-network compensation parameters. As introduced previously, this compensation is narrowband. It is found from our simulation that the resonance frequency $f_s$ shifts down with the increase of $l$, $l_c$, or $w_c$. In addition, the decrease of $w_1$ will help to achieve better matching at $f_s$. When the T-network compensation structure is fabricated, the wire bonding process variation will cause the shift of the $f_s$. Usually the bond wire will be over lengthened. One technique is trimming the $w_c$ to a smaller value to compensate it. Fig. 5.32(f) and (g) shows the bond wire compensated MSL-CPW and CPW-CPW configurations, respectively.

Table 5.6: SUMMARY

| Parameters | $TL_{bw} = 400\ \mu m$, $H_{bw} = 0.1\ mm$, $g = 0.4\ mm$, $w_c = 0.15\ mm$, $l_c = 0.1\ mm$, $l = 0.7\ mm$, $w_1 = 0.1\ mm$ | | |
|---|---|---|---|
| Bondwire | $\|S11\|$ @60GHz | $\|S22\|$ @60GHz | $\|S21\|$ @60GHz |
| 2-mil bw | -8 | -8 | -1.65 |
| double 1-mil bw | -8.5 | -8.5 | -1.65 |
| 2-mil bwc | -16 | -18 | -0.85 |

For the MSL-CPW configuration as shown in Fig. 5.32 (f), it is seen that choices are summarized in TABLE 5.6. Fig. 5.33 shows the simulation results for the MSL-CPW configuration in LTCC, which usually appears in the packaging between microstrip-based active devices and CPW-based LTCC transmission lines. The performances are still poor by using one 2-mil or double 1-mil bond wires even at the shortest length of 400$\mu m$. In contrast, using the bond wire compensation for 2-mil bond wires, the insertion loss can be improved to 0.85 dB. The design difficulty is that the smallest line width and spacing is 100 $\mu m$ in LTCC, making the better matching hard to be achieved. It also should be noted that the bond wire length should be controlled at 400 $\mu m$ with small variation. Otherwise

the best performance can not be guaranteed.

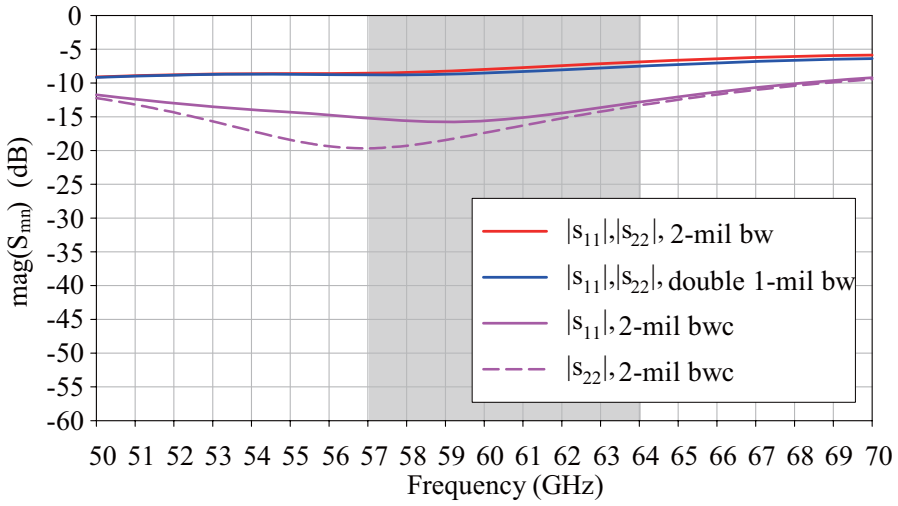


(a)

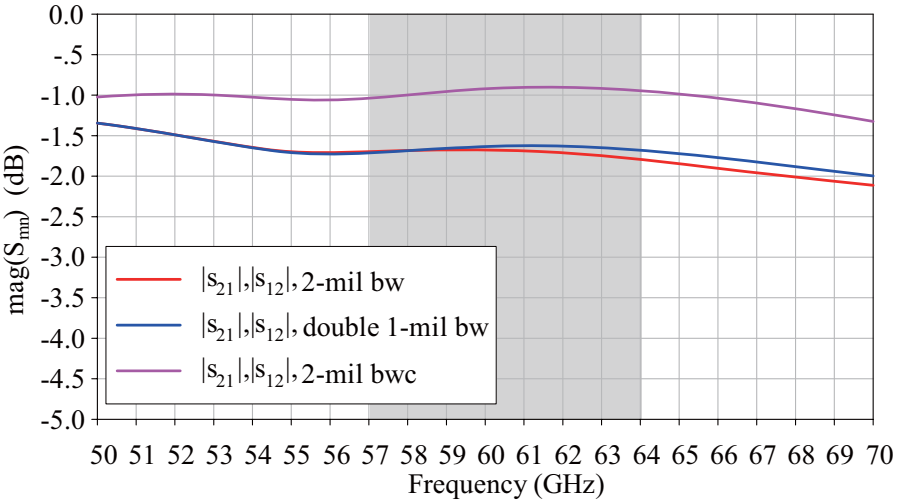


(b)

Figure 5.33: Bond wire interconnects for MSL-CPW configuration.

**Bond Wire Compensation in Integrated Array Antenna with LNA in LTCC**

The bond wire compensation at mmWave frequencies, especially 60 GHz is studied in detail in the previous parts. It provides the important information to guide the integration of 60-GHz chip into the package.

As shown in Fig. 5.29 (c) we use a T-network [90] to compensate for the series inductance introduced by the bond wire. The bond wire length is fixed at 500 $\mu m$ to facilitate the compensation structure design. In addition, to simplify the design the 50-$\Omega$ dummy microstip line on chip is used in simulation. The transition 1 as shown in Fig. 5.29(c) is simulated, where a 50-$\Omega$ GCPW is cascaded by a T-junction bond wire compensation line (by layers of $M2$ and $M3$-4) to connect to the chip 50-$\Omega$ dummy line using bond wires. The effect of the bond wire compensation network on the electrical performance is shown in Fig. 5.34, where the 2-mil bond wire is used. As we can see, the matching is optimized at 60 GHz, leading to a better return loss from 9 dB to 18 dB and a reduction in insertion loss from 1.18 to 0.6 dB at this frequency. In simulation, it is also found that the bond wire length variation of $\pm$25 $\mu m$ will have insignificant effect on performance. Tables 5.7 and 5.8 also show the variation of the return loss and insertion loss with the bond wire diameter. As expected with thinner bond wires, the transition 1 has the worse performance, indicated by an increased insertion loss value. However, if the wire bonding condition in fabrication is limited to 1-mil the performance is still acceptable with less stringent requirement.

To study the bond wire compensation experimentally, one 1-mil bonding wire and two 1-mil bonding wires for back-to-back cases are employed as shown in Fig. 5.35. Fig. 5.36 shows the measured results. It is demonstrated that the wire bondings with compensation show better performance at 60 GHz band than their un-compensated counterparts. As expected, the 2-wire bondings with compensation achieves best performance in terms of

matching and insertion loss.

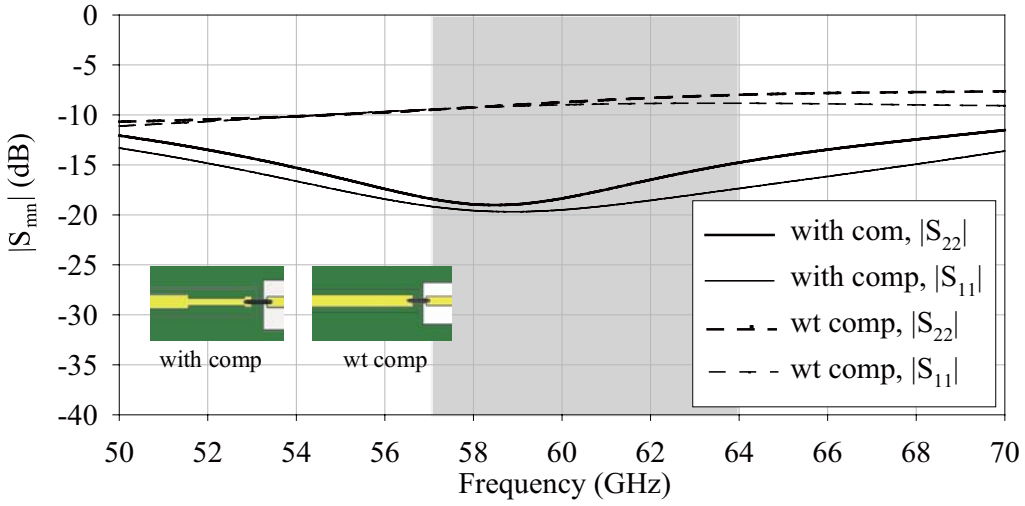


(a)

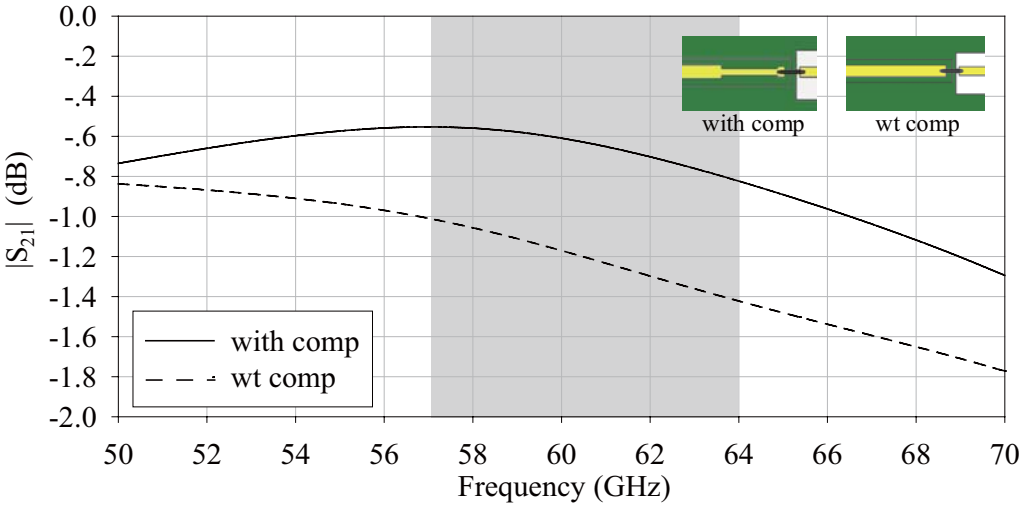


(b)

Figure 5.34: Simulated results for transition 1 compared with the results without compensation (500-$\mu m$ long 2-mil bond wire is used): (a) $|S11|$, $|S22|$ and (b) $|S21|$.

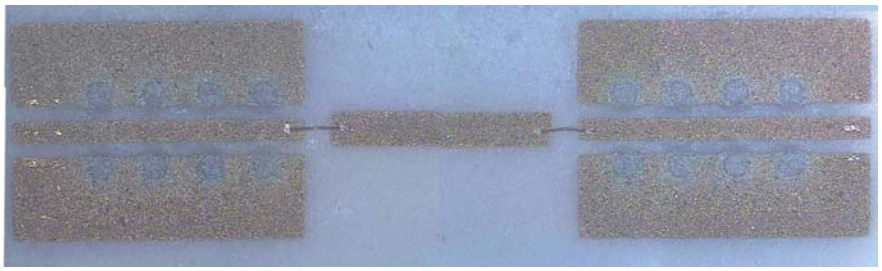

(a) 1-wire bonding, wt comp

(b) 2-wire bonding, wt comp

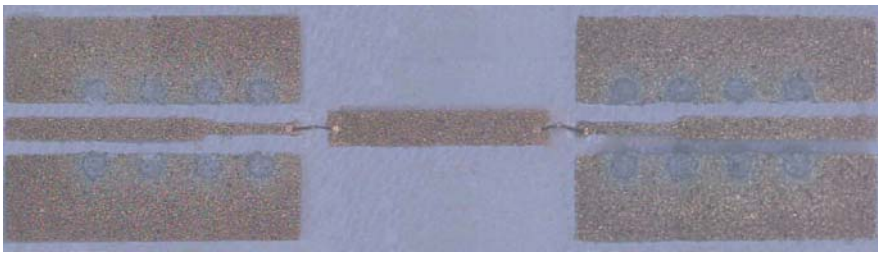

(c) 1-wire bonding, with comp

(d) 2-wire bonding, with comp

Figure 5.35: Bond wire compensation study.

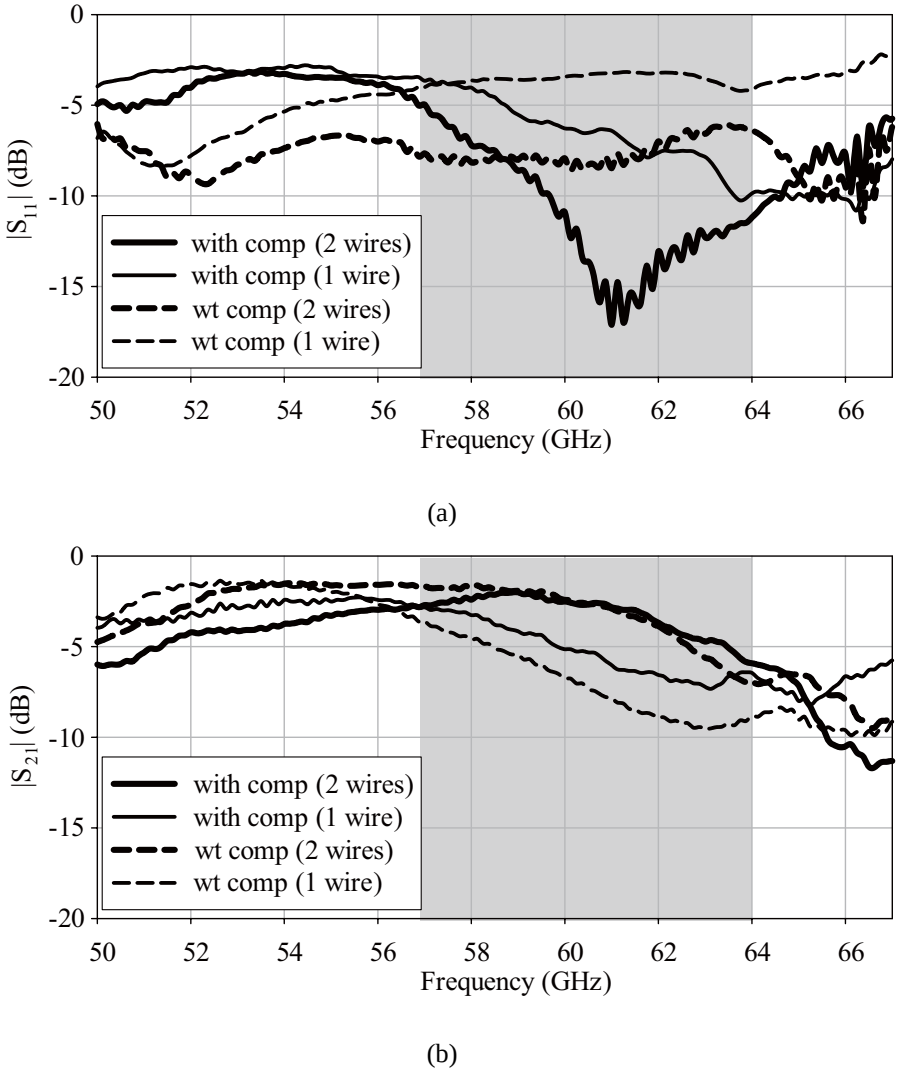


Figure 5.36: Measured results for bond wire compensation study: (a)$|S11|$ and (b) $|S21|$.

### 5.6.2 Low loss transitions

In the integration design, attenuation caused by radiations at the discontinuities and impedance mismatch along the transmission lines and integrated devices should be minimized for power efficiency and noise performance of the mm-wave system. By properly designing the structure and placing grounding vias around the transitions the attenuation

can be remedied. In our transition 2 design, the GCPW is cascaded by a signal via and finally fed to the stripline of the antenna. Through this transition the stripline fed antenna is transformed to GCPW-fed format making it convenient for probe-touching test. Fig. 5.37 shows the performance of this transition. It is seen that the matching is optimized at 60 GHz, leading to a good return loss of 20 dB and insertion loss of 0.28 dB. In the transition 3 design, the bond wire compensation structure is cascaded by the transition 2. This increases the insertion loss to 0.57 dB at 60 GHz with input and output matching still better than 20 dB. In the transition 4 design, the transition 1 and transition 3 combined to lead to a further increased insertion loss of 0.7 dB at 60 GHz while input and output matching still better than 20 dB. It should be noted that 0.7 dB attenuation is quite satisfactory for this complex transition with bond wires. Table 5.7 and 5.8 also show the variation of the return loss and insertion loss with the bond wire diameter. As expected with thinner bond wires the transitions 3 and 4 have the worse performance, indicated by an increased insertion loss value. It should be noted that the whole transition performance in some bond wire cases is better than its part performance owing to the global optimization.

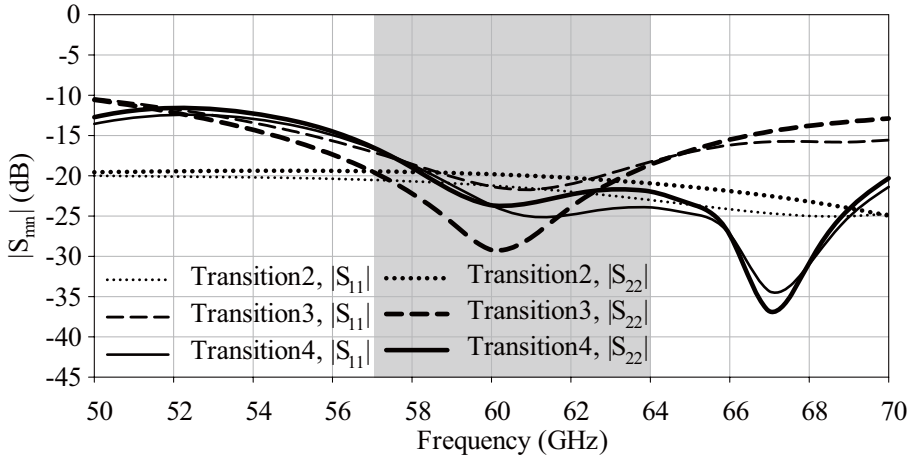


(a)

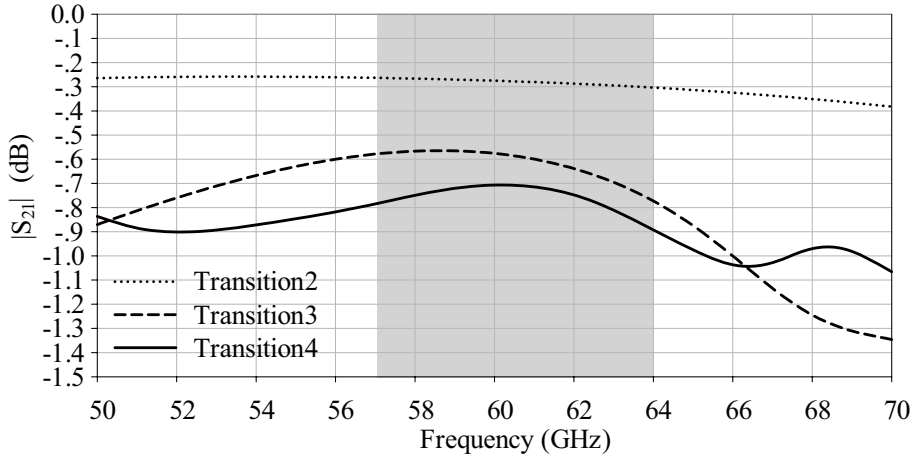


(b)

Figure 5.37: Simulated results for transitions 2-4: (a) $|S11|$, $|S22|$ and (b) $|S21|$.

Table 5.7: BOND WIRE EFFECT ON $|S21|$ PERFORMANCE OF TRANSITIONS

| 500-$\mu m$ long Bondwire | Transition1 | Transition2 | Transition3 | Transition4 |
|---|---|---|---|---|
| 2 mil | $> -0.82^1, -0.61^2$ | >-0.3, -0.27 | >-0.77, -0.57 | > -0.9,- 0.7 |
| 1 mil | >-1.3, -0.89 | >-0.3, -0.27 | >-1.12, -0.77 | >-1.1, -0.8 |

[1]performance over 57-64 GHz, [2]performances at 60 GHz, unit: dB

Table 5.8: BOND WIRE EFFECT ON $|S11|$ / $|S22|$ PERFORMANCE OF TRANSITIONS

| 500-$\mu m$ long Bondwire | Transition1 | Transition2 | Transition3 | Transition4 |
|---|---|---|---|---|
| 2 mil | $< -14.7^1, < -18^2$ | <-19.5,-19.8 | <-18,-21 | < -16, -23 |
| 1 mil | <-9, -11 | <-19.5,-19.8 | <-11,-13 | <-18, -18 |

[1]performance over 57-64GHz, [2]performances at 60 GHz, unit: dB

**Integration simulation**

With a dummy 50-$\Omega$ microstrip line on chip, we evaluate the performance of the whole active antenna as shown in Fig. 5.29. It is found from Fig. 5.38 that transitions degrade the impedance bandwidth. It is reduced to 16.5 GHz (53-69.5 GHz) from 18.5 for VSWR<2.

The transitions also lead to a slightly larger LHCP radiation component while 3-dB beam width still remains unchanged. In addition, the peak gain is reduced from 16.8 dBi to 14.9 dBi by 1.9 dB. The 3-dB gain bandwidth remains 10 GHz but shifts to the lower frequency band of 54.5-64.5 GHz. The 3-dB axial ratio bandwidth broadens to 9 GHz (54.25-63.25 GHz) due to the AR performance improvement at the lower frequency. As a summary the integrated array antenna with transitions still exhibits a wideband impedance matching and wideband circularly polarized performances at 60 GHz.

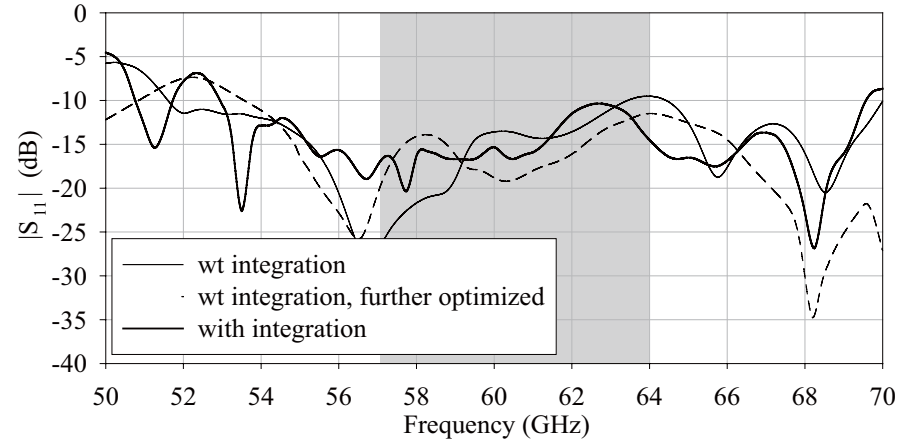


(a)

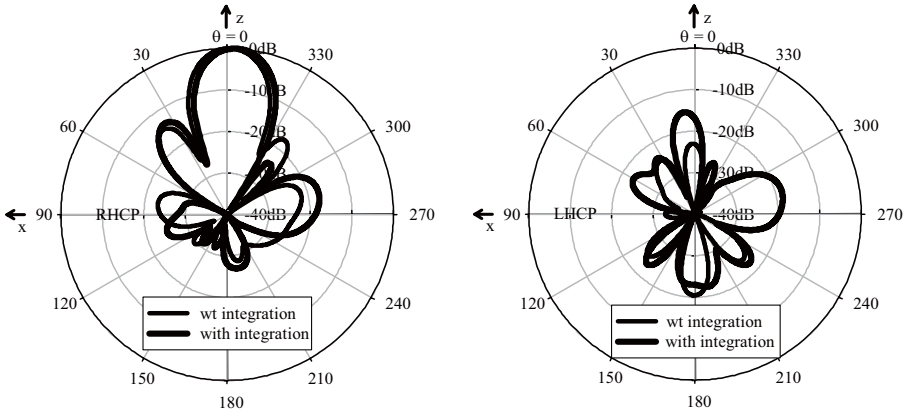


(b)

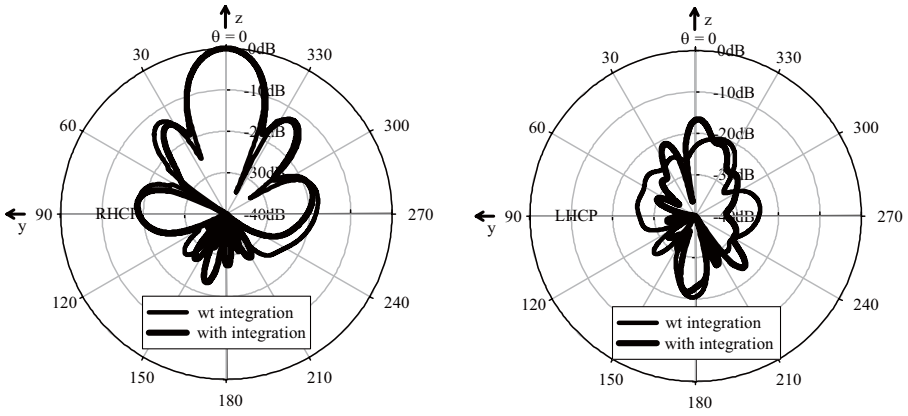


(c)

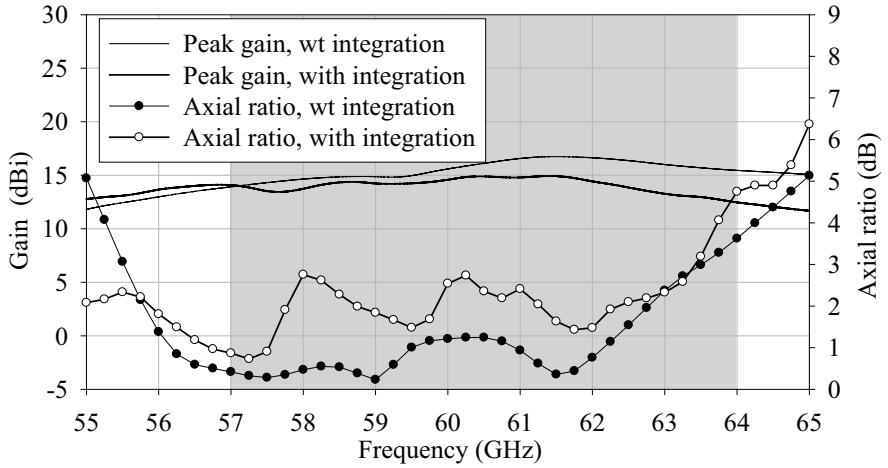


(d)

Figure 5.38: Simulated performance of the array antenna with transition 4: (a) $|S11|$, (b) $xz$- plane and (c) $yz$- plane radiation pattern at 60 GHz, (d) gain and axial ratio at the main radiation direction.

### 5.6.3 Antenna wireless test

CP array without LNA was fabricated as shown in Fig. 5.39(a). Note that the GCPW-SL transition as used in the Section 5.6.2 is added to this sample to facilitate testing. In

simulation, it is found that GCPW-SL transition does not degrade obviously the antenna performance presented in Fig. 5.38 except of a 0.6-dB peak gain penalty (from 16.8 dBi to 16.2 dBi). The antennas were tested by Agilent E8361A vector network analyzer (VNA) up to a frequency of 67 GHz. A GSG RF probe with a pitch of 250 m was touched on the GCPW line of the antenna for testing. With proper probe touching, the tested antenna senses the radiation in the boresight direction from a WR-15 standard pyramidal horn antenna. The horn antenna has an aperture size of $13 \times 10\ mm^2$ and a gain of 15 dBi. The far field region limit of the horn antenna can be calculated as $2D^2/\lambda_0 \approx 10.8cm$, where $D$ is the largest dimension of the horn and $\lambda_0$ is the free space wavelength. The distance between the horn aperture and the antenna under test is set around 15 $cm$. The antenna patterns were also measured with the set up as shown in Fig. 5.40(a).

Fig. 5.41 and Fig. 5.42 show the simulated and measurement results for the antenna without LNA. It is found from Fig. 5.41(a) that the antenna has a wide impedance matching bandwidth larger than 8 GHz, which is 11.5 GHz from 50.5-62 GHz for $SWR < 2$. If there was no measured hump around 63.5 GHz the bandwidth would be even larger. The occurrence of the similar bump in Fig. 5.38 (a) enlightens us to improve our basic array matching performance to eliminate this hump in the next round fabrication. This can be done by optimizing the antenna dimensions. Fig. 5.38(a) also shows one optimized result. Fig. 5.41(b) shows a measured peak gain $> 16$ dBi over 60 GHz band. Fig. 5.41(c) also confirms the good AR bandwidth performance in measurement. Fig. 5.42 presents the measured patterns with upward radiations.

A 21-dB Low noise amplifier (LNA), HMC-ALH382 [93] is used in the finally fabricated active antenna. The amplifier die has a size of $1.55 \times 0.73 \times 0.1\ mm^3$ with pads laid

out as illustrated in Fig. 5.29 to facilitate the wire bonding. Fig. 5.39 (b) shows the photograph of the final fabricated active antenna for measurement. It measures only $13 \times 20 \times 1.4$ $mm^3$.The active antenna was also measured with VNA. However, another DC probe was touched to provide a biasing drain voltage of $+2.5$ V and a gate voltage of $-0.3$ V. A total 64 $mA$ drain current was thus obtained in measurement. Fig. 5.43 shows a measured bandwidth of 4.3 GHz (60.7-65 GHz) for $SWR < 2$.

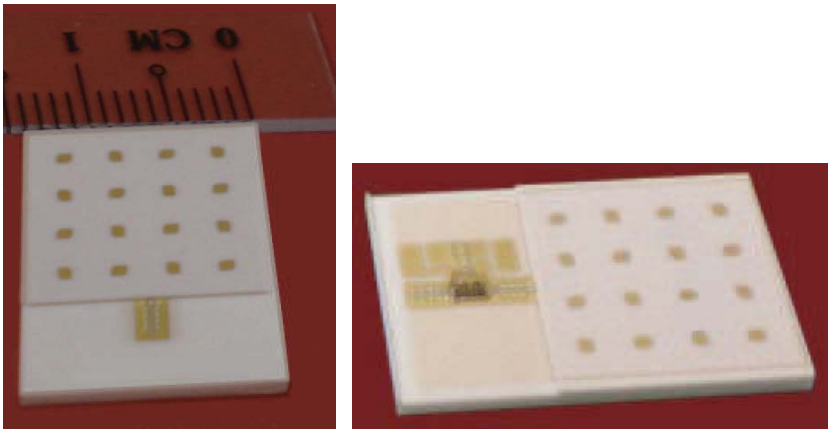

(a) (b)

Figure 5.39: Photograph of the fabricated samples for test: (a) the referenced array antenna without amplifier and (b) the active array antenna with amplifier.

Finally, the set up as shown in Fig. 5.40(b) is used to study the polarization characteristic of the antenna. The horn antenna is placed on the top of the AUT antenna. They are both paralleled to $xy - plane$. The tests are then conducted with horn at $0^\circ$ position (E field of horn is in the xz direction) and $90^\circ$ position (E field of horn is in the yz direction), respectively. Fig. 5.44 shows the measured transmission performance. The circularly polarized characteristic is observed with both transmission coefficients at $0^\circ$ and $90^\circ$ positions having the similar amplitude. In addition, compared with the transmission coefficients measured at the case of without amplifier, those measured with amplifier show an average increase

of approximately 19 dB from 60.7-65 GHz, which is very close to the amplifier gain value of 21 dB deducted by a 1.9-dB loss as evaluated in Section 5.6.2. Based on the above the final estimated peak gain of the active antenna is at least 35 dBi.

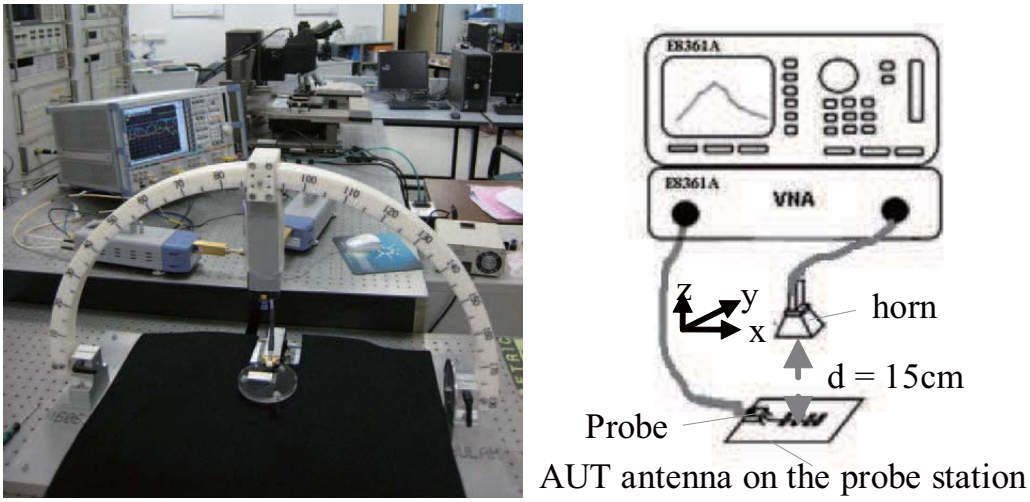


(a) (b)

Figure 5.40: Antenna wireless test set up.

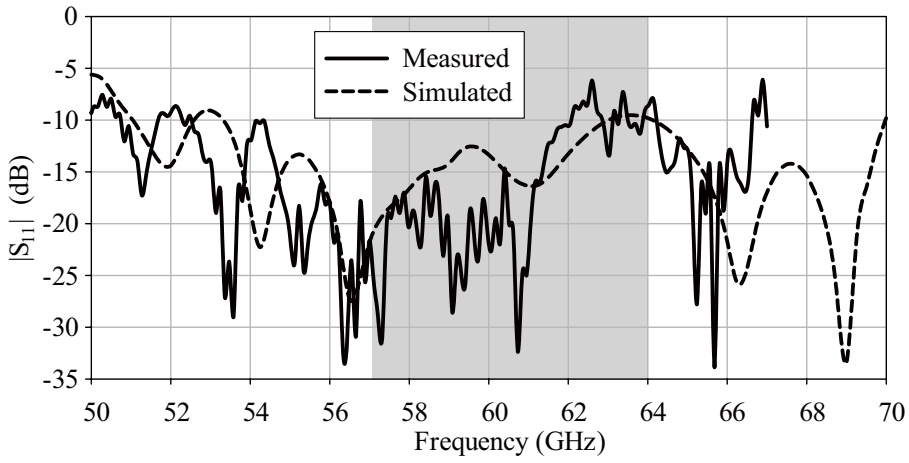


(a)

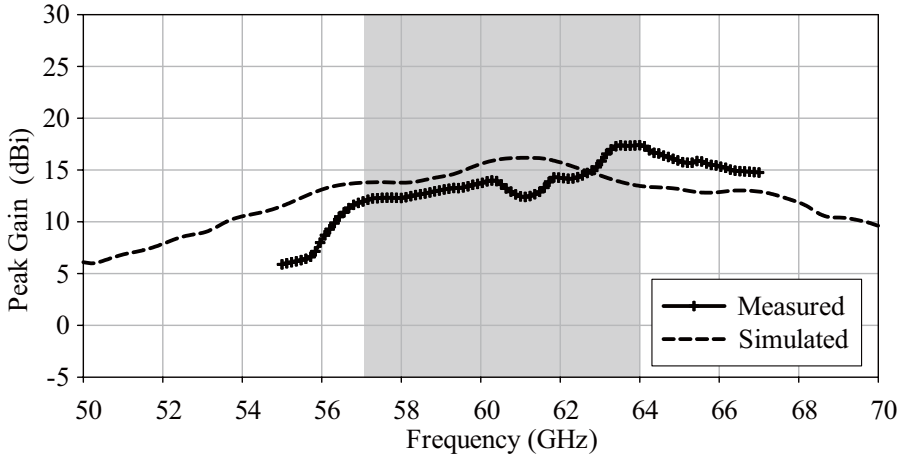


(b)

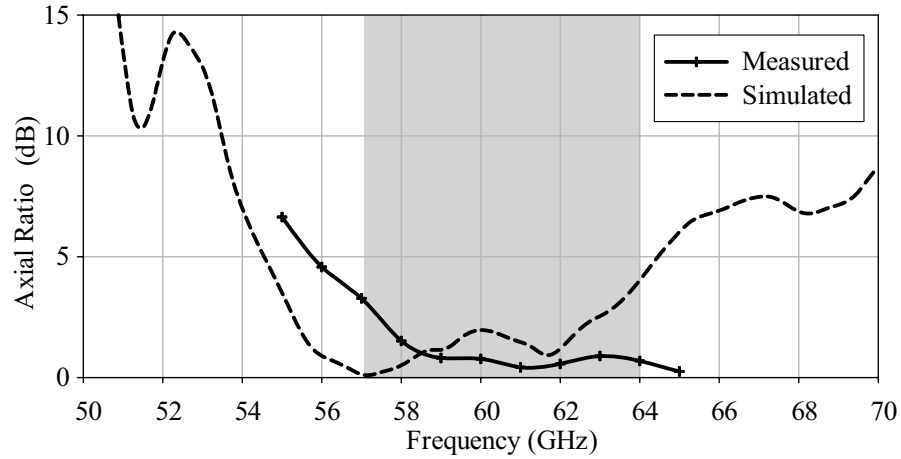


(c)

Figure 5.41: Measured and simulated performance for the antenna without LNA: (a) $|S11|$, (b) peak gain, (c) axial ratio at the main radiation direction.

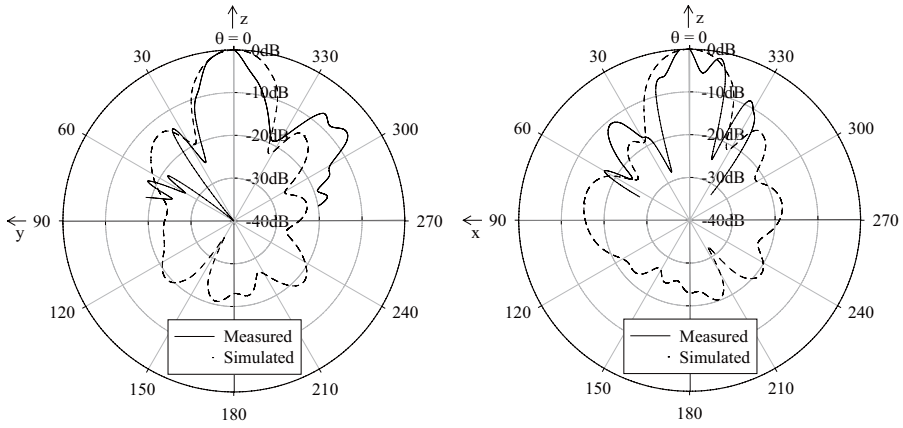


(a) 57 GHz

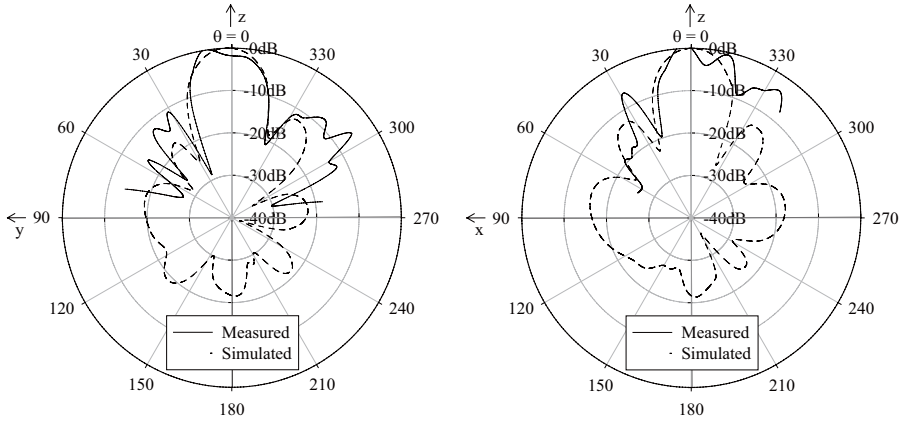


(b) 60 GHz

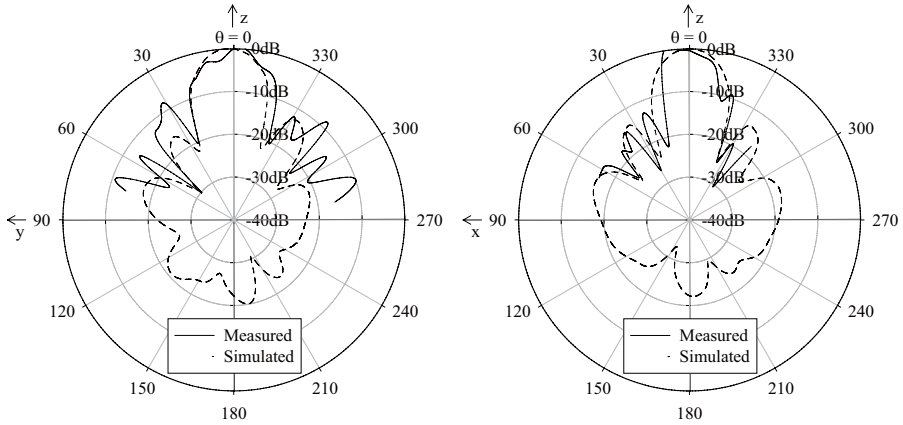


(c) 64 GHz

Figure 5.42: Measured and simulated xz- plane & yz- plane radiation pattern at 57, 60 and 64 GHz.

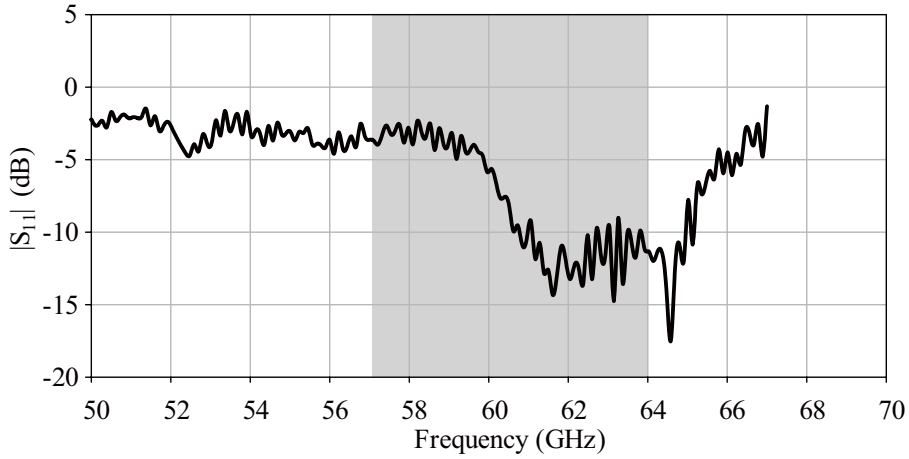


Figure 5.43: Measured $|S11|$ for the antenna with LNA.

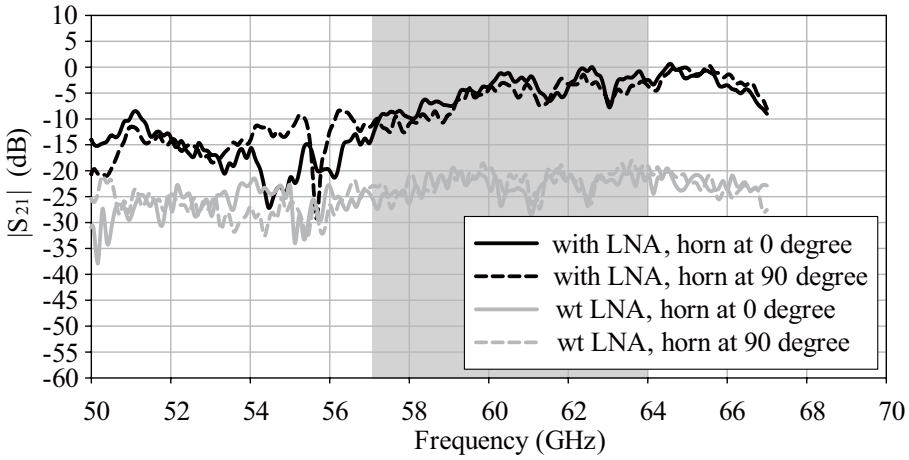


Figure 5.44: Measured $|S21|$ for the antenna with and without LNA. $0^{\circ}$ position: E field of horn in the xz direction, and $90^{\circ}$ position: E field of horn is in the yz direction

## 5.7 Conclusion

Various 60 GHz wideband antennas and arrays are designed in LTCC technology. A planar helical antenna array in LTCC at 60 GHz is proposed. This helical antenna array

takes the advantage of both traditional helical antenna and LTCC technology and achieves a good CP characteristic over wide operating frequency band (around 15 GHz). The planar structure and the stripline feeding scheme give a good solution for helical antennas and circuits' integration. Another $4 \times 4$ antenna array with a stripline sequential rotation feeding scheme exhibits a wide impedance bandwidth (VSWR$<$2) and 3-dB AR bandwidth, both over 8 GHz. The array also achieves a beam-shaped pattern with a 3-dB beam width of $20^{\circ}$ and peak gain of 16.8 dBi. This array was further integrated with a 21-dB LNA to form a compact 60-GHz active receiving antenna, where the low loss transition structures were optimized and the bond wire compensations were used to improve the performance of the 60-GHz chip-package interconnection. The fabricated active antenna prototype measures only $13 \times 20 \times 1.4\ mm^3$. The wireless test was finally conducted to study antenna performance. The wide impedance bandwidth was confirmed in measurement. The circularly polarized characteristic was also observed with co- and cross-polarization having the similar transmission amplitude in wireless test with the help of the horn antenna. The final estimated peak gain of the active antenna is at least 35 dBi. The designed active receiving antenna will find its application in the 60-GHz wireless personal area networks.

# Chapter 6

# Conclusions and Suggestions for Future Works

## 6.1 Conclusion

The main focus of the work presented in this thesis is on the design and analysis of UWB and mmWave antennas and arrays for developing high-speed short-range wireless communications. Various novel wideband antennas and arrays are designed for UWB and mmWave applications. The major original contributions are made as below.

As the bandwidth demand of modern wireless communication systems is expanding, especially for UWB applications, it is necessary to use antennas that have wide impedance bandwidth. Several novel UWB probe-fed antennas are developed in Chapter 2. A probe-fed crossed circle-disc monopole UWB antenna is cut by half to form a novel crossed semi-circle monopole antenna with a top-loaded patch to reduce its height. The radiation properties of the proposed UWB probe-fed antennas are fully investigated both in frequency domain and time domain. The cross-circle disc and semi-circle cross-plate antennas perform wide impedance bandwidths, stable radiation pattern and good time-domain

responses. Moreover, a new semi-ring monopole antenna with band-notched function is developed by adding four L-shaped slots in the radiating plates.

In chapter 3, a new compact and multilayer UWB planar antenna is designed using the low-temperature co-fired ceramics (LTCC) technology, which gives the possibility of integrating RF circuits and antennas in a single substrate. Utilizing the LTCC technology, two narrow band radiation elements are combined together to achieve a UWB antenna over 7 GHz. The configuration of the proposed multilayer UWB LTCC planar antenna fully exploits the three-dimensional (3-D) integration feature of the LTCC technology and explores a new way for antenna size reduction technique.

In chapter 4, an effective equivalent circuit for a UWB antenna is proposed for possible co-designing with analog/digital integrated circuits in the time domain by using a new automatic physical augmentation with tuning method. For the new automatic physical augmentation with tuning method, all series augmentation elements are transformed into their parallel equivalents, which reduced the preliminary analysis of the circuit to decide the augmentation type. Tuning is treated as a special case of augmentation by allowing negative valued element augmentation in some circumstances. The proposed method has been validated for modeling a spiral inductor and an MIM capacitor in a wide bandwidth. Further, the new method has been successfully applied to extract the equivalent circuits for two UWB antennas.

In chapter 5, novel 60 GHz integrated antenna and arrays using the LTCC technology are developed. A new wideband planar circularly polarized helical antenna array has

been designed and realized in LTCC for the first time. Moreover, a 60-GHz wideband LTCC aperture-coupled truncated-corner circularly polarized patch antenna with a sequential rotation feeding scheme is proposed and further integrated with a 21-dB LNA to form a compact active receiving antenna. The low loss transition structures are optimized and the bond wire packaging technology with a T-network compensation are studied and used to improve the performance of the 60-GHz chip-package interconnection. The fabricated active antenna prototype demonstrated its wide impedance bandwidth, circularly polarized characteristic and enhanced receiving power.

## 6.2 Suggestions for Future Works

Antenna design is under rapid progress with the fast development in technology in this area. With the growing requirements on wireless communication, there is plenty of room for future extension of antenna design. The following items represent some possible future research directions.

1. Since UWB antenna with band-pass filter property has great potential for commercial application, new compact UWB antenna structure which can provide higher rejection performance at 5 GHz WLAN band is desired to increase the whole system's rejection ability.

2. Co-design of an antenna and an LNA is necessary for practical UWB application. An integrated solution to suppress the in-band/out-band interference without system size increase and compromise in system performance is highly desirable. Extension of our wideband circuit modeling method to co-design an antenna and an LNA for UWB system is a suitable research topic.

3. New techniques should be explored to further reduce the size of the UWB antennas to suit practical applications. Meta-material is a promising candidate since it can reduce the antenna size greatly in theory. Although most of current meta-material antennas are narrow bandwidth applications, we believe that it will become available for wideband operation in the near future.

4. The mmWave technology is being developed rapidly in recent years due to its high-data rate transmission ability. As a critical element of wireless communication system, mmWave antennas are nearly always be integrated with the chip or chip package. As a result, wideband interconnection compensation techniques are necessary to mitigate the packaging challenges. On the other hand, mmWave antennas and arrays with new packaging means could be developed.

# Bibliography

[1] M. Pelissier, F. Demeestere, F. Hameau, D. Morche, and C. Delaveaud, “LNA-antenna codesign for UWB systems”, in *Proc. IEEE Int. Symp. Circuits and Systems (ISCAS)*, pp. 4711-4714, May 2006.

[2] S. K. Moore, “Cheap chips for next wireless frontier”, *IEEE Spectrum*, vol. 43, no. 6, pp. 8-9, Jun. 2006.

[3] I. Oppermann, M. Hamalainen and J. Iinatti, “UWB Theory and Applications”, John Wiley & Sons, pp. 130, 2004.

[4] Y. Mushiake, “Self-complementary antennas,” *IEEE Trans. Antennas Propagat. Mag.*, vol. 34, no. 6, pp. 23 - 29, Dec. 1992.

[5] P. E. Mayes, “Frequency-independent antennas and broad-band derivatives thereof” *Proc. IEEE*, vol. 80, no. 1, pp. 103 - 112, Jan. 1992.

[6] T. W. Hertel and G. S. Smith, “On the dispersive properties of the conical spiral antenna and its use for pulsed radiation,” *IEEE Trans. Antennas Propagat.*, vol. 51, no. 7, pp. 1426 - 1433, Jul. 2003.

[7] L. Chang and W. Burnside, “An ultrawide-bandwidth tapered resistive TEM horn antenna,” *IEEE Trans. Antennas Propagat.*, vol. 48, no. 12, pp. 1848 - 1857, Dec. 2000.

[8] C. W. Harrison, and C. S. Williams, “Transients in wide-angle conical antennas,” *IEEE Trans. Antennas Propagat.*, vol. 13, no. 2, pp. 236 - 246, Mar. 1965.

[9] N. P. Agrawall, G. Kumar, and K. P. Ray , “Wide-band planar monopole antenna,” *IEEE Trans. Antennas Propagat.*, vol. 46, no. 2, pp. 294 - 295, Feb. 1998.

[10] L. Guo, J. Liang, C. C. Chiau, X. Chen, C. G. Parini and J. Yu, “Time domain characteristics of UWB disc monopole antennas,” *2005 European Microwave Conference*, vol. 3, pp. 4, Oct. 2005.

[11] P. V. Anob, K. P. Ray, and G. Kumar, “Wideband orthogonal square monopole antennas with semi-circular base,” *IEEE Antennas Propagat. Soc. Int. Symp.*, vol. 3, pp.294-297, 2001.

[12] M. J. Ammann, R. S. Cordoba, M. Uzelac, J. A. Evans, and A. T. Schwarzbacher, “On pattern stability of the crossed planar monopole,” *Microwave Opt. Technol. Lett.*, vol. 40, no. 4, pp. 294-296, Feb. 2004.

[13] Y. Zhang, W. Hong, Y. Chen, Z. Q. Kuai, Y. D. Don, and J. Y. Zhou, “Planar Ultrawideband Antennas With Multiple Notched Bands Based on Etched Slots on the Patch and/or Split Ring Resonators on the Feed Line,” *IEEE Trans. Antennas Propagat.*, vol. 56, no. 9, pp. 3063-3068, Sept. 2008.

[14] T. G. Ma and S. J. Wu, “Ultrawideband Band-Notched Folded Strip Monopole Antenna,” *IEEE Trans. Antennas Propagat.*, vol. 55, no. 9, pp. 2473-2479, Sept. 2007.

[15] S. Nikolaou, N. D. Kingsley, G. E. Ponchak, J. Papapolymerou, and M. M. Tentzeris, "UWB Elliptical Monopoles With a Reconfigurable Band Notch Using MEMS Switches Actuated Without Bias Lines," *IEEE Trans. Antennas Propagat.*, vol. 57, no. 8, pp. 2242-2251, Aug. 2009.

[16] S. H. Min, and M. Swaminathan, "Efficient Construction of Two-port Passive Macro-models for Resonant Networks," in *IEEE Proc. Of 10th Topical Meeting of Electrical Performance of Electronic Packaging*, pp. 229-232, Oct. 2001.

[17] J. Kolstad, C. Blevins, J. M. Dunn, and A. Weisshaar, "A new circuit augmentation method for modeling of interconnects and passive components," *IEEE Trans. Advanced Packaging*, vol. 29, no. 1, pp. 67-77, Feb. 2006.

[18] D. Paul, M. S. Nakhla, R. Achar, and A. Weisshaar, "A passive algorithm for modeling frequency-dependent parameters of coupled interconnects," in *IEEE Proc. of Topical Meeting on Electrical Performaice of Electronic Packaging*, pp. 185-188, Oct. 2006.

[19] D. Paul, M. S. Nakhla, R. Achar, and A. Weisshaar, "Broadband modeling of high-frequency microwave devices," *IEEE Trans. Microw. Theory Tech.*, vol. 57, no. 2, pp. 361-373, Feb. 2009.

[20] S. Mukherjee, M. Swaminathan, and S. N. Lalgudi, "Broadband Modeling and Tuning of Multi-layer RF Circuits using Physical Augmentation Methodology," in *Proc. of APMC*, pp. 1-4, Dec. 2007.

[21] Y. X. Guo, A. Rasmita, and A. Alphones, "Wideband Modeling of RF Circuits Using Automatic Physical Augmentation," *Proc. Euro. Microw. Conf.*, pp. 1191 - 1194, Oct. 2009.

[22] S. Mukherjee, “Layout-level Circuit Sizing and Design-for- manufacturability Methods for Embedded Passive RF Circuits,” PhD thesis, Georgia Institute of Technology, 2007.

[23] Z. N. Chen, M. J. Ammann, X. Qing, X. H. Wu, T. S. P. See, and A. Cai, “Planar antennas: Promising solutions for microwave UWB applications,” *IEEE Microw. Magazine,* vol. 7, no. 6, pp. 63-73, Dec. 2006.

[24] J. Liang, C. C. Chiau, X. D. Chen, and C. G. Parini, “Study of a Printed Circular Disc Monopole Antenna for UWB Systems,” *IEEE Trans. Antennas Propagat.*, vol. 53, no. 11, pp. 3500-3504, Nov. 2005.

[25] A. M. Abbosh and M. E. Bialkowski, “Design of Ultrawideband Planar Monopole Antennas of Circular and Elliptical Shape,” *IEEE Trans. Antennas Propagat.*, vol. 56, no. 1, pp. 17-23, Jan. 2008.

[26] S. K. Padhi, S. Zagriatski, S. Crozier and M. E. Bialkowski, “Investigations into printed monopole antennas for Ultra-Wideband applications,” *IEEE Antennas Propagat. Soc. Int. Symp.*, vol. 2A, pp. 651-654, Jul. 2005.

[27] X. S. Yang, K. F. Man, S. H. Yeung, and B. Z. Wang, “Planar monopole ultra-wide band antenna optimized by Jumping Genes Genetic Algorithm,” *IEEE Int. Conf. on Industrial Technol., ICIT 2008*, pp. 1-5, Apr. 2008.

[28] C. Ying and Y. P. Zhang, “A planar antenna in LTCC for single-package ultrawideband radio,” *IEEE Trans. Antennas Propagat.* , vol. 53, no. 9, pp. 3089-3093, Sept. 2005.

[29] X. M. Qing, Z. N. Chen, “Monopole-like Slot UWB Antenna on LTCC,” *IEEE Int. Conf. on Ultra-Wideband, ICUWB 2008*, vol. 2, pp. 121-124, Sept. 2008.

[30] D. Manteuffel and M. Arnold, “Considerations on configurable multi-standard antennas for mobile terminals realized in LTCC technology,” *3rd European Conference on Antennas Propagat.,EuCAP 2009*, pp. 2541-2545, Mar. 2009.

[31] G. Brzezina, L. Roy, and M. L. MacEachern, “Planar antennas in LTCC technology with transceiver integration capability for ultra-wideband applications,” *IEEE Trans. Microw. Theory Tech.*, vol. 54, no. 6, pp. 2830-2839, Jun. 2006.

[32] A. Yamada, E. Suematsu, K. Sato, M. Yamamoto, and H. Sato, “60GHz ultra compact transmitter/receiver with a low phase noise PLL-oscillator”, *IEEE MTT-S Int. Microw. Symp. Dig.*, vol.3, pp. 2035-2038, Jun. 2003.

[33] R. R. Tummala, M. Swaminathan, M. M. Tentzeris, J. Laskar, G. K. Chang, S. Sitaraman, D. Keezer, D. Guidotti, Z. R. Huang, K. Lim, L. X. Wan, S. K. Bhattacharya, V. Sundaram, F. H. Liu, and P. M. Raj, “The SOP for miniaturized, mixed-signal computing, communication, and consumer systems of the next decade,” *IEEE Trans. Advanced Packaging*, vol. 27, no. 2, pp. 250-267, May 2004.

[34] Y. C. Lee, W. Chang, and C. S. Park, “Monolithic LTCC SiP transmitter for 60GHz wireless communication terminals,” *IEEE MTT-S Int. Microw. Symp. Dig.*, pp. 1015-1018, Jun. 2005.

[35] Y. P. Zhang, and M. Sun, “An overview of recent antenna array designs for highly-integrated 60-GHz radios,” *3rd Euro. Conf. Antennas Propagat. (EuCAP)*, pp. 3783-3786, 2009.

[36] Y. P. Zhang, “Antenna-on-Chip and Antenna-in-Package Solutions to Highly Integrated Millimeter-Wave Devices for Wireless Communications,” *IEEE Trans. Antennas Propagat.*, vol. 57, no. 10, pp. 2830 -2841, Oct. 2009.

[37] U. Pfeiffer, J. Grzyp, D. Liu, B. Gaucher, T. Beukema, B. Floyd, and S. Reynolds, “A chip-scale packaging technology for 60-GHz wireless chipsets,” *IEEE Trans. Microw. Theory Tech.*, vol. 54, no. 8, pp. 3387-3397, Aug. 2006.

[38] D. Liu, and B. Gaucher, “Design consideration for millimetre wave antennas within a chip package,” *Proc. of IEEE Int. Workshop on Antenna Technol.*, pp. 13-16, Apr. 2007.

[39] Y. P. Zhang, M. Sun, K. M. Chua, L. L. Wai, and D. Liu, “Integration of Slot Antenna in LTCC Package for 60-GHz Radios,” *Electron. Lett.*, vol. 44, no. 5, pp. 330-331, Mar. 2008.

[40] M. Sun, Y. P. Zhang, K. M. Chua, L. L. Wai, D. Liu, and B. Gaucher, “Integration of Yagi antenna in LTCC package for differential 60-GHz radio,” *IEEE Trans. Antennas Propagat.*, vol. 56, no. 8, pp. 2780-2783, Aug. 2008.

[41] B. Pan, Y. Li, G.E.Ponchak, J. Papapolymerou, and M. M. Tentzeris, “A 60-GHz CPW-Fed High-Gain and Broadband Integrated Horn Antenna,” *IEEE Trans. Antennas Propagat.*, vol. 57, no. 4, Part 2, pp. 1050-1056, Apr. 2009.

[42] Y. P. Zhang, M. Sun, and L. H. Guo, “On-Chip Antennas for 60-GHz Radios in Silicon Technology,” *IEEE Trans. Electron. Devices*, vol. 52, no.7, pp. 1664-1668, 2005.

[43] A. E. I. Lamminen, J. Säily, and A. R. Vimpari, “60 GHz patch antennas and arrays on LTCC with embedded-cavity substrates,” *IEEE Trans. Antennas Propagat.*, vol. 56, no. 9, pp. 2865-2874, Sept. 2008.

[44] D. Nesic, A. Nesic, and V. Brankovic, “Circular polarized printed antenna array with broadband axial ratio,” *IEEE Antennas Propagat. Soc. Int. Symp.*, vol. 2, pp. 912-915, Jun. 2003.

[45] H. Uchimura, N. Shino, and K. Miyazato, “Novel circular polarized antenna array substrates for 60GHz-band,” *IEEE MTT-S Int. Microw. Symp. Dig.*, pp. 1875-1878, Jun. 2005.

[46] S. Pinel, Il Kwon Kim, K. Yang, and J. Laskar, “60 GHz Linearly and Circularly Polarized Antenna Arrays on Liquid Christal Polymer Substrate”, in *Proc. of the 3rd Euro. Microw. Conf.*, pp. 858 - 861, Sept. 2006.

[47] N. Caillet, S. Pinel, C. Quendo, C. Person, E. Rius, J. F. Favennec, and J. Laskar, “A Wideband Circularly Polarized Patch Array for V-band Low-Cost Applications”, *APMC*, pp. 1-4, Dec. 2007.

[48] R. G. Zhou, D. X. Liu, H. Xin, “Design of circularly polarized antenna for 60 GHz wireless communications,” *3rd Euro. Conf. on Antennas and Propagat., EuCAP 2009*, pp. 3787-3789, Mar. 2009.

[49] “First order and report, revision of part 15 of the commission’s rules regarding UWB transmission systems,” Fed Commun. Comm., FCC 02-48, Apr.22, 2002.

[50] Z. N. Chen, X. H. Wu, N. Yang and M. Y. W. Chia, “Design consideration for antennas in UWB wireless communication systems,” *IEEE AP-S Int. Symp. Dig.*, vol. 1, pp. 822-825, Jun. 2003.

[51] M. J. Ammann, and Z. N. Chen, “Wideband monopole antennas for multi-band wireless systems,” *IEEE antennas Propag. Mag.*, vol. 45, no. 2, pp. 146-150, Apr. 2003.

[52] J. Liang, C. C. Chiau, X. Chen, and C. G. Parini, “Study of a printed circular disc monopole antenna for UWB systems,” *Electron. Lett.*, vol. 40, no. 20, pp. 1246-1247, Oct. 2004.

[53] N. P. Agrawall, G. Kumar, and K. P. Ray, “Wide-Band Planar Monopole Antennas,” *IEEE Trans. Antennas Propagat.*, vol. 46, no. 2, pp. 294-295, Feb. 1998.

[54] K. L. Wong, C. H. Wu and F. S. Chang, “A compact wideband omnidirectional cross-plate monopole antenna,” *Microwave Opt. Technol. Lett.*, vol. 44, no. 6, pp. 492-494, Mar. 2005.

[55] W. S. Chen, M. K. Hsu, K. N. Yang, H. C. Su and H. M. Chen, “The Design of cross semi-elliptic disc monopole antenna and the band-rejected cross semi-elliptic monopole antenna for UWB Applications,” *IEEE Antennas Propagat. Soc. Int. Symp.*, pp.4649-4652, Jul. 2006.

[56] S. Honda, M. Ito, H. Seki, and Y. Jinbo, “A disk monopole antenna with 1:8 impedance bandwidth and omnidirectional radiation pattern,” in *Proc. Int. Symp. Antennas Propagat.*, Sapporo, Japan, pp. 1145-1148, 1992.

[57] M. Hammoud, P. Poey, and F. Colombel, “Matching the input impedance of a broadband disc monopole,” *Electron. Lett.*, vol. 29, no. 4, pp. 406-407, Feb. 1993.

[58] N. P. Agrawall, G. Kumar, and K. P. Ray, “Wide-band planar monopole antennas,” *IEEE Trans. Antennas Propagat.*, vol. 46, no. 2, pp. 294-295, Feb. 1998.

[59] A. Kerkhoff and H. Ling, “A parametric study of band-notched UWB planar monopole antennas,” in *Proc. IEEE Antennas and Propag. Soc. Int. Symp.*, vol. 2, pp. 1768-1771, Jun. 2004.

[60] J. N. Lee and J. K. Park, “Impedance characteristics of trapezoidal ultra-wideband antennas with a notch function,” *Microw. Opt. Technol. Lett.*, vol. 46, no. 5, pp. 503-506, Sep. 2005.

[61] H. K. Lee, J. K. Park, and J. N. Lee, “Design of a planar half-circleshaped UWB notch antenna,” *Microw. Opt. Technol. Lett.*, vol. 47, no. 1, pp. 9-11, Oct. 2005.

[62] K. L. Wong, Y. W. Chi, C. M. Su, and F. S. Chang, “Band-notched ultra-wideband circular-disk monopole antenna with an arc-shaped slot,” *Microw. Opt. Technol. Lett.*, vol. 45, no. 3, pp. 188-191, May 2005.

[63] C. Y. Huang, W. C. Hsia, and J. S. Kuo, “Planar ultra-wideband antenna with a band-notched characteristic,” *Microw. Opt. Technol. Lett.*, vol. 48, no. 1, pp. 99-101, Jan. 2006.

[64] C. Y. Huang and W. C. Hsia, “Planar ultra-wideband antenna with a frequency notch characteristic,” *Microw. Opt. Technol. Lett.*, vol. 49, no. 2, pp. 316-320, Feb. 2007.

[65] Y. Gao, B. Ooi, and A. Popov, “Band-notched ultra-wideband ringmonopole antenna,” *Microw. Opt. Technol. Lett.*, vol. 48, no. 1, pp.125-126, Jan. 2006.

[66] J. M. Qiu, Z. W. Du, J. H. Lu and K. Gong, “A planar monopole antenna design with band-notched characteristic,” *IEEE Trans. Antennas Propagat.*, vol. 54, no. 1, pp.288-292, Jan. 2006.

[67] C. Hong, C. Ling, I. Tarn, and S. Chung, “Design of a planar ultrawideband antenna with a new band-notched structure,” *IEEE Trans. Antennas Propagat.*, vol. 55, no. 12, pp. 3391-3397, Dec. 2007.

[68] K. Kim, Y. Cho, S. Hwang, and S. Park, “Band-notched UWB planar monopole antenna with two parasitic patches,” *Electron. Lett.*, vol. 41, no. 14, pp. 783-785, Jul. 2005.

[69] S. Suh, W. Stutzman, W. Davis, A. Waltho, K. Skeba, and J. Schiffer, “A UWB antenna with a stop-band notch in the 5-GHz WLAN band,” in *Proc. IEEE ACES Int. Conf.*, pp. 203-207, Apr. 2005.

[70] B. L. Ooi, Y. Q. Zhang, I. Ang, and M. S. Leong, “UWB half-circle cross-plate monopole antenna”, *IEEE Antennas Propagat. Int. Symp.*, pp. 5717-5720, Jun. 2007.

[71] Y. Wang, J. Z. Li, and L. X. Ran, “An equivalent circuit modelling method for ultra-wideband antenna,” *PIER*, vol. 82, pp. 433-445, 2008.

[72] R. A. Rohrer, “Circuit Partitioning Simplified,” *IEEE Trans. Circuits and Systems*, vol. 35, no. 1, pp. 2-5, Jan. 1988.

[73] J. Sherman and W. J. Morrison, “Adjustment of an Inverse Matrix Corresponding to Changes in the Elements of a Given Column or a Given Row of the Original Matrix,” *Ann. Math. Statist.*, vol. 20, no. 4, pp. 621, 1949.

[74] W. Ciccognani, A. Durantini, and D. Cassioli, “Time domain propagation measurements of the UWB indoor channel using PN-sequence in the FCC-compliant band 3.6-6 GHz,” *IEEE Trans. Antennas Propagat.*, vol. 53, no. 4, pp. 1542-1549, Apr. 2005.

[75] R. Kohno and K. Takizawa, “Overview of research and development activities in NICT UWB consortium,” *IEEE Int. Conf. on Ultra-Wideband, ICU 2005*, pp. 735-740, Sept. 2005.

[76] K. L. Wong, Y. W. Chi, C. M. Su, and F. S. Chang, “Band-notched ultra-wideband circular-disk monopole antenna with an arc-shaped slot,” *Microw. Opt. Technol. Lett.*, vol. 45, no. 3, pp. 188-191, May 2005.

[77] I. Makris, D. Manteuffel, R. D. Seager and J. C. Vardaxoglou, “Modified Designs for UWB Planar Monopole Antennas,” *2007 Loughborough Antennas Propagat. Conf.*, pp.249-252, Apr. 2007.

[78] K. K. Kang, J. W. Lee, C. S. Cho, and T. K. Lee, “An improved Impedance Bandwidth of Modified UWB Antenna With Staircased Parasitic Rings,” *IEEE Antennas Wireless Propagat. Lett.*, vol. 6, pp. 521-524, 2007.

[79] Y. Duroc, A. Ghiotto, T. P. Vuong, and S. Tedjini, “Ultra-Wideband Antennas: Design and Modeling,” *Second Int. Conf. on Communications and Electronics, ICCE 2008*, pp. 318-323, Jun. 2008.

[80] Shenario Ezhil Valavan A, B. Yang, A. Yarovoy, and L. Ligthart, “Stacked patch UWB antenna in LTCC technology,” *3rd Euro. Conf. on Antennas Propagat., EuCAP 2009*, pp. 1467-1468, Mar. 2009.

[81] N. Hoivik, D. Liu, C. V. Jahnes, J. M. Cotte, C. Tsang, C. Patel, U. Pfeiffer, J. Grzyb, J. Knickerbocker, J. H. Magerlein, and B. Gaucher, "High-efficiency 60 GHz antenna fabricated using low-cost silicon micromachining techniques," *IEEE Antennas Propagat. Soc. Int. Symp.*, pp. 5043-5046, Jun. 2007.

[82] C. Karnfelt, P. Hallbjorner, H. Zirath, and A. Alping, "High gain active microstrip antenna for 60-GHz WLAN/WPAN applications," *IEEE Trans. Microw. Theory Tech.*, vol. 54, no. 6, pp. 2593-2603, Jun. 2006.

[83] J. R. James, and P.S. Hall, *Handbook of Microstrip Antennas*, Peter Peregrinus, London, UK, 1989.

[84] Y. Y. Du, and F. L. Liu, "A novel broadband circularly polarized microstrip helical antenna," *8th Int. Symp. Antennas Propagat. EM Theory (ISAPE)*, pp. 374-376, 2008.

[85] R. H. Caverly, "Characteristic impedance of integrated circuit bond wires," *IEEE Trans. Microw. Theory Tech.*, vol. 34, no. 9, pp. 982-984, Sept. 1986.

[86] G. Baumann, et al., "51 GHz frontend with flip chip and wire bond interconnections from GaAs MMICs to a planar patch antenna," *IEEE MTT-S Int. Microw. Symp. Dig.*, pp. 1639-1642, May 1995.

[87] T. Krems, W. Haydl, H. Massler, and J. Rudiger, "Millimeter-wave performance of chip interconnections using wire bonding and flip chip," *IEEE MTT-S Int. Microwave Symp. Dig.*, pp. 247-250, Jun. 1996.

[88] G. Felic, and E. Skafidas, "Flip-Chip Interconnection Effects on 60 GHz Microstrip Antenna Performance," *IEEE Antennas Wireless Propagat. Lett.*, vol. 8, pp. 283-286, May 2009.

[89] S. T. Choi, K. S. Yang, K. Tokuda and Y. H. Kim, “60 GHz Transceiver Module with Coplanar Ribbon Bonded Planar Millimeter-wave Bandpass Filter,” *Microw. Opt. Technol. Lett.*, vol.49, no. 5, pp. 1212-1214, May 2007.

[90] Y. Sun, S. Glisic, F. Herzel, K. Schmalz, E. Grass, W. Winkler, and R. Kraemer, “An integrated 60 GHz transceiver front end for OFDM in SiGe: BiCMOS,” presented at *Wireless World Research Forum 16*, Shanghai, China, Apr. 2006.

[91] M. Sun, and Y. P. Zhang, “A Chip Arrangement and A method of Determining and Inductivity Compensation Structure for Compensating a Bond Wire Inductivity in a Chip Arrangement”, filed US patent by NTU, Mar. 18, 2008.

[92] Y. P. Zhang, M. Sun, K. M. Chua, L. L. Wai, and D. Liu, “Wirebond Antenna-in-Package Design for Highly- Integrated 60-GHz Radios,” *IEEE Trans. Antennas Propagat.*, vol. 57, no. 10, pp. 2842-2852, Oct. 2009.

[93] $http://www.hittite.com/content/documents/data_sheet/hmc-alh382.pdf.$

[94] C. L. Lin, Antenna Engineering Handbook. Beijing, China: Electronics Industry Press, 2002.

[95] T. P. Budka, “Wide-bandwidth millimeter-wave bond-wire interconnects,” *IEEE Trans. Microw. Theory Tech.*, vol.49, no.4, pp. 715-718, Apr. 2001.